# Modelling, Estimation and Compensation of Imbalances in Quadrature Transceivers

by
Josias Jacobus de Witt

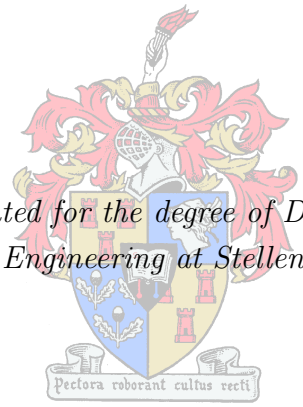


*Dissertation presented for the degree of Doctor of Philosophy in the Faculty of Engineering at Stellenbosch University*

Supervisor: Dr Gert-Jan van Rooyen
Department of Electrical and Electronic Engineering

March 2011

# Declaration

By submitting this dissertation electronically, I declare that the entirety of the work contained therein is my own, original work, that I am the sole author thereof (save to the extent explicitly otherwise stated), that reproduction and publication thereof by Stellenbosch University will not infringe any third party rights and that I have not previously in its entirety or in part submitted it for obtaining any qualification.

Date: March 2011

# Abstract

**Keywords:** frequency translation, quadrature mixing, quadrature modulation, $I/Q$ imbalance compensation, software-defined radio.

The use of the quadrature mixing topology has been severely limited in the past due to its sensitivity towards mismatches between its signal paths. In recent years, researchers have suggested that digital techniques can be used to compensate for the impairments in the analogue quadrature mixing front-end. Most authors, however, focus on the modelling and compensation of frequency-independent imbalances, reasoning that this approach is sufficient for narrow band signal operation. This common assumption is, however, becoming increasing less applicable as the use of wider bandwidth signals and multi-channel systems becomes more prevalent.

In this dissertation, baseband equivalent distortion models are derived, which model frequency-independent, as well as frequency-dependent contributions towards the imbalances of the front-end. Both lowpass and bandpass imbalances are modelled, which extends current modelling approaches found in literature. The resulting baseband models are shown to be capable of explaining the imbalance characteristics observed in practical quadrature mixing front ends, where existing models fail to do so.

The developed imbalance models is then used to develop novel frequency-dependent imbalance extraction and compensation techniques, which directly extract the exact quadrature imbalances of the front end, using simple test tones. The imbalance extraction and compensation procedures are implemented in the digital baseband domain of the transceiver and do not require high computational complexity. The performance of these techniques are subsequently verified through simulations and a practical hardware implementation, yielding significant improvement in the image rejection capabilities of the quadrature mixing transceiver.

Finally, a novel, blind imbalance compensation technique is developed. This technique is aimed at extracting frequency-independent $I/Q$ imbalances in systems employing digital modulation schemes. No test tones are employed and the imbalances of the modulator and demodulator are extracted from the second order statistics of the received signal. Simulations are presented to investigate the performance of these techniques under various operating conditions.

# Opsomming

**Sleutelwoorde:** frekwensieverskuiwing, haaksfasige mengproses, haaksfasige modulasie, $I/Q$ wanbalans-kompensasie, sagteware-gedefinieerde radio

Die gebruik van die haaksfasige mengtopologie word geweldig beperk deur die sensitiwiteit vir wanbalanse wat mag bestaan tussen die twee analoog seinpaaie. In die afgelope paar jaar het navorsers digitale metodes begin voorstel om te kompenseer vir hierdie wanbalanse in die analooggebied. Meeste navorsers fokus egter op frekwensie-onafhanklike wanbalanse. Hulle staaf hierdie aanslag deur te redineer dat dit 'n aanvaarbare aaname is vir 'n nouband stelsel. Hierdie algemene aanvaarding is egter besig om minder akkuraat te raak, namate wyeband- en multikanaalstelses aan die orde van die dag raak.

In hierdie tesis word basisband-ekwiwalente wanbelansmodelle afgelei wat poog om die effek van frekwensie-afhanklike en -onafhanklike wanbalanse akkuraat voor te stel. Beide laagdeurlaat- en banddeurlaatwanbalanse word gemodelleer, wat 'n uitbreiding is op die huididge modellerings benaderings wat in literatuur gevind word. Dit word aangetoon dat die modelle van hierdie tesis daarin slaag om die karakteristieke van 'n werklike haaksfasige mengstelsel akkuraat te vervat – iets waarin huidige modelle in die literatuur nie slaag nie.

Die basisband-ekwiwalente modelle word dan gebruik om nuwe digitale kompensasie metodes te ontwikkel, wat daarin slaag om die frekwensie-afhanklike wanbalanse van die haaksfasige mengstelsel af te skat, en daarvoor te kompenseer in die digitale deel van die stelsel. Hierdie kompensasiemetodes gebruik eenvoudige toetsseine om die wanbalanse af te skat. Die werksverrigting van hiedie kompensasiemetodes word dan ondersoek deur middel van simulasies en 'n praktiese hardeware-implementasie. Die resultate wys daarop dat hierdie metodes daarin slaag om 'n aansienlike verbetering in die beeldonderdrukkingsvermoëns van die haaksfasige mengers te weeg te bring.

Laastens word daar ook 'n blinde kompensasiemetode ontwikkel, wat gemik is op frekwensie-onafhanklike wanbalanse in digital-modulasie-skama stelsels. Vir hierdie metodes is geen toetsseine nodig om die wanbalanse af te skat nie, en word dit gedoen vanuit die tweede-orde statistiek van die ontvangde sein. Die werksverrigting van hierdie tegnieke word verder bevestig deur middel van simulasies.

# Acknowledgements

Thanks be to God for making all of this possible! I would also like to express a special word of thanks to the following people who have played a valuable part in the completion this work:

- Firstly to my study leader, Dr Gert-Jan van Rooyen, for your enormous amount of enthusiasm and expert advice. Thank you for your dedication throughout this study.
- To my wife, Francisca, for your love and dedication throughout this time. Thank you for always believing in me and encouraging me towards greater things.
- To my parents, for their unconditional love and never-ending support.

I would also like to thank the Telkom Center of Excellence for providing financial support for this study.

# List of Publications

The following publications have resulted from the work documented in this dissertation:

## International Journal Papers

1. De Witt, J.J., and Van Rooyen, G.-J., "A Blind I/Q Imbalance Compensation Technique for Direct-Conversion Digital Radio Transceivers", *IEEE Transactions on Vehicular Technology*, Vol. 58, No. 4, May 2009, pp. 2077-2082, ISSN: 0018-9545.

## International Conference Papers

1. De Witt, J.J., and Van Rooyen, G.-J., "A Self-Calibrating Quadrature Mixing Front-End for SDR", *Proceedings of the 2008 IEEE Radio and Wireless Symposium (RWS 2008)*, 22-24 January 2008, Orlando, FL., ISBN: 1-4244-1463-6.

## Local Conference Papers

1. De Witt, J.J., and Van Rooyen, G.-J., "Advanced quadrature imbalance compensation techniques for the SDR mobile platform" (poster), *Southern African Telecommunication Networks Applications Conference (SATNAC) 2005 Proceedings CD-ROM*, 11-14 September 2005, ISBN: 0-620-34907-7.

2. De Witt, J. J., and Van Rooyen, G.-J.,"Novel IQ imbalance and offset compensation techniques for quadrature mixing radio transceivers." *Southern African Telecommunication Networks Applications Conference (SATNAC) 2006 Proceedings CD-ROM*, 3–6 September 2006, ISBN: 0-620-37043-2.

# Contents

# List of Figures

# List of Tables

# Nomenclature

## Acronyms

| | |
|---|---|
| ADC | analogue-to-digital converter |
| ACF | autocorrelation functions |
| AWGN | additive white Gaussian noise |
| BER | bit-error rate |
| BPF | bandpass filter |
| BSS | blind source separation |
| CACF | complimentary autocorrelation function |
| CDMA | code division multiple access |
| CPFSK | continuous-phase frequency shift keying |
| DAC | digital-to-analogue converter |
| DC | direct current |
| DFT | discrete Fourier transform |
| DTFT | discrete-time Fourier transform |
| DSP | digital signal processor |
| EASI | equivariant adaptive separation via independence |
| FFT | fast Fourier transform |
| FIR | finite impulse response |
| GSM | global system for mobile communication |
| GSO | Gram Schmidt orthogonalization |
| IC | interference canceller |
| $I/Q$ | in-phase/quadrature |
| IF | intermediate frequency |
| IR | image-reject |
| LMS | least-mean-square |
| LO | local oscillator |
| LPF | lowpass filter |
| LS | least-squares |
| MLS | maximum-length sequence |
| NLS | nonlinear least-squares |
| OFDM | orthogonal frequency division multiplexing |
| PA | power amplifier |

| | |
|---|---|
| PN | pseudo noise |
| QAM | quadrature amplitude modulation |
| QPSK | quadrature phase shift keying |
| RF | radio frequency |
| RIR | relative image ratio |
| RLS | recursive least-squares |
| RX | receiver |
| SDR | software-defined radio |
| SINAD | signal-to-noise and distortion |
| SFDR | Spurious-free dynamic range |
| SIR | signal-to-interference ratio |
| SNR | signal-to-noise ratio |
| SMA | SubMiniature version A |
| SSB | single-sideband |
| SU | Stellenbosch University |
| TDM | time-division multiplexing |
| ZFE | zero-forcing equaliser |

**Principle variables**

| **symbol** | **description** |
|---|---|
| $A_r$ | Amplitude of passband demodulator input signal |
| $a(t)$ | Complex-valued baseband signal |
| $a_{fm}(t)$ | Complex-valued baseband tone at frequency $f_m$ |
| $a_{-fm}(t)$ | Complex-valued baseband tone at frequency $-f_m$ |
| $a_{\mathrm{pc}}(t)$ | Pre-compensated complex-valued baseband signal |
| $a_I(t)$ | In-phase component of $a(t)$ |
| $a_Q(t)$ | Quadrature component of $a(t)$ |
| $A(f)$ | Fourier transform of $a(t)$ |
| $A_I(f)$ | Fourier transform of $a_I(t)$ |
| $A_Q(f)$ | Fourier transform of $a_Q(t)$ |
| $A'_I(f)$ | $A_I(f)$ including the lowpass frequency response of the modulator's $I$-channel |
| $A'_Q(f)$ | $A_Q(f)$ including the lowpass frequency response of the modulator's $Q$-channel |
| $\boldsymbol{a}(n)$ | Symbol space (vector) representation of the $n$-th baseband transmit symbol |
| $A_{kI}$ | In-phase component in digital symbol space |
| $A_{kQ}$ | Quadrature component in digital symbol space |

| **symbol** | **description** |
|---|---|
| $A_l$ | Carrier amplitude in a carrier-phase-amplitude modulation scheme |
| $B$ | Bit precision of sampler system |
| $\boldsymbol{C}$ | Noise covariance matrix |
| $\boldsymbol{C}'$ | Noise covariance matrix after demodulator imbalances |
| $\boldsymbol{D}$ | Matrix of demodulator imbalances |
| $\boldsymbol{D}_{\text{res}}$ | Resultant demodulator imbalance matrix after compensation |
| $E_I(f)$ | Lowpass frequency response of modulator $I$ channel |
| $E_Q(f)$ | Lowpass frequency response of modulator $Q$ channel |
| $\boldsymbol{E}$ | Lower-triangular matrix - Cholesky factorisation of $\boldsymbol{Y'}$ |
| $\boldsymbol{E'}$ | $\boldsymbol{E}$ with the effect of $\lambda_M$ removed |
| $E_0$ | Quantisation interval |
| $f$ | Frequency domain variable |
| $f_0$ | Input frequency |
| $f_A$ | Baseband signal frequency |
| $f_c$ | Carrier (center) frequency |
| $f_D$ | Demodulator oscillator frequency |
| $f_\Delta$ | Frequency difference between the LOs of the modulator and demodulator |
| $f_{\text{IF}}$ | Intermediate frequency |
| $f_M$ | Modulator oscillator frequency |
| $f_r$ | Offset frequency of demodulator input signal |
| $f_s$ | Sampling rate |
| $f_{s\uparrow}$ | Oversampled sampling rate |
| $\boldsymbol{F}$ | Covariance matrix of signal at demodulator input |
| $\boldsymbol{F'}$ | Covariance matrix of signal at demodulator output |
| $g_I(t)$ | Bandpass impulse response of modulator $I$ channel |
| $g_Q(t)$ | Bandpass impulse response of modulator $Q$ channel |
| $\tilde{g}_I(t)$ | Complex-valued baseband-equivalent of $g_I(t)$ |
| $\tilde{g}_Q(t)$ | Complex-valued baseband-equivalent of $g_Q(t)$ |
| $g_T(t)$ | Baseband pulse shaping function |
| $G_I(f)$ | Fourier transform of $g_I(t)$ |
| $G_Q(f)$ | Fourier transform of $g_Q(t)$ |
| $\tilde{G}_I(f)$ | Fourier transform of $\tilde{g}_I(t)$ |
| $\tilde{G}_Q(f)$ | Fourier transform of $\tilde{g}_Q(t)$ |
| $h(l)$ | Complex channel impulse response |
| $H_I(f)$ | Lowpass frequency response of demodulator $I$ channel |
| $H_Q(f)$ | Lowpass frequency response of demodulator $Q$ channel |
| $H$ | Lower-triangular matrix - Cholesky factorisation of $\boldsymbol{F'}$ |
| $\boldsymbol{H}(l)$ | Matrix containing elements of complex channel impulse response |

| **symbol** | **description** |
|---|---|
| $I_M(f)$ | Relative image ratio of the imbalanced modulator |
| $I_D(f)$ | Relative image ratio of the imbalanced demodulator |
| $\boldsymbol{I}$ | Identity matrix |
| $j$ | $\sqrt{-1}$ |
| $K_1$ | Power ratio |
| $K_2$ | Power ratio |
| $k$ | Iterator |
| $l$ | Iterator |
| $L$ | Length of complex channel impulse response |
| $L_I(f)$ | Bandpass frequency response of demodulator $I$ channel |
| $L_Q(t)$ | Bandpass frequency response of demodulator $Q$ channel |
| $\tilde{L}_I(f)$ | Baseband-equivalent of $L_I(f)$ |
| $\tilde{L}_Q(f)$ | Baseband-equivalent of $L_Q(f)$ |
| $\boldsymbol{M}$ | matrix of modulator imbalances |
| $\boldsymbol{M}_{\text{res}}$ | Resultant modulator imbalance matrix after compensation |
| $M$ | Digital alphabet size |
| $M1$ | Number of amplitude positions in a carrier-phase-amplitude modulation scheme |
| $M2$ | Number of phase positions in a carrier-phase-amplitude modulation scheme |
| $N$ | Number of frequency points where the desired filter response is specified |
| $N$ | Estimation block size |
| $N$ | FFT length |
| $n$ | Discreet time sample iterator |
| $O_1$ | Observation 1: Complex scaling of desired component for $f = f_m$ |
| $O_2$ | Observation 2: Complex scaling of image component for $f = -f_m$ |
| $O_3$ | Observation 3: Complex scaling of desired component for $f = -f_m$ |
| $O_4$ | Observation 4: Complex scaling of image component for $f = f_m$ |
| $O_{1,\Delta}$ | Observation 1: Complex scaling of desired component for $f = f_m$, after applying gain scaling $\Delta\eta$ |
| $O_{4,\Delta}$ | Observation 4: Complex scaling of image component for $f = f_m$, after applying gain scaling $\Delta\eta$ |
| $O_{d,f_r}$ | Scaling of desired component at demodulator output for, an input tone at frequency $f_r$. |
| $O_{i,f_r}$ | Scaling of image component at demodulator output for, an input tone at frequency $f_r$. |
| $O_{M1}$ | Observation of desired component |
| $O_{M2}$ | Observation of image component due to modulator imbalances |

| **symbol** | **description** |
|---|---|
| $O_{M3}$ | Observation of desired component |
| $O_{M4}$ | Observation of image component due to modulator imbalances |
| $O_{D1}$ | Observation of desired component |
| $O_{D2}$ | Observation of image component due to demodulator imbalances |
| $O_{D3}$ | Observation of desired component |
| $O_{D4}$ | Observation of image component due to demodulator imbalances |
| $P_1(f)$ | Frequency response of demodulator compensation filter |
| $P_2(f)$ | Frequency response of optimum demodulator post-compensation filter |
| $P_{Qn}$ | Quantisation noise power |
| $P_s$ | Desired signal power |
| $Q_1(f)$ | Frequency response of modulator compensation filter |
| $Q_2(f)$ | Frequency response of optimum modulator pre-compensation filter |
| $r(t)$ | Real-valued passband signal at the input to the demodulator |
| $R(f)$ | Fourier transform of $r(t)$ |
| $r_a(t)$ | Analytical signal corresponding to $r(t)$ |
| $r_{f_r}(t)$ | Passband demodulator input signal at center frequency $f_r$ |
| $R_{f_r}(f)$ | Fourier transform of $r_{f_r}(t)$ |
| $\tilde{R}_{f_r}(f)$ | Baseband equivalent of $R_{f_r}(f)$ |
| $\tilde{r}(t)$ | Complex-valued baseband equivalent of $r(t)$ |
| $\tilde{R}(f)$ | Fourier transform of $\tilde{r}(t)$ |
| $\tilde{r}_{\mathrm{Des}}(t)$ | Desired demodulator output signal |
| $\tilde{R}_{\mathrm{Des}}(f)$ | Desired demodulator output spectrum |
| $R'_I(f)$ | Received signal after passing through the bandpass response of the $I$-channel of the demodulator |
| $R'_Q(f)$ | Received signal after passing through the bandpass response of the $Q$-channel of the demodulator |
| $\boldsymbol{R'}(n)$ | Rotation matrix |
| $s(t)$ | Complex-valued passband signal at modulator output |
| $S(f)$ | Fourier transform of $s(t)$ |
| $S_I(f)$ | Spectrum of $I$-channel output of modulator quadrature mixer |
| $S_Q(f)$ | Spectrum of $Q$-channel output of modulator quadrature mixer |
| $S_{\mathrm{SFDR}}$ | Spurious free dynamic range due to quantisation noise |
| $t$ | Continuous time variable |
| $t_0$ | Start time |
| $\Delta t$ | Demodulator sampling delay |
| $\Delta t_{f_m}$ | Demodulator sampling delay, during modulator transmission of tone at frequency $f = f_m$ |
| $\Delta t_{-f_m}$ | Demodulator sampling delay, during modulator transmission of tone at frequency $f = -f_m$ |

| **symbol** | **description** |
|---|---|
| $T$ | Pulse period |
| $u(t)$ | Real-valued passband signal at modulator output |
| $u_{\mathrm{RF}}(t)$ | Real-valued passband signal at imbalanced modulator output |
| $U_{\mathrm{RF}}(f)$ | Fourier transform of $u_{\mathrm{RF}}(t)$ |
| $\tilde{U}_{\mathrm{RF}}(f)$ | Baseband equivalent of $U_{\mathrm{RF}}(f)$ |
| $\tilde{u}_{\mathrm{pc,RF}}(t)$ | Pre-compensated baseband equivalent of modulator output |
| $\tilde{U}_{\mathrm{RF}}(f)$ | Baseband equivalent response of modulator output after it has passed through the feedback path. |
| $\tilde{u}_{\mathrm{RF,f_m}}(t)$ | Baseband equivalent response of imbalanced modulator output for input baseband tone at frequency $f_m$ |
| $\tilde{\boldsymbol{u}}(n)$ | Baseband-equivalent representation of the $n$-th symbol at the modulator output |
| $v(t)$ | Passband noise signal |
| $\tilde{\boldsymbol{v}}(n)$ | Baseband-equivalent noise vector |
| $V_1(f)$ | Frequency weighting of desired signal component at modulator output |
| $V_2(f)$ | Frequency weighting of image signal component at modulator output |
| $W_1(f)$ | Frequency weighting of desired signal component at demodulator output |
| $W_2(f)$ | Frequency weighting of image signal component at demodulator output |
| $W_n[n]$ | Digital windowing function |
| $\boldsymbol{W}(k)$ | Adapted Cholesky factorisation of a covariance matrix at iteration $k$ |
| $x$ | Temporary variable |
| $x_D(t)$ | Complex oscillator signal of demodulator |
| $x_M(t)$ | Complex oscillator signal of modulator |
| $x_{M_I}(t)$ | Imbalanced modulator oscillator signal mixing with the $I$ channel |
| $x_{M_Q}(t)$ | Imbalanced modulator oscillator signal mixing with the $Q$ channel |
| $X_{M_I}(f)$ | Fourier transform of $x_{M_I}(t)$ |
| $X_{M_Q}(f)$ | Fourier transform of $x_{M_Q}(t)$ |
| $x_{D_I}(t)$ | Imbalanced demodulator oscillator signal mixing with the $I$ channel |
| $x_{D_Q}(t)$ | Imbalanced demodulator oscillator signal mixing with the $Q$ channel |
| $X_{D_I}(f)$ | Fourier transform of $x_{D_I}(t)$ |
| $X_{D_Q}(f)$ | Fourier transform of $x_{D_Q}(t)$ |
| $x_{\mathrm{real}}(t)$ | Real-valued oscillator signal |
| $\boldsymbol{x}$ | Covariance matrix |
| $y$ | Temporary variable |
| $\boldsymbol{y}$ | Temporary vector |
| $y(t)$ | Complex-valued signal at the output of the quadrature mixer in the demodulator |
| $Y_I(f)$ | Received signal response in demodulator $I$-channel after mixer |
| $Y_Q(f)$ | Received signal response in demodulator $Q$-channel after mixer |

| symbol | description |
|---|---|
| $\boldsymbol{Y_R}$ | Covariance matrix of signal at the input to the demodulator for the special case where a perfect modulator was used |
| $\boldsymbol{Y}$ | Covariance matrix of the baseband signal |
| $z$ | Z-transform discreet time variable |
| $z(t)$ | Complex-valued lowpass filtered version of $y(t)$ |
| $Z_I(f)$ | Lowpass filtered version of $Y_I(f)$ |
| $Z_Q(f)$ | Lowpass filtered version of $Y_Q(f)$ |
| $Z'_I(f)$ | Spectrum of received signal at the $I$-channel output of demodulator, including the LPF response of the $I$-channel |
| $Z'_Q(f)$ | Spectrum of received signal at the $Q$-channel output of demodulator, including the LPF response of the $Q$-channel |
| $z'(t)$ | Imbalanced demodulator output signal |
| $Z'(f)$ | Imbalanced demodulator output spectrum |
| $z'_{\text{pc}}(t)$ | Imbalanced demodulator signal after $I/Q$ post correction |
| $Z'_{f_r}(f)$ | Imbalanced demodulator output spectrum for input signal $r_{f_r}(t)$ |
| $Z'_{f_m,\Delta t}(f)$ | Imbalanced demodulator output spectrum including the effect of a sampling delay $\Delta t$, for modulator input tone at frequency $f = f_m$ |
| $Z'_{-f_m,\Delta t}(f)$ | Imbalanced demodulator output spectrum including the effect of a sampling delay $\Delta t$, for modulator input tone at frequency $f = -f_m$ |
| $Z'_{f_m,\Delta t_{f_m}}(f)$ | Imbalanced demodulator output spectrum including the effect of a sampling delay $\Delta t_{f_m}$, for modulator input tone at frequency $f = f_m$ |
| $Z'_{-f_m,\Delta t_{-f_m}}(f)$ | Imbalanced demodulator output spectrum including the effect of a sampling delay $\Delta t_{-f_m}$, for modulator input tone at frequency $f = -f_m$ |
| $Z'_{-f_m,\Delta t_{f_m}}(f)$ | Imbalanced demodulator output spectrum including the effect of a sampling delay $\Delta t_{f_m}$, for modulator input tone at frequency $f = -f_m$ |
| $Z'_{f_m,\Delta t_{-f_m}}(f)$ | Imbalanced demodulator output spectrum including the effect of a sampling delay $\Delta t_{-f_m}$, for modulator input tone at frequency $f = f_m$ |
| $\boldsymbol{z'}(n)$ | $n$-th symbol at the output of the demodulator |
| $\alpha_I$ | Amplitude of in-phase component of the imbalanced modulator oscillator signal |
| $\alpha_Q$ | Amplitude of quadrature component of the imbalanced modulator oscillator signal |
| $\beta_I$ | Amplitude of in-phase component of the imbalanced demodulator oscillator signal |
| $\beta_Q$ | Amplitude of quadrature component of the imbalanced demodulator oscillator signal |
| $\delta(\cdot)$ | Dirac's delta function |
| $\eta_I(f)$ | Magnitude response of modulator $I$ channel |
| $\eta_Q(f)$ | Magnitude response of modulator $Q$ channel |

| **symbol** | **description** |
|---|---|
| $\eta_M(f)$ | Gain imbalance of modulator |
| $\Delta\eta$ | Temporary gain adjustment during imbalance extraction process |
| $\xi_{f_m}$ | Amplitude of baseband input signal $a_{f_m}(t)$ |
| $\xi_{-f_m}$ | Amplitude of baseband input signal $a_{-f_m}(t)$ |
| $\kappa_I(f)$ | Magnitude response of demodulator $I$ channel |
| $\kappa_Q(f)$ | Magnitude response of demodulator $Q$ channel |
| $\kappa_D(f)$ | Gain imbalance of demodulator |
| $\lambda$ | Standard deviation of the baseband signal at the modulator input |
| $\lambda_I$ | Standard deviation of the in-phase component of the baseband signal at the modulator input |
| $\lambda_Q$ | Standard deviation of the quadrature component of the baseband signal at the modulator input |
| $\lambda_M$ | Ratio of $\lambda_I$ and $\lambda_Q$ |
| $\mu$ | Adaptive compensation algoritm step size |
| $\rho$ | Standard deviation of signal at the input to the demodulator |
| $\phi_I$ | Phase of in-phase component of the imbalanced modulator oscillator signal |
| $\phi_Q$ | Phase of quadrature component of the imbalanced modulator oscillator signal |
| $\psi_I(f)$ | Phase response of modulator $I$ channel |
| $\psi_Q(f)$ | Phase response of modulator $Q$ channel |
| $\psi_M(f)$ | Phase imbalance of modulator |
| $\sigma$ | Standard deviation of communication channel noise |
| $\theta_\Delta$ | Phase offset of demodulator LO signal, relative to that of the modulator |
| $\theta_{f_m}$ | Phase of baseband input signal $a_{f_m}(t)$ |
| $\theta_{-f_m}$ | Phase of baseband input signal $a_{-f_m}(t)$ |
| $\theta_p$ | Carrier phase in a carrier-phase-amplitude modulation scheme |
| $\varphi_I$ | Phase of in-phase component of the imbalanced demodulator oscillator signal |
| $\varphi_Q$ | Phase of quadrature component of the imbalanced demodulator oscillator signal |
| $\mathcal{U}(f)$ | Heaviside step function |
| $\chi_I(f)$ | Phase response of demodulator $I$ channel |
| $\chi_Q(f)$ | Phase response of demodulator $Q$ channel |
| $\chi_D(f)$ | Phase imbalance of demodulator |
| $\tilde{\Upsilon}(f)$ | Baseband-equivalent frequency response of modulator-demodulator calibration feedback path |
| $\omega_n$ | $n^{th}$ frequency point at which desired filter response is specified |
| $\omega_s$ | Sampling rate in radians |

## Operations

| | |
|---|---|
| $\mathcal{Im}\{\cdot\}$ | Imaginary part of a complex value |
| $\mathcal{Re}\{\cdot\}$ | Real part of a complex value |
| $\lvert\tilde{x}(t)\rvert$ | Magnitude of complex signal $x(t)$ |
| $\angle\tilde{x}(t)$ | Phase of complex signal $x(t)$ |
| $\det(\boldsymbol{A})$ | Determinant of matrix $\boldsymbol{A}$ |
| $\mathrm{E}\{\cdot\}$ | Expectation |
| $\mathcal{F}\{\cdot\}$ | Fourier transform |
| $(\cdot)^*$ | Complex conjugate |
| $[\cdot]_{\mathrm{LPF}}$ | Lowpass filtering |
| $\hat{\kappa}$ | Estimate of variable $\kappa$ |
| $\hat{r}(t)$ | Hilbert transform of signal $r(t)$[1] |
| $\tilde{r}(t)$ | Complex baseband equivalent of bandpass signal $r(t)$ |
| $\otimes$ | Convolution operator |
| $u_{-1}(\cdot)$ | Unit step function |
| $\boldsymbol{A}^T$ | Transpose of matrix $\boldsymbol{A}$ |
| $\mathrm{tril}(\boldsymbol{A})$ | Lower triangular matrix of $\boldsymbol{A}$ |

## Conventions

| | |
|---|---|
| $\mathcal{F}\{x(t)\} = X(f)$ | Time-domain signals are denoted by non-capitalised letters, while capital letters denote the frequency domain representation of a signal. |
| $\tilde{x}(t)$ | Baseband-equivalent of the passband signal $x(t)$ |
| $\boldsymbol{a}$ | Boldface symbol indicates a vector |
| $\boldsymbol{A}$ | Capital boldface symbol indicates a matrix |
| $[\boldsymbol{a}]_1$ | First element of previously declared vector $\boldsymbol{a}$ |
| $[\boldsymbol{A}]_{12}$ | First element in the second column of previously declared matrix $\boldsymbol{A}$ |

[1]The distinction between using $\hat{}$ to indicate an estimate of a variable or the Hilbert transform, will be clear from the context in which it is used.

# Chapter 1

# Introduction

## 1.1 Background

In a time of vast numbers of ever-changing communication standards, it is becoming increasingly impractical to design standards-specific, hardware radio transceivers. The current drive seems to be towards low-cost, low-power, flexible radio transceivers that are able to handle multiple communication standards in a single transceiver [12, 41, 45, 46, 56, 60, 71]. Software-define radio (SDR) seems to offer a viable way to achieve this [34, 45, 56, 60].

SDR essentially implies that the functionality of the radio transceiver be fully specified in software [34]. This affords the designer the flexibility of software reconfigurability as well as the precision of digital signal processing. Multiple communication standards could be supported by simply loading the appropriate software. This, of course, implies a hardware radio front-end that is able to cope with the differences in carrier frequencies and bandwidth requirements of all these configurations.

One approach would be to sample at higher rates, ideally at the RF frequency itself, thus avoiding frequency translation all together. However, this approach is often fundamentally limited by the current state of the art in signal converters [34]. Furthermore, Van Rooyen argues in [67] that by doing this, the signal processing complexity will no longer be a function of the information rate, but rather of the arbitrary frequency band assigned to the communication system.

An alternative approach would be to employ a front-end that would allow radio signals to be processed at baseband, while performing signal translation without the need for fixed, external hardware, such as image-reject filters or multiple mixing and filtering stages. In this dissertation such a hardware front-end, employing quadrature mixing, is investigated.

Quadrature mixing is essentially an elegant implementation of frequency translation, which eliminates the need for many of the hardware components found in traditional radio front-ends. Quadrature mixing exploits the fact that complex signals are not restricted to exhibit Hermitian symmetry in their frequency responses and utilises this to reject the image frequency component of the desired signal during the mixing process itself. The quadrature mixing topology therefore employs two signal paths, representing the real and imaginary

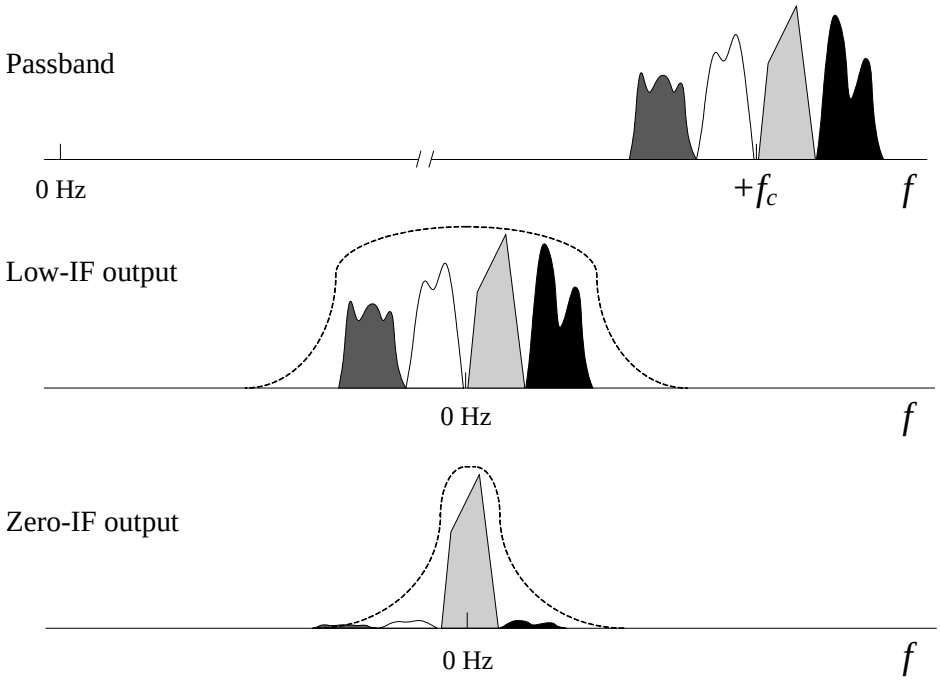


**Figure 1.1:** *Sample magnitude spectra illustrating the frequency down conversion process as implemented in low-IF receivers vs. zero-IF receivers. The typical LPF response of the front end is also shown.*

part of a complex signal.

This theoretically infinite image-rejection property of quadrature mixers, means that bulky image rejection filters and multiple mixing stages can be avoided. In fact, the desired signal can now be translated in frequency directly to DC. Such receivers are termed zero-IF quadrature receivers, as opposed to low-IF (sometimes termed digital low-IF) quadrature receivers, which use quadrature mixing to down convert a few adjacent frequency channels to DC (i.e. different frequency channels spanning the negative and positive frequencies at baseband), after which digital down conversion is employed to select the appropriate channel. Fig. 1.1 graphically illustrates these two different approaches using sample magnitude spectra. The only parameter that needs to be fixed in the quadrature mixing topology is the cut-off frequency of the baseband lowpass filters. This should make quadrature mixing an excellent choice for SDR front-ends [56], since it provides the required hardware flexibility. The quadrature mixing architecture lends itself well towards being monolithically integrated, while generally consuming little power at a low cost [77, 54, 41, 25, 33].

## 1.2 Quadrature imbalances and their compensation

The concept of quadrature mixing is not new. It has been discussed as early as 1924 [1]. The use of the quadrature mixing topology has, however, been severely limited in the past

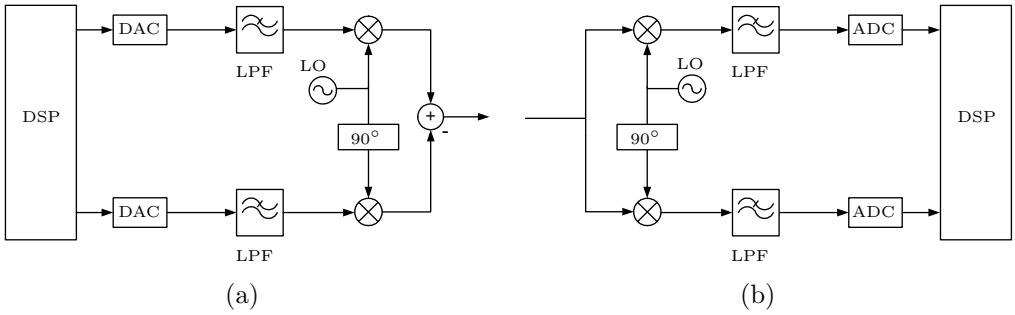


**Figure 1.2:** *The basic topologies of the quadrature modulator (a) and the quadrature demodulator (b).*

due to its sensitivity towards mismatches between its signal paths (as well as the presence of DC offset and carrier leak-through components in the zero-IF topology). [9, 17, 25, 41, 65].

The basic topologies of the quadrature modulator and the quadrature demodulator are shown in Fig. 1.2. When the amplitude and phase of the two signal paths are not perfectly matched, or the two local oscillator (LO) signals of the mixer do not exhibit equal amplitudes and an exact 90° relative phase difference, then the infinite image-rejection performance of these mixing front ends is compromised. These mismatches in the quadrature mixing front ends are termed quadrature imbalances or $I/Q$ imbalances, referring to the in-phase $I$ and quadrature $Q$ signal paths in the quadrature mixing topology. Even with careful analogue front-end design, a practical quadrature mixing front-end can typically only provide 30 to 40 dB of image rejection [9, 65], rendering their performance insufficient for high-quality communication systems [33].

The image rejection performance of the quadrature mixing front end will inherently vary over frequency, although some contributions toward the total imbalances are generally considered to be frequency-independent. The gain imbalance and phase error of the LO signals of the quadrature mixer are commonly considered to be frequency-independent, for a certain LO frequency [9, 21, 25, 29, 32]. It may, however, vary slowly with time, with choice of LO frequency and drive power [25]. The frequency-dependent imbalances of the quadrature mixing front-end may include contributions from the analogue-to-digital converter (ADCs) and digital-to-analogue converters (DACs), the lowpass filters (LPFs), as well as the signal paths themselves [60].

In recent years, researchers have suggested that digital techniques can be used to compensate for the impairments in the analogue quadrature mixing front-end. Most authors focus on the modelling and compensation of frequency-independent imbalances, reasoning that this approach is sufficient for narrow band signal operation. This common assumption is, however, becoming increasing less applicable as the use of wider bandwidth signals and multi-channel systems become more prevalent.

In the literature, techniques for demodulator frequency-independent imbalance compen-

sation have received much more attention, compared to techniques for modulator compensation. Quadrature modulator imbalance compensation is complicated by the fact that the imbalances of the front end occur after the digital domain of the modulator, and therefore some means to obtain a reference of the distortion of the final up converted signal is required. Demodulator compensation techniques operate on the digital signal after the imbalance distortion has occurred, arguably offering a simpler scenario to estimate the imbalance present in the mixing front end.

A brief synopsis will now be presented of current compensation techniques found in literature, emphasising their applicability and limitations. This will provide the context within which the contribution of this dissertation will be formulated.

### 1.2.1 Frequency-independent compensation techniques

When frequency-independent imbalance techniques are presented in literature, only the assumed frequency-independent contribution of the quadrature mixer with its two LO signals, is modelled. Any frequency-dependent imbalance contributions of the signal converters, LPFs, signal paths or even the mixer itself, are ignored.

#### Quadrature modulator compensation

In order for the quadrature modulator to obtain a reference of the imbalances present in its front end, many authors suggest adding a hardware feedback path to the modulator in order to feed the RF signal back into the digital domain of the transmitter [8, 9, 21, 25, 71]. This feedback path typically includes an envelope detector, such as a diode [8, 9, 21] or an adjacent power detector circuit [25, 71] to provide a baseband signal, which can be used as an indication of the imbalances that are present in the analogue front end. Modulator extraction in this fashion is aided by the fact that perfect knowledge exists of what has been transmitted.

Test signals [8, 9, 21], or real information-carrying data [25, 33, 71] are used to identify the imbalances of the front-end. The use of test signals, of course, requires a short break in normal operation. The extraction of the imbalance compensation parameters are then achieved through iterative search techniques, which aim to minimise cost functions related to the presence of image frequency components, such as the power level in the image frequency band.

#### Quadrature demodulator compensation

Compensation techniques presented in literature for demodulator compensation also include the use of test signals and iterative algorithms to estimate and correct imbalance errors [9, 13, 50]. These techniques are applicable to digital modulation schemes where exact knowledge exists of the transmitted symbol. The difference between the received signal and

its theoretical position in the symbol space is used to update adaptive algorithms, such as the least mean square (LMS) algorithm, in order to correct the signal constellation.

In some modulation schemes, such as orthogonal frequency division multiplexing (OFDM), the transmission of test tones (referred to as 'pilots') form part of the communication protocol, and are used for carrier synchronisation and channel estimation. In [55] these test signals are then used to adapt equaliser-type compensation structures. The authors of [57] even manage to combine $I/Q$ imbalance extraction with channel estimation.

An attractive alternative approach for demodulator imbalance compensation, is the use of so called 'blind techniques'. Blind techniques imply that the receiver does not have knowledge of the data that is transmitted. The receiver must rely on other information and assumptions, such as the expected statistics of the received signal, in order to extract the imbalances of its front end. Popular blind approaches include the use interference canceller (IC) based methods [12, 61, 65, 78], techniques based on blind source separation (BSS) algorithms [45, 60, 62, 63, 65] and methods using the second-order statistics of the received signal [3, 66, 72, 73, 48].

IC based techniques use the principles of adaptive noise cancelling to attempt to cancel the image signal interference (the 'noise signal'), from the signal-plus-interference observation. The difficulty in these implementations lies in obtaining the reference of the interfering image signal. In practice these techniques often suffer from the well known 'signal leakage problem', since the reference of the image signal also contains contributions from the desired signal.

Techniques based on blind source separation (BSS) algorithms aim to separate individual signal sources when only a mixture of them is observable. BSS relies on the assumed independence between the source signals.

Methods based on second-order statistics assume that the desired signal is proper (or circular), i.e. that the signal and its image component are uncorrelated. Based on the calculation of the second-order statistics of the received signal, imbalance correction factors can then be applied to restore the circularity of the received signal, which was distorted due to $I/Q$ imbalances. The computational complexity of these techniques is generally quite low, compared to the BSS approach.

**Summary**

Current modulator imbalance techniques require additional hardware complexity to be added to the modulator front end, in the form of a hardware feedback path, consisting of a power detector or complete superheterodyne down conversion chain, with an additional analogue to digital converter (ADC). The compensation techniques do not directly extract the compensation parameters, but rather employ iterative search techniques to determine the optimal parameters.

Demodulator compensation techniques do not generally require the addition of any hardware in order to facilitate imbalance extraction.

The limitations of demodulator compensation techniques using digital modulation schemes and test signals, revolve around the assumption of a specific modulation scheme or protocol, limiting their applicability often even in terms of the receiver topology, e.g. low-IF vs. zero-IF. Many of the presented techniques also rely on adaptive or iterative search methods to derive the optimal compensation parameters.

Blind methods have the advantage that knowledge of the theoretical received signal is not required and thus they can be implemented in an operational scenario, estimating the imbalances of the demodulator during operation in a parallel process. The trade-off is that many of the suggested methods such as the IC- and BSS-based methods suffer from slow conversion, sensitivity towards noise [65], computational complexity [5] and are only applicable to the low-IF receiver. In contrast to these methods, the methods based on second-order statistics seem to offer a truly attractive solution, being widely applicable and requiring low computational complexity.

### 1.2.2 Frequency-dependent compensation techniques

A common assumption in quadrature imbalance literature, is that frequency-dependent $I/Q$ mismatches are mainly due to mismatches between the analogue LPFs of the $I$ and $Q$ signal paths [20, 29, 59]. Some authors choose to view the equalisation of these filters as a separate procedure from compensating for the frequency-independent $I/Q$ imbalances of the mixer (see e.g. [31, 58, 59]), while others choose to compensate for the combined LPF and mixer imbalances (see e.g. [5, 4, 55]).

#### Quadrature modulator compensation

Existing methods dedicated to frequency-dependent imbalance compensation for the modulator, mainly aim to separate the imbalances of the LPFs, from that of the (frequency-independent) mixer. In order to accomplish this, additional feedback paths with additional ADCs are fitted to the modulator, feeding back the signals after the LPFs to be examined. Compensation is realised through digital filters, added to the baseband processing in the modulator, which equalise the difference between the frequency response of the two filters. The compensation filter response is derived using either adaptive [31] or block-based [59, 58] least squares (LS) optimisation routines.

#### Quadrature demodulator compensation

OFDM involves transmitting signals on multiple (orthogonal) sub-carriers, and as such lends itself well towards extracting frequency-dependent $I/Q$ imbalances. Based on knowledge of the expected and actual received pilot signals, the authors of [77] employ a nonlinear least squares (NLS) estimator to simultaneously derive the real-valued taps of the equalisation FIR filter, as well as a frequency-independent phase compensator, from a stored block of

pilot signals. The authors of [55] also use the pilot signals of an OFDM system along with LMS optimisation to derive the frequency-dependent compensation strategy.

For non-OFDM systems, all the BSS- and IC-based techniques mentioned earlier can also be applied to the frequency-dependent case, since their structures are filter based. Their operation is, however, still restricted to the low-IF case and all the limitations listed previously still apply.

Lastly, the authors of [4] also manage to extend the imbalance extraction techniques based on the second-order statistics, to frequency-dependent imbalances. Their technique employs an adaptive filter, which aims to restore the properness of the received signal. The adaptive filter uses a stochastic Newton zero search to minimise the complementary autocorrelation function (CACF) of the output signal.

**Summary**

Very few compensation techniques for frequency-dependent imbalance compensation has been proposed in literature. Those that have been proposed, aim to equalise the responses of the two LPFs, and require feedback paths after their outputs.

For demodulator frequency-dependent compensation, the IC and BSS techniques are again applicable; however, the same limitations to their application apply. The OFDM based techniques are of course tailored toward this specific modulation technique and therefore their applicability to systems employing different modulation schemes is limited. The second order statistical approach presented in [4] seems attractive, although it should be noted that the demodulator imbalances are, as is often the case, extracted through an adaptive (iterative) search technique, minimising the defined cost function.

## 1.3 Research objectives

In the literature synopsis, it was seen that the field of quadrature imbalance compensation is not new, with many authors presenting digital compensation techniques to compensate for the imbalances in the analogue front end. It was found that the various techniques each rely on different underlying assumptions and are often limited to a specific implementation topology or modulation scheme.

Modulator imbalance compensation has not received much attention in literature, with current solutions mostly requiring significant modification the the front end and relying on iterative search techniques for the estimation of optimal compensation parameters.

Demodulator techniques have received much more attention in literature, although the current solutions mostly cater for frequency-independent imbalances and rely on iteratively searching for or adapting the compensation parameters.

The compensation of frequency-dependent imbalances has not received much attention in literature, although this is becoming increasingly important for modern wide band systems. In Chapter 4 of this dissertation, it will be shown that the measured imbalances of practical

modulator and demodulator hardware systems exhibit a strong frequency dependence, thus necessitating frequency-dependent imbalance compensation techniques in more situations than the work in literature might suggest.

The frequency-dependent compensation techniques that are presented in literature assume that the frequency dependence of the quadrature front ends is sufficiently modelled through the inclusion of the LPFs in the models. This modelling approach fails to explain the observed imbalance characteristics of the practical quadrature mixing front ends measured in the course of this study (see Chapter 4).

Given these observations, the research objectives of this dissertation are stated as follow:

**Research objective 1:**

To perform extensive mathematical analysis of the detrimental effects of hardware imbalances on the performance of the quadrature mixing process. This modelling will be performed for both the quadrature modulator and demodulator and will take frequency-independent and frequency-dependent contributions into account.

**Research objective 2:**

To formulate unified frequency-dependent, baseband-equivalent, imbalance distortion models for the quadrature modulator and demodulator, which accurately model the imbalance behaviour observed in practical quadrature mixer implementations.

**Research objective 3:**

To use these baseband-equivalent imbalance models to develop novel frequency-dependent imbalance extraction and compensation techniques, which directly extracts the exact quadrature imbalances of the front end, without requiring any iterative search procedure. The imbalance extraction and compensation procedures are to be implemented in the digital baseband domain of the transceiver. The techniques should not require high computational complexity and should be generally applicable, i.e. not specific to a chosen modulation scheme.

**Research objective 4:**

To present practical solutions to achieve automatic transceiver imbalance compensation, i.e. correcting the imbalances of both the modulator and demodulator, exploiting the fact that they might exist on the same transceiver.

**Research objective 5:**

To show that the derived baseband-equivalent imbalance models can be used to develop a novel blind imbalance compensation method, aimed at the narrow-band case where frequency-independent imbalance behaviour can be assumed. The technique should cater for both modulator and demodulator imbalance extraction and compensation and include the case where both an imbalanced modulator and demodulator is used for communication.

## 1.4 Dissertation statements and hypotheses

**Dissertation statement 1:**

In this dissertation, baseband-equivalent imbalance models will be derived from first principles, which address the frequency-dependent nature of the $I/Q$ imbalances in the quadrature modulator and demodulator. The current modelling approach found in literature will be extended with the additional modelling of bandpass imbalances, which leads to asymmetrical gain and phase imbalance functions. It will be shown how the frequency-dependent and frequency-independent models found in literature, can be seen as special cases of the model derived in this dissertation. The validity of the modelling approach proposed in this dissertation will be established through measurements on a practical hardware implementation of the quadrature modulator and demodulator.

**Hypothesis 1.1:**

The common modelling approach in literature, where frequency-dependent imbalances are modelled as mismatched LPFs, fail to explain the asymmetrical gain and phase imbalance characteristics observed in practical hardware quadrature mixer implementations.

**Hypothesis 1.2:**

The modelling approach proposed in this dissertation is capable of modelling the asymmetrical frequency-dependent imbalance characteristics observed in practical hardware quadrature mixer implementations.

---

**Dissertation statement 2:**

By using the derived baseband-equivalent imbalance models, this dissertation will develop novel imbalance extraction and compensation techniques suitable for modulator and demodulator frequency-dependent imbalance compensation. These techniques will rely on the use of simple test signals together with spectral analysis and will not be specific to any particular modulation scheme or communications protocol. The imbalance extraction techniques will aim to derive the imbalances of the modulator and demodulator directly, without the need for iterative search techniques. The resulting compensation approach will be suitable to be implemented in the digital domains of the modulator and demodulator, and will take the form of a complex-valued FIR compensation filter. The validity and performance of the extraction and compensation techniques will be established through simulation, as well as a practical hardware implementation.

**Hypothesis 2.1:**

The baseband-equivalent models of this dissertation, together with simple test signals, will enable the direct extraction of quadrature imbalances, through spectral analysis.

**Hypothesis 2.2:**

In order to effectively compensate for the frequency-dependent characteristics of the imbalances exhibited by practical modulators and demodulators, a complex-valued compensation filter is essential.

**Hypothesis 2.3:**

The imbalance extraction and compensation techniques of this dissertation will be effective in significantly improving the image rejection capabilities of a practical hardware implementation of a quadrature modulator and demodulator.

---

**Dissertation statement 3:**

The derived frequency-dependent compensation techniques will be used to develop an efficient compensation strategy and transceiver architecture, to facilitate automatic quadrature transceiver compensation, as a start-up procedure. This involves separating and extracting the frequency-dependent imbalances of a quadrature modulator and demodulator which exists on the same transceiver front end, with minimal modifications to the standard hardware topology.

**Hypothesis 3:**

The frequency-dependent imbalance contributions of a cascaded quadrature modulator and demodulator can be separated and extracted from the same test signal, given an appropriate choice of this signal and a small frequency difference between the local oscillator (LO) signals of the two quadrature mixers.

---

**Dissertation statement 4:**

As a further application of the imbalance modelling performed in this dissertation, a novel, blind imbalance compensation technique will also be developed. This technique will be applicable to narrowband digital modulation systems, where frequency-independent imbalance behaviour can be assumed. The technique will use the second-order statistics of the received signal during normal operation in order to separate and extract the imbalance contributions of the quadrature modulator and demodulator pair that were employed during transmission and reception.

**Hypothesis 4:**

The frequency-independent imbalances of a cascaded quadrature modulator and demodulator can be separated and extracted using the second-order statistics of the

received signal, during normal operation, without knowledge of the exact data that was transmitted.

## 1.5 Novel contributions of this work

This study will make novel contributions in terms of the mathematical modelling of quadrature imbalanced front ends, as well as by the development of novel imbalance extraction and compensation techniques. This section will now elaborate on these envisioned contributions.

### 1.5.1 Modelling

This study will perform a thorough mathematical modelling of the effect of frequency-dependent imbalances on the quadrature mixing front end of both the modulator and demodulator. Very little literature exists on the modelling of frequency-dependent imbalances. Although some work has been done on the modelling of frequency-dependent imbalances at the demodulator, the techniques assume that the frequency dependence of the quadrature front end can be modelled as mismatches between the two LPFs. From this approach, it also therefore follows that equalisation of the two LPF responses in the front end, would provide effective compensation for the frequency-dependent component of quadrature imbalances. It will be shown in this dissertation that such an approach is insufficient to fully represent the characteristics of the frequency-dependent imbalances measured in practical implementations. Therefore, this dissertation will perform frequency-dependent imbalance modelling, for the modulator and demodulator, from first principles. Included in the models will be a bandpass imbalance response, which will be shown to result in models capable of explaining the observed imbalance characteristics of practical quadrature mixing front ends.

The aim of the modelling approach will be to present baseband-equivalent models which could be used to derive novel digital baseband compensation techniques. It will be shown from the modelling in this dissertation that three different approaches to compensation can be followed: firstly, frequency-independent compensation can be applied, secondly, frequency-dependent compensation can be applied using a real-valued compensation filter with a separate frequency-independent phase compensator, or thirdly, frequency-dependent compensation can be applied using a complex-valued compensation filter. The scenarios where each approach is applicable will be illustrated through the developed imbalance models, by analysing the underlying assumptions of each approach. These represent new insights that have not been presented in literature before.

### 1.5.2 Novel imbalance extraction and compensation techniques

The derived baseband-equivalent imbalance models will then be used to develop novel imbalance extraction and compensation techniques. It will be shown how, through appropriately chosen test signals, the frequency-dependent imbalances of the modulator and demodulator

can be extracted directly from spectral measurements, without the need for an iterative search for the optimal imbalance parameters. The developed techniques will rely on very simple test signals and will not be specific to a particular modulation scheme.

The case where imbalances of the modulator and demodulator are cascaded will be analysed, which has not been presented before. From this analysis, it will be shown how the imbalance contributions of the modulator and demodulator can be separated and extracted from only analysing the received signal at the output of the demodulator. This separation will be made possible by introducing a small frequency offset between the LO signals of the modulator and demodulator.

The approach for separating the imbalances of a cascaded quadrature modulator and demodulator will then be used to develop a solution for automatic transceiver calibration, which can be used as rapid start-up calibration procedure. The aim will be to require only minimal modifications to the existing transceiver hardware.

These developed techniques will be validated and their performance verified through simulation as well as a practical hardware implementation.

In addition to the compensation techniques described above, the derived baseband models will also be used to develop a novel blind imbalance compensation approach, which uses the second-order statistics of the received signal to estimate the imbalances of the front end.

During this analysis, it will be shown analytically and verified through simulation that the frequency-independent imbalances of the cascaded modulator and demodulator can be separated and extracted from real data without knowledge of the transmitted data, even when transmission occurs over a noisy and fading communications channel. This cascaded, blind case has also not been analysed formally in literature before, as far as could be established.

It will finally also be shown, analytically and through simulation, how the underlying principles of this blind technique is independent of carrier frequency or phase synchronisation, or the effect of a noisy, frequency-selective channel.

## 1.6 Scope of this work

Practical quadrature mixing transceivers are plagued by many non-idealities reducing their spurious free dynamic range. Factors limiting the spurious performance include, but are not limited to: quadrature imbalances, DC offsets, harmonic distortion, intermodulation distortion, quantisation noise, oscillator leakage, and oscillator phase noise.

The scope of this dissertation is, however, strictly limited to quadrature imbalances and their compensation. Careful design and mitigation strategies will typically be required to increase the overall SFDR of the transceiver, due to other non-idealities, to a usable level after quadrature imbalances has been compensated for.

## 1.7 Dissertation structure

The rest of this dissertation will be structured as follow:

**Chapter 2** introduces the principles behind quadrature modulation and demodulation. It will be shown how quadrature mixing could potentially provide infinite image signal rejection, through a simple and low-cost architecture. The chapter subsequently presents detailed mathematical analysis of the $I/Q$ imbalances encountered in practical quadrature modulators and demodulators. Baseband-equivalent distortion models are derived from first principles, to not only model frequency-independent mixer effects, but arrive at complete frequency-dependent, baseband-equivalent, imbalance models for the quadrature modulator and demodulator. These models provided insight into the frequency-independent nature of $I/Q$ imbalances that are not found in open literature. By including bandpass frequency responses to the distortion models, the models are able to explain the asymmetrical imbalance behaviour observed in practical quadrature converters. At the end of this chapter, it will be clear that some form of compensation is required to improve the image rejection performance of practical quadrature mixing front ends, in order for them to be used in high quality radio applications.

**Chapter 3** presents a study of the current imbalance compensation techniques found in literature. The literature synopsis presented in this introduction chapter will be expanded, providing a more detailed look at current techniques, their application, assumptions and limitations. This literature study is presented after the mathematical modelling of Chapter 2, to make use of the mathematical basis of Chapter 2 in order to compare relevant compensation approaches from literature in terms of a common mathematical model.

**Chapter 4** represents one of the main contributions of this dissertation. In this chapter the mathematical models for the quadrature imbalances of the modulator and demodulator (Chapter 2), will be used to develop novel compensation techniques addressing frequency-dependent imbalances. Techniques for modulator and demodulator frequency-dependent imbalance compensation will be presented, which rely on the use of simple test tones and spectral analysis. It will be shown how a small frequency difference between the LOs of the modulator and demodulator, enables the cascaded imbalances of an imbalanced modulator and demodulator to be separated and extracted by analysing only the received signal at the demodulator. The chapter will also present solutions for converting the extracted imbalance parameters to a frequency-dependent compensation filter. The characteristics of this filter will be shown to depend on the underlying nature of the imbalances in the front end.

**Chapter 5** evaluates the effectiveness of the imbalance extraction and compensation techniques of Chapter 4, through simulations and a hardware implementation. The performance of the techniques are evaluated in the presence of noise and quantisation. The

effectiveness of designing compensation filters from the extracted imbalances, is also investigated. Through the hardware implementation, the imbalance characteristics of a practical quadrature modulator and demodulator will be investigated and used to validate the modelling approach proposed in Chapter 2.

**Chapter 6** represents another main contribution of this dissertation, by presenting a novel, computationally efficient blind $I/Q$ compensation technique that targets inaccuracies across the full transmitter-receiver system, and extracts the actual $I/Q$ impairments of both the quadrature modulator and demodulator. A vector notation will be used to enable the used of linear algebra techniques to accomplish imbalance extraction and compensation. The proposed method relies on knowledge of the second-order statistics of the received signal and uses a Cholesky decomposition of the received signal's covariance matrix to extract the $I/Q$ imbalances. The blind technique is applicable to narrow band scenarios where the imbalances of the front end can reasonably be assumed to be frequency-independent. Various simulations are presented to verify its performance under different operating conditions.

**Chapter 7** concludes the dissertation with a summary of the main findings and contributions of this work.

# Chapter 2

# Mathematical modelling of quadrature mixing and its associated limitations

## 2.1 Introduction

Frequency translation is one of the most important functions of radio transceivers. A transmitter will typically be assigned a specific frequency band in the radio frequency (RF) spectrum. To utilise this band it will have to translate its baseband signal to the passband frequency. Similarly, a desired signal will typically occupy a specific channel in an assigned RF band. To be able to process this signal efficiently, it first has to be down-converted to a lower frequency.

This chapter starts with a brief review of conventional mixing techniques, referred to as 'real mixing', as used in superheterodyne mixing topologies. Real mixing faces the challenge of removing the undesired image frequency replica of the desired signal, by means of filtering. This leads to the the well known trade-off between sensitivity and selectivity, as will be discussed below. An alternative mixing technique, known as quadrature mixing, is then presented. Quadrature mixing theoretically provides infinite rejection of the image frequency components, by employing two oscillator signals which are quadrature in phase, relative to each other. It is, however, well known that the image rejection performance of quadrature mixing relies on accurate matching of its two signal paths [9, 17, 25, 41, 65].

The main focus of this chapter is the mathematical analysis and modelling of the quadrature mixing process, including its associated limitations – its sensitivity towards mismatches in its two quadrature signal paths, referred to as $I/Q$ imbalances. This analysis forms the basis of all the novel imbalance extraction and compensation techniques that will be presented in subsequent chapters.

Although quadrature imbalances have been analysed in literature (see Chapter 3), the analysis often assumes frequency-independent $I/Q$ imbalances. This may be sufficient over a relatively narrow band, but fails to describe the observed behaviour in wideband systems

[20]. In the cases where a frequency-dependent analysis is presented (see e.g. [31, 58, 59, 5, 4, 55]), the authors model the frequency dependence of the quadrature imbalances as a consequence of mismatched low pass filters (LPFs) before the actual mixing process (in the case of a modulator configuration), or after the mixing process (in the case of a demodulator configuration).

It will be shown in Section 2.5.1 and 2.5.2 that the consequence of this modelling approach, is that the frequency-dependent gain imbalance function of the quadrature modulator and demodulator, is constrained to be an even function of frequency and the phase imbalance function is constrained to be and odd (when the DC phase offset is removed) function. When the gain and phase imbalance functions of a practical quadrature modulator and demodulator were measured in Chapter 4, it will be seen that both these functions exhibit asymmetrical shapes as a function of frequency, thus rendering this modelling approach inaccurate.

In this chapter, frequency-dependent, baseband-equivalent, $I/Q$ imbalance models are derived from first principles, for both the quadrature modulator and demodulator. These models aim to model the existence of asymmetrical gain and phase imbalance functions, by also modelling the bandpass imbalances of the quadrature front end.

Frequency-independent models are furthermore derived as a special case of the frequency-dependent models. The frequency-independent models are general, with regards to the choice of a phase reference. It will be shown that the different models presented in literature are equivalent up to the choice of a reference channel. Although it is argued that all the models are equivalent up to the choice of a reference, a carefully selected reference may lead to significant simplification during the imbalance extraction process. This subject is revisited in Chapter 6.

The fact that the derived models are 'baseband-equivalent' models, is significant, since the imbalance extraction and compensation techniques that form the main contribution of this dissertation (Chapters 4 and 6), will also be baseband techniques. The baseband-equivalent models can thus be used directly to derive the required extraction and compensation techniques.

Once the principles behind quadrature mixing, as well as the effects of imbalances on its performance have been fully explored, the reader will be presented with compensation techniques which have been proposed in literature, in Chapter 3. This is followed by the novel compensation techniques derived during the course of this study, in Chapters 4 and 6.

## 2.2 Notes on notation

During the mathematical development of this chapter, the following conventions regarding notation will be followed:

- Time-domain signals are denoted by non-capitalised letters, while capital letters usually denote the frequency-domain representation of a signal.

- $\mathcal{F}\{x(t)\}$ denotes the Fourier transform of the time signal $x(t)$, thus

$$\mathcal{F}\{x(t)\} = X(f).$$

- The tilde symbol (e.g. $\tilde{x}(t)$) indicates that the signal represents the baseband-equivalent of the corresponding signal without the tilde. Note that a time-domain signal with a tilde symbol is always complex.

- The operators $\mathcal{Re}\{\tilde{x}(t)\}$ and $\mathcal{Im}\{\tilde{x}(t)\}$ denote, respectively, the real and imaginary components of the complex signal $\tilde{x}(t)$.

- The operators $|\tilde{x}(t)|$ and $\angle\tilde{x}(t)$ denote the magnitude and phase of the complex signal $\tilde{x}(t)$.

## 2.3 Real mixing

In this study, real mixing refers to the translation of a signal in frequency by multiplying it with a single oscillator signal. Real mixing has the problem of dealing with image frequency components due to the Hermitian symmetry of the frequency spectrum of real signals. This section will highlight this issue by looking at a widely implemented mixing architecture that utilises real mixing, namely the superheterodyne receiver.

In superheterodyne receivers, the received RF signal is typically mixed down with a real oscillator signal to a lower intermediate frequency (IF) [36, 41, 42, 60]. Because a real signal has a Hermitian frequency response, [40, p. 35], multiplying the RF signal with a real oscillator signal will result in two frequency translations, rather than one [60, p. 16]. To illustrate this, consider the case where the desired signal is located at a centre frequency equal to $f_c + f_{\text{IF}}$ (low side injection), with its conjugate, mirror component located at $-f_c - f_{\text{IF}}$. $f_c - f_{\text{IF}}$ will typically fall within an adjacent channel's signal, with a mirror image component at $-f_c + f_{\text{IF}}$. When the RF signal is multiplied with the real oscillator signal, $x_{\text{real}}(t)$, given by

$$x_{\text{real}}(t) = \cos(2\pi f_c t) = \frac{e^{j2\pi f_c t}}{2} + \frac{e^{-j2\pi f_c t}}{2} \tag{2.1}$$

the desired signal will indeed be translated to $f_c + f_{\text{IF}} - f_c = f_{\text{IF}}$. However, a second frequency translation will take place, also translating the mirror image components of the adjacent channel's signal to $-f_c + f_{\text{IF}} + f_c = f_{\text{IF}}$. This problem is referred to as the problem of image [36, 42], [60, p. 16], and is illustrated graphically in Fig. 2.1.

To combat the image signal problem, superheterodyne receivers typically implement an image reject (IR) filter to reject the image signal located at $2 \times$ IF from the desired signal's centre frequency before mixing the RF signal down. Once the RF signal is mixed down to an IF, a channel-select filter is employed to isolate the desired channel and suppress any nearby interfering signals [41, 42].

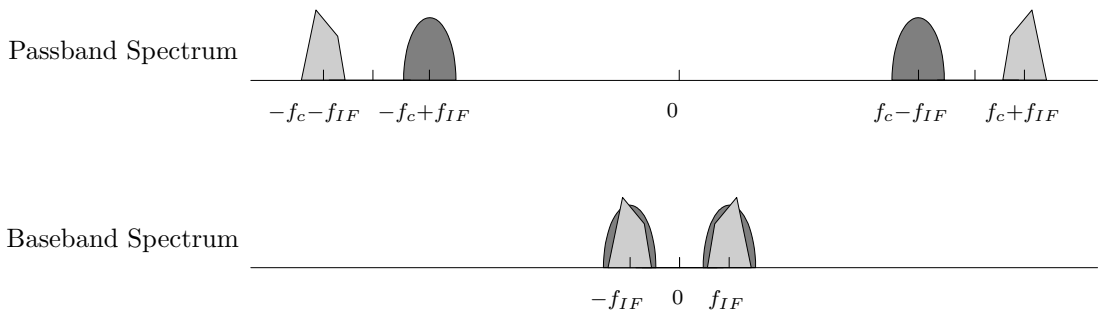


**Figure 2.1:** *Magnitude plots in the frequency-domain illustrating the problem of image.*

There exists a trade-off for the choice of an IF. A low IF means that the desired signal and the image signal is closely spaced in the RF spectrum, requiring an IR filter with a high quality (Q) factor, in order to properly reject the image signal. Increasing the Q-factor of the IR filter also increases the loss incurred in the desired signal band [42]. A high IF relaxes the specifications of the IR filter, but increases the required Q-factor of the IF filter in order to perform proper channel selection and reject interferers sufficiently. In [42] and [41] this design choice in heterodyne receivers is referred to as the trade-off between sensitivity and selectivity. This trade-off often results in receivers employing multiple mixing and filtering stages, in order to alleviate the specifications of the filters at each intermediate stage [42].

Direct conversion of the desired signal to baseband – that is, selecting the oscillator's frequency to be the same as the centre frequency of the desired signal – is also not possible with a real-valued oscillator signal, since the undesired image signal is a self-image of the desired signal around 0 Hz.

## 2.4 Complex mixing

The Fourier transform of a complex signal does not need to have a symmetrical magnitude response. By using complex signals instead of real signals, it is possible to process positive and negative frequencies separately. This means that it is possible to create a complex baseband message signal that occupies only a single sideband in the range $[0, B]$ Hz or one that carries unique information in the frequencies $[-B, 0)$ Hz and $[0, B]$ Hz. By using complex signal processing, it is possible to perform a true single frequency translation, with theoretically infinite image frequency rejection. This concept is used in the quadrature modulator and quadrature demodulator, which will be discussed next.

Before the discussion on complex mixing commences, some definitions need to be made. The use of the following terms conform to those used by Van Rooyen [67, p. 37].

**Baseband modulation** refers to the generation of two baseband message signals ($I$ and $Q$ channels) in the digital domain of the transmitter. These two signals represent the real and imaginary components of a complex signal. These digital signals are converted to

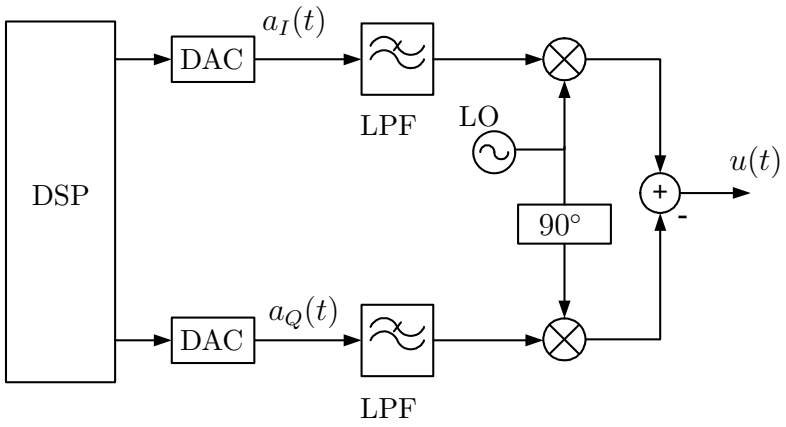


**Figure 2.2:** *The topology of the ideal quadrature modulator.*

the analogue domain and passed to the quadrature upmixer for frequency translation.

**Quadrature up-mixing** refers to the analogue multiplication of the two baseband signals resulting from two signal paths ($I$ and $Q$ channels) with two quadrature local oscillators (LOs), and summing them.

**Quadrature down-mixing** refers to the analogue multiplication of the received RF signal with two quadrature LOs, thus producing two signals on two separate signal paths (the $I$ and $Q$ channels). These $I$ and $Q$ signals can be seen as the real and imaginary components of a complex signal.

**Baseband demodulation** refers to the extraction of the modulated signal from the $I$ and $Q$ baseband channels. This happens in the digital domain, after the signals on the $I$ and $Q$ channels have been converted into the digital domain by using two analogue-to-digital converters (ADCs).

### 2.4.1 Perfect quadrature modulation

Quadrature modulation refers to the process of using baseband modulation to create a complex message signal and then using quadrature up-mixing to translate this signal to an RF passband. In this section the mathematical principles behind quadrature mixing will be discussed.

Consider the complex baseband signal $a(t)$, which can be expanded as

$$a(t) = a_I(t) + ja_Q(t) \tag{2.2}$$

where

$$j = \sqrt{-1}. \tag{2.3}$$

$a_I(t)$ and $a_Q(t)$ are called the in-phase and quadrature components respectively of the complex signal $a(t)$. If this signal is to be translated in frequency to a carrier frequency of $f_c$ Hz, it can multiply it with the complex signal $x_M(t)$

$$\begin{aligned} x_M(t) &= e^{j2\pi f_c t} \\ &= \cos(2\pi f_c t) + j\sin(2\pi f_c t). \end{aligned} \tag{2.4}$$

The complex signal $s(t)$ can thus be written as

$$s(t) = a(t)e^{j2\pi f_c t}. \tag{2.5}$$

In the frequency-domain, this operation becomes

$$S(f) = A(f) \otimes \delta(f - f_c) = A(f - f_c), \tag{2.6}$$

It is seen that this mixing process is a perfect single frequency translation. Note that $A(f)$ and $S(f)$ represent the Fourier transforms of $a(t)$ and $s(t)$ respectively, with $\delta(f)$ being Dirac's delta function. Of course, in a practical radio system only real signals can be transmitted. Thus only the real part of $s(t)$ is used: [67]

$$\begin{aligned} u(t) &= \mathcal{R}e\left\{s(t)\right\} \\ &= \mathcal{R}e\Big\{\big[a_I(t) + ja_Q(t)\big]\big[\cos(2\pi f_c t) + j\sin(2\pi f_c t)\big]\Big\} \\ &= a_I(t)\cos(2\pi f_c t) - a_Q(t)\sin(2\pi f_c t). \end{aligned} \tag{2.7}$$

This expression is exactly the implementation of the quadrature modulator, which is shown in Figure 2.2. The complex baseband signal, $a(t)$, is generated in the digital domain and is then converted to the analogue domain using two digital-to-analogue converters (DACs). The two lowpass filters (LPFs) are reconstruction filters and are required to smooth the staircase-like output of the DACs [37, p. 299]. The in-phase and quadrature parts of this signal are subsequently mixed with two quadrature LOs with a quadrature phase relationship. These two quadrature LOs can be considered to be the components of the complex signal $x_M(t)$. By finally adding the two signals at the output of the LOs, the single real signal is created, which can now be transmitted.

As was suggested in [60], it is instructive to expand (2.7) using Euler's complex expansion of cosine and sine functions. Doing this yields

$$\begin{aligned} s(t) &= a_I(t)\left(\frac{e^{j2\pi f_c t}}{2} + \frac{e^{-j2\pi f_c t}}{2}\right) - a_Q(t)\left(\frac{e^{j2\pi f_c t}}{2j} - \frac{e^{-2\pi f_c t}}{2j}\right) \\ &= \left(\frac{a_I(t) + ja_Q(t)}{2}\right)e^{j2\pi f_c t} + \left(\frac{a_I(t) - ja_Q(t)}{2}\right)e^{-j2\pi f_c t} \\ &= \frac{a(t)}{2}e^{j2\pi f_c t} + \frac{a^*(t)}{2}e^{-j2\pi f_c t}\ . \end{aligned} \tag{2.8}$$

As can be seen from (2.8), due to the fact that only the real part of $s(t)$ was used as the transmitted signal, $a(t)$ undergoes two frequency translations and $u(t)$ exhibits Hermitian symmetry around zero Hz. What is gained through this process, though, is the fact that

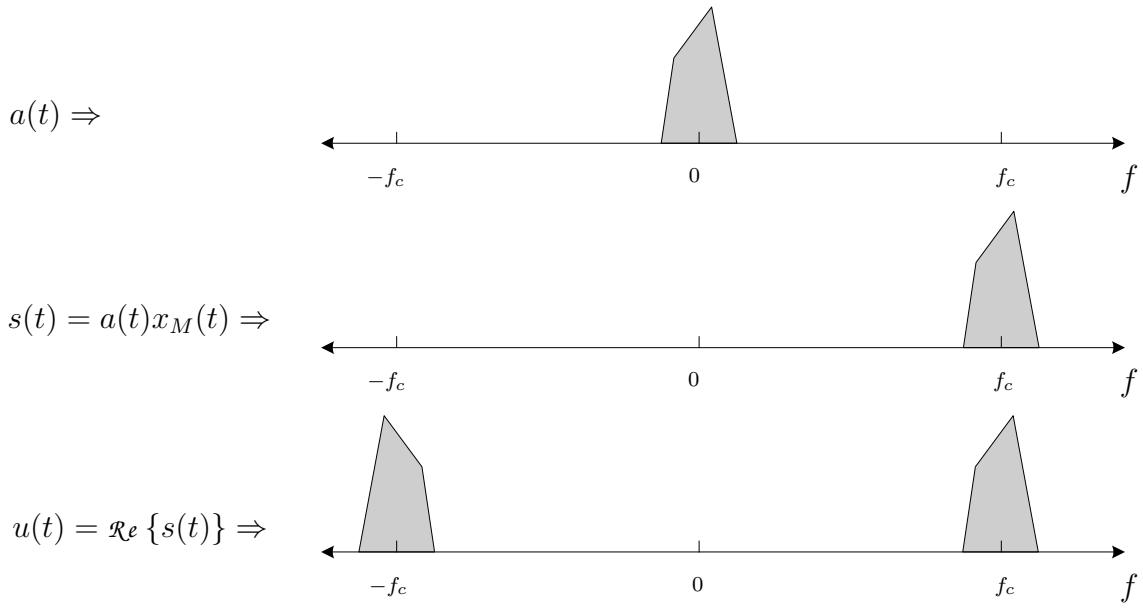


**Figure 2.3:** *Magnitude spectra during the quadrature up-mixing process. The factor 1/2 scaling is not shown.*

the baseband image signal component of $a(t)$ is not present in the passband signal. This eliminates the need for multiple mixing and filtering stages in the transmitter's front-end to remove the unwanted image component.

### 2.4.2 Perfect quadrature demodulation

Quadrature demodulation refers to the process of using quadrature down-mixing to translate a received passband signal down to baseband, converting it to the digital domain and demodulating it there.

Similar to quadrature modulation, complex mixing may be used to avoid the imaging problem when translating a bandpass signal located at a frequency $f_c$ Hz to baseband. Recall that the received passband signal will be real and therefore symmetrical around 0 Hz. This means that the negative frequency components contribute no unique information and are therefore redundant. In order to translate only the positive frequency components, a complex-valued oscillator is employed [67].

To illustrate this fact, consider the passband signal $r(t)$ centred at a frequency of $f_c$ Hz, being received at the antenna. It can now be down-converted using the complex oscillator $x_D(t)$, which is defined as

$$x_D(t) = e^{-j2\pi f_c t} \tag{2.9}$$

$$= \cos(2\pi f_c t) - j\sin(2\pi f_c t)\ . \tag{2.10}$$

The architecture of the quadrature demodulator splits the received RF signal into two identical signal paths, each mixing with either the real or the imaginary part of the complex

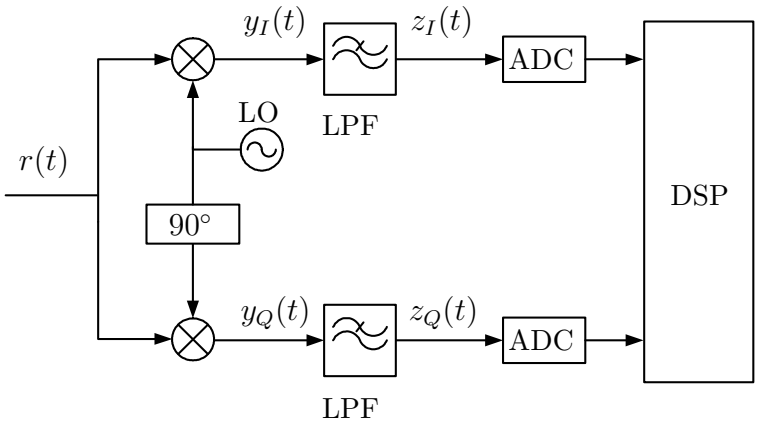


**Figure 2.4:** *Quadrature demodulator topology.*

LO signal. By treating the two signals at the output of the quadrature mixer as the real and imaginary components of a complex signal, the complex signal at the output of the quadrature mixer can be written as

$$\begin{aligned} y(t) &= r(t)x_D(t) = r(t)e^{-j2\pi f_c t} \\ &= r(t)\cos(2\pi f_c t) - jr(t)\sin(2\pi f_c t) \ . \end{aligned} \tag{2.11}$$

The result of (2.11) can be written in a more instructive form. First the (complex-valued) analytical signal, $r_a(t)$, corresponding to the passband signal $r(t)$[1], is defined as: [40, p. 51]

$$r_a(t) = r(t) + j\hat{r}(t) \ , \tag{2.12}$$

where $\hat{r}(t)$ denotes the Hilbert transform of $r(t)$. The lowpass or baseband-equivalent (complex-valued) representation of the bandpass signal $r(t)$, denoted by $\tilde{r}(t)$, can now be written in terms of $r_a(t)$ as: [40, p. 52]

$$\tilde{r}(t) = r_a(t)e^{-j2\pi f_c t} \ . \tag{2.13}$$

$r(t)$ is related to $\tilde{r}(t)$ with the following relationship

$$r(t) = \tilde{r}(t)e^{j2\pi f_c t} + \tilde{r}^*(t)e^{-j2\pi f_c t}. \tag{2.14}$$

This relationship between a passband signal and its corresponding analytical and baseband-equivalent representations, is illustrated in Fig. 2.5. When (2.14) is now substituted into (2.11), it is seen that

$$\begin{aligned} y(t) &= \left[\tilde{r}(t)e^{j2\pi f_c t} + \tilde{r}^*(t)e^{-j2\pi f_c t}\right] e^{-j2\pi f_c t} \\ &= \tilde{r}(t) + \tilde{r}^*(t)e^{-j4\pi f_c t} \ . \end{aligned} \tag{2.15}$$

[1] $r_a(t)$ is also called the pre-envelope of $r(t)$.

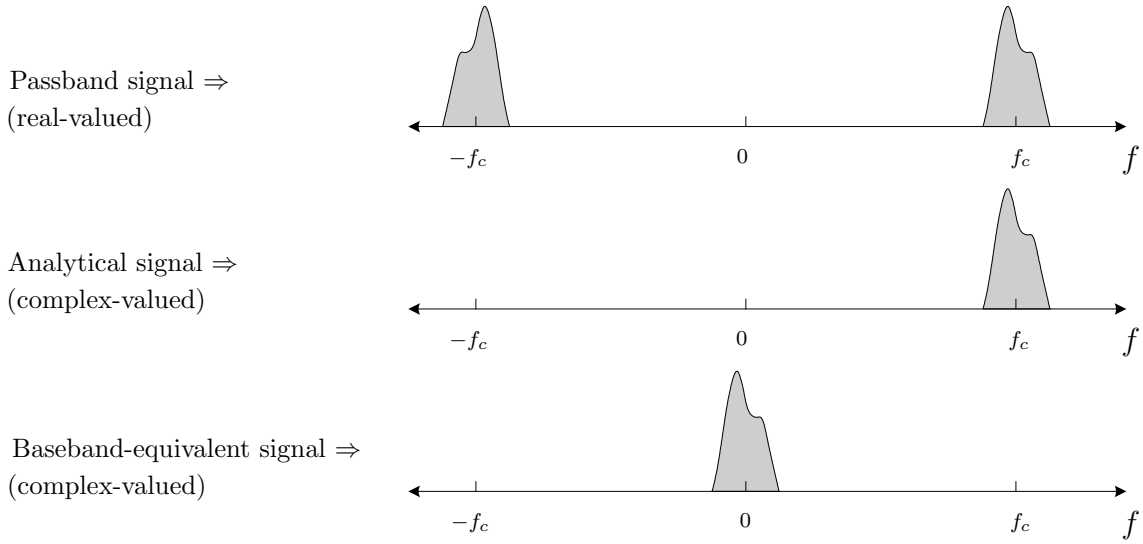


**Figure 2.5:** *Sample magnitude spectra, indicating the relationship between a passband signal and its corresponding analytical and baseband-equivalent representations.*

From (2.15), it is observed that $y(t)$ contains the desired result (first term), as well as a double frequency term at $-2f_c$ Hz (second term). Passing both the in-phase and quadrature components of $y(t)$ through low-pass filters (LPFs) to reject the double frequency component, will yield the desired signal. $z(t)$ is defined as the low-pass filtered version of $y(t)$, thus

$$\begin{aligned} z(t) &= [y(t)]_{\text{LPF}} \\ &= \tilde{r}(t). \end{aligned} \tag{2.16}$$

The above expression shows that after the LPFs, the baseband-equivalent signal of the received signal is obtained, which is exactly what was set out to be achieve. The topology of the quadrature demodulator is shown in Figure 2.4, and is a direct implementation of the above discussion. A graphical representation of spectra involved in the quadrature demodulation process is shown in Figure 2.6.

## 2.5 Imbalances in quadrature mixing

From the previous discussion, it was seen that the quadrature modulator and demodulator can theoretically provide infinite image signal suppression without the need for expensive, extra hardware or multiple mixing and filtering stages. This is, however, only true for theoretical, ideal quadrature modulators and demodulators. In practice, the image-rejection capabilities of the quadrature mixing architecture deteriorates in the presence of so-called quadrature imbalances [9, 25, 41, 65]. Quadrature imbalances, or $I/Q$ imbalances, occur when the gains of the $I$ and $Q$ channels are not perfectly matched, or the phase difference between them is not exactly 90°. In the rest of this chapter we will investigate and

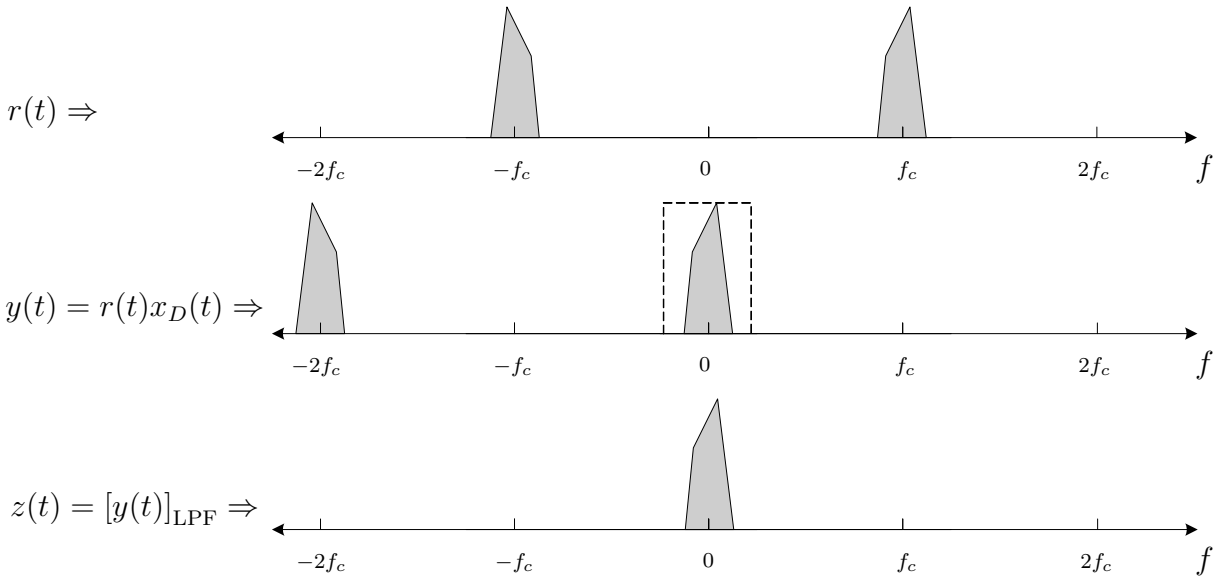


**Figure 2.6:** *Magnitude spectra during the quadrature down-mixing process.*

quantify the quadrature mixing front-end's loss in performance when it contains quadrature imbalances and offset errors.

$I/Q$ imbalances are commonly modelled as having frequency-independent as well as frequency-dependent components. The gain imbalance and phase error (i.e. the difference from 90° of the phase of its two oscillator signals) of the quadrature mixer are commonly modelled to be frequency-independent to a first order approximation, for a certain LO frequency [9, 21, 25, 29, 32]. It may, however, vary with time, choice of LO frequency and drive power [25].

The frequency-dependent imbalances of the quadrature mixing front-end may include contributions from the ADCs and DACs, the LPFs, as well as the signal paths themselves [60]. Frequency-dependent $I/Q$ imbalance compensation techniques presented in literature, often only consider ways to remedy the mismatches between these LPFs [29, 31, 58, 59].

It will be shown in Section 2.5.1 and 2.5.2, that the consequence of this modelling approach is that the frequency-dependent gain imbalance function of the quadrature modulator and demodulator are constrained to be an even function of frequency and the phase imbalance function (after the DC phase offset is removed) is constrained to be an odd function. When the gain and phase imbalance functions of a practical quadrature modulator and demodulator were, however, measured (results presented in Chapter 4) it was seen that both these functions exhibit an asymmetric form as a function of frequency. The measured characteristics of the gain and phase imbalance functions can therefore not be explained if only LPF mismatches are modelled.

In this section, frequency-dependent, baseband-equivalent $I/Q$ imbalance models will be derived from first principles, for both the quadrature modulator and demodulator. The models which are derived here, include a bandpass imbalance response, in addition to the

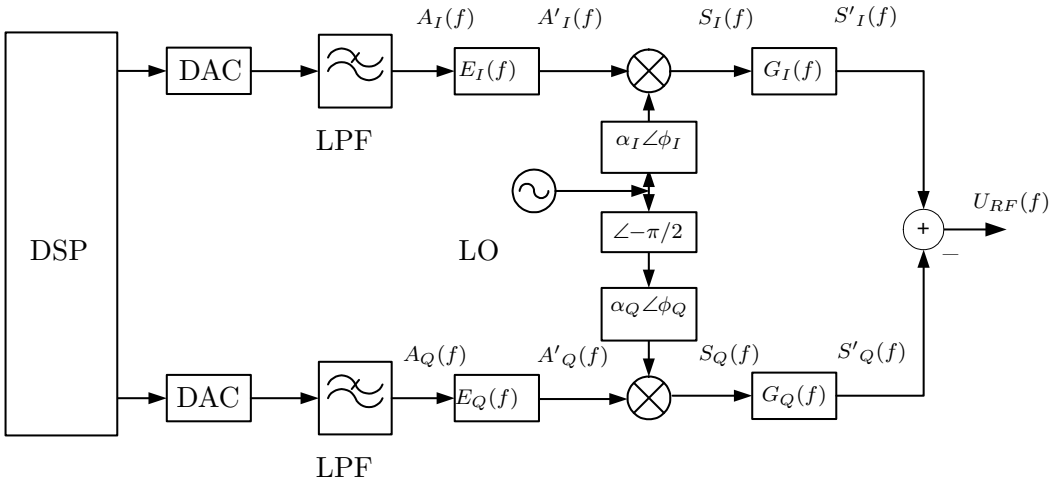


**Figure 2.7:** *The topology of the quadrature modulator, including imbalances.*

effect of imbalanced lowpass filters. This approach accounts for the asymmetrical imbalance response observed during practical measurements, as presented in Chapter 4. These baseband-equivalent models will be used to derive the novel baseband imbalance extraction and compensation techniques, presented in Chapter 4, which forms the main contribution of this dissertation.

The section then continues to show how these models simplify to the frequency-dependent models often used in literature. A commonly used vector notation is introduced, which describes the frequency-independent models in terms of matrix manipulations. This allows linear algebra techniques to be used to derive the extraction and compensation strategies. A novel extraction and compensation technique, which utilises this approach, is presented in Chapter 6 and represents another major contribution of this dissertation.

### 2.5.1 Modulator modelling

The discussion of the effect of frequency-dependent $I/Q$ imbalances will be considered separately for the modulator and demodulator. This section will focus on the quadrature modulator.

#### Frequency-dependent distortion model

The aim of the quadrature modulator is to translate and transform a complex baseband signal to a real-valued, passband signal. In most modern modulators, this baseband signal is generated in the digital domain of the transmitter, due to the increased flexibility and precision that this domain allows. This will also be the assumption of this dissertation.

In the topology of the quadrature modulator, the reconstruction (lowpass) filters following the DACs are responsible for filtering these undesired spectral replicas due to the sampling process. When the responses of these filters are not identical, the image rejection capability

of the modulator is compromised [20, 29, 59]. For modelling purposes, these reconstruction filters will be decomposed into a cascade of a perfect lowpass filters, responsible for removing the replicas of the signals due to the digital-to-analogue conversion process, and another filter response modelling the deviation from this perfect response. This can be done without loss of generality in terms of $I/Q$ imbalances, since it essentially only means that the filter eliminates the presence of the sampling signal replicas to such an extent that it does not need to be considered further. It is therefore assumed that the signals at the output of the perfect lowpass filters do not contain any signal replicas at multiples of the sampling frequency, and thus represents the continuous time equivalent of the digital baseband signal intended to be translates in frequency to the passband. Subsequent analysis will investigate the distortion that the imbalanced modulator causes, using this signal as the reference of the perfect baseband signal.

In quadrature modulation, the real and imaginary parts of the complex baseband signal are, respectively, used as inputs to the $I$ and $Q$ signal paths of the quadrature modulator. As discussed above, this digital baseband signal will subsequently be converted to the analogue domain, and passed through the analogue reconstruction filters to remove the signal replicas at multiples of the digital sampling rate. Let $a_I(t)$ and $a_Q(t)$ denote the time domain output of the respective perfect lowpass reconstruction filters. As indicated in Fig. 2.7, these two signals have frequency-domain representations $A_I(f)$ and $A_Q(f)$. The signal

$$A(f) = A_I(f) + jA_Q(f) \tag{2.17}$$

therefore represents the spectrum that should ideally be present around the carrier frequency at the output of the quadrature modulator. It is assumed that the spectrum of $A(f)$ is band limited to $[-B/2, B/2]$ Hz. Note that at this stage no imperfections have been introduced, since any linear imperfections before this stage (e.g. resulting from the DACs) can be lumped with the responses denoted by $E_I(f)$ and $E_Q(f)$, which will be discussed next.

The frequency responses of the $I$ and the $Q$ channels, including the contributions of the DACs and LPFs, are represented by the functions $E_I(f)$ and $E_Q(f)$. Taking their effect into account yields the signals

$$A'_I(f) = A_I(f)E_I(f) \tag{2.18}$$

and

$$A'_Q(f) = A_Q(f)E_Q(f). \tag{2.19}$$

The two quadrature LO signals of the mixer typically contribute significantly towards the total $I/Q$ imbalance [9, 13, 50]. The LO signal mixed with the baseband signal of the $I$ channel can be written as

$$x_{M,I}(t) = \alpha_I \cos(2\pi f_M t + \phi_I) \tag{2.20}$$

or in the frequency-domain

$$X_{M,I}(f) = \alpha_I/2 \left[\delta(f - f_M)e^{j\phi_I} + \delta(f + f_M)e^{-j\phi_I}\right]. \tag{2.21}$$

The LO signal mixing with the baseband signal of the $Q$ channel can similarly be written as

$$x_{M,Q}(t) = \alpha_Q \sin(2\pi f_M t + \phi_Q) \tag{2.22}$$

and in the frequency-domain as

$$X_{M,Q}(f) = \alpha_Q/(2j)\left[\delta(f - f_M)e^{j\phi_Q} - \delta(f + f_M)e^{-j\phi_Q}\right]. \tag{2.23}$$

The phase imbalance of the mixer is defined as the difference in phase, from 90 degrees, of its two oscillator signals, thus represented by $\phi_I - \phi_Q$. Similarly the gain imbalance of the mixer is represented by the scaling factor $\alpha_I/\alpha_Q$.

The signals at the output of the mixing process is given by

$$\begin{aligned} S_I(f) &= A'_I(f) * X_{M,I}(f) \\ &= \frac{1}{2}\left[A_I(f)E_I(f) * \alpha_I\delta(f - f_M)e^{j\phi_I} + A_I(f)E_I(f) * \alpha_I\delta(f + f_M)e^{-j\phi_I}\right] \\ &= \frac{\alpha_I}{2}\left[A_I(f - f_M)E_I(f - f_M)e^{j\phi_I} + A_I(f + f_M)E_I(f + f_M)e^{-j\phi_I}\right] \end{aligned} \tag{2.24}$$

Similarly

$$\begin{aligned} S_Q(f) &= A'_Q(f) * X_{M,Q}(f) \\ &= \frac{\alpha_Q}{2j}\left[A_Q(f - f_M)E_I(f - f_M)e^{j\phi_Q} - A_Q(f + f_M)E_I(f + f_M)e^{-j\phi_Q}\right] \end{aligned} \tag{2.25}$$

Note that the real-valued signals $S_I(f)$ and $S_Q(f)$ are now located in the passband, with their Hermitian symmetrical spectra components located at the frequencies $f = f_M$ and $f = -f_M$, respectively.

In order to model any passband frequency response of the $I$ and $Q$ signal paths (including any passband frequency response contributed by the mixer), bandpass filters (BPFs) with impulse responses of $g_I(t)$ and $g_Q(t)$ are defined. Since the aim of this chapter is to derive a baseband-equivalent distortion model for the modulator, the BPFs will be defined in terms of their complex lowpass equivalent representations $\tilde{g}_I(t)$ and $\tilde{g}_Q(t)$. The concept of the baseband-equivalent signal was introduced in Section 2.4.2 on p. 22. The frequency-domain representations of $\tilde{g}_I(t)$ and $\tilde{g}_Q(t)$ are denoted by $\tilde{G}_I(f)$ and $\tilde{G}_Q(f)$, respectively. These spectra are defined to span the frequency band $[-B/2, B/2]$ Hz, where $B \ll F_M$. The relation between real BPFs and their complex-valued lowpass equivalent representations are given by

$$g_I(t) = \tilde{g}_I(t)e^{j2\pi f_M t} + \tilde{g}_I^*(t)e^{-j2\pi f_M t} \tag{2.26}$$

and

$$g_Q(t) = \tilde{g}_Q(t)e^{2\pi f_M t} + \tilde{g}_Q^*(t)e^{-2\pi f_M t}. \tag{2.27}$$

Equivalently, in the frequency-domain this becomes

$$G_I(f) = \tilde{G}_I(f - f_M) + \tilde{G}_I^*(-f - f_M) \tag{2.28}$$

and

$$G_Q(f) = \tilde{G}_Q(f - f_M) + \tilde{G}_Q^*(-f - f_M)\,. \tag{2.29}$$

The signal in the $I$ signal path, after the effect of these bandpass responses has been included, can be written as

$$\begin{aligned}
S_I'(f) &= S_I(f)G_I(f) \\
&= \frac{\alpha_I}{2}\left[A_I(f-f_M)E_I(f-f_M)e^{j\phi_I} + A_I(f+f_M)E_I(f+f_M)e^{-j\phi_I}\right] \\
&\quad \times \left[\tilde{G}_I(f-f_M) + \tilde{G}_I^*(-f-f_M)\right] \\
&= \frac{\alpha_I}{2}\Big[A_I(f-f_M)E_I(f-f_M)e^{j\phi_I}\tilde{G}_I(f-f_M) \\
&\quad + A_I(f-f_M)E_I(f-f_M)e^{j\phi_I}\tilde{G}_I^*(-f-f_M) \\
&\quad + A_I(f+f_M)E_I(f+f_M)e^{-j\phi_I}\tilde{G}_I(f-f_M) \\
&\quad + A_I(f+f_M)E_I(f+f_M)e^{-j\phi_I}\tilde{G}_I^*(-f-f_M)\Big]
\end{aligned} \tag{2.30}$$

Removing the terms where there are no overlap in frequency, yields

$$\begin{aligned}
S_I'(f) &= \frac{\alpha_I}{2}\Big[A_I(f-f_M)E_I(f-f_M)\tilde{G}_I(f-f_M)e^{j\phi_I} \\
&\quad + A_I(f+f_M)E_I(f+f_M)\tilde{G}_I^*(-f-f_M)e^{-j\phi_I}\Big]\,.
\end{aligned} \tag{2.31}$$

Using the same approach, the $Q$ channel's signal is given by

$$\begin{aligned}
S_Q'(f) &= S_Q G_Q(f) \\
&= j\,\frac{\alpha_Q}{2}\Big[A_Q(f+f_M)E_Q(f+f_M)\tilde{G}_Q^*(-f-f_M)e^{-j\phi_Q} \\
&\quad - A_Q(f-f_M)E_Q(f-f_M)\tilde{G}_Q(f-f_M)e^{j\phi_Q}\Big]\,.
\end{aligned} \tag{2.32}$$

The transmitted signal is given by the subtraction of $S_I'(f)$ and $S_Q'(f)$ and thus becomes

$$\begin{aligned}
U_{RF}(f) &= S_I'(f) - S_Q'(f) \\
&= \frac{\alpha_I}{2}\Big[A_I(f-f_M)E_I(f-f_M)\tilde{G}_I(f-f_M)e^{j\phi_I} \\
&\quad + A_I(f+f_M)E_I(f+f_M)\tilde{G}_I^*(-f-f_M)e^{-j\phi_I}\Big] \\
&\quad -j\,\alpha_Q/2\Big[A_Q(f+f_M)E_Q(f+f_M)\tilde{G}_Q^*(-f-f_M)e^{-j\phi_Q} \\
&\quad - A_Q(f-f_M)E_Q(f-f_M)\tilde{G}_Q(f-f_M)e^{j\phi_Q}\Big]\,.
\end{aligned} \tag{2.33}$$

Using the following identities,

$$A(f+f_M) = A_I(f+f_M) + jA_Q(f+f_M) \tag{2.34}$$

$$A(f-f_M) = A_I(f-f_M) + jA_Q(f-f_M) \tag{2.35}$$

$$A^*(-f-f_M) = A_I(f+f_M) - jA_Q(f+f_M) \tag{2.36}$$

$$A^*(-f+f_M) = A_I(f-f_M) - jA_Q(f-f_M) \tag{2.37}$$

(2.33) may also be expressed as

$$\begin{aligned} U_{RF}(f) &= \frac{\alpha_I}{2}\Big\{\Big[A^*(-f+f_M)+jA_Q(f-f_M)\Big]E_I(f-f_M)\tilde{G}_I(f-f_M)e^{j\phi_I} \\ &\quad+\Big[A(f+f_M)-jA_Q(f+f_M)\Big]E_I(f+f_M)\tilde{G}_I^*(-f-f_M)e^{-j\phi_I}\Big\} \\ &\quad-\frac{\alpha_Q}{2}\Big\{\Big[A(f+f_M)-A_I(f+f_M)\Big]E_Q(f+f_M)\tilde{G}_Q^*(-f-f_M)e^{-j\phi_Q} \\ &\quad+\Big[A_I(f-f_M)-A^*(-f+f_M)\Big]E_Q(f-f_M)\tilde{G}_Q(f-f_M)e^{j\phi_Q}\Big\}. \end{aligned} \tag{2.38}$$

By adding the expressions of (2.33) and (2.38) and using the identities given in (2.34) to (2.37), the following is obtained:

$$\begin{aligned} &2U_{RF}(f) = \\ &\underbrace{A(f-f_M)\Big[\alpha_I E_I(f-f_M)\tilde{G}_I(f-f_M)e^{j\phi_I}+\alpha_Q E_Q(f-f_M)\tilde{G}_Q(f-f_M)e^{j\phi_Q}\Big]}_{\text{Desired component around frequency } f_M} \\ &+\underbrace{A^*(-f+f_M)\Big[\alpha_I E_I(f-f_M)\tilde{G}_I(f-f_M)e^{j\phi_I}-\alpha_Q E_Q(f-f_M)\tilde{G}_Q(f-f_M)e^{j\phi_Q}\Big]}_{\text{Image component around frequency } f_M} \\ &+\underbrace{A^*(-f-f_M)\Big[\alpha_I E_I(f+f_M)\tilde{G}_I^*(-f-f_M)e^{-j\phi_I}+\alpha_Q E_Q(f+f_M)\tilde{G}_Q^*(-f-f_M)e^{-j\phi_Q}\Big]}_{\text{Desired component around frequency } -f_M} \\ &+\underbrace{A(f+f_M)\Big[\alpha_I E_I(f+f_M)\tilde{G}_I^*(-f-f_M)e^{-j\phi_I}-\alpha_Q E_Q(f+f_M)\tilde{G}_Q^*(-f-f_M)e^{-j\phi_Q}\Big]}_{\text{Image component around frequency } -f_M}. \end{aligned} \tag{2.39}$$

If two weighting functions are defined as

$$V_1(f) = \alpha_I/2E_I(f)\tilde{G}_I(f)e^{j\phi_I}+\alpha_Q/2E_Q(f)\tilde{G}_Q(f)e^{j\phi_Q} \tag{2.40}$$

$$V_2(f) = \alpha_I/2E_I(f)\tilde{G}_I(f)e^{j\phi_I}-\alpha_Q/2E_Q(f)\tilde{G}_Q(f)e^{j\phi_Q}\ , \tag{2.41}$$

then the output signal, $U_{RF}(f)$, may be rewritten as

$$\begin{aligned} U_{RF}(f) &= A(f-f_M)V_1(f-f_M)+A^*(-f+f_M)V_2(f-f_M) \\ &\quad+A^*(-f-f_M)V_1^*(-f-f_M)+A(f+f_M)V_2^*(-f-f_M). \end{aligned} \tag{2.42}$$

Note that in the previous step the fact that $E_I(f)$ and $E_Q(f)$ are the frequency spectra of real-valued filters, was exploited in the sense that $E_I^*(-f-f_M)=E_I(f+f_M)$ and $E_Q^*(-f-f_M)=E_Q(f+f_M)$.

In order to obtain a complex baseband-equivalent model, it is necessary to derive the baseband-equivalent signal of $U_{RF}(f)$, denoted by $\tilde{U}_{RF}(f)$. $\tilde{U}_{RF}(f)$ is related to $U_{RF}(f)$ by the following relationship [40, p. 52]

$$\tilde{U}_{RF}(f)=2\mathcal{U}(f+f_M)U_{RF}(f+f_M) \tag{2.43}$$

where $\mathcal{U}(f)$ denotes the Heaviside step function, which is defined as

$$\mathcal{U}(f)=\begin{cases}0 & \text{if } f<0\\ 1 & \text{if } f\geq 0\end{cases} \tag{2.44}$$

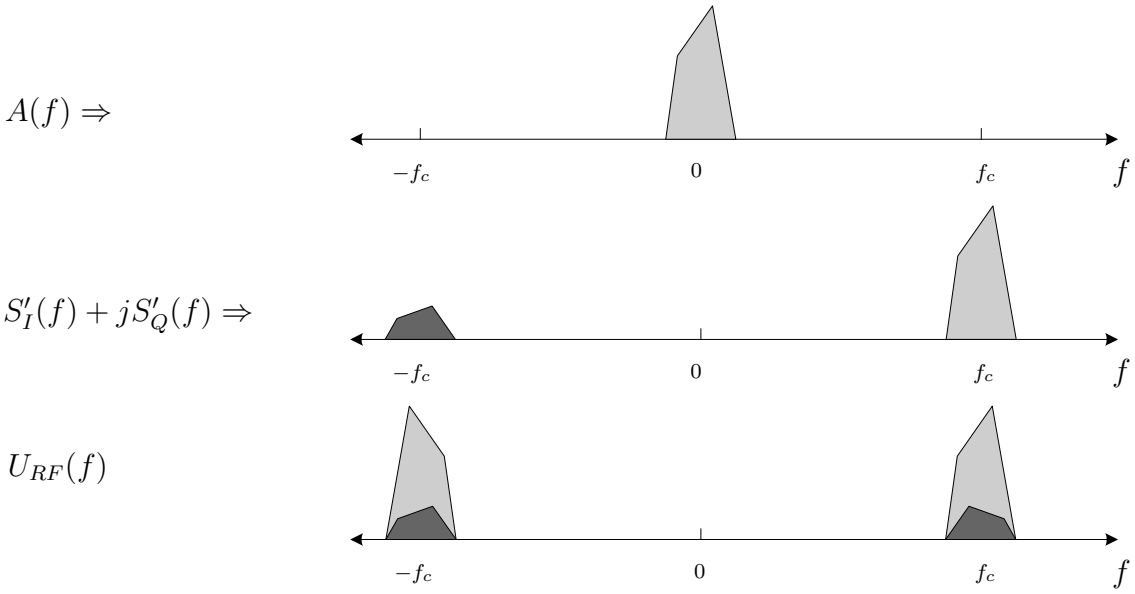


**Figure 2.8:** *Magnitude spectra during the up-mixing process in the presence of $I/Q$ imbalances. The unwanted image frequency components are indicated with dark grey shading.*

Accordingly, the baseband-equivalent model for the quadrature modulator becomes

$$\tilde{U}_{RF}(f) = A(f)V_1(f) + A^*(-f)V_2(f). \tag{2.45}$$

This baseband-equivalent representation will also be used to the derive the baseband modulator imbalance extraction and compensation techniques presented in Chapter 4.

From (2.45) it is seen that, in contrast to the perfect quadrature modulator, when the weighting function $V_2(f)$ is not zero, a second undesired frequency translation takes place. This second frequency translation contributes an unwanted image frequency component. In (2.45), the first term, associated with $A(f)$, represents the desired signal component, and the second term, associated with $A^*(-f)$, represents the undesired image frequency component. This unwanted image component will interfere with the desired signal component, if the complex baseband signal contained unique information in both positive and negative frequency components. This reduces its signal-to-noise-and-distortion (SINAD) ratio [67, p. 54]. This is shown graphically in Figure 2.8. For the case where the complex baseband signal only contained information in either the positive or the negative frequencies, as is the case for a transmitter employing a digital low-IF [71], the unwanted image signal component will not interfere with the desired signal component. Rather, it could now occupy an adjacent channel's allocated frequency band, and interfere with the signal that is assigned to that part of the frequency spectrum. This out-of-band transmission is clearly undesirable, since the SINAD of this adjacent channel's signal is thereby degraded. The next section investigates the relative power of this undesired image component in more detail.

### Relative Image Ratio (RIR)

By examining the expression for $\tilde{U}_{RF}(f)$ in (2.45), it is seen that when an imbalanced quadrature modulator is used, a desired signal component at frequency $f = f_A$ will result in an undesired image frequency component at frequency $f = -f_A$. The relative image ratio (RIR) is an indication of the amount by which the modulator suppresses this unwanted image frequency component. The RIR is defined to be the ratio between the power of the desired and image signal components and can therefore be written as

$$I_M(f) = \left| \frac{V_2(-f)}{V_1(f)} \right|^2 . \tag{2.46}$$

$I_M(f_A)$ should therefore be interpreted as the RIR that will be measured for a desired component at baseband frequency of $f_A$ and an image component at $-f_A$.

Substituting the expressions for $V_1(f)$ and $V_2(-f)$ into the above equation yields

$$I_M(f) = \left| \frac{\alpha_I |E_I(-f)||\tilde{G}_I(-f)| e^{j[\angle E_I(-f)+\angle \tilde{G}_I(-f)+\phi_I]} - \alpha_Q |E_Q(-f)||\tilde{G}_Q(-f)| e^{j[\angle E_Q(-f)+\angle \tilde{G}_Q(-f)+\phi_Q]}}{\alpha_I |E_I(f)||\tilde{G}_I(f)| e^{j[\angle E_I(f)+\angle \tilde{G}_I(f)+\phi_I]} + \alpha_Q |E_Q(f)||\tilde{G}_Q(f)| e^{j[\angle E_Q(f)+\angle \tilde{G}_Q(f)+\phi_Q]}} \right|^2 \tag{2.47}$$

By defining the following

$$\eta_I(f) = \alpha_I |E_I(f)||\tilde{G}_I(f)| \tag{2.48}$$

$$\eta_Q(f) = \alpha_Q |E_Q(f)||\tilde{G}_Q(f)| \tag{2.49}$$

$$\psi_I(f) = \angle E_I(f) + \angle \tilde{G}_I(f) + \phi_I \tag{2.50}$$

$$\psi_Q(f) = \angle E_Q(f) + \angle \tilde{G}_Q(f) + \phi_Q \tag{2.51}$$

the expression for $I_M(f)$ can be simplified to

$$I_M(f) = \left| \frac{\eta_I(-f) e^{j\psi_I(-f)} - \eta_Q(-f) e^{j\psi_Q(-f)}}{\eta_I(f) e^{j\psi_I(f)} + \eta_Q(f) e^{j\psi_Q(f)}} \right|^2 \tag{2.52}$$

which, after basic algebraic manipulation, can be written in the following form

$$I_M(f) = \left[ \frac{|\tilde{G}_Q(-f)|}{|\tilde{G}_Q(f)|} \right]^2 \left\{ \frac{\left[\frac{\eta_I(-f)}{\eta_Q(-f)}\right]^2 + 1 - 2\left[\frac{\eta_I(-f)}{\eta_Q(-f)}\right] \cos\left[\psi_I(-f) - \psi_Q(-f)\right]}{\left[\frac{\eta_I(f)}{\eta_Q(f)}\right]^2 + 1 + 2\left[\frac{\eta_I(f)}{\eta_Q(f)}\right] \cos\left[\psi_I(f) - \psi_Q(f)\right]} \right\} \tag{2.53}$$

or equivalently

$$I_M(f) = \left[ \frac{|\tilde{G}_I(-f)|}{|\tilde{G}_I(f)|} \right]^2 \left\{ \frac{\left[\frac{\eta_Q(-f)}{\eta_I(-f)}\right]^2 + 1 - 2\left[\frac{\eta_Q(-f)}{\eta_I(-f)}\right] \cos\left[\psi_Q(-f) - \psi_I(-f)\right]}{\left[\frac{\eta_Q(f)}{\eta_I(f)}\right]^2 + 1 + 2\left[\frac{\eta_Q(f)}{\eta_I(f)}\right] \cos\left[\psi_Q(f) - \psi_I(f)\right]} \right\} . \tag{2.54}$$

By defining the gain imbalance of the modulator as

$$\eta_M(f) = \eta_I(f)/\eta_Q(f) \tag{2.55}$$

and the phase imbalance as

$$\psi_M(f) = \psi_I(f) - \psi_Q(f)\,, \tag{2.56}$$

eqs.(2.53) and (2.54) can be written as

$$I_M(f) = \left[\frac{|\tilde{G}_Q(-f)|}{|\tilde{G}_Q(f)|}\right]^2 \left[\frac{[\eta_M(-f)]^2 + 1 - 2\eta_M(-f)\cos\Big(\psi_M(-f)\Big)}{[\eta_M(f)]^2 + 1 + 2\eta_M(f)\cos\Big(\psi_M(f)\Big)}\right] \tag{2.57}$$

or equivalently

$$I_M(f) = \left[\frac{|\tilde{G}_I(-f)|}{|\tilde{G}_I(f)|}\right]^2 \left[\frac{[1/\eta_M(-f)]^2 + 1 - 2/\eta_M(-f)\cos\Big(-\psi_M(-f)\Big)}{[1/\eta_M(f)]^2 + 1 + 2/\eta_M(f)\cos\Big(-\psi_M(f)\Big)}\right]. \tag{2.58}$$

These expressions provide insight into the causes of finite rejection of the image frequency components in practical quadrature modulators. The first observation is that the relative power in the undesired image component can be reduced to zero, if

$$[\eta_M(-f)]^2 + 1 - 2\eta_M(-f)\cos\Big(\psi_M(-f)\Big) = 0\,, \tag{2.59}$$

or

$$[1/\eta_M(-f)]^2 + 1 - 2/\eta_M(-f)\cos\Big(-\psi_M(-f)\Big) = 0\,. \tag{2.60}$$

This requirement is satisfied when

$$\eta_M(-f) = \frac{\eta_I(-f)}{\eta_Q(-f)} = 1 \tag{2.61}$$

and

$$\psi_M(-f) = \psi_I(-f) - \psi_Q(-f) = 0. \tag{2.62}$$

In other words, the cascaded gain and phase responses of the $I$ and $Q$ channels need to be equal. When this is not the case, the channels are imbalanced, and the image component is not rejected completely. Note that the *cascaded* gain and phase response of each channel is of importance here. This means that in each channel, the baseband frequency response can compensate for distortion caused by passband imbalances or mixer imbalances, or vice versa. It is this principle that will be exploited in the compensation techniques presented in this dissertation, i.e. that digital baseband compensation filters can be used to compensate for the baseband, mixer and passband imbalances of the quadrature modulator, even when these imbalances are frequency dependent. This approach is discussed in detail in Chapter 4.

The second observation involves the position in the frequency spectrum where the gain and phase responses of the $I$ and $Q$ channels need to be matched. It can easily be verified that in order to avoid the image frequency component of a desired signal at a frequency $f = f_A$, the baseband-equivalent response of the quadrature modulator should be exactly matched

in gain and phase at the frequency $f = -f_A$ ( (2.59) is a function of $-f$). Matching the two channels' responses perfectly at the frequency of the desired component will not prevent the image signal from being present. Rather, the two signal channels should be exactly matched at the image component's frequency.

The third observation relates to the symmetry of the gain $\eta_M(f)$ and phase $\psi_M(f)$ imbalance functions. If the frequency-dependent imbalances of the quadrature modulator were only modelled through mismatched LPFs, as is done in literature (see e.g. [31, 58, 59, 5, 4, 55]), i.e. $\tilde{G}_I(f) = \tilde{G}_Q(f) = 1$, then the symmetry of $\eta_M(f)$ and $\psi_M(f)$ would be well defined. $\eta_M(f)$ would be an even function of frequency, since $|E_I(f)|$ and $|E_Q(f)|$ represent the magnitude responses of real filters, which are constrained to be even. Similarly, $\psi_M(f)$ would be an odd function of frequency if its offset phase at DC is subtracted. To understand this, consider the fact that the phase responses $\angle E_I(f)$ and $\angle E_Q(f)$ are constrained to be odd functions since they represent the phase responses of the real filters $E_I(f)$ and $E_I(f)$, respectively. Both $\angle E_I(f)$ and $\angle E_Q(f)$ will therefore necessarily be zero at DC, yielding the DC value of $\psi_M(f)$ equal to $\phi_I - \phi_Q$. Subtracting the DC value of $\psi_M(f)$ will therefore remove the effect of the mixer phase imbalance $\phi_I - \phi_Q$, and make $\psi_M(f)$ only a function of $\angle E_I(f)$ and $\angle E_Q(f)$, and therefore necessarily also an odd function of frequency. In Chapter 4, the gain and phase imbalance functions of a hardware implemented quadrature modulator will be measured, yielding asymmetrical functions. The measured characteristics of the gain and phase imbalance functions can therefore not be explained if only LPF mismatches are modelled. The inclusion of the imbalances due to BPF mismatches are therefore crucial to explain this observed asymmetry, since $\tilde{G}_I(f)$ and $\tilde{G}_Q(f)$ are not restricted to exhibit Hermitian symmetry, they represent the baseband-equivalent responses of passband filters.

A final note involves the scaling factor $|\tilde{G}_Q(-f)|/|\tilde{G}_Q(f)|$ (or $|\tilde{G}_I(-f)|/|\tilde{G}_I(f)|$ ). It is seen that these scaling factors further modify the RIR performance of the modulator. It can therefore be concluded that the RIR of the modulator is inherently caused by the $I/Q$ imbalances of the front-end at the image frequency, but that the effects of these imbalances are scaled by the relative gain of the BPF at the image frequency. This makes intuitive sense, since once the image component is present, its relative power, compared to the power of the desired component, will be scaled by the gain of the BPF at the image frequency, relative to the gain of the BPF at the desired component.

### Model validation through simulation

The derived expression for the frequency-dependent imbalanced modulator represents a potentially significant result and needs to be verified before continuing. For this purpose, a MATLAB simulation architecture was developed, which will now be briefly described. This simulation architecture will be used again in Chapter 4, in order to validate the novel imbalance compensation techniques presented there. In this section, the simulation model for the imbalanced modulator will be described, after which it will be used to validate the expressions for the RIR derived in the previous subsection.

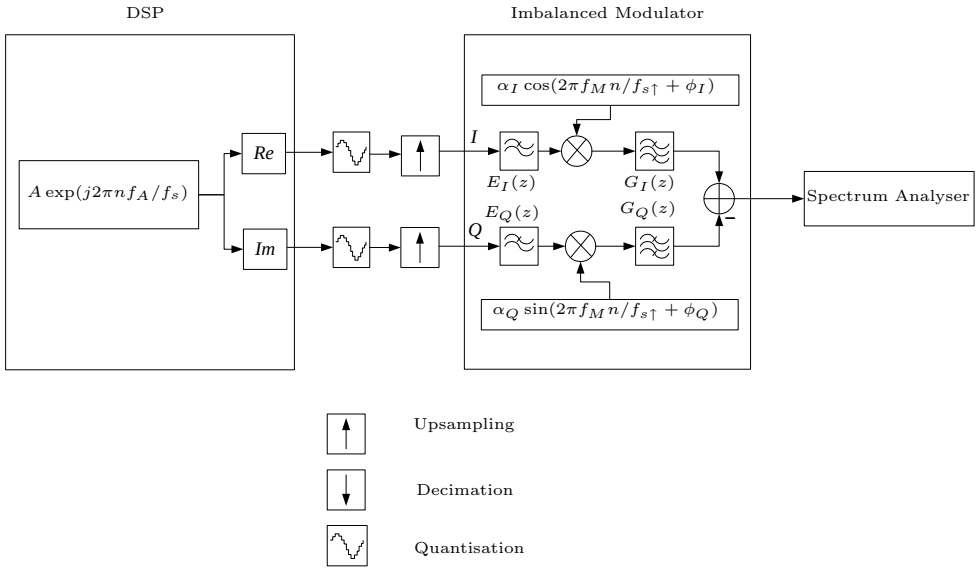


**Figure 2.9:** *Block diagram of the imbalanced modulator within the developed MATLAB simulation architecture.*

*Simulation overview*

Fig. 2.9 depicts a block diagram of the imbalanced modulator, as implemented in the MATLAB simulation. The complex, digital baseband signal is generated in the DSP (Digital Signal Processing) block, at a sampling rate of $f_s$ samples/sec. The real and imaginary parts of this signal are then split to be processed separately as the $I$ and $Q$ signals in the imbalanced quadrature modulator. Quantisation blocks are included, which allow the modelling of finite bit precision DAC converters. In the simulations of this chapter these blocks were not enabled, since the goal was to validate the theoretical imbalance model.

Simulation of the continuous time domain using an inherently discrete time simulation platform, poses a challenge. It was decided to represent the continuous-time as a discrete signal at a much higher sampling rate than the discrete-time baseband signal. For this purpose, MATLAB's `resample` function was used to upsample the digital baseband signal by a factor of 10. The effective sampling rate used for the 'continuous time' portion of the simulation, is denoted by $f_{s\uparrow}$. The `resample` function adjusts the sampling rate of a signal using a polyphase implementation. Anti-aliasing or interpolation filtering is performed, while compensating also for the filter's delay. It was verified that these blocks do not contribute at all to the quadrature imbalances observed in the simulation.

The imbalanced modulator is a direct implementation of the modulator topology that was presented in Fig. 2.7 on p. 25. The lowpass filters and bandpass filters are implemented as Chebyshev, real valued, IIR, digital filters. Frequency-dependent imbalances between the $I$ and $Q$ channels are realised by introducing differences between the cut off frequencies of these filters. Frequency-independent imbalances are introduced by controlling the amplitude

**Table 2.1:** *Simulation filter specifications.*

| **Parameter** | $E_I(z)$ | $E_Q(z)$ | $G_I(z)$ | $G_Q(z)$ |
|---|---|---|---|---|
| Filter type | Chebyshev Lowpass | Chebyshev Lowpass | Chebyshev Bandpass | Chebyshev Bandpass |
| Order | 6 | 6 | 12 | 12 |
| Coefficients | real | real | real | real |
| Passband ripple [dB] | 1 | 1 | 1 | 1 |
| Cut off frequency (normalised to $f_{s\uparrow}$) | 0.0510 | 0.0475 | 0.2705 and 0.3303 | 0.2695 and 0.3310 |

**Table 2.2:** *Simulation filter coefficients.*

| | | |
|---|---|---|
| $E_I(z)$ | $a_l$ | 1; -5.5543; 13.0029; -16.4160; 11.7842; -4.5595; 0.7428 |
| | $b_l$ | 0.0091e-4; 0.0544e-4; 0.1360e-4; 0.1814e-4; 0.1360e-4; 0.0544e-4; 0.0091e-4 |
| $E_Q(z)$ | $a_l$ | 1; -5.5940; 13.1686; -16.6926; 12.0141; -4.6542; 0.7581 |
| | $b_l$ | 0.0060e-4; 0.0358e-4; 0.0896e-4; 0.1194e-4; 0.0896e-4; 0.0358e-4; 0.0060e-4 |
| $G_I(z)$ | $a_l$ | 1; 3.6315; 10.9641; 21.1004; 34.9715; 43.8993; 48.1891; 41.4296; 31.1476; 17.7310; 8.6937; 2.7151; 0.7057 |
| | $b_l$ | 0.0231e-4; 0; -0.1384e-4; 0; 0.3460e-4; 0; -0.4613e-4; 0; 0.3460e-4; 0; -0.1384e-4; 0; 0.0231e-4; |
| $G_Q(z)$ | $a_l$ | 1; 3.6138; 10.8898; 20.8986; 34.5910; 43.3441; 47.5487; 40.8374; 30.7060; 17.4732; 8.5771; 2.6791; 0.6986 |
| | $b_l$ | 0.0273e-4; 0; -0.1637e-4; 0; 0.4093e-4; 0; -0.5457e-4; 0; 0.4093e-4; 0; -0.1637e-4; 0; 0.0273e-4 |

and phase of the two oscillator signals in the quadrature mixer. The normalised frequency of the oscillator signals are given by $f_M/f_{s\uparrow}$. $n$ denotes the discrete time sample iterator.

Table 2.1 provides the specifications of the filters used in the simulation. The coefficients for their implementation are listed in Table 2.2, where each filter's coefficients are related to its transfer function as follow (using $E_I(z)$ as an example),

$$E_I(z) = \frac{\sum_{l=0}^{N} a_l z^{-l}}{\sum_{l=0}^{L} b_l z^{-l}} \,. \tag{2.63}$$

The magnitude responses of these filters are also shown in Fig. 2.10. The normalised cut off frequencies of the LPFs are chosen such that they are nominally equal to the Nyquist zone of the baseband signal after upsampling, i.e. $-f_s/(2f_{s\uparrow})$ to $f_s/(2f_{s\uparrow})$, or $-0.05$ to 0.05 for an upsampling factor of 10. The quadrature mixer frequency translates the baseband signal to a normalised carrier frequency of 0.3 (normalised to $f_{s\uparrow}$)). The BPFs are designed such that their passbands are also centered around this frequency. The normalised passband width of the BPFs is chosen to be 0.06, which is narrower than the Nyquist zone width of the baseband digital signal (0.1). The reason for this is to tightly channelise the frequency band of interest, in the passband. The frequency band of interest was chosen from $-0.2$ to 0.2, in the digital domain of the modulator, equalling a total frequency band of 0.04 when normalised to $f_{\uparrow s}$. Table 2.3 presents the parameters for the oscillator's frequency and imbalances. The chosen oscillator imbalances are representative of typical imbalances found in a practical quadrature modulator [9, 65].

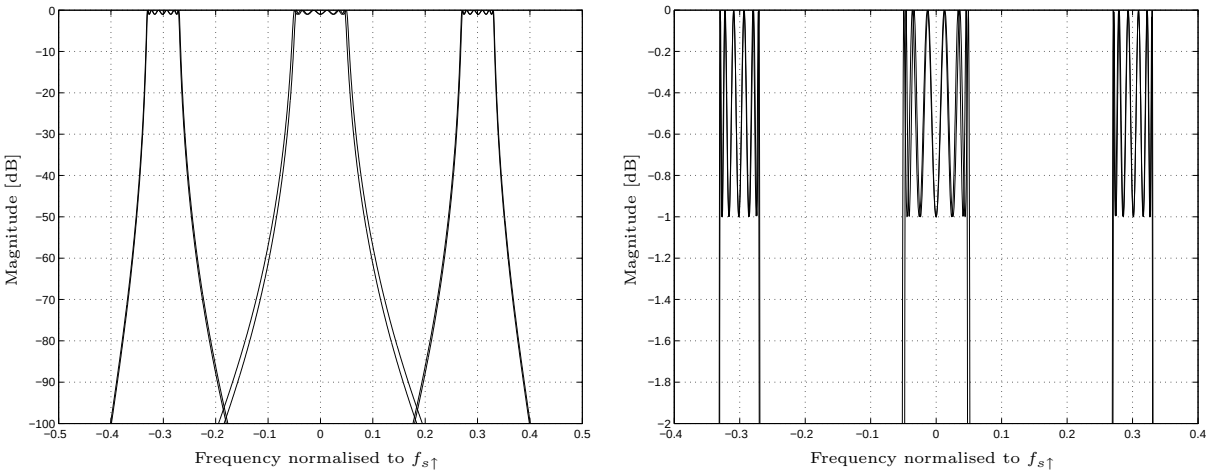


(a) (b)

**Figure 2.10:** *Magnitude spectra of the digital filters used during simulation.*

**Table 2.3:** *Simulation parameters.*

| Parameter | Value |
|---|---|
| $f_{s\uparrow}/f_s$ | 10 |
| $f_M/f_{s\uparrow}$ | 0.3 |
| $\alpha_I/\alpha_Q$ | 1.05 |
| $\phi_I - \phi_Q$ | 3 ° |

*Validation of modulator RIR*

In order to validate the expression for the modulator RIR in (2.47), complex valued, single frequency test tones were generated in the baseband digital domain of the modulator. The advantage of using single frequency tones as test signals, is that they can easily be decomposed into a desired and image component at the output of the imbalanced modulator. Fig. 2.11 shows an example magnitude spectra, where the test tone

$$Ae^{j2\pi n f_A/f_s}$$

with normalised frequency $f_A/f_s = 0.164$ is generated and upconverted using the imbalanced modulator. According to (2.42), the passband signal should contain desired components at the normalised frequencies $(-f_A - f_M)/f_{s\uparrow}$ and $(f_A + f_M)/f_{s\uparrow}$, and image components at $(f_A - f_M)/f_{s\uparrow}$ and $(-f_A + f_M)/f_{s\uparrow}$. This can clearly be verified in the figure. The baseband frequencies of these test tones were chosen such that they cover the normalised frequency range from $-0.2$ to $0.2$ (normalised to their sampling rate $f_s$). For each test tone, the RIR of the upcoverted, passband signal was measured in the 'Spectrum Analyser' block in MATLAB, using a Fast Fourier Transform (FFT). This was accomplished by taking the ratio between the signal value in the FFT bin containing the image component and dividing it by the signal value in the bin containing the desired component. This measured value of the

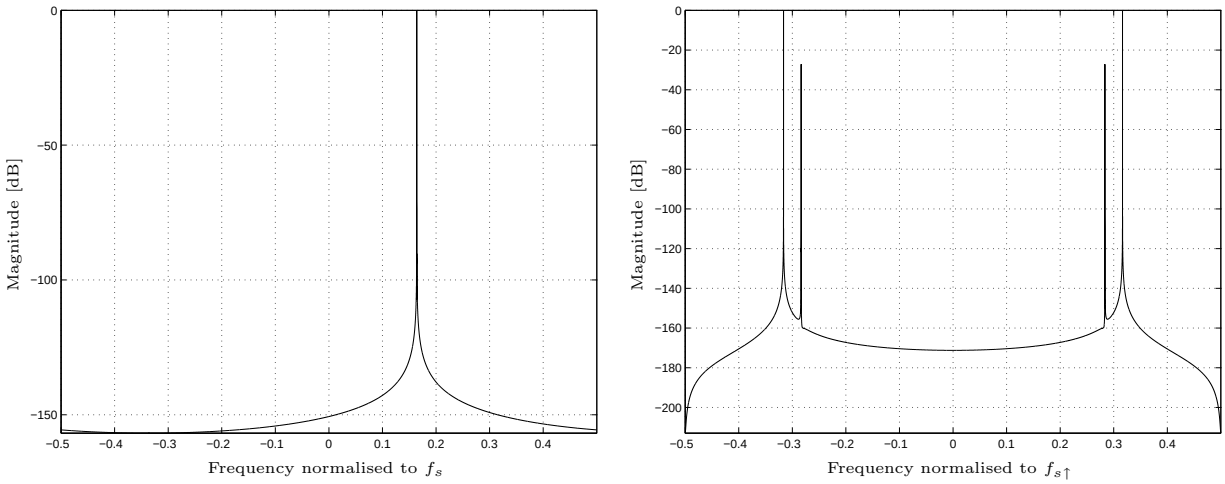


(a) (b)

**Figure 2.11:** *Magnitude spectra of a test tone at $f_m = 0.164$, at baseband (a) and after it has been upsampled and frequency translated to the passband with the imbalanced modulator (b). The presence of the image frequency component is clearly visible in (b), mirroring the desired components around the normalised carrier frequency of 0.3.*

RIR, as a function of baseband input frequency, could then be compared to a RIR computed using the theory derived in this chapter.

The expression for the theoretical RIR was derived in ( 2.47) (with equivalent forms presented in (2.53) and (2.52). To compute the theoretical RIR of the simulation topology, the frequency response of the various filters were obtained at each desired and image frequency position, using MATLAB's `freqz` command. These frequency response values, together with the gain and phase imbalances of the mixer, were subsequently substituted into (2.47), to produce the theoretical RIR for a tone at a particular input frequency. The results of the simulation is presented in Fig. 2.12. The theoretical and measured RIR corresponds well. In turn, this result also validates the baseband-equivalent model that was developed to derive the expression for the RIR. This baseband-equivalent model will be employed in Chapter 4 to derive novel imbalance extraction methods.

### Special case: Frequency-independent $I/Q$ imbalances

Consider now the special case where the imbalances of the quadrature modulator can be considered to be independent of frequency. This is the case that is most often considered in literature (see e.g. [25, 9, 8, 60]) and is often a fair assumption for narrowband signals. In order to derive the frequency-independent model, the expressions for $V_1(f)$ and $V_2(f)$, as given in (2.40), should be re-evaluated. Upon inspection of these expressions, it is seen that both $V_1(f)$ and $V_2(f)$ are functions of the terms

$$\frac{\alpha_I}{2} E_I(f) \tilde{G}_I(f) e^{j\phi_I}$$

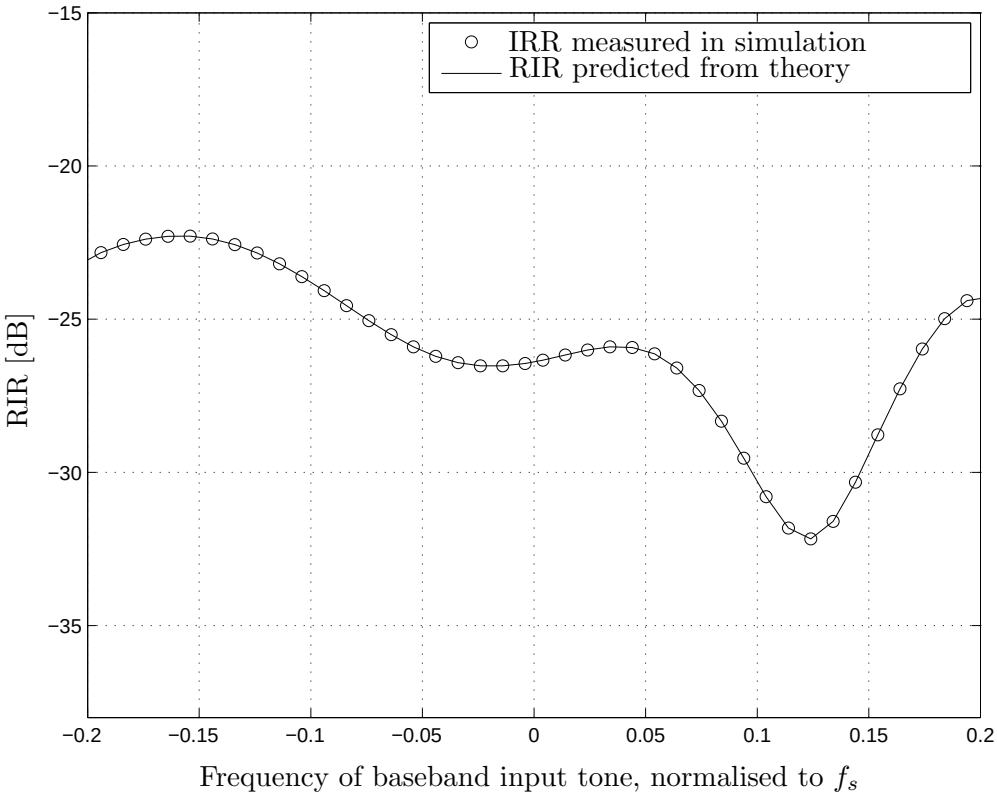


**Figure 2.12:** *The RIR of the simulated modulator setup, measured using spectral analysis and predicted from the developed theoretical model.*

and

$$\frac{\alpha_Q}{2} E_Q(f)\tilde{G}_Q(f)e^{j\phi_Q},$$

which can be seen as the frequency responses of the $I$ and $Q$ channels, respectively. The assumption for the frequency-independent model is that each of these terms only contribute a single amplitude and phase scaling factor, which is independent of frequency. Let the frequency-independent complex scaling of the $I$ channel be given by $\eta_I e^{j\psi_I}$ and that of the $Q$ channel by $\eta_Q e^{j\psi_Q}$. Using this frequency-independent model, the gain imbalance of the modulator is given by

$$\eta_M = \frac{\eta_I}{\eta_Q} \tag{2.64}$$

and the phase imbalance is given by,

$$\psi_M = \psi_I - \psi_Q. \tag{2.65}$$

In literature, the frequency-independent gain and phase imbalances are commonly modelled as the imbalances associated with the LO signals of the quadrature mixer (i.e. the gain difference and deviation from 90° phase between its two oscillator signals) [9, 13, 50]. However,

it was seen in the extended model of the previous section, that the gain and phase error is due to the cascaded response of all the components in the channel.

Using the above assumptions, the frequency-independent expressions for $V_1$ and $V_2$ can then be written as

$$V_1 = \eta_I e^{j\psi_I} + \eta_Q e^{j\psi_Q} \tag{2.66}$$

$$V_2 = \eta_I e^{j\psi_I} - \eta_Q e^{j\psi_Q} \tag{2.67}$$

It is insightful to now revisit the RIR for the frequency-independent case.

*The RIR*

The RIR for the frequency-independent case is defined using the expressions for $V_1$ and $V_2$ in (2.66) and (2.67). Therefore

$$\begin{aligned} I_M &= \left|\frac{V_2}{V_1}\right|^2 \\ &= \left|\frac{\eta_I e^{j\psi_I} - \eta_Q e^{j\psi_Q}}{\eta_I e^{j\psi_I} + \eta_Q e^{j\psi_Q}}\right|^2 \\ &= \frac{\left(\frac{\eta_I}{\eta_Q}\right)^2 + 1 - 2\left(\frac{\eta_I}{\eta_Q}\right)\cos(\psi_I - \psi_Q)}{\left(\frac{\eta_I}{\eta_Q}\right)^2 + 1 + 2\left(\frac{\eta_I}{\eta_Q}\right)\cos(\psi_I - \psi_Q)} \,. \end{aligned} \tag{2.68}$$

Since $\eta_M = \eta_I/\eta_Q$ and $\psi_M = \psi_I - \psi_Q$, we may rewrite the above equation in terms of the gain and phase imbalances of the modulator, as

$$I_M = \frac{\eta_M^2 + 1 - 2\eta_M \cos(\psi_M)}{\eta_M^2 + 1 + 2\eta_M \cos(\psi_M)} \,. \tag{2.69}$$

The result of (2.69) agrees with expressions presented in [9, 29] and [60, p. 13]. For small imbalances, (2.69) can be approximated as [9]

$$I_M \approx \frac{(\eta_M - 1)^2 + \psi_M^2}{4} \,. \tag{2.70}$$

It can be verified that the quantity of (2.69) remains the same if $\eta_M$ is replaced by $1/\eta_M$ or if $\psi_M$ is replaced by $-\psi_M$. This indicates that the RIR of the quadrature modulator only depends on the relative error between the two signal paths, a fact also observed by Kiss et. al. [29].

Figure 2.13 shows the RIR for different imbalance combinations of the modulator. Even with careful analogue front-end design, a practical quadrature mixing front-end would typically still have a gain imbalance of about $1 - 5\%$ and a phase error of about $1 - 5°$ [9, 65]. These levels of imbalances are usually not adequite for high quality communication systems and have severely limited the use of quadrature mixing in radio transceivers in the past [17]. Substituting these typical imbalance parameters into (2.69), it is found that a typical quadrature mixer would only suppress the unwanted image signal about 30 dB to 40 dB, relative to the desired signal.

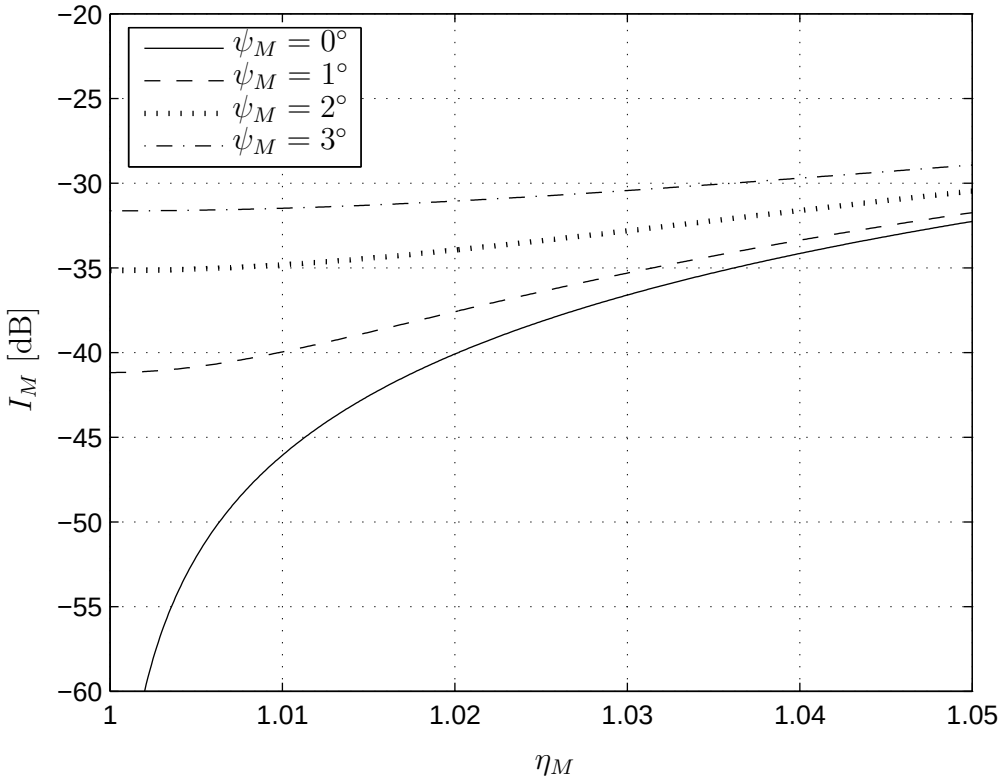


**Figure 2.13:** *The RIR of an imbalanced quadrature modulator.*

The amount of out-of-band suppression required from a transmitter is often governed by a regulatory body and depends on the particular frequency band and the type of transmission that are used. Table 2.4 offers a few examples of the required out-of-band suppression required for various transmission types. It is seen from this table that a typical quadrature modulator will either offer marginally sufficient or insufficient image or out-of-band suppression. Some form of compensation is therefore needed to make the quadrature modulator a viable alternative in these and other even more stringent applications.

*Baseband-equivalent vector model*

A common practice in literature (see e.g. [25, 9, 8, 60]) is to express the frequency-independent imbalances of the quadrature mixers in a vector format. In so doing, it allows the problem of $I/Q$ imbalance compensation to be approached using linear algebra techniques, therefore bringing the problem into a well established mathematical domain. The blind compensation techniques derived in Chapter 6 utilise this linear algebra approach to arrive at novel imbalance extraction techniques. This vector model will now be derived.

To derive these expressions, consider that, analogous to the expression in (2.45), the baseband-equivalent output of the quadrature modulator can be written as a function of $V_1$ and $V_2$ as

$$\tilde{U}_{RF}(f) = A(f)V_1 + A^*(-f)V_2 \ . \tag{2.71}$$

**Table 2.4:** *Required out-of-band suppression for various transmission types.*

| **Transmission type** | **Adjacent channel** | **Two channels separation** |
|---|---|---|
| Low power FM broadcasting [52] | 25 dBc | 35 dBc |
| Global System for Mobile communication (GSM) [43] | 30 dBc | 60 dBc |
| Wideband CDMA systems [68] | 33 dBc | |
| Code Division Multiple Access (CDMA) systems [68] | 42 dBc | |
| Digital broadcasting systems for television, sound and data services [51] | $\geq$ 43 dBc | $\geq$ 43 dBc |

Since $V_1$ and $V_2$ are frequency-independent, complex-valued scalars, the time domain representation of this signal will be more suitable to derive the vector model, i.e.

$$\tilde{u}_{RF}(t) = a(t)V_1 + a^*(t)V_2 \ . \tag{2.72}$$

Recall that the complex signal $a(t)$ is theoretically constructed by defining the signal in the $I$ channel, $a_I(t)$, as the real part, and the signal in the $Q$ channel, $a_Q(t)$, as the imaginary part of a complex signal, i.e.

$$a(t) = a_I(t) + ja_Q(t) \ . \tag{2.73}$$

Using the above expression, with the expressions for $V_1$ and $V_2$ that were given in (2.66) and (2.67), (2.72) can be expanded as

$$\begin{aligned} \tilde{u}_{RF}(t) &= [a_I(t) + ja_Q(t)]\left[\eta_I e^{j\psi_I} + \eta_Q e^{j\psi_Q}\right] \\ &\quad + [a_I(t) - ja_Q(t)]\left[\eta_I e^{j\psi_I} - \eta_Q e^{j\psi_Q}\right] \end{aligned} \tag{2.74}$$

which, after some basic trigonometric manipulation, can be written as

$$\begin{aligned} \tilde{u}_{RF}(t) &= a_I(t)\eta_I \cos(\psi_I) - \underbrace{a_Q(t)\eta_Q \sin(\psi_Q)}_{\text{Leakage Term}} \\ &\quad + j\Big[\underbrace{a_I(t)\eta_I \sin(\psi_I)}_{\text{Leakage Term}} + a_Q(t)\eta_Q \cos(\psi_Q)\Big]. \end{aligned} \tag{2.75}$$

In a perfect quadrature modulator, it is expected that the real part of $\tilde{u}_{RF}(t)$ should only be a function of $a_I(t)$. Similarly the imaginary part should only be a function of $a_Q(t)$. The imbalanced quadrature modulator therefore clearly causes leakage of the original $I$ and $Q$ channels into the real and imaginary part of the output baseband-equivalent signal, therefore establishing correlation in terms of the original real and imaginary components of the baseband transmit signal.

At this stage a vector notation to represent complex signals can be introduced. This notation has also been used in literature [25, 9, 8, 60]. Accordingly, the complex signal $a(t) = a_I(t) + ja_Q(t)$ is represented by the two element vector $\boldsymbol{a}(t) = [a_I(t), a_Q(t)]^T$, where the first

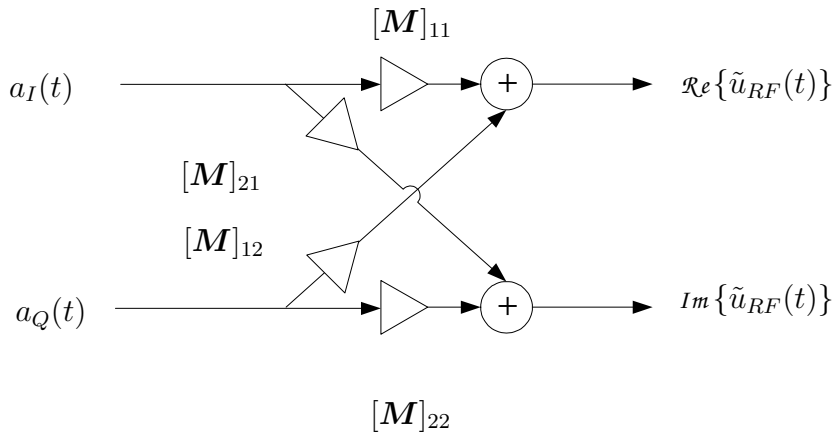


**Figure 2.14:** *Graphical representation of the equivalent baseband model for the modulator's $I$ and $Q$ channels in the presence of frequency-independent quadrature imbalances.*

element represents the real component and the second element the imaginary component. We may therefore write the expression for $\tilde{u}_{RF}(t)$, in (2.75), in vector form as

$$\tilde{\boldsymbol{u}}_{\boldsymbol{RF}}(t) = \boldsymbol{M}\boldsymbol{a}(t) \ , \tag{2.76}$$

where

$$\boldsymbol{M} \ = \ \begin{bmatrix} \eta_I \cos(\psi_I) & -\eta_Q \sin(\psi_Q) \\ \eta_I \sin(\psi_I) & \eta_Q \cos(\psi_Q) \end{bmatrix} \ . \tag{2.77}$$

The vector representation of the transmitted signal can be visualised with the leakage model shown in Fig. 2.14. $[\boldsymbol{M}]_{nk}$ denotes the $n^{th}$ element in the $k^{th}$ column of the matrix $\boldsymbol{M}$.

It was seen in (2.69) (p. 39) that the image suppression capability of the modulator only depends on the absolute phase error between the $I$ and the $Q$ channels. Therefore we may choose any convenient phase reference. Usually, the phase reference is chosen to be either the $I$ or the $Q$ channel's phase, or exactly in the middle of the two. Each choice of a phase reference results in a different distortion matrix, $\boldsymbol{M}$.

**Using the $I$ channel as reference.** When the $I$ channel's phase is used as the reference phase, then $\psi_I = 0$ and $\psi_Q = -\psi_M$. This effectively means that the phase error of the modulator, $\psi_M$, is attributed to the $Q$ channel. Recall that the phase imbalance of the modulator was defined as $\psi_M = \psi_I - \psi_Q$. The modulator imbalance matrix $\boldsymbol{M}$ therefore becomes

$$\boldsymbol{M} \ = \ \eta_I \begin{bmatrix} 1 & 1/\eta_M \sin(\psi_M) \\ 0 & 1/\eta_M \cos(\psi_M) \end{bmatrix} . \tag{2.78}$$

The factor $\eta_I$ only attributes an overall system gain, and can, without loss of generality, be normalised to unity.

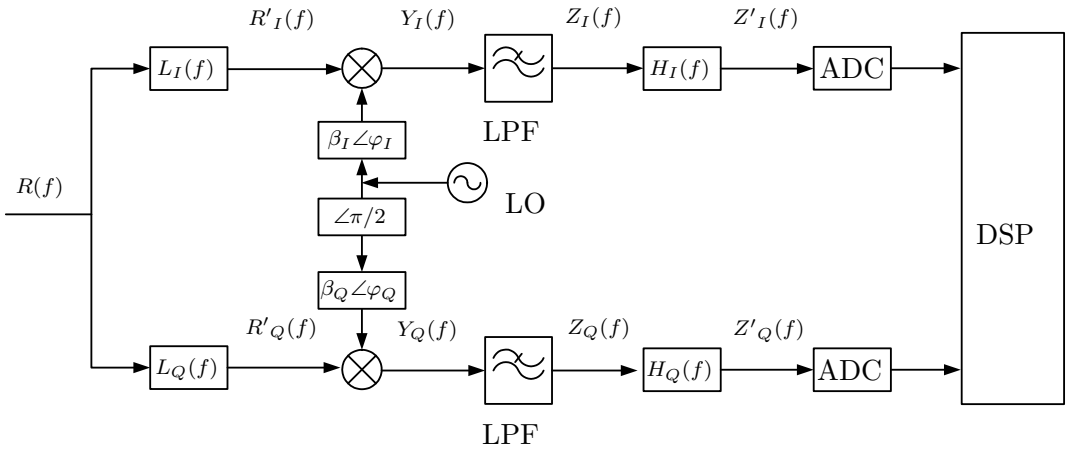


**Figure 2.15:** *The topology of the quadrature modulator in the presence of imbalances.*

**Using the $Q$ channel as reference.** When the $Q$ channel's phase is used as the reference phase, then $\psi_Q = 0$ and $\psi_I = \psi_M$. The modulator imbalance matrix $\boldsymbol{M}$ therefore becomes

$$\boldsymbol{M} = \eta_Q \begin{bmatrix} \eta_M \cos(\psi_M) & 0 \\ \eta_M \sin(\psi_M) & 1 \end{bmatrix}. \tag{2.79}$$

In this case the $Q$ channel's gain may be normalised to unity. This model agrees with the those used in [25, 9].

**Using an equally distributed phase reference.** This model distributes the phase error equally between the $I$ and the $Q$ channels. We therefore have that $\phi_I = \phi_M/2$ and that $\phi_Q = -\phi_M/2$. The modulator imbalance matrix $\boldsymbol{M}$ therefore becomes

$$\boldsymbol{M} = \begin{bmatrix} \alpha_I \cos(\phi_M/2) & \alpha_Q \sin(\phi_M/2) \\ \alpha_I \sin(\phi_M/2) & \alpha_Q \cos(\phi_M/2)\,. \end{bmatrix} \tag{2.80}$$

This model agrees with the models used in [8, 9, 25].

## 2.5.2 Demodulator modelling

### Distortion model

The development of the demodulator's distortion model follows a similar approach to that of the modulator. For reference, the topology of the quadrature demodulator is presented in Fig. 2.15, indicating the signals that will be used in the development of the imbalance model of the quadrature demodulator.

Consider the band-limited passband signal, $r(t)$, at the input to the demodulator. Let the centre frequency of this signal be $f_\Delta$ Hz above the LO frequency of the quadrature demodulator's LO signal, which is denoted by $f_D$. Furthermore, let $\tilde{r}(t)$ denote the baseband-equivalent signal of $r(t)$ at the centre frequency $f = f_D + f_\Delta$, and be band-limited to the

frequency range $[-B/2, B/2]$, where $B \ll f_D$. $r(t)$ can then be written as

$$r(t) = \tilde{r}(t)e^{j[2\pi(f_D+f_\Delta)t+\theta_\Delta]} + \tilde{r}^*(t)e^{-j[2\pi(f_D+f_\Delta)t+\theta_\Delta]} \tag{2.81}$$

where $\theta_\Delta$ denotes an arbitrary phase offset. Using the fact that

$$\mathcal{F}\{r^*(t)\} = R^*(-f) \tag{2.82}$$

the frequency-domain representation of $r(t)$ can be written as

$$R(f) = \tilde{R}(f - f_D - f_\Delta)e^{j\theta_\Delta} + \tilde{R}^*(-f - f_D - f_\Delta)e^{-j\theta_\Delta}. \tag{2.83}$$

As illustrated in Fig. 2.15, the signal at the input to the demodulator is split into two separate signal paths, termed the $I$ and the $Q$ channels. Similarly to the modulator, a BPF response for each channel is defined. These BPFs are denoted by $L_I(f)$ and $L_Q(f)$ and are written in terms of their baseband-equivalent responses, centred in the passband around the LO frequency $f_D$, as

$$L_I(f) = \tilde{L}_I(f - f_D) + \tilde{L}_I^*(-f - f_D) \tag{2.84}$$

and

$$L_Q(f) = \tilde{L}_Q(f - f_D) + \tilde{L}_Q^*(-f - f_D). \tag{2.85}$$

Note that it is assumed that the baseband-equivalent responses $\tilde{L}_I(f)$ and $\tilde{L}_Q(f)$ are also bandlimited to the frequency range $[-B/2, B/2]$.

After taking the effect of the BPF into account, the signal in the $I$ channel can be written as

$$\begin{aligned} R_I'(f) &= R(f)L_I(f) \\ &= \left[\tilde{R}(f - f_D - f_\Delta)e^{j\theta_\Delta} + \tilde{R}^*(-f - f_D - f_\Delta)e^{-j\theta_\Delta}\right]\left[\tilde{L}_I(f - f_D) + \tilde{L}_I^*(-f - f_D)\right] \\ &= \tilde{R}(f - f_D - f_\Delta)e^{j\theta_\Delta}\tilde{L}_I(f - f_D) \\ &\quad + \tilde{R}^*(-f - f_D - f_\Delta)e^{-j\theta_\Delta}\tilde{L}_I^*(-f - f_D). \end{aligned} \tag{2.86}$$

In the final step the rest of the terms were eliminated since there was no frequency overlap between the products. Similarly to the $I$ channel, the signal in the $Q$ channel can be written as

$$\begin{aligned} R_Q'(f) &= R(f)L_Q(f) \\ &= \tilde{R}(f - f_D - f_\Delta)e^{j\theta_\Delta}\tilde{L}_Q(f - f_D) \\ &\quad + \tilde{R}^*(-f - f_D - f_\Delta)e^{-j\theta_\Delta}\tilde{L}_Q^*(-f - f_D). \end{aligned} \tag{2.87}$$

As with the modulator, the quadrature LO signals of the mixer contributes significantly to the $I/Q$ imbalances of the quadrature demodulator. To model these imbalances, let the LO signal mixing with the $I$ channel be given by

$$x_{D,I}(t) = \beta_I \cos(2\pi f_D t + \varphi_I) \tag{2.88}$$

with frequency-domain representation

$$X_{D,I}(f) = \frac{\beta_I}{2}\left[\delta(f-f_D)e^{j\varphi_I} + \delta(f+f_D)e^{-j\varphi_I}\right]. \tag{2.89}$$

The LO signal mixing with the $Q$ channel is given by

$$x_{D,Q}(t) = -\beta_Q \sin(2\pi f_D t + \varphi_Q) \tag{2.90}$$

and in the frequency-domain

$$X_{D,Q}(f) = \frac{-\beta_Q}{2j}\left[\delta(f-f_D)e^{j\varphi_I} - \delta(f+f_D)e^{-j\varphi_I}\right]. \tag{2.91}$$

The gain imbalance of the quadrature LO signal is given by $\beta_I/\beta_Q$. The phase imbalance, i.e. the difference in phase from 90°, is given by $\varphi_I - \varphi_Q$.

After mixing with the LO signal, the $I$ channel's signal is given by

$$\begin{aligned} Y_I(f) &= R'_I(f) \otimes X_{D,I}(f) \\ &= \frac{\beta_I e^{j\varphi_I}}{2}\left[\tilde{R}(f-2f_D-f_\Delta)e^{j\theta_\Delta}\tilde{L}_I(f-2f_D) + \tilde{R}^*(-f-f_\Delta)e^{-j\theta_\Delta}\tilde{L}_I^*(-f)\right] \\ &\quad + \frac{\beta_I e^{-j\varphi_I}}{2}\left[\tilde{R}(f-f_\Delta)e^{j\theta_\Delta}\tilde{L}_I(f) + \tilde{R}^*(-f-2f_D-f_\Delta)e^{-j\theta_\Delta}\tilde{L}_I^*(-f-2f_c)\right] \end{aligned} \tag{2.92}$$

and the $Q$ channel by

$$\begin{aligned} Y_Q(f) &= R'_Q(f) \otimes X_{D,Q}(f) \\ &= \frac{-\beta_Q e^{j\varphi_Q}}{2j}\left[\tilde{R}(f-2f_D-f_\Delta)e^{j\theta_\Delta}\tilde{L}_Q(f-2f_D) + \tilde{R}^*(-f-f_\Delta)e^{-j\theta_\Delta}\tilde{L}_Q^*(-f)\right] \\ &\quad + \frac{\beta_Q e^{-j\varphi_Q}}{2j}\left[\tilde{R}(f-f_\Delta)e^{j\theta_\Delta}\tilde{L}_Q(f) + \tilde{R}^*(-f-2f_D-f_\Delta)e^{-j\theta_\Delta}\tilde{L}_Q^*(-f-2f_D)\right]. \end{aligned} \tag{2.93}$$

It is seen that the signals $Y_I(f)$ and $Y_Q(f)$ contain, in addition to baseband terms, some double frequency terms which need to be filtered out. The required lowpass filtering will be modelled as a cascade of perfect LPFs (to remove the double frequency components), followed by additional transfer functions denoting the deviations of the $I$ and $Q$ channels from the perfect LPF response.

Let $Z_I(f)$ and $Z_Q(f)$ represent the spectra of the signals in the $I$ and $Q$ channels, respectively, after the perfect LPF operation to remove the double frequency components. Accordingly, these signals are given by

$$\begin{aligned} Z_I(f) &= \text{LPF}\{Y_I(f)\} \\ &= \frac{\beta_I e^{j\varphi_I}}{2}\tilde{R}^*(-f-f_\Delta)e^{-j\theta_\Delta}\tilde{L}_I^*(-f) + \frac{\beta_I e^{-j\varphi_I}}{2}\tilde{R}(f-f_\Delta)e^{j\theta_\Delta}\tilde{L}_I(f) \end{aligned} \tag{2.94}$$

and

$$\begin{aligned} Z_Q(f) &= \text{LPF}\{Y_Q(f)\} \\ &= \frac{-\beta_Q e^{j\varphi_Q}}{2j}\tilde{R}^*(-f-f_\Delta)e^{-j\theta_\Delta}\tilde{L}_Q^*(-f) + \frac{\beta_Q e^{-j\varphi_Q}}{2j}\tilde{R}(f-f_\Delta)e^{j\theta_\Delta}\tilde{L}_Q(f) \end{aligned} \tag{2.95}$$

The imbalances of the LPFs can now be modelled by letting $H_I(f)$ and $H_Q(f)$ denote the deviation of the $I$ and $Q$ channels, from the perfect LPF response employed in the previous step. Note that $H_I(f)$ and $H_Q(f)$ are lowpass responses, stemming from filters with real impulse responses. As such, the spectra $H_I(f)$ and $H_Q(f)$ exhibit Hermitian symmetry around 0 Hz. Incorporating these responses, yields the following baseband signals:

$$\begin{aligned} Z'_I(f) &= Z_I(f)H_I(f) && (2.96)\\ &= \frac{\beta_I e^{j\varphi_I}}{2} H_I(f)\tilde{R}^*(-f-f_\Delta)e^{-j\theta_\Delta}\tilde{L}_I^*(-f) \\ &\quad + \frac{\beta_I e^{-j\varphi_I}}{2} H_I(f)\tilde{R}(f-f_\Delta)e^{j\theta_\Delta}\tilde{L}_I(f) && (2.97) \end{aligned}$$

$$\begin{aligned} Z'_Q(f) &= Z_Q(f)H_Q(f) && (2.98)\\ &= \frac{j\beta_Q e^{j\varphi_Q}}{2} H_Q(f)\tilde{R}^*(-f-f_\Delta)e^{-j\theta_\Delta}\tilde{L}_Q^*(-f) \\ &\quad - \frac{j\beta_Q e^{-j\varphi_Q}}{2} H_Q(f)\tilde{R}(f-f_\Delta)e^{j\theta_\Delta}\tilde{L}_Q(f). && (2.99) \end{aligned}$$

These signals will now be digitised in order to be demodulated in the digital domain of the demodulator. In the digital domain, the $I$ channel's signal will be used as the real part and the $Q$ channel as the complex part of a complex signal. By keeping the analysis in the continuous time, though, the theoretical complex signal before digitisation can therefore be written as

$$\begin{aligned} Z'(f) &= Z'_I(f) + jZ'_Q(f) \\ &= \frac{\tilde{R}(f-f_\Delta)e^{j\theta_\Delta}}{2}\left[\beta_I e^{-j\varphi_I}H_I(f)\tilde{L}_I(f) + \beta_Q e^{-j\varphi_Q}H_Q(f)\tilde{L}_Q(f)\right] \\ &\quad + \frac{\tilde{R}^*(-f-f_\Delta)e^{-j\theta_\Delta}}{2}\left[\beta_I e^{j\varphi_I}H_I(f)\tilde{L}_I^*(-f) - \beta_Q e^{j\varphi_Q}H_Q(f)\tilde{L}_Q^*(-f)\right] && (2.100) \end{aligned}$$

The desired signal at the demodulator is represented by the baseband-equivalent signal $\tilde{R}(f)$, offset by a frequency of $f_\Delta$ from 0 Hz, with a phase offset of $\theta_\Delta$. Mathematically, this desired signal is therefore given by

$$\tilde{R}_{\text{Des}}(f) = \tilde{R}(f-f_\Delta)e^{j\theta_\Delta}. \qquad (2.101)$$

$Z'(f)$ can then be written in terms of this desired signal, as

$$Z'(f) = \tilde{R}_{\text{Des}}(f)W_1(f) + \tilde{R}^*_{\text{Des}}(-f)W_2(f) \qquad (2.102)$$

where

$$W_1(f) = \frac{1}{2}\left[\beta_I e^{-j\varphi_I}H_I(f)\tilde{L}_I(f) + \beta_Q e^{-j\varphi_Q}H_Q(f)\tilde{L}_Q(f)\right] \qquad (2.103)$$

$$W_2(f) = \frac{1}{2}\left[\beta_I e^{j\varphi_I}H_I(f)\tilde{L}_I^*(-f) - \beta_Q e^{j\varphi_Q}H_Q(f)\tilde{L}_Q^*(-f)\right]. \qquad (2.104)$$

As was seen with the quadrature modulator, the output signal contains, in addition to the desired signal, the image frequency component associated with $\tilde{R}^*_{\text{Des}}(-f)$. This image signal

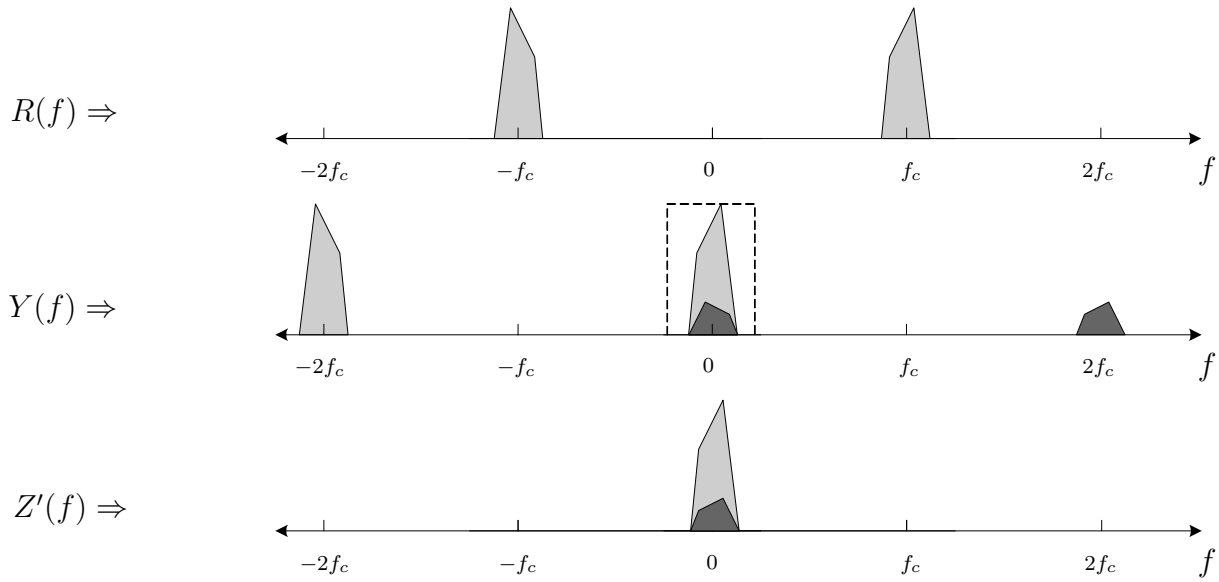


**Figure 2.16:** *Magnitude spectra during the down-mixing process in the presence of $I/Q$ imbalances. The unwanted image frequency components are indicated with dark grey shading.*

will either be an image of the signal from an adjacent channel (if $f_\Delta > B/2$) or the image of the desired signal itself (if $f_\Delta = 0$) or a combination of the two cases (if $0 < f_\Delta < B/2$). This image signal will occupy the same frequency band and interfere with the desired signal. Fig. 2.16 graphically illustrates the effect of this undesired image frequency component in the demodulation process, for the case where $f_\Delta = 0$. In the next subsection, the relative weighting of this undesired image component will be investigated in detail.

### Relative image ratio

By examining the expression for $Z'(f)$ in (2.102), it can be seen that when an imbalanced quadrature demodulator is used, a desired signal component at frequency $f = f_R$ will result in an undesired image frequency component at frequency $f = -f_R$. The relative image ratio (RIR) of the demodulator is defined to be the ratio between the power of the desired and image signal components. The RIR of an imbalanced demodulator can therefore be written as

$$I_D(f) = \left| \frac{W_2(-f)}{W_1(f)} \right|^2 . \tag{2.105}$$

Substituting the expressions for $W_1(f)$ and $W_2(-f)$ into the above equation yields

$$I_D(f) = \left| \frac{\beta_I |H_I(f)||\tilde{L}_I(f)| e^{j[-\varphi_I + \angle H_I(f) + \angle \tilde{L}_I(f)]} + \beta_Q |H_Q(f)||\tilde{L}_Q(f)| e^{j[-\varphi_Q + \angle H_Q(f) + \angle \tilde{L}_Q(f)]}}{\beta_I |H_I(-f)||\tilde{L}_I^*(f)| e^{j[\varphi_I + \angle H_I(-f) + \angle \tilde{L}_I^*(f)]} - \beta_Q |H_Q(-f)||\tilde{L}_Q^*(f)| e^{j[\varphi_Q + \angle H_Q(-f) + \angle \tilde{L}_Q^*(f)]}} \right|^2 \tag{2.106}$$

Since $H_I$ and $H_Q$ are both real filters it follows that their magnitude responses will be symmetrical around 0 Hz in the frequency-domain, and their phase responses will be odd functions. This means that

$$|H_I(-f)| = |H_I(f)| \tag{2.107}$$
$$|H_Q(-f)| = |H_Q(f)| \tag{2.108}$$
$$\angle H_I(-f) = -\angle H_I(f) \tag{2.109}$$
$$\angle H_Q(-f) = -\angle H_Q(f). \tag{2.110}$$

This does not hold true for $\tilde{L}_I$ and $\tilde{L}_Q$, since they are the complex baseband-equivalent filters of $L_I$ and $L_Q$, respectively. The following, however, does hold true from standard complex numbers arithmetic,

$$|\tilde{L}_I^*(f)| = |\tilde{L}_I(f)| \tag{2.111}$$
$$|\tilde{L}_Q^*(f)| = |\tilde{L}_Q(f)| \tag{2.112}$$
$$\angle \tilde{L}_I^*(f) = -\angle \tilde{L}_I(f) \tag{2.113}$$
$$\angle \tilde{L}_Q^*(f) = -\angle \tilde{L}_Q(f). \tag{2.114}$$

By utilising these identities and defining the following terms

$$\kappa_I(f) = \beta_I |H_I(f)||\tilde{L}_I(f)| \tag{2.115}$$
$$\kappa_Q(f) = \beta_Q |H_Q(f)||\tilde{L}_Q(f)| \tag{2.116}$$
$$\chi_I(f) = \varphi_I - \angle H_I(f) - \angle \tilde{L}_I(f) \tag{2.117}$$
$$\chi_Q(f) = \varphi_Q - \angle H_Q(f) - \angle \tilde{L}_Q(f) \tag{2.118}$$

$I_D(f)$ can be rewritten as

$$I_D(f) = \left| \frac{\kappa_I(f) e^{j\chi_I(f)} - \kappa_Q(f) e^{j\chi_Q(f)}}{\kappa_I(f) e^{-j\chi_I(f)} + \kappa_Q(f) e^{-j\chi_Q(f)}} \right|^2 . \tag{2.119}$$

After some standard algebraic manipulation, this expression becomes

$$I_D(f) = \frac{\left[\frac{\kappa_I(f)}{\kappa_Q(f)}\right]^2 + 1 - 2\left[\frac{\kappa_I(f)}{\kappa_Q(f)}\right] \cos\left[\chi_I(f) - \chi_Q(f)\right]}{\left[\frac{\kappa_I(f)}{\kappa_Q(f)}\right]^2 + 1 + 2\left[\frac{\kappa_I(f)}{\kappa_Q(f)}\right] \cos\left[\chi_I(f) - \chi_Q(f)\right]} . \tag{2.120}$$

It is clear that the relative power of the undesired image component depends on the phase difference $\chi_I(f) - \chi_Q(f)$ and the gain ratio $\kappa_I(f)/\kappa_Q(f)$. We can therefore define the phase error of the demodulator as $\chi_D(f) = \chi_I(f) - \chi_Q(f)$ and the gain imbalance of the demodulator as $\kappa_D(f) = \kappa_I(f)/\kappa_Q(f)$. As with the modulator, when $\kappa_D(f) = 1$ and $\kappa_D(f) = 0$, the undesired image component is completely suppressed. It is also clear that once again the gain and phase imbalances are due to the cascaded effect of all the components in the channels, therefore enabling a baseband response to compensate for the imbalances contributed by a passband filter.

An interesting and important difference between the RIR of the modulator (see Section 2.5.1 on p. 31) and that of the demodulator, is the position in the frequency-domain at which the gain and phase responses of the two channels need to be matched. With the modulator it was seen that, in order to suppress the undesired image component, the $I$ and $Q$ channels have to be matched at the frequency of the image signal. For the demodulator, it can be seen that $I_D(f)$ is a function of $f$ and not $-f$ (which was the case for $I_M(f)$ in Section 2.5.1). From this observation it can be concluded that, for the case of a quadrature demodulator, the presence of the undesired image frequency component can be avoided by matching the gain and phase response of the $I$ and $Q$ channels at the frequency of the *desired* component. This is an important insight, which, as far as we could establish, has not been reported in open literature.

Using the same reasoning as presented at the modulator discussion, it can be observed that if only LPF mismatches were modelled (i.e. $\tilde{H}_I(f) = \tilde{H}_Q(f) = 1$) then the gain imbalance function $\kappa_D(f)$ would be an even function of frequency, and phase imbalance function $\chi_I(f)$ (after removing the DC phase offset) would be an odd function of frequency. Since this is inconsistent with the asymmetrical gain and phase imbalance functions measured for the practical quadrature demodulator implemented in Chapter 4, it can be concluded that this modelling approach is inadequate to fully model the observed characteristics of the practical quadrature demodulator. The inclusion of the imbalances due to BPF mismatches are therefore crucial to explain this observed asymmetry, since $\tilde{H}_I(f)$ and $\tilde{H}_Q(f)$ are not restricted to exhibit Hermitian symmetry since they represent the baseband-equivalent responses of passband filters.

Unlike the quadrature modulator, there is no additional RIR scaling factor contributed by the ratio between the BPF responses at desired and image frequencies (see (2.53) on p. 31 for comparison). This can be explained by realising that in the case of the demodulator, the image signal is not yet present when the RF signal passes through the BPFs. In the case of the modulator, the imbalances responsible for the image signal component has occurred by the stage that the signal reaches the BPFs. The BPF can therefore exacerbate the situation by amplifying the image signal frequencies (or suppressing of the desired signal frequencies).

With typical gain imbalances and phase errors of $1\% - 5\%$ and $1^\circ - 5^\circ$ respectively [9, 65], it means that practical quadrature demodulators only provide about 30–40 dB of image signal suppression. Whether this amount of suppression is sufficient, will ultimately dependend on the application. It should be kept in mind that receivers that employ a digital low-IF (receivers where the desired frequency channel's signal is not mixed down to 0 Hz but rather to some digital low-IF) the interfering channel's signal, located at the image frequency location, may be much stronger than the desired one. For this reason, some authors propose image rejection capablities of 60–90 dB [12] or even 80–100 dB [64, 78].

**Table 2.5:** *Simulation filter specifications.*

| **Parameter** | $H_I(z)$ | $H_Q(z)$ | $L_I(z)$ | $L_Q(z)$ |
|---|---|---|---|---|
| Filter type | Chebyshev Lowpass | Chebyshev Lowpass | Chebyshev Bandpass | Chebyshev Bandpass |
| Order | 6 | 6 | 12 | 12 |
| Coefficients | real | real | real | real |
| Passband ripple [dB] | 1 | 1 | 1 | 1 |
| Cut off frequency (normalised to $f_{s\uparrow}$) | 0.0515 | 0.0475 | 0.2703 and 0.3300 | 0.2687 and 0.3310 |

### Model validation through simulation

As was done in the previous section for the imbalanced modulator, the expression for the RIR of the imbalanced demodulator will now be validated through a simulation. The MATLAB simulation architecture that was developed for this purpose will now be presented. This simulation architecture will again be used in Chapter 4, during the validation and performance verification of the developed imbalance extraction techniques.

*Simulation overview*

A block diagram illustrating the simulation topology of the imbalanced demodulator, is shown in Fig. 2.17. In this simulation, a passband test tone is injected into the imbalanced demodulator, frequency down-converted to baseband and sampled to be processed further as a complex signal in the digital domain of the demodulator.

As was done in the simulation of the imbalanced modulator (see Section 2.5.1), the continuous time domain is simulated by discrete time signals at a higher sampling rate ($f_{s\uparrow}$), compared to the sampling rate used for the discrete time signals ($f_s$) in the 'Digital signal processing' section of the demodulator. The decimation blocks therefore represent the sampling process of the ADCs of a practical demodulator setup. As with the upsampling blocks of the modulator, these decimation blocks are also implemented using MATLAB's `resample` command. Once again the quantisation blocks were not activated, since the goal is to confirm the demodulator model that has been developed. In Chapter 4 these blocks will be activated to investigate the effect of quantisation on the extraction techniques presented there.

All filters are implemented as digital Chebyshev filters with real valued coefficients. The cut off frequencies of the corresponding $I$ and $Q$ channel filters were varied slightly in order to introduce frequency-dependent $I/Q$ imbalances between the two channels. The gain and phase of the two oscillator signals of the quadrature mixer can also be controlled in order to introduce frequency-independent imbalances.

Table 2.5 provides the specifications of the filters used in the simulation. The coefficients for their implementation are listed in Table 2.6, where each filter's coefficients are related to

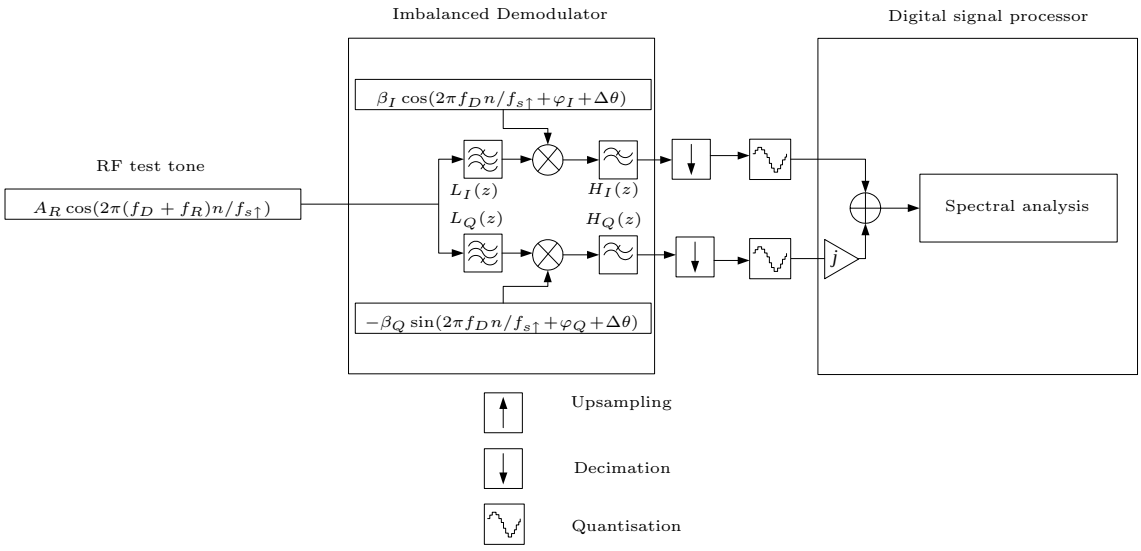


**Figure 2.17:** *Block diagram of the imbalanced demodulator within the developed MATLAB simulation architecture.*

**Table 2.6:** *Simulation filter coefficients.*

| | | |
|---|---|---|
| $H_I(z)$ | $a_l$ | 1; -5.5485; 12.9790; -16.3763; 11.7513; -4.5461; 0.7406 |
| | $b_l$ | 0.0096e-4; 0.0576e-4; 0.1441e-4; 0.1921e-4; 0.1441e-4; 0.0576e-4; 0.0096e-4 |
| $H_Q(z)$ | $a_l$ | 1; -5.5940; 13.1686; -16.6926; 12.0141; -4.6542; 0.7581 |
| | $b_l$ | 0.0060e-4; 0.0358e-4; 0.0896e-4; 0.1194e-4; 0.0896e-4; 0.0358e-4; 0.0060e-4 |
| $G_I(z)$ | $a_l$ | 1; 3.6108; 10.9019; 20.9308; 34.6976; 43.5022; 47.7838; 41.0574; 30.9074; 17.5916; 8.6465; 2.7003; 0.7060 |
| | $b_l$ | 0.0229; 0; -0.1376; 0; 0.3439; 0; -0.4586; 0; 0.3439; 0; -0.1376; 0; 0.0229 |
| $G_Q(z)$ | $a_l$ | 1; 3.5842; 10.7910; 20.6300; 34.1313; 42.6767; 46.8320; 40.1775; 30.2511; 17.2083; 8.4727; 2.6466; 0.6953 |
| | $b_l$ | 0.0295e-4; 0; -0.1767e-4; 0; 0.4419e-4; 0; -0.5892e-4; 0; 0.4419e-4; 0; -0.1767e-4; 0; 0.0295e-4 |

its transfer function as follows (using $H_I(z)$ as an example),

$$H_I(z) = \frac{\sum_{l=0}^{N} a_l z^{-l}}{\sum_{l=0}^{L} b_l z^{-l}} \tag{2.121}$$

The magnitude responses of these filters are also shown in Fig. 2.18. The normalised passband width of the BPFs are chosen to be nominally 0.06, which is narrower than the Nyquist zone width of the baseband digital signal (0.1), around a normalised center frequency of 0.3. The quadrature mixer frequency translates the passband signal around $f_D/f_{s\uparrow} = 0.3$ to DC. The normalised cut off frequencies of the LPFs are chosen such that they are nominally equal to the Nyquist zone of the baseband signal after decimation, i.e. $-f_s/(2f_{s\uparrow})$ to $f_s/(2f_{s\uparrow})$, or $-0.05$ to 0.05 for a decimation factor of 10. Table 2.7 presents the parameters for the oscillator's frequency and imbalances. The chosen oscillator imbalances are representative of typical imbalances found in a practical quadrature demodulator [9, 65].

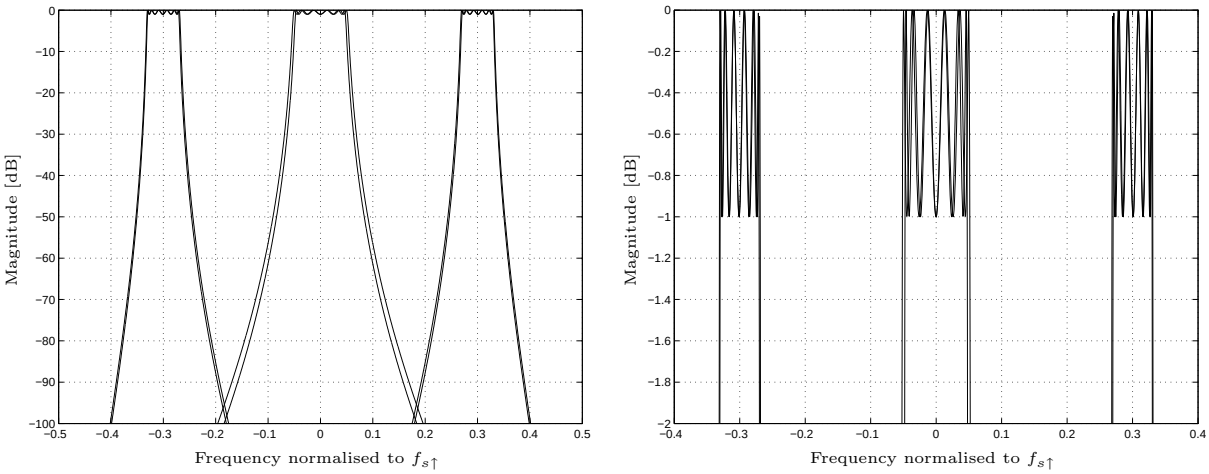


(a) (b)

**Figure 2.18:** *Magnitude spectra of the digital filters use during simulation.*

**Table 2.7:** *Simulation parameters.*

| Parameter | Value |
|---|---|
| $f_{s\uparrow}/f_s$ | 10 |
| $f_D/f_{s\uparrow}$ | 0.3 |
| $\beta_I/\beta_Q$ | 0.93 |
| $\varphi_I - \varphi_Q$ | -3 ° |

*Validation of demodulator RIR*

In order to validate the expression for the demodulator RIR in (2.119), real valued, passband test tones were injected into the quadrature demodulator. As was mentioned in the discussion of the modulator simulation, single frequency tones can easily be decomposed into a desired and an image component, in order to measure the RIR as a function of the input frequency.

Fig. 2.19(a) shows a sample magnitude spectrum of the passband test tone $A_R \cos(2\pi[f_D + f_R]n/f_{s\uparrow})$, with $f_D/f_{s\uparrow} = 0.3$ and $f_R/f_{s\uparrow} = 0.0164$, while the resultant baseband spectrum, after frequency down conversion and decimation by the imbalanced demodulator, is shown in Fig. 2.19(b). It is clearly seen how, as predicted by (2.102) the upper sideband input signal in Fig. 2.19(a), results in two frequency components in Fig. 2.19(b), due to the imbalances of the demodulator. Of course, only the positive frequency component in Fig. 2.19(b) is desired.

A number of passband test tones were injected during several measurements, in order to measure the RIR of the demodulator as a function of frequency. The frequencies of the test tones were chosen such that their their down-converted and decimated frequencies would cover the frequency region -0.2 to 0.2, normalised to $f_s$. For each down-converted tone, spectral analysis was performed on the down-converted and decimated 'digital' baseband signal, using an FFT with Blackman amplitude windowing. This measured values of the demodulator RIR, as a function of baseband output frequency $f_R$, could then be compared

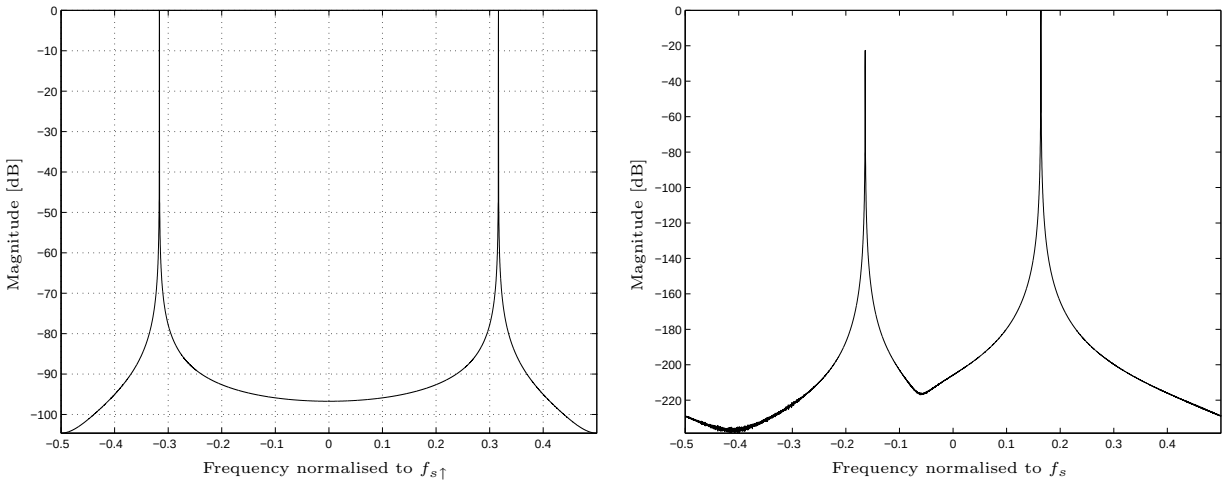


(a) (b)

**Figure 2.19:** *Magnitude spectra of a test tone with passband frequency of* $(f_D + f_R)/f_{s\uparrow} = 0.3164$ *(a), and after it has been frequency translated to baseband with the imbalanced demodulator and decimated by a factor of 10 (b). The resultant baseband signal exhibits a desired component at* $f_R/f_s = 0.164$ *and a unwanted image component at* $-f_R/f_s = -0.164$.

to a RIR computed using the theory derived in this chapter.

The expression for the theoretical RIR was derived in (2.119). To compute the theoretical RIR of the simulation topology, the frequency responses of the various filters were evaluated at each required frequency value, using MATLAB's `freqz` command. These frequency response values, together with the gain and phase imbalances of the mixer, were subsequently substituted into (2.119) to produce the theoretical RIR for a tone at a particular input frequency.

The results of the simulation is presented in Fig. 2.20. The theoretical and measured RIR agree well. In turn, this result also validates the baseband-equivalent model that was developed to derive the expression for the RIR. This baseband-equivalent model will be employed in Chapters 4 and 6 to derive novel imbalance extraction methods.

### Special case: Frequency-independent $I/Q$ imbalances

Similarly to the quadrature modulator, the demodulator model can also easily be simplified to a frequency-independent model. Such frequency-independent models are frequently used in literature.

In order to accomplish this, consider the functions $W_1(f)$ and $W_2(f)$ that were presented in (2.103) and (2.104), presented below again for convenience.

$$\begin{aligned} W_1(f) &= \beta_I/2e^{-j\varphi_I}H_I(f)\tilde{L}_I(f) + \beta_Q/2e^{-j\varphi_Q}H_Q(f)\tilde{L}_Q(f) \\ W_2(f) &= \beta_I/2e^{j\varphi_I}H_I(f)\tilde{L}_I^*(-f) - \beta_Q/2e^{j\varphi_Q}H_Q(f)\tilde{L}_Q^*(-f) \end{aligned}$$

It can be seen that these expressions are both functions of the mixer imbalances ($\beta_I$,$\beta_Q$,$\varphi_I$,$\varphi_Q$)

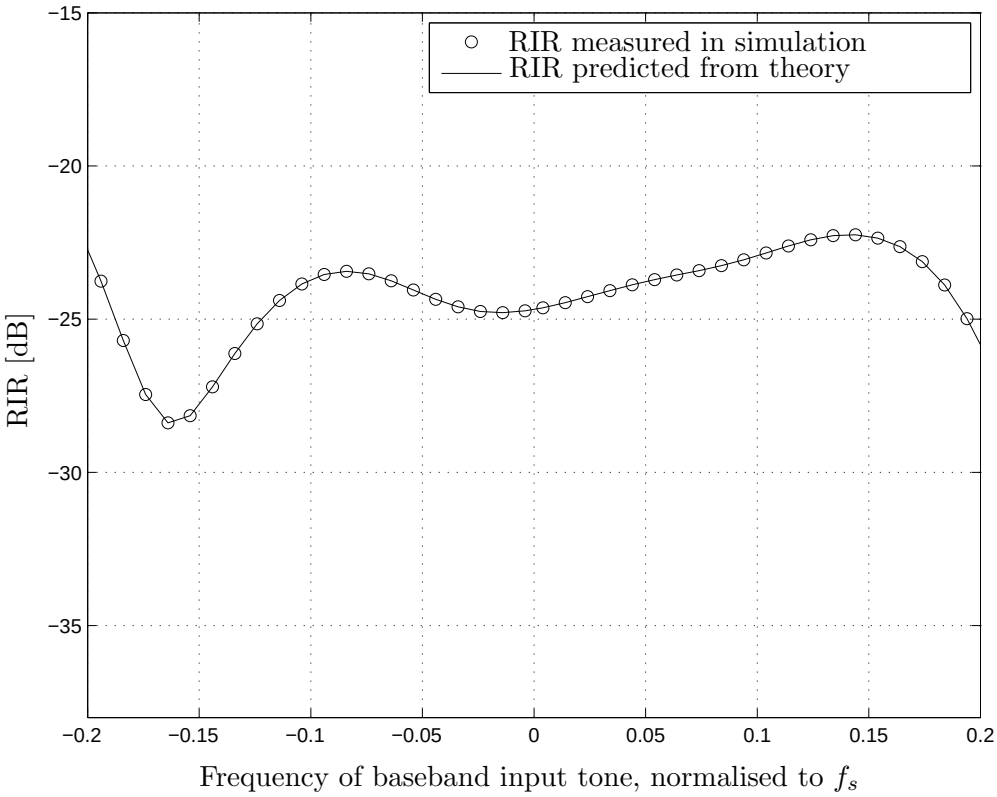


**Figure 2.20:** *The RIR of the simulated demodulator setup, measured using spectral analysis and predicted from the developed theoretical model.*

the LPF responses ($H_I(f)$ and $H_Q(f)$) and baseband-equivalent representations of the BPFs ($\tilde{L}_Q(f)$ and $\tilde{L}_Q(f)$) of the $I$ and $Q$ signal paths. In order to derive the frequency-independent distortion model, the assumption has to be made that each LPF and BPF in the two signal paths essentially only contributes a complex scaling factor, which is independent of frequency over the narrow frequency band of interest. When this is the case, the following definitions may be made

$$\beta_I/2e^{-j\varphi_I}H_I(f)\tilde{L}_I(f) \approx \kappa_I e^{-j\chi_I} \tag{2.122}$$

and

$$\beta_Q/2e^{-j\varphi_Q}H_Q(f)\tilde{L}_Q(f) \approx \kappa_Q e^{-j\chi_Q}. \tag{2.123}$$

The gain imbalance of the demodulator is then defined as

$$\kappa_D = \frac{\kappa_I}{\kappa_Q} \tag{2.124}$$

and the phase imbalance by

$$\chi_D = \chi_I - \chi_Q. \tag{2.125}$$

The frequency-independent expressions for $W_1$ and $W_2$ can then be written as

$$W_1 = \kappa_I e^{-j\chi_I} + \kappa_Q e^{-j\chi_Q} \tag{2.126}$$

$$W_2 = \kappa_I e^{j\chi_I} - \kappa_Q e^{j\chi_Q}. \tag{2.127}$$

The RIR for the frequency-independent case will now be investigated.

*Relative image ratio*

For the frequency-independent case, the RIR, i.e. the ratio of the power of the image frequency component relative to the power of the desired frequency component is given by

$$\begin{aligned} I_D &= \left|\frac{W_2}{W_1}\right|^2 \\ &= \frac{\kappa_D^2 + 1 - 2\kappa_D \cos(\chi_D)}{\kappa_D^2 + 1 + 2\kappa_D \cos(\chi_D)}. \end{aligned} \tag{2.128}$$

This result is equivalent to the expression presented in the frequency-independent model of the modulator in (2.69) on p. 39. Once again it can be verified that the quantity in (2.128) remains unchanged when $\kappa_D$ is replaced by $1/\kappa_D$ or $\chi_D$ with $-\chi_D$. The frequency-independent RIR of the demodulator is therefore only dependent on the relative error between the two signal paths.

*Baseband-equivalent vector model*

The merits of a vector model were discussed in Section 2.5.1 p. 40. This section will derive the demodulator vector model for frequency-independent imbalances.

Analogous to (2.102) the output of the quadrature demodulator for the frequency-independent model can be written as

$$Z'(f) = \tilde{R}_{\text{Des}}(f)W_1 + \tilde{R}^*_{\text{Des}}(-f)W_2 \tag{2.129}$$

or in the time domain

$$z'(t) = \tilde{r}_{\text{Des}}(t)W_1 + \tilde{r}^*_{\text{Des}}(t)W_2. \tag{2.130}$$

Once again, the complex signal will be decomposed into its in-phase and quadrature components as

$$\tilde{r}_{\text{Des}}(t) = \mathcal{Re}\{\tilde{r}_{\text{Des}}(t)\} + j\,\mathcal{Im}\{\tilde{r}_{\text{Des}}(t)\}. \tag{2.131}$$

Using this representation of $\tilde{r}_{\text{Des}}(t)$, along with the expressions for $W_1$ and $W_2$ in (2.66) and (2.66), the output of the quadrature demodulator can be written, after some trigonometric manipulation, as

$$\begin{aligned} z'(t) &= \mathcal{Re}\{\tilde{r}_{\text{Des}}(t)\}\kappa_I \cos(\chi_I) + \underbrace{\mathcal{Im}\{\tilde{r}_{\text{Des}}(t)\}\kappa_I \sin(\chi_I)}_{\text{Leakage term}} \\ &\quad -j\Big[\underbrace{\mathcal{Re}\{\tilde{r}_{\text{Des}}(t)\}\kappa_Q \sin(\chi_Q)}_{\text{Leakage term}} - \mathcal{Im}\{\tilde{r}_{\text{Des}}\}(t)\kappa_Q \cos(\chi_Q)\Big] \end{aligned} \tag{2.132}$$

$$= z'_I(t) + jz'_Q(t). \tag{2.133}$$

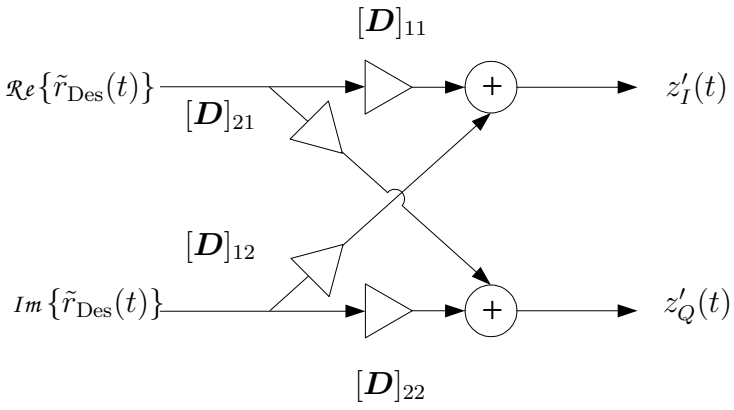


**Figure 2.21:** *Graphical representation of the equivalent baseband model for the demodulator's $I$ and $Q$ channels, for the frequency-independent case.*

Using the result of (2.132), $z'(t)$ can now be represented using the vector notation, introduced in Section 2.5.1 p. 41, as

$$\boldsymbol{z'}(t) = \boldsymbol{D}\ \boldsymbol{r}_{\text{Des}}(t)\ , \tag{2.134}$$

where

$$\begin{aligned} \boldsymbol{r}_{Des}(t) &= \left[\begin{array}{cc} \mathcal{R}e\{\tilde{r}_{\text{Des}}(t)\} & Im\{\tilde{r}_{\text{Des}}(t)\} \end{array}\right]^T \\ \boldsymbol{D} &= \left[\begin{array}{cc} \kappa_I \cos(\chi_I) & \kappa_I \sin(\chi_I) \\ -\kappa_Q \sin(\chi_Q) & \kappa_Q \cos(\chi_Q) \end{array}\right] . \end{aligned} \tag{2.135}$$

The vector representation of the received signal can be visualised with the leakage model shown in Fig. 2.21.

For a perfect quadrature demodulator, it is expected that the $I$ channel output ($z_I(t)$), would only be a function of the real part of the baseband-equivalent representation of the input RF signal. Similarly, the $Q$ channel ($z_Q(t)$) should only contain the the imaginary part of the baseband-equivalent representation of the input RF signal. (2.132) and the leakage model shown in Fig. 2.21, clearly illustrates how the imbalanced quadrature demodulator causes leakage between the real and imaginary parts of the complex baseband-equivalent input signal, at the output of the $I$ and $Q$ channels.

As was seen during the discussion of the modulator, the image rejection capability of the demodulator is also only dependent on the absolute phase error between the $I$ and the $Q$ channels. We may therefore choose any arbitrary phase reference. Usually, the phase reference is chosen to be either the $I$ or the $Q$ channel's phase, or exactly in the middle of the two. Each choice of a phase reference results in a different $\boldsymbol{D}$ matrix. Three commonly chosen references will now be discussed.

**Using the $I$ channel as reference.** When the $I$ channel's phase is used as the reference phase, then $\chi_I = 0$ and $\chi_Q = -\chi_D$. This effectively means that the phase error of the

demodulator, $\chi_D$, is attributed solely to the $Q$ channel. Recall that the phase imbalance of the modulator was defined as $\chi_D = \chi_I - \chi_Q$. The modulator imbalance matrix $\boldsymbol{D}$ therefore becomes

$$\boldsymbol{D} = \kappa_I \begin{bmatrix} 1 & 0 \\ 1/\kappa_D \sin(\chi_D) & 1/\kappa_D \cos(\chi_D) \end{bmatrix}. \tag{2.136}$$

The factor $\kappa_I$, only contributes an overall system gain, and can, without loss of generality, be normalised to unity. This model agrees with that presented in [60, p. 26].

**Using the $Q$ channel as reference.** When the $Q$ channel's phase is used as the reference phase, then $\chi_Q = 0$ and $\chi_I = \chi_D$. The modulator imbalance matrix $\boldsymbol{D}$ therefore becomes

$$\boldsymbol{D} = \kappa_Q \begin{bmatrix} \kappa_D \cos(\chi_D) & \kappa_D \sin(\chi_D) \\ 0 & 1 \end{bmatrix}. \tag{2.137}$$

In this case the $Q$ channel's gain may be normalised to unity.

**Using an equally distributed phase reference.** This model distributes the phase error equally between the $I$ and the $Q$ channels. We therefore have that $\chi_I = \chi_D/2$ and that $\chi_Q = -\chi_D/2$. The modulator imbalance matrix $\boldsymbol{D}$ then becomes

$$\boldsymbol{D} = \begin{bmatrix} \kappa_I \cos(\chi_D/2) & \kappa_I \sin(\chi_D/2) \\ \kappa_Q \sin(\chi_D/2) & \kappa_Q \cos(\chi_D/2) \end{bmatrix}. \tag{2.138}$$

This model agrees with the one suggested in [9].

## 2.6 Conclusions

In this chapter the principles behind quadrature modulation and demodulation were presented. It was shown that quadrature mixing could theoretically provide infinite image signal rejection, through a simple and low-cost architecture. This holds many practical advantages, especially when designing low-cost, low-power, compact systems. It was, however, shown that the quadrature mixing architecture is very sensitive, in practice, towards mismatches ($I/Q$ imbalances) between its two signal paths and LO signals, which severely impacts its image rejection performance.

This chapter subsequently presented detailed mathematical analysis of the $I/Q$ imbalances encountered in practical quadrature modulators and demodulators. Baseband-equivalent distortion models were derived from first principles, to not only model frequency-independent mixer effects, but arrive at complete frequency-dependent, baseband-equivalent, imbalance models for the quadrature modulator and demodulator. These models provided insights into the the frequency-independent nature of $I/Q$ imbalances that are not found in open literature. By including bandpass frequency responses to the distortion models, the

models are able to explain the asymmetrical behaviour of the gain and phase imbalance functions (over frequency) observed in practical quadrature converters, that will be demonstrated in Chapter 4.

By analysing both the modulator and demodulator, many similarities in the nature of their $I/Q$ imbalances were found. However, some notable exceptions were shown. It was shown that the RIR of both the modulator and demodulator are dependent on the cascaded frequency response of their $I$ and $Q$ channels, as well as the LO signals of their mixers. This is significant because the imbalances contributed by any one of the subsections in the channels (baseband imbalances, mixer LO imbalances or passband imbalances) can compensated for the imbalances of any of the other sections. This forms the basis of the imbalance compensation techniques presented in Chapters 4 and 6, where digital baseband techniques are presented to compensate for the complete cascaded $I/Q$ imbalances of the front-end.

The most interesting difference between the $I/Q$ imbalances of the modulator and demodulator involves the position in the frequency-domain where the $I$ and $Q$ channels need to be matched to ensure image rejection, as well as the role of the BPFs. For the modulator, it was seen that, in order to reject the image frequency related to some desired signal, the frequency response of the $I$ and $Q$ channels (including the mixer LO signals), should be matched in gain and phase, at the frequency where the image signals need to be suppressed. In the case of the demodulator, it was seen that the image signal component is suppressed if the channels are matched at the frequency of the desired component. Furthermore, it was shown that the ratio between the gain of BPFs at the frequencies of the image and desired component, can further scale the RIR of the modulator. No such effect exists for the demodulator.

The chapter continued to derive frequency-independent, baseband-equivalent, imbalance models as a special case of the frequency-dependent models. These models are frequently used in the compensation techniques presented in literature, as will be discussed in the next chapter. From these frequency-independent models, vector based models were derived, which enable linear algebra techniques to be used in deriving compensation solutions. This vector model is used extensively in Chapter 6, where novel blind imbalance techniques are derived using matrix manipulations.

In conclusion, it can be said that the quadrature mixing architecture presents some promising advantages over the conventional super-heterodyne topology. However, for many applications, practical quadrature modulators and demodulators will not deliver sufficient image rejection performance. Some form of compensation is required to improve their performance. The next chapter presents a summary of some of the $I/Q$ imbalances compensation techniques that have been presented in literature. Chapters 4 and 6 then continue to present the novel imbalance extraction and compensation techniques that form the main contribution of this dissertation.

# Chapter 3

# Digital I/Q imbalance compensation methods in literature

In the previous chapter a mathematical model for quadrature mixing, including imbalances, was introduced. The effect of imbalances on the performance of the quadrature modulator and demodulator was analysed. Such a mathematical analysis was necessary, in order to determine the exact nature of the limitations of quadrature mixing front-ends. It was seen that, in order to increase the image rejection performance of quadrature mixing front-ends to a level where it is acceptable for high quality radio applications, some form of compensation has to be performed to improve the matching between the $I$ and $Q$ signal paths, as well as the LO signals of the mixer.

Due to the flexibility and precision that the digital domain affords the designer, numerous digital quadrature imbalance compensation techniques have been proposed. This chapter presents some of the techniques that have been proposed in literature to correct the inaccuracies in the analogue front-end of the quadrature modulator and demodulator. This chapter also aims to group the various techniques found in literature according to the specific approach that was taken. Links are drawn between similar techniques, which allow a better insight to be gained into what the reasoning behind a certain approach was. The first part of the chapter will look at techniques that compensate for frequency-independent imbalances, while the second part will discuss techniques for frequency-dependent imbalance compensation.

## 3.1 Frequency-independent mismatch compensation

As was shown in Chapter 2 in Sections 2.5.1 and 2.5.2, frequency-independent quadrature mismatches (gain and phase errors) in the analogue front-end, can be modelled as a linear transformation on the $I$ and $Q$ channels. In principle, when this linear transform is invertible it should always be possible to compensate for these imbalances, by applying the inverse transform [67, 54]. This concept will be further investigated in Chapter 6, where it will also be shown that for practical quadrature imbalance situations, it is always possible to invert

the transformation matrices $\boldsymbol{M}$ and $\boldsymbol{D}$.

Digital compensation for quadrature imbalance and offset errors is accomplished by pre-distorting or post-correcting the information signal, in the digital domain of the quadrature transceiver, using the appropriate compensation transformation. The main difficulty in quadrature imbalance compensation is identifying the exact mismatch. The next few sections will discuss various techniques to accomplish imbalance extraction and subsequent compensation, as presented in literature. Since the techniques in literature tend to focus on either modulator or demodulator compensation, their discussions will also be treated separately here.

### 3.1.1 Modulator compensation

Modulator $I/Q$ compensation is complicated by the fact that the imbalances occur in the analogue domain after the digital signal processing is performed. In order for the transmitter to digitally pre-distort the transmitted signal, some reference of the imbalances present in the up-mixed signal is needed. This reference is usually generated by adding a hardware feedback path to the modulator in order to feed the RF signal back into the digital domain of the transmitter [8, 9, 21, 25, 71]. This feedback path often includes an envelope detector, such as a diode [8, 9, 21] or an adjacent power detector circuit [25, 71] to provide a baseband signal, which can be used as a indication of the imbalances that are present in the analogue front-end.

Once a baseband reference signal is obtained, there exist different methods to extract the imbalances. These methods can be broadly classified into those using test tones to identify the imbalances of the analogue front-end [8, 9, 21] and methods involving the real information-carrying data [25, 33, 71]. In all of the following modulator compensation techniques, some form of feedback circuitry is added to the transmitter after the modulator or power amplifier, in order to obtain a reference of the imbalances of the modulator.

#### Methods involving test signals (off-line compensation)

In [9] and [21], compensation methods are presented in which test signals are generated by the transmitter, and the output of a diode-envelope detector feedback-path is sampled by an added ADC on the transmitter. Although the response of the envelope detector path is not known exactly, it is shown that it does provide a quadratic search space for iteratively adjusting the compensation parameters.

Faulkner et al. [21] use a symmetric model for the quadrature imbalances, as was presented in (2.80) on p. 43. By using the symmetrical model, the authors show that the gain and phase compensation parameters can be adjusted independently of each other. The gain compensation is done by iteratively and interchangeably transmitting either a tone in the $I$ or the $Q$ channel and adjusting the gain compensation parameter until both tones result in the same amplitude at the output of the envelope detector. Phase imbalance compensa-

tion is done by transmitting a complex tone (therefore using both $I$ and $Q$ channels) and adjusting the phase compensation parameter until the envelope detector delivers a constant envelope. This stems from the fact that the phasor locus for a complex tone exhibits an elliptical shape in the presence of gain and phase imbalances and regains its circular form once these imbalances are compensated for [67, p. 70].

Cavers and Liao [9] use an asymmetrical model, as was presented in (2.78) on p. 42, to represent the quadrature imbalances in the modulator, resulting in fewer computations when performing compensation. Using the asymmetrical model for quadrature imbalances does, however, mean that gain and phase compensation can no longer be applied independently of each other. The $I/Q$ imbalances are determined iteratively by the use of four test tones at the channel's centre frequency. All four test tones have the same amplitude but different phase offsets. The compensation parameters are adjusted iteratively, until all four test signals result in the same amplitude at the envelope detector's output. In [8], Cavers presents an improved technique where test signals that are offset from the channel's centre frequency are used, and measurements are made in a more continuous fashion. The adaptation algorithm is modified to estimate the quadrature imbalances in a faster and more numerically robust way, compared to the method of [9]. In [8] Cavers also introduces a multiple-amplitude variant of the algorithm in which the parameters of the envelope detection path is also estimated, therefore eliminating the need for multiple iterations in the estimation process.

The abovementioned compensation methods rely on transmitting a test tone and then analysing the envelope detector's output to identify the $I/Q$ imbalances that are present in the transmitter front-end. Although these methods result in satisfactory compensation, their operation requires that the transmitter be taken off-line to perform the calibration, or that test signals be incorporated into the transmitted data signal. This results in breaks in transmission, which need to recur over time in order to track drifts in the front-end imbalances over time. Fortunately, $I/Q$ imbalances drift relatively slowly over time [20], therefore making this less of a concern.

#### Methods involving real transmitted data (on-line compensation)

The required break in normal transmission that is associated with off-line calibration, is circumvented in [25, 33, 71], where real data is used to estimate the imbalance of the modulator front-end.

The technique by Marchesani [33] is only applicable to zero-IF transmitters that employ digital modulation schemes. The proposed compensation scheme implements an adaptive algorithm to identify the imbalances and offset errors of the front-end. This adaptive algorithm is adapted through the generation of appropriate error signals using knowledge of the transmitted symbol and the sampled output of the envelope detector. This requires symbol synchronisation, in order to sample the envelope detector at exactly the right instant.

The method presented by Hilborne et al. in [25], uses an adjacent-channel power meter in order to simultaneously compensate for quadrature imbalances, as well as power amplifier

(PA) non-linearities. The transmitted signal is tapped off after the PA and fed back through an adjacent channel power detector, yielding a DC error signal which is proportional to the amount of power that leaked into the adjacent channel. The authors show that the output of this adjacent power meter is quadratically proportional to both quadrature imbalances, as well as the non-linearities of the PA. The output of the adjacent power meter therefore provides a uni-modal error surface for adaptation of the quadrature imbalance and pre-distorter parameters. These parameters are adapted during normal transmission, using the recursive-least-squares (RLS) method to fit the measured power samples to the power surface and find the optimal compensation values that minimise the sum of squared errors.

A similar approach for low-IF transmitters is presented by Windisch and Fettweis in [71]. Low-IF refers to the case where the transmitted signal is first modulated onto an IF in the digital domain, before using quadrature mixing to translate this single-sideband (SSB) signal to RF [71]. In their work, Windisch and Fettweis add a feedback path to the transmitter, that resembles a classic heterodyne receiver structure, in order to obtain a reference of the residual image component present in the up-converted signal. This image component is then used as a approximation of the cost function to be minimised by iteratively adjusting the compensation parameters.

### 3.1.2 Demodulator compensation

Compensation techniques presented in literature for demodulator compensation include the use of test signals and iterative algorithms to estimate and correct imbalance errors [9, 13, 14, 50]. The use of test signals results in a break in normal reception. Blind compensation techniques, where no training or calibration signals are used, are also popular. Compensation is therefore done on-line using real received data. Commonly used blind techniques include interference-canceller (IC) based methods [12, 60, 61, 64, 65, 78], blind source separation (BSS) [45, 60, 62, 63, 65] and methods utilising the second-order statistics of the received signal [72, 73, 3, 48, 66]. The following subsections will investigate each of these approaches.

#### Test-signal based methods

Test-signal based compensation schemes operate with exact knowledge of what the desired signal should be and are mostly employed along with digital modulation schemes. Adaptive algorithms are then typically employed, which use the difference between the received signal and the theoretical signal, to arrive at the optimal $I/Q$ imbalance compensation parameters.

Chakra and Huyart [13] discuss a quadrature phase shift keying (QPSK) digital modulation scheme for a zero-IF receiver. A pseudonoise (PN) data sequence is transmitted as a test signal, while a least-mean-squares (LMS) adaptive algorithm is implemented at the receiver to centre and normalise the constellation. The LMS algorithm adapts on the difference between the actual received signal value and its theoretical value. The method presented by Sohn et al. in [50] also employs a QPSK digital modulation scheme with training signals, but

instead of using an adaptive algorithm, the compensation parameters are determined from a block of training symbols using a least-squares (LS) fit. In [9] Cavers and Liao suggests that the test sequences in digital modulation schemes can be substituted with the decisions at the output of the detector, therefore operating in a decision directed fashion. In fact, in [9], Cavers implements a decision directed compensation scheme resembling an adaptive equaliser, that can be switched to operate on real data instead of test signals.

The above techniques all rely on measuring the difference between the received symbol and the expected symbol. This approach has the following implications:

1. They are only applicable to zero-IF receivers, since the interference is assumed to be a self-image, ie. a skewing of the signal constellation, compared to an interference from an independent signal, as in the low-IF case.

2. Carrier synchronisation and symbol timing synchronisation is required, since the adaptive algorithms operate on the symbol level. Consequently, imperfect carrier or symbol synchronisation, will adversely effect the performance of the imbalance estimation process.

Tubbax et al. [57] utilise the fact that orthogonal frequency division multiplexing (OFDM) systems already employ test (or 'pilot') signals for synchronisation and channel estimation. In their work, the authors use these pilot signals for simultaneous channel and $I/Q$ imbalance estimation. Their approach is based on the assumption that, since the coherence bandwidth of the received signal is generally much larger than the channel bandwidth, the estimated channel response should be a smooth function. They show that $I/Q$ imbalances result in discrete jumps in the channel estimate, and subsequently continues to find the $I/Q$ imbalance parameters which maximise the smoothness of the channel estimate, in a mean square sense. OFDM training sequences are also used by Tarighat et al. in [55], where they derive a LMS based equaliser for $I/Q$ imbalance compensation.

It should be noted that, in all the above-mentioned techniques, the transmitter generates the test signals, which means that it is assumed that the transmitter does not contribute to the $I/Q$ imbalance distortion of the signal, or that it is sufficient to compensate for the combined transmitter-receiver effect at the receiver.

One way to isolate the effect of the receiver, is to use analogue test tones which are inserted directly at the receiver. Churchill et al. implement such a technique in [14], where the test tone is an analogue tone with a frequency located at the channel's centre frequency. Their compensation method is related to the Gram-Schmidt orthogonalisation (GSO) method and employs the discrete Fourier transform (DFT) to form digital filters, one at the test signal frequency and one at the image frequency. The outputs of these filters are then used to re-orthogonalise the $I$ and the $Q$ channels.

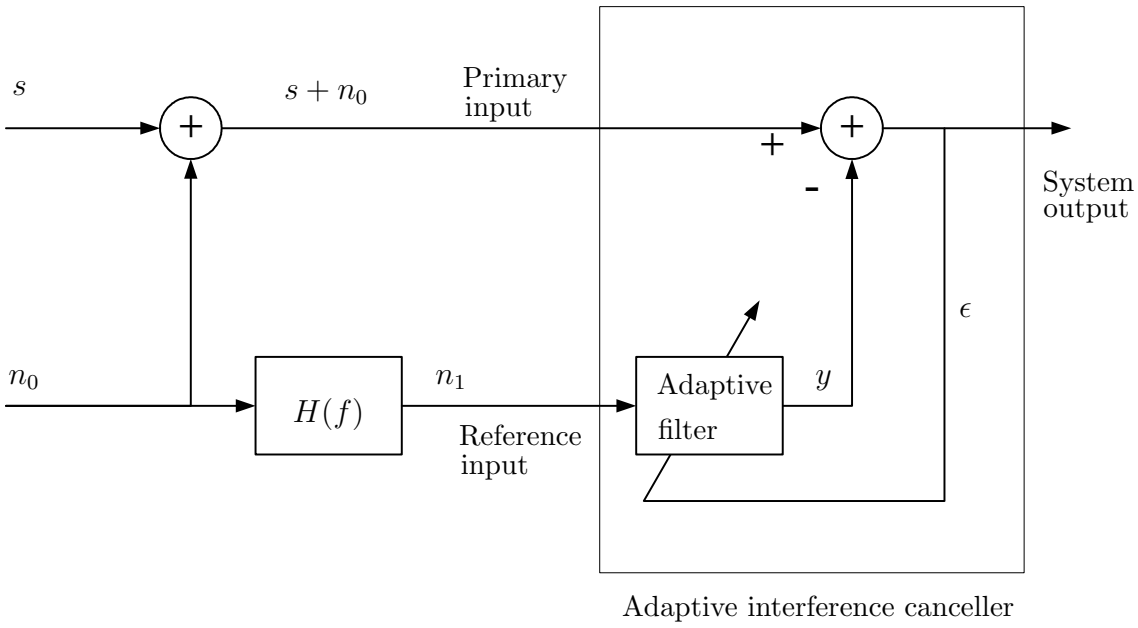


**Figure 3.1:** *Adaptive interference canceller topology. Adapted from [70, p. 304].*

### Blind methods

Blind methods imply that the receiver does not have knowledge of the data that is transmitted. The receiver must rely on other information, such as the expected statistics of the received signal, in order to extract the imbalances of its front-end. The following subsections highlight the most popular approaches.

*Interference canceller (IC) based methods*

A commonly used blind compensation technique is the use of an adaptive interference or noise canceller (IC) topology [12, 61, 65, 78] to decorrelate the desired signal from the interfering image signal. Figure 3.1 shows the basic interference canceller topology, as adapted from [70]. In a typical IC scenario, a desired signal, $s$, is corrupted by an uncorrelated interfering signal $n_0$. The two signals that can be observed are the desired signal along with the interfering signal, $s + n_0$, called the primary input, as well as some observation of the interfering signal, $n_1$, which consists of $n_0$ that has passed through an unknown transfer function $H(f)$. $n_1$ is called the reference input, since it provides a reference of the undesired interfering signal that has to be cancelled from the primary input. The reference signal is passed through an adaptive filter, which is responsible for transforming $n_1$ to be as close as possible to the interfering signal $n_0$. The output of the adaptive filter, $y$, therefore provides an estimate of $n_0$. The output of the adaptive filter is subtracted from the primary signal to provide an error signal, $\epsilon$, which is also the system output. The impulse response of the adaptive filter is adapted according to a least-squares algorithm (such as the LMS algorithm), which aims to minimise the power of the error signal, i.e. the system output. In [70] it is shown

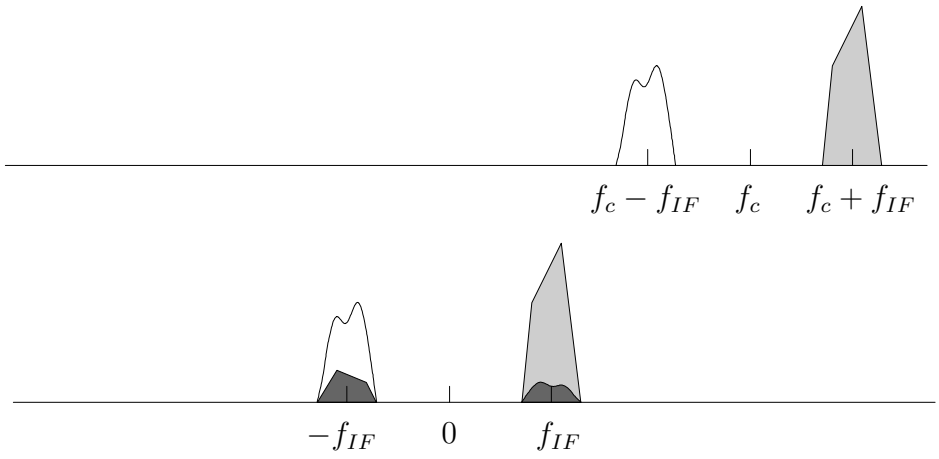


**Figure 3.2:** *Magnitude frequency spectra illustrating the effect of quadrature imbalances on a low-IF receiver.*

that minimising the output power of the system, has the effect of decorrelating the reference input from the primary input. Due to the adaptive nature of the IC, it is able to adapt to changes in the unknown transfer function $H(f)$.

To extend the idea of an IC to quadrature imbalance compensation, it is necessary to reconsider the expression for the demodulated signal that was derived in (2.130) on p. 55, presented here again:

$$z'(t) = \tilde{r}_{\text{Des}}(t)W_1 + \tilde{r}^*_{\text{Des}}(t)W_2. \tag{3.1}$$

From (3.1) it is seen that its image signal, $\tilde{r}^*_{Des}(t)$, interferes with the desired signal, $\tilde{r}_{Des}(t)$. As illustrated in Fig. 3.2 for the low-IF case, this has the effect that the desired signal at frequency $f_{\text{IF}}$ also contains the components of the adjacent channel's signal located at a frequency of $-f_{\text{IF}}$. Theoretically, if $\tilde{r}^*_{Des}(t)$ could be obtained, it could be used as a reference signal in an IC based topology with $z'(t)$ as the primary signal. In fact, if $\tilde{r}^*_{Des}(t)$ was indeed available, its complex conjugate would be the desired signal, and no further compensation would have been necessary. One way to obtain some reference of $\tilde{r}^*_{Des}(t)$ is to compute the complex conjugate of $z'(t)$, denoted by $z'^*(t)$. The problem with this approach is that $z'^*(t)$ also contains a component of the desired signal, and therefore part of the desired signal will also be cancelled in the process. This problem is known as the 'signal leakage' problem [60, 65, 72, 78], which is a common obstacle in interference cancellation. In [78], Yu and Snelgrove shown that using $z'^*(t)$ as reference signal in the simple IC based topology shown in Figure 3.1, does not improve the signal-to-interference (SIR) ratio of the received signal.

To combat the signal leakage problem, Yu and Snelgrove [78] suggest implementing a modified IC topology containing two adaptive filters. This topology was introduced by Compernolle and Van Gerven [16] and is termed a signal separation system. As implemented by Yu and Snelgrove, the signal separation system uses the signals $z'(t)$ and $z'^*(t)$ as primary and reference inputs respectively. This modified IC uses an extra adaptive filter to cancel

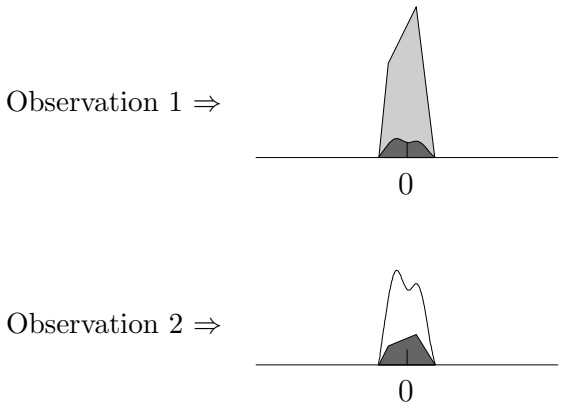


**Figure 3.3:** *Magnitude spectra of two baseband observations used in [60, 61, 64, 65].*

the desired signal component in the interference reference, whereafter this 'clean reference' is used as a reference to cancel the interfering signal in the primary signal. Although this method does improve the SIR of the receiver, Yu and Snelgrove concludes that an IC-based approach does not yield sufficient improvement to be implemented in a practical system.

The authors of [60, 61, 64, 65] disagree with the conclusion of Yu and Snelgrove in [78]. They show that a simple IC-based compensation method can indeed yield sufficient image rejection, if given the correct reference signal generation. Recall that after the down-mixing procedure, for the low-IF case, the desired signal is located at a frequency of $f_{\text{IF}}$, and is interfered with by the adjacent channel's signal located at a frequency of $-f_{\text{IF}}$. The authors now propose processing the signals at $f_{\text{IF}}$ and $-f_{\text{IF}}$ separately, therefore obtaining two baseband observations. This is done by digitally mixing the down-converted signal with the complex exponentials $e^{j2\pi f_{\text{IF}}}$ and $e^{-j2\pi f_{\text{IF}}}$ respectively, and lowpass filtering each observation. The resulting baseband observations are represented graphically in Figure 3.3 (where the sample spectrum of Figure 3.2 is used for illustration). Observation 1 is formed by multiplying the down-converted signal with $e^{-j2\pi f_{\text{IF}}}$ and lowpass filtering the output. Observation 2 is formed by multiplying the down-converted signal with $e^{j2\pi f_{\text{IF}}}$ and taking the complex conjugate before lowpass filtering.

When the interfering signal is much stronger than the desired signal, then observation 2 will be highly correlated with the interfering signal that needs to be cancelled in the primary signal (observation 1). The authors of [60, 61, 64, 65] show that by using observation 1 as the primary input and observation 2 as the reference input to a simple IC, the SIR ratio of the receiver can be increased significantly. This results in an IC-based compensation scheme that delivers better performance than the method proposed in [78], while involving less complexity since only one adaptive filter is needed.

*Blind source separation (BSS)*

Another popular blind approach to low-IF quadrature imbalance compensation, is the use of blind source separation (BSS) algorithms [45, 60, 62, 63, 65]. The aim of BSS is to separate

$m$ individual signal sources, when only $l \geq m$ mixtures of the sources can be observed [24, 27, 65]. The source signals are separated on grounds of statistical independence by using their higher order statistics. It should be noted that, in BSS, both the mixing parameters and the individual sources are unknown.

Following the discussion presented by Haykin in [24, p. 768], a typical noiseless BSS scenario can be stated mathematically as:

$$\boldsymbol{x}(n) = \boldsymbol{A}\boldsymbol{s}(n) \ , \tag{3.2}$$

where $\boldsymbol{x}(n)$ is the $l \times 1$ observation vector, $\boldsymbol{s}(n)$ is the $m \times 1$ source vector and $\boldsymbol{A}$ is the $l \times m$ mixing matrix. The variable $n$ denotes discrete time, since BSS is performed in the digital domain. It is now the aim of BSS methods to find a separation matrix $\boldsymbol{W}$ such that

$$\begin{aligned} \boldsymbol{y}(n) &= \boldsymbol{W}\boldsymbol{u}(n) & (3.3) \\ &= \boldsymbol{W}\boldsymbol{A}\boldsymbol{s}(n) = \boldsymbol{D}\boldsymbol{P}\boldsymbol{s}(n), & (3.4) \end{aligned}$$

where $\boldsymbol{D}$ is a diagonal scaling matrix, and $\boldsymbol{P}$ is a permutation matrix. BSS can therefore ideally only separate the individual source signals, without preserving their scaling, and some additional information is usually needed to reorder the sources after separation, and correct their scaling [65].

The separation matrix $\boldsymbol{W}$ is adapted to make the components of the output vector $\boldsymbol{y}(n)$ statistically independent from each other. The fact that $\boldsymbol{W}$ is adapted iteratively means that BSS methods are also able to track changes in the mixing matrix over time. Although there exist various methods to adapt $\boldsymbol{W}$ (see [27] for a review), a popular approach used in the particular case of quadrature imbalance compensation, is the class of equivariant adaptive separation via independence (EASI) algorithms [45, 46, 60, 62, 63, 65]. The development of the EASI algorithms is quite involved and will not be discussed here. For an in-depth discussion on the subject, the reader is referred to [27] and [7].

To relate the idea of BSS to quadrature imbalance compensation, the authors of [60, 62, 65] propose generating the same two baseband observations, as was discussed in Section 3.1.2 (p. 64) and illustrated in Figure 3.3. Let the digital equivalent of observation 1 and 2 be denoted by $o_1(n)$ and $o_2(n)$ respectively, each containing components of a desired signal, $d(n)$, and an image signal, $i(n)$. The two observations can now be related to the desired and image signal as [65, 62, 60],

$$\begin{bmatrix} o_1(n) \\ o_2(n) \end{bmatrix} = \begin{bmatrix} W_1\sqrt{P_{\text{desired}}} & W_2\sqrt{P_{\text{image}}} \\ W_2^*\sqrt{P_{\text{desired}}} & W_1^*\sqrt{P_{\text{image}}} \end{bmatrix} \begin{bmatrix} d(n)/\sqrt{P_{\text{desired}}} \\ i^*(n)/\sqrt{P_{\text{image}}} \end{bmatrix} \ , \tag{3.5}$$

where $P_{\text{desired}}$ and $P_{\text{image}}$ represent the power of the desired and image signal respectively, and $W_1$ and $W_2$ are the same scaling coefficients as in equation (3.1). Equation (3.5) has the same form as (3.2) and therefore, when the mixing matrix of (3.5) is invertible, BSS methods can be used to separate the desired and image signal components, based on their independence. The authors show that the mixing matrix of (3.5) will be invertible for all practical quadrature imbalance scenarios.

BSS techniques generally outperform interference cancelling methods in terms of image suppression, but their performance tends to be more sensitive to additive noise and symbol timing errors [65]. The computational complexity of BSS methods is considered to be high [5]. Both IC and BSS are only applicable to low-IF receivers, where the desired signal is subjected to interference by another channel's signal, located at the desired signal's image frequency. In the implementations presented in this chapter, it was also seen that accurate digital frequency synchronisation is also needed in order to generate the two required observation signals $o_1(n)$ and $o_2(n)$.

*Methods using second order statistics*

Another popular blind approach involves the use of the second-order statistics of the received signal to extract the imbalances of the receiver front-end. The main advantage of this approach is that it often leads to computationally less expensive solutions, compared to IC and BSS methods.

The common assumption used in second-order statistics-based methods, is based on the assumed circularity or properness of the original complex baseband signal [3, 66]. Properness refers to the fact that the complementary autocorrelation functions (CACF) of the signal vanishes [3]. This has the effect that the received signal and its complex conjugate are uncorrelated. For zero-IF receivers this further implies that the signals of the $I$ and $Q$ channels should have equal power and should be instantaneously mutually uncorrelated [5], which is satisfied by many digital modulation schemes, such as M-ary PSK and M-ary QAM, for example [3]. For multi-channel signals, as are received by low-IF receivers and OFDM systems, the circularity requirement is extended in the sense that the signals on the desired and interfering frequency channels should also be jointly circular.

As was already seen in Chapter 2, $I/Q$ imbalances destroy the circularity of the received signal, since it contains not only the desired signal, but also its complex conjugate (in the zero-IF case) or the complex conjugate of the signal at the image frequency (in the low-IF case). $I/Q$ imbalance compensation methods in this class therefore analyse the circularity properties of the received signal and use the deviation from the expected statistics to extract compensation parameters which would restore the circularity of the received signal. The authors of [3, 66] also show how a fading channel and frequency offsets between the LO frequency of the demodulator and the centre frequency of the received signal, do not affect the circularity properties of the signal. The performance of techniques based on the circularity assumption is therefore independent of these factors.

In [72, 73], Windisch and Fettweis present a blind frequency-independent compensation method, applicable to low-IF receivers. In their work, they generate the same two baseband observations, $o_1(n)$ and $o_2(n)$, as was discussed in the previous section. Their technique assumes these signals to have zero mean be uncorrelated. They subsequently continue to show that by using two statistics, namely that of $\mathrm{E}\{o_1(n)o_2^*(n)\}$ and $\mathrm{E}\{|o_1(n)+o_2(n)|^2\}$, where $\mathrm{E}\{\cdot\}$ denotes the expectation operator, the product $W_1W_2$ can be obtained. From the

product $W_1W_2$, the imbalances $g_D$ and $\varphi$ can be extracted as

$$g_D = \sqrt{1 - 4\mathcal{R}e\{W_1W_2\}} \tag{3.6}$$

$$\varphi = \arcsin\left(\frac{2}{g_D}\mathcal{I}m\{W_1W_2\}\right) . \tag{3.7}$$

The expectation operation is approximated by a time average over $N$ samples and therefore the resultant product $W_1W_2$ becomes an estimate of the real quantity. Performance analysis by the authors shows that their compensation method does not yield deterministic performance, since random signals are used in the estimation process. They do however show through simulation that the worst-case performance of their method does not deviate severely from its mean performance.

Antilla et al. [3] employ a method similar to that presented by Windisch and Fettweis in [72, 73], where they relate the CACF and the normal autocorrelation function (ACF) of the received signal, to the frequency-independent scaling factors $W_1$ and $W_2$. They compute the ACF and CACF from blocks of stored data and subsequently solve for the ratio $W_2/W_1$, which they show is sufficient information for restoring the circularity of the received signal. In contrast with the method presented by Windisch and Fettweis, Antilla et al.'s method is applicable to zero-IF as well as low-IF receivers, and do not require the two observations $o_1(n)$ and $o_2(n)$ to be computed. Furthermore their method does not rely on a specific structure of $W_1$ and $W_2$, but is derived for any arbitrary complex scaling $W_2/W_1$.

Valkama et al. [66] propose a whitening transform, based on eigenvalue decomposition of a stored block of a received data, to restore the circularity of received signal. Since a whitening transform does not yield unique solutions, an unknown phase rotation and an ambiguity in terms of desired and image signal (or I and Q channel for the zero-IF case), is left in the compensated signal. Some additional information is required to resolve these unknowns. The authors extend their technique with an adaptive variant of the whitening transform, mitigating the need to store a block of data, and enabling their technique to track changes in the distortion parameters over time.

Rykaczewski and Jondral base their approach in [48] on a slightly different premise. In their work, they make the assumption that the desired $I$ and $Q$ signals are statistically independent and have equal mean power. This enables them to use the variance and covariance of the distorted $I$ and $Q$ channels, computed in a block-based fashion from sample estimates, to extract the gain and phase imbalances of the front-end. In comparative simulations they show how such a second order method performs equally well compared to a BSS method, but is much less computationally intensive.

*Gram-Schmidt orthogonalisation*

Another blind approach includes the use of Gram-Schmidt orthogonalisation (GSO) to re-orthogonalise the $I$ and the $Q$ channels. In [26], Huang discusses a GSO compensation method that is applicable to zero-IF receivers, and employs digital modulation schemes together with quadrature mixing. In order to re-orthogonalise the symbol streams on the $I$ and $Q$ channels using GSO, carrier and symbol synchronisation must be established.

## 3.2 Frequency-dependent mismatch compensation

Frequency-dependent quadrature mismatch compensation has received much less attention in literature, compared to frequency-independent compensation [5, 77], but is becoming increasingly important with the use of wider bandwidth signals and multi-channel systems. The common assumption is that frequency-dependent $I/Q$ mismatches are mainly due to mismatches between the analogue LPFs of the $I$ and $Q$ signal paths [20, 29, 59]. Some authors choose to view the equalisation of these filters as a separate procedure from compensating for the frequency-independent $I/Q$ imbalances of the mixer (see e.g. [31, 58, 59]), while others choose to compensate for the combined LPF and mixer imbalances (see e.g. [5, 4, 55]). Note that it will be shown in Chapter 4, that simply modelling the frequency-dependent imbalance of the quadrature front-end as mismatched LPFs, is inadequate to explain the observed imbalance characteristics of a measured hardware quadrature mixer implementation.

The following subsections discuss different techniques presented in literature to compensate for frequency-independent $I/Q$ imbalances. Since the approaches for modulator and demodulator compensation differ quite substantially, they will again be considered separately.

### 3.2.1 Modulator compensation

The existing methods dedicated to frequency-dependent imbalance compensation for the modulator, aim to separate the imbalances of the LPFs from those of the mixer, which is assumed to have frequency-independent imbalances. In order to accomplish this, additional feedback paths are fitted to the modulator, feeding back the signals after the LPFs to be examined. Compensation is realised through digital filters added to the digital baseband processing of the modulator.

The estimation of the filter responses can be subdivided into two main approaches, that are either static [58, 59, 58] or adaptive [31]. The static filters are designed from recorded training or test sequences, and aim to modify the frequency response of the $I$ and $Q$ channels to resemble some desired response. These filters are not updated on-line and make it impossible to track changes in the analogue front-end that may occur over time. Adaptive filters on the other hand, are adapted to minimise the channels' response from a desired response during the normal operation of the transceiver, therefore also tracking changes in the analogue front-end over time.

#### Static pre-compensation filters using test sequences

In [58], Tuthill and Cantoni discuss using two finite impulse response (FIR) filters to predistort the $I$ and the $Q$ channels of a zero-IF transmitter that employs continuous-phase frequency shift keying (CPFSK). A test sequence is transmitted and fed back into the transmitter's digital domain, using the topology shown in Figure 3.4. This technique adds two extra ADCs to the transmitter, in order to digitise the feedback signal. Since these ADCs are

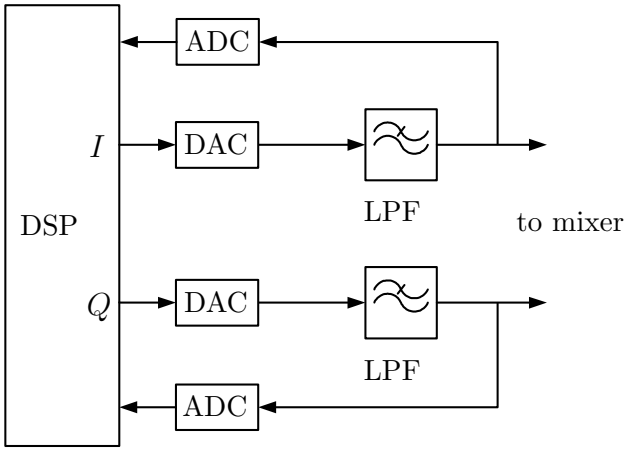


**Figure 3.4:** *The feedback topology implemented in [31, 58, 59]. Adapted from [58].*

not in the normal transmission path, care should be taken to ensure that they do not contribute significantly to the mismatches of the front-end. A cost function for LS optimisation is then defined in the frequency domain, which minimises the difference between a desired response and that measured from the $I$ and $Q$ channels respectively. The filter weights are determined as those that minimise the cost function in the least-squares sense. The desired response is chosen to have the same magnitude response as the nominal LPF response, but with linear phase. The compensation procedure is done separately for the $I$ and $Q$ channel.

In [59], Tuthill and Cantoni extend their previous work in [58] by providing a better-conditioned solution matrix. They also present a method to decrease the computational cost of the LS technique and the complexity of the resulting filter, by spacing the taps of the filter more than a sample apart. Practically, this results in a pre-compensation filter that delivers roughly the same performance as that in [58], but with only about a third as many active (non-zero) filter taps.

A different approach is suggested by Kiss and Prodanov in [29]. In their work, the authors did an extensive statistical trial of different LPF topologies and implementations. They found that at low frequencies, the $I/Q$ mismatches are generally dominated by gain imbalances, while the mismatches at the passband edges are dominated by the phase imbalances. They propose that the gain mismatch can be approximated by a single scaling value and that the phase mismatch between the two LPFs can be approximated by a pure time delay. Their compensation scheme therefore involves only an amplitude scaling for gain compensation and a first order interpolating filter for phase imbalance compensation. The exact values for the amplitude scaling and interpolating filter is obtained by inserting test tones (with frequencies at the channel's centre frequency and at the passband edge) at the LPFs of the $I$ and $Q$ channels and measuring the scaling and time difference between the two channels' signals in the digital domain. Although the assumptions of their compensation method do not always hold equally well for all LPF topologies and implementations, the authors' reasoning is that,

by choosing the right LPF topology and implementation, the process of compensating for frequency-dependent mismatches can be greatly reduced in complexity.

#### Adaptive pre-compensation filters using real data

Lim et al. [31] extends the compensation FIR filters of Tuthill and Cantoni in [58] to be adaptive, by using the LMS algorithm. The same feedback system as in Fig. 3.4 is used to generate an error signal in the digital domain of the transmitter, for the adaptation of the compensation filters. The desired response is once again chosen to have a magnitude response equivalent to the nominal LPF response, and its phase is constrained to be linear. The pre-compensation filters of both the $I$ and $Q$ channels are adapted in this way, resulting in two FIR filters that are constantly adapted from real transmitted data. The adaptive nature of this technique enables the pre-compensation filters to track any change in the analogue LPFs response which may occur over time, without having to take the transmitter off-line.

### 3.2.2 Demodulator compensation

Methods to compensate for the frequency-dependent imbalances of the demodulator, include the use of test signals and blind compensation using real received data. The test signal approaches are mostly applicable to OFDM systems where the pilot symbols that are required in the communication protocol are used for imbalance extraction as well. The following subsections investigates these approaches.

#### Methods involving test signals

As was mentioned in Section 3.1.2, OFDM systems already include the use of pilot symbols during normal operation for carrier synchronisation and channel estimation. Since OFDM involves transmitting signals on multiple (orthogonal) sub-carriers, it lends itself well towards extracting frequency-dependent $I/Q$ imbalances.

Xing et al. [77] assume OFDM operation and the associated pilot sequences for imbalance extraction. They propose transmitting the same training symbol on each sub-carrier, changing only the phase of every even pilot by 45 degrees. They split the compensation into a two-stage procedure, employing a digital FIR filter in the $I$ channel to compensate for the frequency-dependent imbalances and frequency-independent gain imbalance of the mixer, followed by a frequency-independent compensation network, to compensate for the frequency-independent phase imbalance of the mixer. The authors employ a non-linear least mean squares (NLMS) optimisation procedure, on a block of received pilot symbols, to estimate the FIR filter's taps and the phase imbalance parameter, which would restore the expected relationship between the theoretical and received symbols. Since the optimisation procedure optimises over all pilot symbols, each one being on a different sub-carrier, the

extracted compensation filter effectively takes into account the imbalances of the whole frequency band spanned by the pilot symbols. It should be noted that this procedure requires accurate frequency synchronisation in order to work, for which the authors present a separate solution.

Tarighat et al. [55] also show how their frequency-independent compensation technique, also based on using training sequences in an OFDM system in cooperation with an LMS optimisation procedure (discussed in Section 3.1.2), can be made frequency-dependent, by utilising pilot symbols on different sub-carriers.

### Blind methods

There are only a few techniques able to address frequency-dependent imbalances compensation in a blind fashion, i.e. extracting the imbalances from the received signal without knowledge of the data that was transmitted. Below are the current approaches found in literature.

*Blind source separation (BSS) and interference cancelling (IC)*

The algorithms for frequency-independent $I/Q$ imbalance compensation using BSS and IC-based methods, as presented in Section 3.1.2, are inherently able to handle the frequency-dependent imbalance scenario as well. This is due to the fact that the compensation parameters are in actual fact filters. Frequency-independent imbalance compensation can be seen as a special case where the filter lengths are chosen to be equal to one.

For frequency-dependent operation, the same limitations, however, hold. These are that BSS techniques are computationally very expensive and sensitive to additive noise and symbol timing errors [65] and exhibit slow convergence performance [57], while IC methods suffer from the signal leakage problem. Both BSS and IC-based methods are only applicable to low-IF receivers.

*Methods involving second order statistics*

Antilla et al. [4] present a frequency-dependent imbalance compensation solution, based on the assumed circularity of the received signal. Their technique employs an adaptive filter, which aims to restore the properness of the received signal. Properness refers to the fact that the complementary autocorrelation functions (CACF) of the signal vanishes [3]. This has the effect that the received signal and its complex conjugate are uncorrelated. The adaptive filter uses a stochastic Newton zero search to minimise the CACF of the output signal. In comparative simulations, the authors illustrate that their technique outperforms LMS based IC methods.

## 3.3 Conclusions

In this chapter various compensation techniques that have been proposed in literature, were presented. It was seen that most methods provide solutions for frequency-independent quadrature imbalances. For modulator compensation, it was seen that most techniques require the addition of extra hardware to the transmitter, in order to obtain a reference of the imbalances of the front-end . For modulator compensation, the techniques are iterative in nature, minimising a quadratic search function [8, 9, 21, 25, 71, 33].

Demodulator imbalance compensation does not generally require additional hardware to be added to the receiver. The techniques ranged from those using test signals to completely blind methods.

The limitations of demodulator compensation techniques using digital modulation schemes and test signals (e.g. [13, 50, 9]), revolve around the assumption of a specific modulation scheme or protocol, limiting their applicability often even in terms of the receiver topology, ie. low-IF vs. zero-IF. Many of the presented techniques also rely on adaptive or iterative search methods to derive the optimal compensation parameters.

Many test-signal based methods (e.g. [57, 55]), are only applicable to OFDM systems that include the use of pilot symbols in the normal operation.

Blind methods have the advantage that knowledge of the theoretical received signal is not required and therefore they can be implemented in an operational scenario, estimating the imbalances of the demodulator during operation in a parallel process. The trade-off is that many of the suggested methods such as the IC [12, 61, 65, 78] and BSS [45, 60, 62, 63, 65] based methods suffer from slow conversion, sensitivity towards noise [65], computational complexity [5] and are only applicable to the low-IF receiver. In contrast to these methods, the methods based on second order statistics [3, 66, 72, 73, 48] seem to offer a truly attractive solution, being widely applicable and requiring low computational complexity.

Frequency-dependent imbalance compensation has received much less attention in literature, compared to that of frequency-independent compensation techniques.

Very few modulator frequency-dependent imbalance compensation techniques have been proposed in literature. Those that have been proposed, aim to equalise the responses of the two LPF, requiring feedback paths after the two LPFs [58, 59, 58, 31].

For demodulator frequency-dependent compensation, the IC and BSS techniques are again applicable, however the same limitations in their application apply. The OFDM based techniques are of course tailored toward OFDM systems and therefore their applicability to systems employing different modulation schemes is limited. The second order statistical approach presented by Antilla et al. in [4] seems attractive, although it should be noted that the demodulator imbalances are, as is often the case, extracted through an adaptive (iterative) search technique, minimising the defined cost function.

It is difficult to label one method as being better than another, since the trade-offs between different compensation techniques will impact differently, depending on the operating scenario. For one application the break in operation required by the use of test tones

might be worth the trade-off to the higher computational complexity needed by most on-line methods. Since the gain and phase imbalances of the quadrature front-end drifts slowly over time [20], a stable operating environment might not require any tracking of imbalance parameters, and therefore the $I/Q$ compensation might only be performed as a start-up procedure, or at irregular intervals. On the other hand, the use of second-order statistics provides a computationally inexpensive way to perform blind compensation, using real data and assumptions which should be applicable to most radio standards. The choice between a frequency-dependent or independent solution also depends on the bandwidth requirements of the signal, and whether the narrowband assumption is acceptable in the specific case.

In the next two chapters, novel techniques for $I/Q$ imbalance extraction will be presented. In Chapter 4, novel frequency-dependent imbalance compensation techniques will be presented, which aim to compensate for both modulator and demodulator imbalances. These techniques are designed to require the addition of very little (if any) extra hardware to the quadrature mixing front-end. Furthermore, their working relies on direct imbalance extraction from spectral analysis of test signals, and are therefore not iterative in nature. This makes them well-suited to be implemented as a rapid, transceiver-start-up calibration procedure.

Chapter 6 presents a novel, frequency-independent, blind compensation scheme, for narrowband signals. The technique uses the second-order statistics of the received signal and provides a computationally efficient compensation strategy. An adaptive variant is also presented, which is able to track imbalances over time and reduce the storage requirement of the block-based version.

# Chapter 4

# Frequency-dependent imbalance estimation and compensation

## 4.1 Introduction

In Chapter 3 various methods for $I/Q$ imbalance compensation that are found in literature, were described. It was clear that most techniques only address the compensation of frequency-independent imbalances. It was seen that modulator compensation required additional hardware to be fitted to the transmitter, in order to obtain a reference of the imbalances in the front end. Iterative search techniques were then often employed to extract the optimal compensation parameters.

In this chapter the mathematical models for the quadrature imbalances of the modulator and demodulator that were developed in Chapter 2, will be used to develop novel compensation techniques addressing frequency-dependent imbalances. The techniques will be implemented in the digital domain of the transmitter and receiver. They will be based on a test signal approach, but, unlike most test signal based methods in literature, they will not be iterative in nature. A test signal approach allows the techniques to be independent of the chosen modulation scheme. As will be shown, the simplicity of the test signals makes the presented techniques generic enough to be applicable to non-communications based systems, such as radar systems. The presented techniques will address quadrature modulator, as well as demodulator compensation and will offer the capability of full transceiver compensation to be performed as a start-up procedure. Due to its non-iterative nature, compensation can be done extremely quickly with minimal measurements needed. A specific transceiver configuration will also be presented which requires only minimal extra hardware to be added to the front-end, in order to facilitate automatic transceiver compensation. The approach will employ a quadrature demodulator as a measuring device. The aim, however, will not be to compensate for the cascaded modulator and demodulator imbalances at the demodulator, but rather to show how the contributions of the modulator and demodulator can be separated by only examining the signal at the demodulator.

This chapter will be structured as follows. To lay the foundation for the rest of the Chap-

ter, Section 4.2 will discuss the principles behind digitally compensating for the frequency-dependent imbalances of the analogue domains of the modulator and the demodulator, respectively. This analysis will clearly show which parameters need to be estimated during the extraction process.

Section 4.3 then continues to present novel imbalance extraction methods that can be used to estimate the imbalances of the modulator and demodulator, respectively, at different frequencies throughout the operating band. The techniques presented here are based on spectral analysis, using test tones. For modulator imbalance extraction, three cases are analysed: the case where the modulator and demodulator are synchronised in frequency and sample timing, the case where they are only synchronised in frequency and finally when they are neither synchronised in frequency nor sample timing. Although the techniques are presented from the view point that a quadrature modulator is fed directly into a quadrature demodulator, which act as the measurement device, the techniques are general and applicable to any setup where spectral analysis can be performed, even when only magnitude information is available (such as when using a spectrum analyser).

Section 4.4 then discusses the procedure of translating the extracted imbalances of the modulator and demodulator into compensation filters, which will facilitate truly frequency-dependent imbalance compensation.

## 4.2 Principles of digital compensation

To start off this chapter on imbalance extraction and compensation, it is important to have an understanding of how the analogue imbalances of the quadrature modulator and demodulator can be compensated for in their respective digital domains. This section will aim to illustrate how this is possible, and will highlight the factors which need to be estimated during imbalance extraction.

### 4.2.1 Demodulator

In equation (2.102) it was shown that the output of an imbalanced quadrature demodulator can be written as

$$Z'(f) = R_{\text{Des}}(f)W_1(f) + R^*_{\text{Des}}(-f)W_2(f) \tag{4.1}$$

where $W_1(f)$ and $W_2(f)$ was defined in (2.103). In the above expression, only the term relating to $R_{\text{Des}}(f)$ is desired. In order to eliminate the undesired image component observed at the output of the demodulator, some form of post-correction should be applied. A simple post-correction operation would be to subtract a filtered version of the conjugate, frequency-reversed signal, from a potentially filtered version of the received signal. Mathematically, this would translate to

$$Z'_{\text{pc}}(f) = P_1(f)Z'(f) - P_2(f)Z'^*(-f) \tag{4.2}$$

where $P_1(f)$ and $P_2(f)$ represent the frequency responses of the post-correction filters. By substituting the expression for $Z'(f)$ and $Z'^*(-f)$ into (4.2) and regrouping the terms, we arrive at

$$\begin{aligned} Z'_{\text{pc}}(f) &= R_{\text{Des}}(f)\Big[W_1(f)P_1(f) - W_2^*(-f)P_2(f)\Big] \\ &\quad + R^*_{\text{Des}}(-f)\Big[W_2(f)P_1(f) - W_1^*(-f)P_2(f)\Big]. \end{aligned} \tag{4.3}$$

In order to eliminate the undesired image frequency component $W_2(f)P_1(f) - W_1^*(-f)P_2(f)$ should be equal to zero. If we arbitrarily choose $P_1(f) = 1$, the optimum value for post-compensation filter $P_2(f)$ becomes

$$P_2(f) = \frac{W_2(f)}{W_1^*(-f)}. \tag{4.4}$$

The above result is also presented in [4, 3] and represents the general approach towards reversing the imbalances of the demodulator's front-end, in the digital domain, as a post-correction procedure. It is seen that the functions $W_1(f)$ and $W_2(f)$ do not need to be estimated seperately, rather, only the the ratio between them needs to be estimated in order to achieve compensation.

### 4.2.2 Modulator

Similarly to the demodulator, it was seen in Chapter 2 on p. 30 that the baseband equivalent output of a quadrature modulator can be written as

$$\tilde{U}_{RF}(f) = A(f)V_1(f) + A^*(-f)V_2(f)\,, \tag{4.5}$$

where $V_1(f)$ and $V_2(f)$ was defined in (2.40). Once again it is noted that only the term relating to $A(f)$ is desired. To achieve modulator compensation, i.e. suppress the presence of the undesired image signal, a pre-compensation approach could be followed. Let $Q_1(f)$ and $Q_2(f)$ denote the frequency responses of two pre-compensation filters, which operate on the baseband signal that is to be transmitted, $A(f)$, and its frequency reversed, complex conjugate, $A^*(-f)$, respectively. The frequency-domain expression for a pre-compensated baseband signal can be written as

$$A_{\text{pc}}(f) = A(f)Q_1(f) - A^*(-f)Q_2(f). \tag{4.6}$$

When this pre-compensated signal is now used as the signal fed into the quadrature modulator, the frequency domain representation of the output of the modulator is now given by

$$\tilde{U}_{\text{pc,RF}}(f) = A_{\text{pc}}(f)V_1(f) + A^*_{\text{pc}}(-f)V_2(f). \tag{4.7}$$

By substituting the expression for $A_{\text{pc}}(f)$ into the above expression and regrouping the terms, the output of the pre-compensated, imbalanced quadrature modulator is written as

$$\begin{aligned} \tilde{U}_{\text{pc,RF}}(f) &= A(f)\Big[Q_1(f)V_1(f) - Q_2^*(-f)V_2(f)\Big] \\ &\quad + A^*(-f)\Big[Q_1^*(-f)V_2(f) - Q_2(f)V_1(f)\Big]. \end{aligned} \tag{4.8}$$

If $Q_1(f)$ is arbitrarily chosen to be equal to unity (similar to the approach followed for demodulator compensation) then, in order to eliminate the undesired image frequency component in the above expression, the response of the pre-compensation filter $Q_2(f)$ should be chosen as

$$Q_2(f) = \frac{V_2(f)}{V_1(f)}. \tag{4.9}$$

Expression (4.9) represents the frequency response for the optimum pre-compensation filter, which will be used in the digital domain of the modulator to pre-distort the $I$ and $Q$ signals, before transmission. Once again, it is seen that only the ratio between $V_2(f)$ and $V_1(f)$ need to be estimated. It is noted, however, that unlike the demodulator, the compensation filter is not a function of the frequency-reversed version of the scaling of the desired component.

It has now been shown that any imbalance extraction technique need only estimate the complex ratio between the scaling of the image and desired signal. The next section will discuss proposed techniques to achieve this.

## 4.3 Imbalance estimation using spectral measurements

In this section, the novel imbalance extraction techniques that represents one of the main contributions of this dissertation, will be presented.

The section will present the techniques along with potential topologies that could be used to realise their implementation. It should be noted that the suggested topologies in each case only serves as an example. It will be clear from each technique's discussion what the underlying principles and assumptions are, leaving the designer free to realise a different implementation which satisfies the assumptions of the technique.

The aim of the compensation techniques are to facilitate complete compensation of a quadrature transceiver, consisting of a quadrature modulator and demodulator on the same device. The idea is to employ these techniques either as a start-up procedure, or as a rapid calibration routine which can be performed from time to time, as required. The techniques that are presented below, address the compensation of the demodulator and modulator as separate entities, by using the demodulator as the measurement device. It will then be shown under what circumstances it is possible to separate the imbalance contributions of the modulator from the demodulator.

It should be noted that the techniques described below, do not assume transmission through a communications channel,but rather through a direct feedback path built into the transceiver, and therefore the signal to noise ratio is assumed to be high. For this reason the effect of additive noise is not modelled. This is not the case for the blind compensation techniques that will presented in Chapter 6, where transmission through a communication channel is assumed and additive noise is modelled. It is true though, that in essence the image rejection attainable with the proposed techniques in this Chapter, will be limited to the signal to noise ratio after processing. For this reason, the performance of the extraction

techniques in the presence of additive white Gaussian noise (AWGN) will be investigated through simulation in Section 6.6.

### 4.3.1 The choice of a test signal

It was seen in Section 4.2 that in order to compensate for quadrature imbalances, the complex ratio between the image and desired signal needs to be estimated. This section will discuss a suitable test signal that would enable this.

In essence, a suitable test signal would be one that could easily be decomposed into a desired and an image component. A single-sideband tone is ideal for this purpose. Although it is difficult to distinguish the desired signal from the unwanted signal in the time domain, it is quite straightforward in the frequency domain (see Fig. 4.1). If it is therefore possible to transmit or receive what is supposed to be a single-sideband tone, it will be shown that spectral analysis of the signal, after it has passed through either the imperfect modulator or demodulator, will render enough information to measure the complex imbalance ratio of the modulator or demodulator.

Of course, using a single sideband tone as a test signal will only yield information about the imbalance ratio at one frequency. It is therefore proposed to use a collection of these tones, spaced throughout the frequency band of interest, in order to characterise the $I/Q$ imbalances across frequency. Section 4.4 presents a solution to translate imbalance measurements at various point throughout the operating frequency band, to a frequency-dependent calibration filter.

### 4.3.2 Demodulator imbalance extraction

The extraction of demodulator imbalances is arguably much simpler than that of the modulator and is presented first. In this subsection, the basic principles for demodulator imbalance extraction will be discussed in isolation. In the next subsection, modulator imbalance extraction will be covered, where demodulator extraction will then be revisited to show how the techniques of this subsection can be used in conjunction to those developed for the modulator, for simultaneous modulator and demodulator imbalance separation and extraction.

To commence the development of the compensation technique, suppose a single frequency tone is received by a quadrature demodulator. Let this tone be located at a frequency offset of $f_r$ Hz from the LO frequency of the demodulator, at $f_D$ Hz, with starting phase relative to the LO signal of $\theta$ radians. We may write this passband signal at the input of the demodulator, as

$$r_{f_r}(t) = 2A_r \cos[2\pi(f_D + f_r)t + \theta] \tag{4.10}$$

The amplitude and phase will probably be unknown in practical scenarios.

In the frequency domain this signal is written as

$$R_{f_r}(f) = A_r e^{j\theta}\delta(f - f_D - f_r) + A_r e^{-j\theta}\delta(-f + f_D + f_r). \tag{4.11}$$

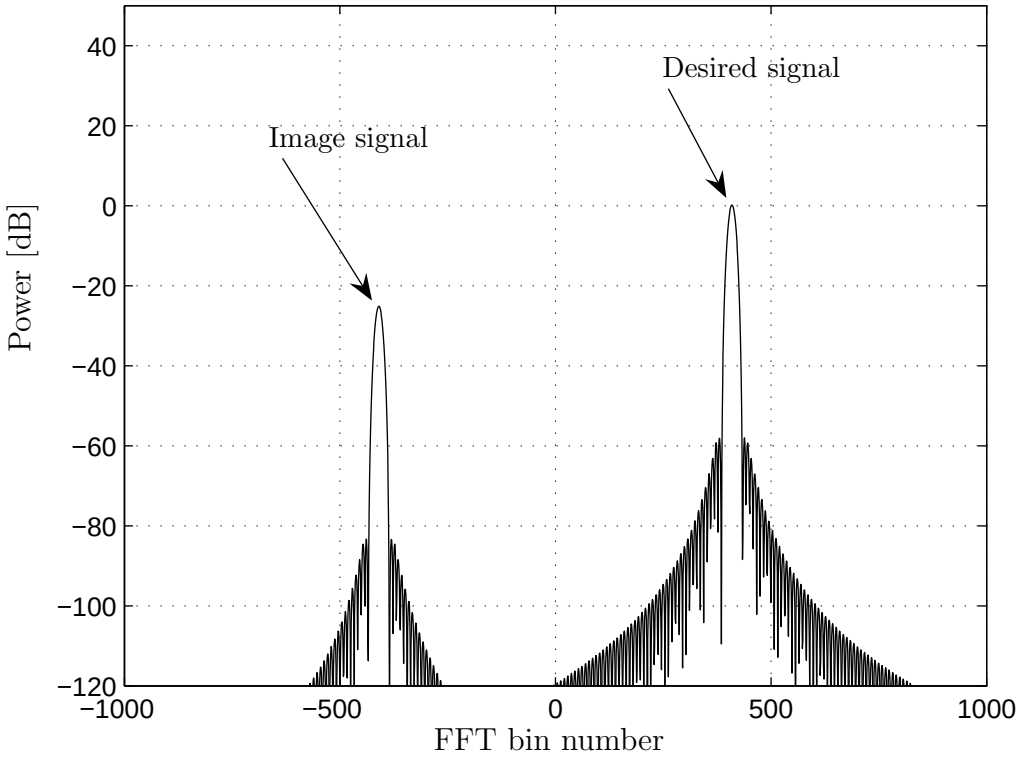


**Figure 4.1:** *An example of the magnitude spectrum a single-sideband tone, mixed down with an imbalanced demodulator, after FFT processing.*

The band-limited baseband equivalent signal in this case is given by

$$\tilde{R}_{f_r}(f) = A_r e^{j\theta}\delta(f - f_r)\,. \tag{4.12}$$

The result of (2.100) on p. 46, can now be used to write the output of the imbalances quadrature demodulator as

$$\begin{aligned} Z'_{f_r}(f) &= \tilde{R}_{f_r}(f)W_1(f) + \tilde{R}^*_{f_r}(-f)W_2(f) \\ &= A_r e^{j\theta}\delta(f - f_r)W_1(f) + A_r e^{-j\theta}\delta(f + f_r)W_2(f) \\ &= \underbrace{A_r e^{j\theta}W_1(f_r)\delta(f - f_r)}_{\text{Desired component}} + \underbrace{A_r e^{-j\theta}W_2(-f_r)\delta(f + f_r)}_{\text{Image component}}\,. \end{aligned} \tag{4.13}$$

The above expression clearly shows how frequency domain representation offers a convenient way to separate the image and desired signal component, since these components exist at different frequencies.

Some form of complex spectral analysis, such as the Fast Fourier Transform (FFT), can therefore be employed in the digital domain of the demodulator, to measure the complex scaling of the desired peak at $f = f_r$ and the image peak at $f = -f_r$. The measurement of

the scaling of the desired signal, for an input signal offset $f_r$ Hz from the LO frequency, is therefore given by

$$O_{d,f_r} = A_r e^{j\theta} W_1(f_r), \tag{4.14}$$

with the measurement of the image signal's scaling, given by

$$O_{i,f_r} = A_r e^{-j\theta} W_2(-f_r). \tag{4.15}$$

Computing the ratio of $O_{i,f_r}$ and the complex conjugate of $O_{d,f_r}$, yields

$$\begin{aligned} \frac{O_{i,f_r}}{O^*_{d,f_r}} &= \frac{A_r e^{-j\theta} W_2(-f_r)}{A_r e^{-j\theta} W_1^*(f_r)} \\ &= \frac{W_2(-f_r)}{W_1^*(f_r)}. \end{aligned} \tag{4.16}$$

By doing this, the above expression shows how the unknown starting phase $\theta$ and amplitude $A_r$ are cancelled. Comparing the above expression with (4.4), it is seen that

$$\frac{O_{i,f_r}}{O^*_{d,f_r}} = P_2(-f_r). \tag{4.17}$$

It is therefore seen that by using a tone at frequency $f = f_D + f_r$ as an input signal to the demodulator, the post-distortion compensation filter's response at frequency $f = -f_r$ can be estimated. Note that if the imbalances of the demodulator could be considered to be independent of frequency (in the narrow band case), this value for $P_2$ can directly be used for compensation directly.

### 4.3.3 Modulator

The imbalance extraction procedure for the modulator is complicated by the fact that a measuring device is required in order to analyse the up-converted signal at the output of the modulator. In this chapter it is proposed that a quadrature demodulator be used for this purpose. The reason for this is that a typical transceiver would contain a quadrature modulator and demodulator pair in the same system, making this a very convenient choice. The approach suggested in this section, is to construct a calibration path which feeds the output of the modulator stage directly into the demodulator. This topology is shown graphically in Fig. 4.2. Of course, this is but one way to realise a measurement device. It should be noted that the extraction techniques can be implemented using any means of measurement, as long as the assumptions under which the techniques were developed, remains true. It does, however, present a challenging scenario, since a quadrature demodulator will most likely contribute its own $I/Q$ imbalances. When a superheterodyne receiver is employed as measurement device, for instance, the same extraction techniques will be applicable, except that there will be no additional demodulator imbalance to complicate matters.

The objective when using an imbalanced quadrature demodulator as measurement device, is therefore to separate the imbalance effect of the demodulator from that of the modulator,

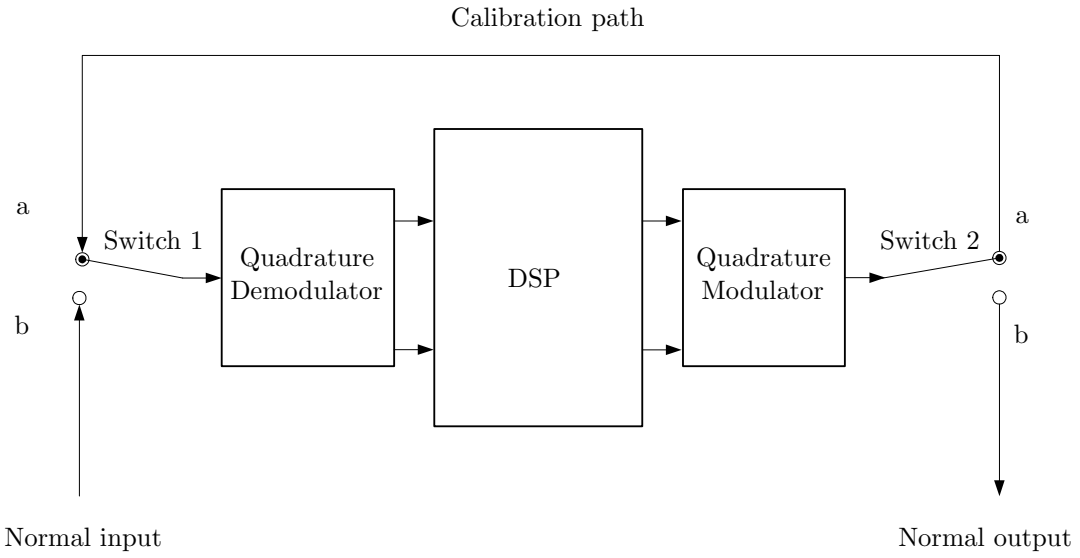


**Figure 4.2:** *Topology for automatic transceiver compensation. The output of the modulator is fed directly into the demodulator through a calibration path. The two switches enable the transceiver to change from normal operation to a calibration mode.*

and to extract the imbalance parameters of both, using only the received signal at the demodulator. This section will explore the conditions under which this is possible and present alternative solutions when it is not.

In this section, three different cases will be investigated:

- **Scenario I:** the modulator and demodulator are synchronised in frequency and in sample timing.
- **Scenario II:** the modulator and demodulator are synchronised in frequency but not in sample timing.
- **Scenario III:** the modulator and demodulator are not synchronised in frequency or in sample timing.

Sample timing synchronisation refers to whether the modulator and demodulator commences its digital sampling process at the same time, or whether there is an unknown delay between the time the modulator starts transmitting its test signal, and the time the demodulator commences its sampling process.

As a first step, a mathematical analysis is presented to describe the cascaded quadrature modulator-demodulator imbalance scenario.

### Baseband equivalent cascaded imbalance model

Recall from (2.45) on p. 30 that the baseband-equivalent output of a quadrature modulator is given by

$$\tilde{U}_{RF}(f) = A(f)V_1(f) + A^*(-f)V_2(f), \tag{4.18}$$

where $A(f)$ represents the frequency response of the complex baseband signal that is to be translated in frequency.

Suppose now that the output of a quadrature modulator is fed directly into a quadrature demodulator, via a calibration feedback path with a (typically unknown) baseband-equivalent frequency response of $\tilde{\Upsilon}(f)$, as illustrated in Fig. 4.2. It will also be assumed that there potentially exists a frequency and phase offset between the LO signals of the quadrature modulator and demodulator. Note that this assumption is applicable to any calibration topology where the modulator output signal is down-converted for baseband analysis (i.e. also for the case where a superheterodyne receiver is employed).

The baseband-equivalent response of the signal that has passed through the feedback loop (i.e. at the input to the demodulator) is given by

$$\tilde{U}_{RF,\Upsilon}(f) = \tilde{U}_{RF}(f)\tilde{\Upsilon}(f). \tag{4.19}$$

Assuming that an imbalanced quadrature demodulator is now employed to downconvert this feedback signal to baseband, its output can be written in the following form:

$$\begin{aligned} Z'(f) &= \tilde{U}_{RF,\Upsilon}(f-\Delta f)e^{j(2\pi\Delta f t_0+\Delta\theta)}W_1(f) \\ &\quad + \tilde{U}^*_{RF,\Upsilon}(-f-\Delta f)e^{-j(2\pi\Delta f t_0+\Delta\theta)}W_2(f), \end{aligned} \tag{4.20}$$

In the above expression $\Delta f$ and $\Delta\theta$ represent, respectively, the relative difference in frequency and phase between the LOs of the quadrature modulator and demodulator. The phase term $2\pi\Delta f t_0$ represents the starting phase at time $t_0$. This term will become significant when the LOs of the modulator and demodulator are not synchronised in frequency, as discussed in Scenario III below.

(4.20) will be used in the subsequent subsections, where three different compensation scenarios involving an imbalanced quadrature modulator fed directly into an imbalanced quadrature demodulator, will be discussed.

### Scenario I: The modulator and demodulator are synchronised in frequency and in sample timing

In systems where the modulator and the demodulator share an LO signal (as is the case in coherent radar systems), or their LOs are locked in frequency, $\Delta f = 0$ in (4.20), and therefore the baseband signal at the output of the demodulator is given by

$$Z'(f) = \tilde{\Upsilon}(f)\tilde{U}_{RF}(f)e^{j\Delta\theta}W_1(f) + \tilde{\Upsilon}^*(-f)\tilde{U}^*_{RF}(-f)e^{-j\Delta\theta}W_2(f). \tag{4.21}$$

Suppose a single-sideband frequency tone at a frequency of $f_m$ Hz is up-converted by the modulator. Let this complex baseband signal to be frequency translated be given by

$$a_{f_m}(t) = \xi_{f_m} e^{j(2\pi f_m t + \theta_{f_m})}, \tag{4.22}$$

or in the frequency domain

$$A_{f_m}(f) = \xi_{f_m} \delta(f - f_m) e^{j\theta_{f_m}}. \tag{4.23}$$

Using (4.18), the baseband-equivalent output of the quadrature modulator in this case becomes

$$\begin{aligned} \tilde{U}_{RF,f_m}(f) &= A_{f_m}(f)V_1(f) + A^*_{f_m}(-f)V_2(f) \\ &= \xi_{f_m} e^{j\theta_{f_m}} V_1(f_m)\delta(f - f_m) + \xi_{f_m} e^{-j\theta_{f_m}} V_2(-f_m)\delta(f + f_m). \end{aligned} \tag{4.24}$$

By substituting this expression into (4.21), the following is obtained at the output of the quadrature demodulator:

$$\begin{aligned} Z'_{f_m}(f) = {} & \xi_{f_m}\delta(f - f_m)e^{j\theta_{f_m}} \left[\tilde{\Upsilon}(f_m)e^{j\Delta\theta}W_1(f_m)V_1(f_m) + \tilde{\Upsilon}^*(-f_m)e^{-j\Delta\theta}W_2(f_m)V_2^*(-f_m)\right] \\ & + \xi_{f_m}\delta(f + f_m)e^{-j\theta_{f_m}} \left[\tilde{\Upsilon}(-f_m)e^{j\Delta\theta}W_1(-f_m)V_2(-f_m) + \tilde{\Upsilon}^*(f_m)e^{-j\Delta\theta}W_2(-f_m)V_1^*(f_m)\right]. \end{aligned} \tag{4.25}$$

In this case it is seen that the undesired image frequency component at $f = -f_m$ is a function of $W_2(f)$, as well as $V_2(f)$, i.e. it depends on the $I/Q$ imbalances of both the modulator and demodulator. This means that in the analysis of the desired and image signal components, the imbalance effect of the quadrature modulator will not be separable from that of the quadrature demodulator. It is possible to compensate for their cascaded imbalance effect, but since this modulator-demodulator pair will typically not be used in this fashion during operation, this will be of little value.

It is therefore seen that, if the LO frequencies of the modulator and demodulator are locked and the quadrature demodulator is to be used as the measuring device, its $I/Q$ imbalances should be compensated for first, during a separate procedure. A practical solution applicable to this scenario, is depicted in Fig. 4.3. It is suggested that a separate, frequency agile, single tone signal is injected directly into demodulator (Switch 1 in position 'b'), performing the imbalance compensation procedure outlined in Section 4.3.2. After the imbalances of the demodulator have been fully compensated for, the modulator can now be fed into the demodulator (Switch 1 position 'a', Switch 2 position 'a'), where the extraction process presented below can then be commenced. Normal operation is resumed by setting Switch 1 to position 'c' and Switch 2 to position 'b'.

The rest of this scenario now assumes that the imbalances of the quadrature demodulator have been compensated for using the procedure outlined above, or that some other form of measuring device (such as a superheterodyne receiver) with an LO frequency that is locked to that of the modulator, is employed. Accordingly, the scaling factor $W_2(f)$ in (4.25) becomes

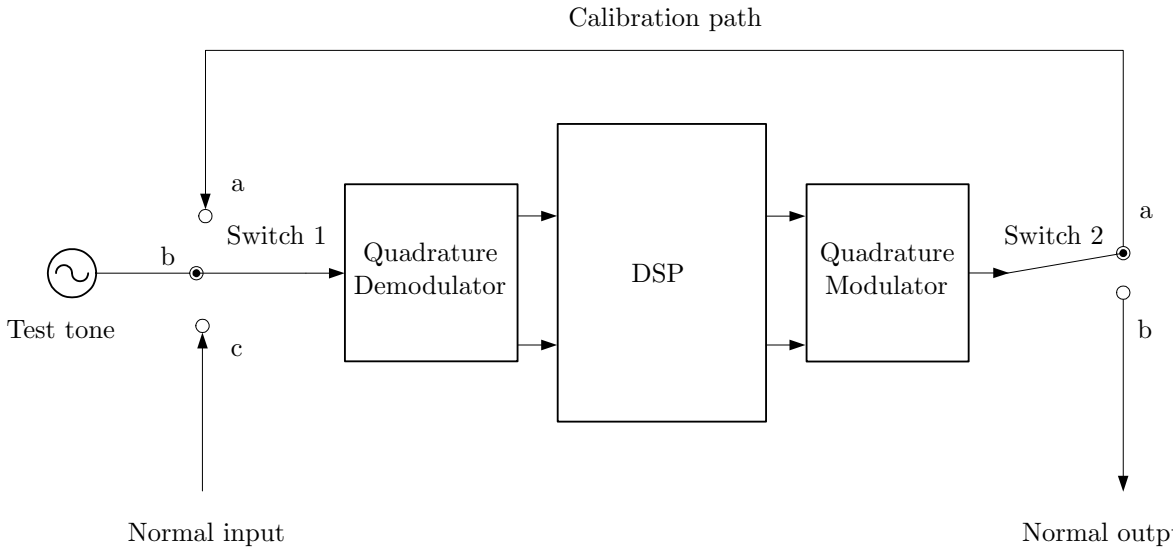


**Figure 4.3:** *A proposed topology for automatic transceiver compensation. With the addition of analogue switches, the output of the modulator can be fed directly into the demodulator.*

zero for all input frequencies. The demodulator will still contribute a frequency response to the the received signal, i.e. $W_1(f)$, however, it can simply be lumped with the unknown response of the feedback path $\tilde{\Upsilon}(f)$. By incorporating these assumptions, the output of the demodulator is now given as

$$\begin{aligned} Z'_{f_m}(f) &= \xi_{f_m}\delta(f-f_m)e^{j(\theta_{f_m}+\Delta\theta)}\tilde{\Upsilon}(f_m)V_1(f_m) \\ &\quad + \xi_{f_m}\delta(f+f_m)e^{-j(\theta_{f_m}-\Delta\theta)}\tilde{\Upsilon}(-f_m)V_2(-f_m). \end{aligned} \tag{4.26}$$

As with the approach followed with the demodulator imbalance extraction, complex spectral analysis may now be employed in the digital domain of the demodulator (e.g. using an FFT) to measure the weighting of the desired and image component. At this stage another factor needs to be included, in order to model any delay that there might exist between the time that the modulator generates the test signal, and the actual time that the demodulator starts their sampling process. If this delay, in seconds, is denoted by $\Delta t$, then the frequency spectrum of the sampled signal, relative to the transmitted signal, contains an additional linear phase shift, or group delay. The spectrum of the demodulator output, as will be observed after sampling with a delayed start, is given as

$$Z'_{f_m,\,\Delta t}(f) = Z'_{f_m}(f)e^{j2\pi f\Delta t}. \tag{4.27}$$

Performing digital spectral analysis to measure the complex scaling of the desired component at $f = f_m$ (i.e. the coefficient of $\delta(f-f_m)$ in (4.26)) yields the first observation

$$O_1 = \xi_{f_m}e^{j(\theta_{f_m}+\Delta\theta)}e^{j2\pi f_m\Delta t}\tilde{\Upsilon}(f_m)V_1(f_m). \tag{4.28}$$

Similarly, the scaling of the image component at $f = -f_m$ can be measured, yielding the second observation,

$$O_2 = \xi_{f_m} e^{-j(\theta_{f_m} - \Delta\theta)} e^{-j2\pi f_m \Delta t} \tilde{\Upsilon}(-f_m) V_2(-f_m). \tag{4.29}$$

Revisiting the expression for the optimal modulator pre-compensation filter, $Q_2(f)$, derived in (4.9), it is seen that $V_1(f)$ and $V_2(f)$ need to be estimated at the same frequency, in order to compute the relevant value of $Q_2(f)$. From the above expressions for $O_1$ and $O_2$, it is seen, however, that this is not the case, since $V_1(f)$ was estimated at $f = f_m$, while $V_2(f)$ was estimated at $f = -f_m$. In order to complete the estimation process, another measurement is required.

Let the modulator now generate another test tone, this time at the negative frequency $f = -f_m$. This complex baseband signal is given as

$$a_{-f_m}(t) = \xi_{-f_m} e^{j(-2\pi f_m t + \theta_{-f_m})}, \tag{4.30}$$

or in the frequency domain

$$A_{-f_m}(f) = \xi_{-f_m} \delta(f + f_m) e^{j\theta_{-f_m}}. \tag{4.31}$$

Feeding the modulator's signal through the calibration path, the output of the compensated quadrature demodulator is given by

$$\begin{aligned} Z'_{-f_m}(f) &= \xi_{-f_m} \delta(f + f_m) e^{j(\theta_{-f_m} + \Delta\theta)} \tilde{\Upsilon}(-f_m) V_1(-f_m) \\ &\quad + \xi_{-f_m} \delta(f - f_m) e^{-j(\theta_{-f_m} - \Delta\theta)} \tilde{\Upsilon}(f_m) V_2(f_m). \end{aligned} \tag{4.32}$$

Recall that $\Delta\theta$ represents the phase offset between the frequency locked LOs of the modulator and demodulator. This phase offset is therefore independent of the transmitted signal and should remain constant over consecutive measurements.

In this scenario, it is also assumed that the sample timing of the receiver can be controlled such that there exists a constant time delay between the time that the samplers of the modulator start transmission and the time that the samplers on the demodulator commence its sampling process. This can be achieved in a system where the modulator and demodulator share a sampling clock and are controlled by the same digital hardware.

Given the assumption of synchronised sample timing between the modulator and demodulator, the digitised spectrum for this second test signal should yield the same linear phase delay as the first signal. This spectrum is

$$Z'_{-f_m,\,\Delta t}(f) = Z'_{-f_m}(f) e^{j2\pi f \Delta t}. \tag{4.33}$$

Two more observations can now be made. Let the third observation be the scaling of the desired component, now located at the frequency $f = -f_m$ :

$$O_3 = \xi_{-f_m} e^{j(\theta_{-f_m} + \Delta\theta)} e^{-j2\pi f_m \Delta t} \tilde{\Upsilon}(-f_m) V_1(-f_m), \tag{4.34}$$

with the fourth observation being the scaling of the image component at $f = f_m$:

$$O_4 = \xi_{-f_m} e^{-j(\theta_{-f_m} - \Delta\theta)} e^{j2\pi f_m \Delta t} \tilde{\Upsilon}(f_m) V_2(f_m). \tag{4.35}$$

$O_3$ is now a function of $V_1(-f_m)$ and $O_4$ a function of $V_2(f_m)$.

By combining these two observations with the observations acquired from the first test signal, the following two ratios can be computed:

$$\begin{aligned}\frac{O_4}{O_1} &= \frac{\xi_{-f_m} e^{-j(\theta_{-f_m}-\Delta\theta)} e^{j2\pi f_m \Delta t}\tilde{\Upsilon}(f_m)V_2(f_m)}{\xi_{f_m} e^{j(\theta_{f_m}+\Delta\theta)} e^{j2\pi f_m \Delta t}\tilde{\Upsilon}(f_m)V_1(f_m)} \\ &= \frac{V_2(f_m)}{V_1(f_m)}\left[\frac{\xi_{-f_m}}{\xi_{f_m}}\ e^{-j(\theta_{-f_m}+\theta_{f_m})}\right], \end{aligned} \tag{4.36}$$

and

$$\begin{aligned}\frac{O_2}{O_3} &= \frac{\xi_{f_m} e^{-j(\theta_{f_m}-\Delta\theta)} e^{-j2\pi f_m \Delta t}\tilde{\Upsilon}(-f_m)V_2(-f_m)}{\xi_{-f_m} e^{j(\theta_{-f_m}+\Delta\theta)} e^{-j2\pi f_m \Delta t}\tilde{\Upsilon}(-f_m)V_1(-f_m)} \\ &= \frac{V_2(-f_m)}{V_1(-f_m)}\left[\frac{\xi_{f_m}}{\xi_{-f_m}}\ e^{-j(\theta_{f_m}+\theta_{-f_m})}\right]. \end{aligned} \tag{4.37}$$

From these two ratios, it can be seen that the required estimation of $V_2(f)/V_1(f)$ can be made if the following criteria are met:

- The amplitudes of the two baseband signals ($\xi_{f_m}$ and $\xi_{-f_m}$) that are generated at the modulator are kept the same.
- The phase offsets of the two baseband signals ($\theta_{f_m}$ and $\theta_{-f_m}$ ) that are generated at the modulator are chosen to be of opposite sign.

These requirements can easily be satisfied, since the amplitude and starting phase of the complex baseband signal can be controlled in the digital domain of the modulator, with high precision. Notice how the phase difference $\Delta\theta$ and the unknown calibration path response $\tilde{\Upsilon}(f)$ are completely cancelled and do not need to be estimated at all. Likewise, the effect of the sample delay $\Delta t$, is also cancelled, if it can be controlled to be constant from one measurement to the next. The third scenario, presented in the next section, deals with the scenario where this cannot be ensured.

When the above criteria are met, the following holds:

$$\begin{aligned}\frac{O_4}{O_1} &= \frac{V_2(f_m)}{V_1(f_m)} \\ &= Q_2(f_m) \end{aligned} \tag{4.38}$$

and

$$\begin{aligned}\frac{O_2}{O_3} &= \frac{V_2(-f_m)}{V_1(-f_m)} \\ &= Q_2(-f_m). \end{aligned} \tag{4.39}$$

Note that although two test signals were required, the estimation of the compensation filter $Q_2(f)$ was also estimated at two frequency points. The number of points at which $Q_2(f)$ is estimated, and the number of test signals required, are therefore still equal.

**Scenario II: The modulator and demodulator are synchronised in frequency but not in sample timing**

In the previous section it was shown that the presence of a delay between the time that the modulator generates the test signal, and the time that the demodulator samples the down-converted signal, does not influence the imbalance extraction method, provided that the delay can be kept constant for both test signals. This section will discuss the scenario where this cannot be ensured, i.e. there does not exist accurate synchronisation between the sampling systems of the modulator and the demodulator modules. Note that if the demodulator employs some form of digital timing synchronisation, the extraction techniques of Scenario II will still be applicable. In this section, however, it will be shown how the imbalance parameters of the modulator can be extracted without employing any form of timing synchronisation. Carrier frequency synchronisation is still assumed between the modulator and demodulator and therefore the assumption is again made that the demodulator imbalances were compensated for before commencing modulator imbalance extraction. In the next section (Scenario III), this restriction will be lifted.

By building on the mathematical development of the previous scenario, but incorporating different sampling delays for each test tone, denoted by $\Delta t_{f_m}$ and $\Delta t_{-f_m}$, the frequency spectrum of the positive frequency test signal is given by

$$Z'_{f_m,\Delta t_{f_m}}(f) = e^{j2\pi f \Delta t_{f_m}} Z'_{f_m}(f) \tag{4.40}$$

and that of the negative frequency test signal by

$$Z'_{-f_m,\Delta t_{-f_m}}(f) = e^{j2\pi f \Delta t_{-f_m}} Z'_{-f_m}(f). \tag{4.41}$$

We now perform the observation process discussed in the previous section for this scenario, and assume that the baseband test signals' amplitudes were chosen to be equal and their phases to be conjugate, as outlined in the previous section. This yields

$$\frac{O_4}{O_1} = \frac{V_2(f_m)}{V_1(f_m)} e^{j2\pi f_m(\Delta t_{-f_m} - \Delta t_{f_m})} \tag{4.42}$$

and

$$\frac{O_2}{O_3} = \frac{V_2(-f_m)}{V_1(-f_m)} e^{j2\pi f_m(\Delta t_{-f_m} - \Delta t_{f_m})}. \tag{4.43}$$

The unknown phase shift $e^{j2\pi f_m(\Delta t_{-f_m} - \Delta t_{f_m})}$ will distort the extracted imbalance parameters and will render them ineffective. Rather than attempting to estimate this unknown phase shift (which is effectively what a timing synchronisation algorithm will achieve), the extraction technique presented here will rely on only using the magnitude of the observations above. The following expressions therefore denote the observations that will be used in this scenario:

$$\left|\frac{O_4}{O_1}\right|^2 = \left|\frac{V_2(f_m)}{V_1(f_m)}\right|^2 \tag{4.44}$$

and

$$\left|\frac{O_2}{O_3}\right|^2 = \left|\frac{V_2(-f_m)}{V_1(-f_m)}\right|^2 . \tag{4.45}$$

Recall from (2.40) that $V_1(f)$ and $V_2(f)$ were defined as

$$V_1(f) = \alpha_I/2E_I(f)\tilde{G}_I(f)e^{j\phi_I} + \alpha_Q/2E_Q(f)\tilde{G}_Q(f)e^{j\phi_Q} \tag{4.46}$$

$$V_2(f) = \alpha_I/2E_I(f)\tilde{G}_I(f)e^{j\phi_I} - \alpha_Q/2E_Q(f)\tilde{G}_Q(f)e^{j\phi_Q} . \tag{4.47}$$

Consider again the gain and phase terms that were defined in (2.48) to (2.51):

$$\eta_I(f) = \alpha_I|E_I(f)||\tilde{G}_I(f)| \tag{4.48}$$

$$\eta_Q(f) = \alpha_Q|E_Q(f)||\tilde{G}_Q(f)| \tag{4.49}$$

$$\psi_I(f) = \angle E_I(f) + \angle\tilde{G}_I(f) + \phi_I \tag{4.50}$$

$$\psi_Q(f) = \angle E_Q(f) + \angle\tilde{G}_Q(f) + \phi_Q . \tag{4.51}$$

The ratio of (4.44) can be rewritten as

$$\begin{aligned}\left|\frac{O_4}{O_1}\right|^2 &= \left|\frac{\eta_I(f_m)e^{j\psi_I(f_m)} - \eta_Q(f_m)e^{j\psi_Q(f_m)}}{\eta_I(f_m)e^{j\psi_I(f_m)} + \eta_Q(f_m)e^{j\psi_Q(f_m)}}\right|^2 \\ &= \frac{\left[\frac{\eta_I(f_m)}{\eta_Q(f_m)}\right]^2 + 1 - 2\left[\frac{\eta_I(f_m)}{\eta_Q(f_m)}\right]\cos\left[\psi_I(f_m) - \psi_Q(f_m)\right]}{\left[\frac{\eta_I(f_m)}{\eta_Q(f_m)}\right]^2 + 1 + 2\left[\frac{\eta_I(f_m)}{\eta_Q(f_m)}\right]\cos\left[\psi_I(f_m) - \psi_Q(f_m)\right]} .\end{aligned} \tag{4.52}$$

By defining the gain imbalance

$$\eta_M(f) = \frac{\eta_{I1}(f_m)}{\eta_{Q1}(f_m)} \tag{4.53}$$

and the phase imbalance

$$\psi_M(f) = \psi_{I1}(f) - \psi_{Q1}(f) \tag{4.54}$$

(4.44) can finally also be rewritten as

$$\left|\frac{O_4}{O_1}\right|^2 = \frac{\eta_M(f_m)^2 + 1 - 2\eta_M(f_m)\cos[\psi_M(f_m)]}{\eta_M(f_m)^2 + 1 + 2\eta_M(f_m)\cos[\psi_M(f_m)]}. \tag{4.55}$$

The relationship between the imbalance parameters $\psi_M(f)$ and $\eta_M(f)$ and the observed power ratio of (4.55), are shown graphically in Fig. 4.4. It shows that there exist an infinite number of combinations of gain imbalance and phase errors which would result in the same power ratio measurement. It is therefore not possible to separate the gain imbalance from phase error from a single measurement of this power ratio. Multiple measurements would also be of no better use, unless it is possible to induce a controlled difference in the observed power ratio from one measurement to the next. This is exactly the approach that will be taken in this section.

To induce a change in the observed power ratio, a scaling value is applied to the $I$ channel's signal in the digital domain of the modulator. If the baseband digital signal in

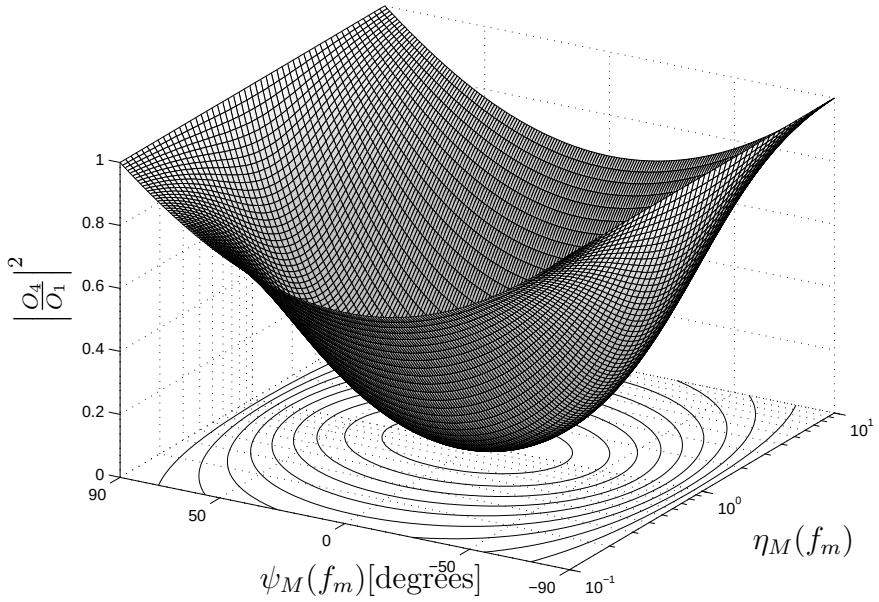


**Figure 4.4:** *The power of the relative sideband as a function of the gain imbalance $\eta_M(f_m)$ and phase error $\psi_M(f_m)$.*

the $I$ channel of the modulator is scaled by $\Delta\eta$ then the observed gain imbalance will also simply be scaled by $\Delta\eta$. By making this adjustment in the digital domain of the modulator, and repeating the two test signals under discussion, the following power ratio measurement will be the result:

$$\left|\frac{O_{4,\Delta}}{O_{1,\Delta}}\right|^2 = \frac{[\Delta\eta\,\eta_M(f_m)]^2 - 2\,\Delta\eta\,\eta_M(f_m)\cos[\psi_M(f_m)] + 1}{[\Delta\eta\,\eta_M(f_m)]^2 + 2\,\Delta\eta\,\eta_M(f_m)\cos[\psi_M(f_m)] + 1}\,. \tag{4.56}$$

Let

$$K_1 = \left|\frac{O_4}{O_1}\right|^2 \tag{4.57}$$

and

$$K_2 = \left|\frac{O_{4,\Delta}}{O_{1,\Delta}}\right|^2. \tag{4.58}$$

There now exist two equations that can be solved to obtain the gain imbalance, $\eta_M(f_m)$, and phase error, $\psi_M(f_m)$. By using the symbolic toolbox of MATLAB, the gain imbalance and cosine of the phase error were found to be:

$$\eta_M(f_m) = \pm\frac{\sqrt{\Delta\eta x\,y}}{\Delta\eta y} \tag{4.59}$$

and

$$\cos[\psi_M(f_m)] = \mp\frac{(\Delta\eta - 1)\,(\Delta\eta + 1)\,(K_2 - 1)\,(K_1 - 1)}{2\sqrt{\Delta\eta x\,y}}\,, \tag{4.60}$$

where

$$x = 1 + K_1 - K_2 - K_2K_1 + \Delta\eta K_1 - \Delta\eta + \Delta\eta K_2K_1 - \Delta\eta K_2 \tag{4.61}$$

$$y = -\Delta\eta - \Delta\eta K_1 + \Delta\eta K_2 + \Delta\eta K_2K_1 + 1 - K_1 + K_2 - K_2K_1. \tag{4.62}$$

By examining the above solutions, some additional knowledge can be employed to eliminate some of the solutions. Since the gain imbalance is by definition positive, the negative solution in (4.59) can be ignored. Furthermore, it may be assumed that the phase error will fall within the range $[-\pi/2, \pi/2]$ rad. This assumption can be made because when the phase error falls outside of these bounds, then negating or swapping the roles of the $I$ and $Q$ channels will ensure that the phase error once again lies within the range $[-\pi/2, \pi/2]$ rad. As such, any negative values of $\cos[\psi_M(f_m)]$ in (4.60) may also be ignored. It is now seen that the extraction process yields the following practical solutions for the $I/Q$ imbalances:

$$\eta_M(f_m) = \left|\frac{\sqrt{\Delta\eta x\, y}}{\Delta\eta y}\right| \tag{4.63}$$

$$\psi_M(f_m) = \pm \arccos\left|\frac{(\Delta\eta - 1)\,(\Delta\eta + 1)\,(K_2 - 1)\,(K_1 - 1)}{2\sqrt{\Delta\eta x\, y}}\right| . \tag{4.64}$$

The correct sign of $\psi_M(f_m)$ is chosen as the sign which achieves the best suppression of the unwanted image component, when used for compensation. Compensation is tested by using $\eta_M(f_m)$ and $\psi_M(f_m)$ to compute the compensation filter value $Q_2(f_m)$ as

$$Q_2(f_m) = \frac{\eta_M(f_m)e^{j\psi_M(f_m)} - 1}{\eta_M(f_m)e^{j\psi_M(f_m)} + 1}. \tag{4.65}$$

and applying it as a scalar compensation value when transmitting a test tone at frequency $f = -f_m$.

Although the choice of $\Delta\eta$ is theoretically arbitrary, it was found during simulation and practical implementation that there do exist choices which perform better in the presence of noise and quantisation than others. It was found that a good choice for $\Delta\eta$ is found when it is assumed that the observed power ratio was caused only by gain imbalance (i.e. that $\psi_M(f_m) = 0$). $\Delta\eta$ is then chosen to compensate for this assumed gain imbalance. Let $\eta_M(f_m)'$ denote the assumed gain imbalance that is responsible for the power ratio $K_1$. According to these assumptions,

$$K_1 = \left(\frac{\eta_M(f_m)' + 1}{\eta_M(f_m)' - 1}\right)^2 \tag{4.66}$$

$$\therefore \eta_M(f_m)' = \frac{1 \pm \sqrt{K_1}}{1 \mp \sqrt{K_1}}\,. \tag{4.67}$$

$\eta_M(f_m)'$ is now arbitrarily chosen such that $\eta_M(f_m)' > 1$. When $\Delta\eta$ is now chosen to compensate for this assumed imbalance, its expression is given by:

$$\begin{aligned}\Delta\eta &= 1/\eta_M(f_m)' \\ &= \frac{1 + \sqrt{K_1}}{1 - \sqrt{K_1}}\,.\end{aligned} \tag{4.68}$$

This is then the value that should be used to induce the change in relative sideband ratio power, by applying it as a scaling value to the $I$ channel's signal at the modulator.

The exact same procedure can be used to extract $\eta_M(-f_m)$ and $\psi_M(-f_m)$ from $|O_2/O_3|^2$ in order to compute $Q_2(-f_m)$.

**Scenario III: The modulator and demodulator are not synchronised infrequency**

In this final scenario, the case will be examined where there exists a frequency difference between the LO signal of the modulator and demodulator. It will be shown that in this case, the imbalances of the modulator and the demodulator can be separated and extracted simultaneously, by examining the received signal in the digital domain of the receiver.

Using (4.20), the output of the demodulator, when receiving the modulator signal directly through a feedback path, can be written as

$$\begin{aligned} Z'(f) &= \tilde{U}_{RF,\Upsilon}(f-\Delta f)e^{j(2\pi\Delta f t_0+\Delta\theta)}W_1(f) \\ &\quad + \tilde{U}^*_{RF,\Upsilon}(-f-\Delta f)e^{-j(2\pi\Delta f t_0+\Delta\theta)}W_2(f)\,. \end{aligned} \tag{4.69}$$

In the above expression, $\Delta f$ and $\theta_\Delta$ represent the relative difference in frequency and phase difference, respectively, between the LOs of the quadrature modulator and demodulator. The phase term $2\pi\Delta f t_0$ represents the arbitrary starting phase at time $t_0$.

Suppose the single frequency test tone is now up-converted by the modulator. Let the complex baseband signal be given by

$$a_{f_m}(t) = \xi_{f_m} e^{j(2\pi f_m t+\theta_{f_m})} \tag{4.70}$$

or in the frequency domain

$$A_{f_m}(f) = \xi_{f_m}\delta(f-f_m)e^{j\theta_{f_m}}\,. \tag{4.71}$$

Using (4.18), the baseband-equivalent output of the quadrature modulator can be written as

$$\begin{aligned} \tilde{U}_{RF,f_m}(f) &= A_{f_m}(f)V_1(f) + A^*_{f_m}(-f)V_2(f) \\ &= \xi_{f_m}e^{j\theta_{f_m}}V_1(f_m)\delta(f-f_m) + \xi_{f_m}e^{-j\theta_{f_m}}V_2(-f_m)\delta(f+f_m). \end{aligned} \tag{4.72}$$

The baseband-equivalent output of the feedback path leading to the demodulator input is given by

$$\begin{aligned} \tilde{U}_{RF,f_m,\Upsilon}(f) &= \tilde{\Upsilon}(f)\tilde{U}_{RF,f_m}(f) \\ &= \xi_{f_m}e^{j\theta_{f_m}}V_1(f_m)\tilde{\Upsilon}(f_m)\delta(f-f_m) \\ &\quad + \xi_{f_m}e^{-j\theta_{f_m}}V_2(-f_m)\tilde{\Upsilon}(-f_m)\delta(f+f_m)\,. \end{aligned} \tag{4.73}$$

Using (4.69) and (4.73), the following is obtained as the output of the quadrature demodulator, when transmitting the positive frequency test tone:

$$\begin{aligned} Z'_{f_m}(f) &= \underbrace{\xi_{f_m} e^{j\theta_{f_m}} e^{j(2\pi\Delta f t_1+\Delta\theta)} V_1(f_m)\tilde{\Upsilon}(f_m) W_1(\Delta f + f_m)\delta(f-\Delta f - f_m)}_{\text{Desired component } \textit{[term 1]}} \\ &\quad + \underbrace{\xi_{f_m} e^{-j\theta_{f_m}} e^{j(2\pi\Delta f t_1+\Delta\theta)} V_2(-f_m)\tilde{\Upsilon}(-f_m) W_1(\Delta f - f_m)\delta(f-\Delta f + f_m)}_{\text{Image due to modulator imbalances } \textit{[term 2]}} \\ &\quad + \underbrace{\xi_{f_m} e^{-j\theta_{f_m}} e^{-(2\pi\Delta f t_1+\Delta\theta)} V_1^*(f_m)\tilde{\Upsilon}^*(f_m) W_2(-\Delta f - f_m)\delta(-f-\Delta f - f_m)}_{\text{Image due to demodulator imbalances } \textit{[term 3]}} \\ &\quad + \underbrace{\xi_{f_m} e^{j\theta_{f_m}} e^{-j(2\pi\Delta f t_1+\Delta\theta)} V_2^*(-f_m)\tilde{\Upsilon}^*(-f_m) W_2(-\Delta f + f_m)\delta(-f-\Delta f + f_m)}_{\text{Image due to demodulator imbalances } \textit{[term 4]}} \end{aligned} \tag{4.74}$$

In the above expression $t_1$ denotes the time instant when the modulator commenced transmission of the tone. The observations that can be made at this point, will be highlighted below under '*Modulator imbalance extraction*'. What is important to note at this stage, is that, due to the frequency difference between the LOs of the modulator and demodulator, the original single-sideband test signal is now split into four components at the output of the demodulator, each at a different frequency. Some of the components are due to the imbalances of the modulator, and some due to those of the demodulator. Importantly, these contributions are now separated in frequency, therefore providing the basis for separating the effects of the modulator and demodulator imbalances, through only analysing the demodulated signal. This effect is illustrated graphically in Fig. 4.5 by means of an example.

As with the Scenario II, another test tone with a negative baseband frequency will employed in order to sample $V_1(-f_m)$ and $V_2(f_m)$. Let this complex baseband signal be given by

$$a_{-f_m}(t) = \xi_{-f_m} e^{j(-2\pi f_m t+\theta_{-f_m})} \tag{4.75}$$

or in the frequency domain

$$A_{-f_m}(f) = \xi_{-f_m}\delta(f+f_m)e^{j\theta_{-f_m}}. \tag{4.76}$$

Using (4.18), the baseband-equivalent output of the quadrature modulator is written as

$$\begin{aligned} \tilde{U}_{RF,-f_m}(f) &= A_{-f_m}(f)V_1(f) + A^*_{-f_m}(-f)V_2(f) \\ &= \xi_{-f_m} e^{j\theta_{-f_m}} V_1(-f_m)\delta(f+f_m) \\ &\quad + \xi_{-f_m} e^{-j\theta_{-f_m}} V_2(f_m)\delta(f-f_m)\,. \end{aligned} \tag{4.77}$$

The baseband-equivalent output of the feedback path leading to the demodulator input is given by

$$\begin{aligned} \tilde{U}_{RF,-f_m,\Upsilon}(f) &= \tilde{\Upsilon}(f)\tilde{U}_{RF,-f_m}(f) \\ &= \xi_{-f_m} e^{j\theta_{-f_m}} V_1(-f_m)\tilde{\Upsilon}(-f_m)\delta(f+f_m) \\ &\quad + \xi_{-f_m} e^{-j\theta_{-f_m}} V_2(f_m)\tilde{\Upsilon}(f_m)\delta(f-f_m)\,. \end{aligned} \tag{4.78}$$

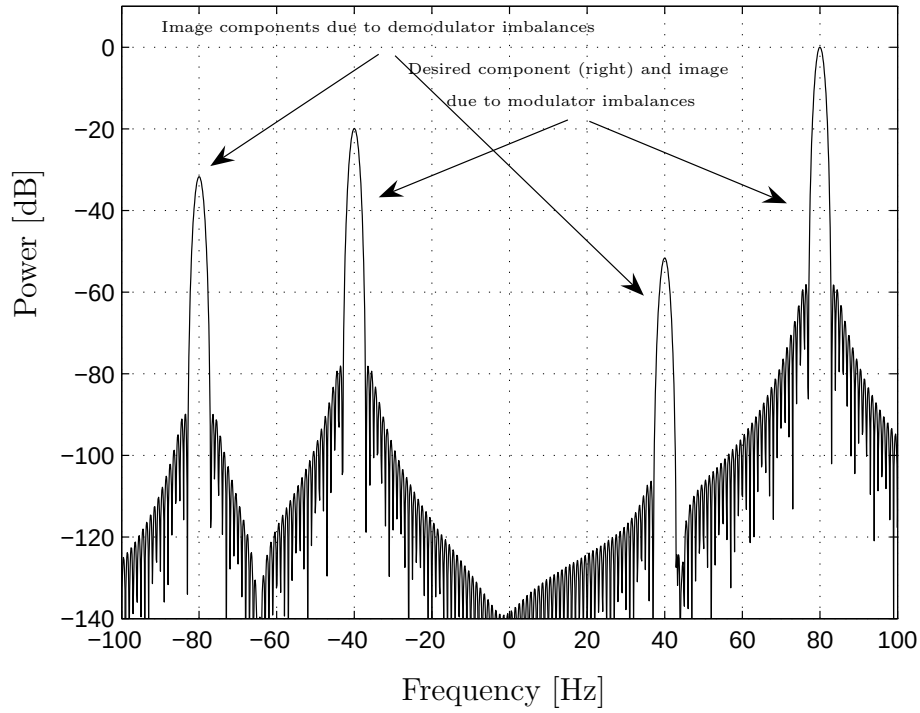


**Figure 4.5:** *Suppose a quadrature modulator generates a single (upper) sideband tone at 60 Hz and mixes it up it to a carrier frequency* $f_{\text{mod}}$*. Due to the imbalances in the modulator's front end, the positive frequency spectrum does not only contain a impulse at* $f_{\text{mod}} + 60$ *Hz, but also the image at* $f_{\text{mod}} - 60$ *Hz. This signal is subsequently down-converted by an imbalanced demodulator with LO frequency* $f_{\text{demod}}$ *at* 20 *Hz lower than that of the modulator's LO, therefore* $f_{\text{demod}} = f_{\text{mod}} - 20$ *Hz. The resultant power spectrum of the complex baseband signal at the output of the demodulator is shown in this figure. The desired signal component is located at* $60 + 20 = 80$ *Hz, with its image due to modulator imbalance, still* 120 *Hz below it at* $-40$ *Hz. As these two components (desired and image) pass through the imbalanced demodulator, each generates an image signal around* 0 *Hz. The image components at* $-80$ *Hz and* 40 *Hz, are therefore due to demodulator imbalances. For additional clarity in the sample spectrum, the modulator's image rejection capability was set to be* 20 *dB while the demodulator's was just over* 30 *dB.*

Using (4.69) and (4.78), the following is obtained as the output of the quadrature de-

modulator

$$
\begin{aligned}
Z'_{-f_m}(f) \;=\; & \underbrace{\xi_{-f_m} e^{j\theta_{-f_m}} e^{j(2\pi\Delta f t_2+\Delta\theta)} V_1(-f_m)\tilde{\Upsilon}(-f_m) W_1(\Delta f - f_m)\delta(f-\Delta f+f_m)}_{\text{Desired component } \textit{[term 1]}} \\
& + \underbrace{\xi_{-f_m} e^{-j\theta_{-f_m}} e^{j(2\pi\Delta f t_2+\Delta\theta)} V_2(f_m)\tilde{\Upsilon}(f_m) W_1(\Delta f + f_m)\delta(f-\Delta f-f_m)}_{\text{Image due to modulator imbalances } \textit{[term 2]}} \\
& + \underbrace{\xi_{-f_m} e^{-j\theta_{-f_m}} e^{-j(2\pi\Delta f t_2+\Delta\theta)} V_1^*(-f_m)\tilde{\Upsilon}^*(-f_m) W_2(-\Delta f + f_m)\delta(-f-\Delta f+f_m)}_{\text{Image due to demodulator imbalances } \textit{[term 3]}} \\
& + \underbrace{\xi_{-f_m} e^{j\theta_{-f_m}} e^{-j(2\pi\Delta f t_2+\Delta\theta)} V_2^*(f_m)\tilde{\Upsilon}^*(f_m) W_2(-\Delta f - f_m)\delta(-f-\Delta f-f_m)}_{\text{Image due to demodulator imbalances } \textit{[term 4]}}
\end{aligned}
\tag{4.79}
$$

where $t_2$ denotes the time instant when the modulator commenced transmission of the second tone.

It will now be shown how the effects of the imbalanced modulator and demodulator can be separated, and the imbalances of both can be extracted through spectral analysis of the above two test signals.

*Modulator imbalance extraction*

Spectral analysis in the digital domain of the receiver can now be used to make the following observations. Once again, a time delay will be assumed between the sampling systems of the modulator and the demodulator. Let a time delay of $\Delta t_{f_m}$ be applicable during transmission of the positive frequency test tone, and $\Delta t_{-f_m}$ during the transmission of the negative frequency tone.

Observation 1 will be the scaling of the desired component (term 1) from $Z'_{f_m}(f)$, measured at frequency $f = \Delta f + f_m$, therefore

$$O_{M1} = \xi_{f_m} e^{j\theta_{f_m}} e^{j(2\pi\Delta f t_1+\Delta\theta)} e^{j2\pi(\Delta f+f_m)\Delta t_{f_m}} V_1(f_m)\tilde{\Upsilon}(f_m) W_1(\Delta f + f_m). \tag{4.80}$$

Observation 2 will be the scaling of the image component due to the modulator imbalances (term 2) from $Z'_{f_m}(f)$, measured at frequency $f = \Delta f - f_m$, therefore

$$O_{M2} = \xi_{f_m} e^{-j\theta_{f_m}} e^{j(2\pi\Delta f t_1+\Delta\theta)} e^{j2\pi(\Delta f-f_m)\Delta t_{f_m}} V_2(-f_m)\tilde{\Upsilon}(-f_m) W_1(\Delta f - f_m). \tag{4.81}$$

Observation 3 will be the scaling of the desired component (term 1) from $Z'_{-f_m}(f)$, measured at frequency $f = \Delta f - f_m$, therefore

$$O_{M3} = \xi_{-f_m} e^{j\theta_{-f_m}} e^{j(2\pi\Delta f t_2+\Delta\theta)} e^{j2\pi(\Delta f-f_m)\Delta t_{-f_m}} V_1(-f_m)\tilde{\Upsilon}(-f_m) W_1(\Delta f - f_m). \tag{4.82}$$

Observation 4 will be the scaling of the image component due to the modulator imbalances (term 2) from $Z'_{-f_m}(f)$, measured at frequency $f = \Delta f + f_m$, therefore

$$O_{M4} = \xi_{-f_m} e^{-j\theta_{-f_m}} e^{j(2\pi\Delta f t_2+\Delta\theta)} e^{j2\pi(\Delta f+f_m)\Delta t_{-f_m}} V_2(f_m)\tilde{\Upsilon}(f_m) W_1(\Delta f + f_m). \tag{4.83}$$

The ratios outlined in the previous sections should now once again be computed. If it is assumed that the amplitudes of the two test tones were chosen to be identical ($\xi_{f_m} = \xi_{-f_m}$), and their phases chosen to be conjugate ($\theta_{f_m} = -\theta_{-f_m}$), then these ratios are given by

$$\begin{aligned}\frac{O_{M4}}{O_{M1}} &= \frac{V_2(f_m)}{V_1(f_m)} e^{j2\pi\Delta f(t_2-t_1)} e^{j2\pi(\Delta f+f_m)(\Delta t_{-f_m}-\Delta t_{f_m})} \\ &= \frac{V_2(f_m)}{V_1(f_m)} e^{j\varsigma_1} \end{aligned} \tag{4.84}$$

and

$$\begin{aligned}\frac{O_{M2}}{O_{M3}} &= \frac{V_2(-f_m)}{V_1(-f_m)} e^{-j2\pi\Delta f(t_2-t_1)} e^{j2\pi(\Delta f-f_m)(\Delta t_{f_m}-\Delta t_{-f_m})} \\ &= \frac{V_2(-f_m)}{V_1(-f_m)} e^{j\varsigma_2}. \end{aligned} \tag{4.85}$$

These expressions have exactly the same form as the ratios presented in (4.42) and (4.43), discussed in Scenario II. The effects of demodulator quadrature imbalances are perfectly cancelled. It is therefore not required to perform demodulator compensation before modulator imbalance extraction is commenced. However, note that the desired complex ratio between $V_2$ and $V_1$ is distorted by (generally) unknown phase rotations, $\varsigma_1$ and $\varsigma_2$. The frequency difference therefore introduced the same distortion as the lack of sample timing synchronisation, presented in Scenario II. If at this stage some phase recovery is implemented to remove the effect of $\varsigma_1$ and $\varsigma_2$, then the imbalance extraction techniques of scenario I are applicable. If such a phase synchronisation procedure is not performed, then the extraction techniques of Scenario II can be readily applied.

*Demodulator imbalance extraction*

$Z'_{f_m}(f)$ and $Z'_{-f_m}(f)$ can also be used to extract the imbalances of the demodulator in the presence of modulator imbalances. In order to achieve this, the following observations can be formed using spectral analysis in the digital domain of the receiver (once again including the sample time delays $\Delta t_{f_m}$ and $\Delta t_{-f_m}$):

Observation 1 will be the scaling of the desired component (term 1) from $Z'_{f_m}$, measured at a frequency of $f = \Delta f + f_m$:

$$O_{D1} = \xi_{f_m} e^{j\theta_{f_m}} e^{j(2\pi\Delta f t_1+\Delta\theta)} e^{j2\pi(\Delta f+f_m)\Delta t_{f_m}} V_1(f_m)\tilde{\Upsilon}(f_m)W_1(\Delta f + f_m). \tag{4.86}$$

Observation 2 will be the scaling of the image component due to demodulator imbalances (term 3) from $Z'_{f_m}$, measured at a frequency of $f = -\Delta f - f_m$:

$$O_{D2} = \xi_{f_m} e^{-j\theta_{f_m}} e^{-j(2\pi\Delta f t_1+\Delta\theta)} e^{j2\pi(-\Delta f-f_m)\Delta t_{f_m}} V_1^*(f_m)\tilde{\Upsilon}^*(f_m)W_2(-\Delta f - f_m). \tag{4.87}$$

Observation 3 will be the scaling of the desired component (term 1) from $Z'_{-f_m}$, measured at a frequency of $f = \Delta f - f_m$:

$$O_{D3} = \xi_{-f_m} e^{j\theta_{-f_m}} e^{j(2\pi\Delta f t_2+\Delta\theta)} e^{j2\pi(\Delta f-f_m)\Delta t_{-f_m}} V_1(-f_m)\tilde{\Upsilon}(-f_m)W_1(\Delta f - f_m). \tag{4.88}$$

Observation 4 will be the scaling of the image component due to demodulator imbalances (term 3) from $Z'_{-f_m}$, measured at a frequency of $f = -\Delta f + f_m$:

$$O_{D4} = \xi_{-f_m} e^{-j\theta_{-f_m}} e^{-j(2\pi\Delta f t_2 + \Delta\theta)} e^{j2\pi(-\Delta f + f_m)\Delta t_{-f_m}} V_1^*(-f_m)\tilde{\Upsilon}^*(-f_m)W_2(-\Delta f + f_m). \tag{4.89}$$

If it is assumed that the amplitudes of the two test tones were chosen to be identical ($\xi_{f_m} = \xi_{-f_m}$), and their phases chosen to be conjugate ($\theta_{f_m} = -\theta_{-f_m}$), then the desired demodulator compensation filter response can then be estimated from the following ratios:

$$\begin{aligned} \frac{O_{D2}}{O_{D1}^*} &= \frac{W_2[-(\Delta f + f_m)]}{W_1^*[\Delta f + f_m]} \\ &= P_2[-(\Delta f + f_m)] \end{aligned} \tag{4.90}$$

end

$$\begin{aligned} \frac{O_{D4}}{O_{D3}^*} &= \frac{W_2[-(\Delta f - f_m)]}{W_1^*[\Delta f - f_m]} \\ &= P_2[-(\Delta f - f_m)]\,. \end{aligned} \tag{4.91}$$

Unlike the extraction of the modulator imbalances, it is noted that the sample time delay, as well as the phase difference due to the frequency difference, completely cancels during demodulator extraction. Demodulator imbalance extraction can therefore be achieved regardless of whether any form of phase or timing synchronisation is performed or not. It should also be noted that the demodulator extraction process actually only requires one test signal in order to calculate response of the compensation filter at a particular frequency – note that $O_{D2}$ and $O_{D1}$ are both observations resulting from $Z'_{f_m}(f)$ and similarly $O_{D4}$ and $O_{D3}$ are both observations resulting from $Z'_{-f_m}(f)$.

## 4.4 Translating the estimated $I/Q$ imbalances to a frequency-dependent compensation solution

Up to this point, the theoretical frequency response of the optimal imbalance compensation filters for both the quadrature modulator and demodulator have been derived (Section 4.2). Furthermore, Section 4.3 presented three novel techniques for extracting the imbalance parameters of the compensation functions. The extraction techniques of Section 4.3 would yield a discretely sampled version of the frequency response of the desired compensation filter, at each frequency where the test signals were employed. This section provides the final step in the process, which is to translate the discretely sampled desired frequency responses of the compensation filters, to filter coefficients which can be practically implemented in the digital domains of the modulator and demodulator. In this way, frequency-dependent imbalance compensation is achieved during normal operation, by pre-filtering the baseband signal with the realised digital compensation filter in the modulator, or, in the case of the demodulator, filtering the received digital signal with the realised compensation filter.

This section will describe the characteristics of the compensation filter, present a design approach for its realisation and comment on its implementation.

### 4.4.1 Compensation filter characteristics

**Standard case: Imbalance contributions from the mixer, LPFs and BPFs**

The desired filter frequency responses for the modulator and demodulator compensation filters, are represented by $Q_2(f)$ and $P_2(f)$, respectively and was defined in Section 4.2 on p. 77. Let us now consider these functions more closely, starting with $Q_2(f)$.

In (4.9) $Q_2(f)$ was defined as

$$Q_2(f) = \frac{V_2(f)}{V_1(f)}\,. \tag{4.92}$$

Recall also the definitions of magnitude and phase functions in (2.48) to (2.51) on p. 31:

$$\eta_I(f) = \alpha_I|E_I(f)||\tilde{G}_I(f)| \tag{4.93}$$
$$\eta_Q(f) = \alpha_Q|E_Q(f)||\tilde{G}_Q(f)| \tag{4.94}$$
$$\psi_I(f) = \angle E_I(f) + \angle\tilde{G}_I(f) + \phi_I \tag{4.95}$$
$$\psi_Q(f) = \angle E_Q(f) + \angle\tilde{G}_Q(f) + \phi_Q \tag{4.96}$$

where the gain and phase imbalance of the modulator is then given by

$$\eta_M(f) = \eta_I(f)/\eta_Q(f) \tag{4.97}$$

and

$$\psi_M(f) = \psi_I(f) - \psi_Q(f)\,, \tag{4.98}$$

respectively. Since $V_2(f)$ and $V_1(f)$ was defined in (2.40) on p. 29 as

$$V_1(f) = \alpha_I/2E_I(f)\tilde{G}_I(f)e^{j\phi_I} + \alpha_Q/2E_Q(f)\tilde{G}_Q(f)e^{j\phi_Q} \tag{4.99}$$
$$V_2(f) = \alpha_I/2E_I(f)\tilde{G}_I(f)e^{j\phi_I} - \alpha_Q/2E_Q(f)\tilde{G}_Q(f)e^{j\phi_Q}\,, \tag{4.100}$$

$Q_2(f)$ can be rewritten as

$$Q_2(f) = \frac{\eta_M(f)e^{j\psi_M(f)} - 1}{\eta_M(f)e^{j\psi_M(f)} + 1}\,. \tag{4.101}$$

The goal now is to determine whether the desired frequency response, $Q_2(f)$, would require the compensation filter to have a real-valued or complex-valued transfer function, when realised. For a real-valued transfer function, the frequency response of the filter should exhibit Hermitian symmetry. This mean that its phase response should be an odd function of frequency and its magnitude response should be an even function of frequency.

Let the phase response of $Q_2(f)$ be considered first. The phase response of $Q_2(f)$ is given by

$$\begin{aligned}\angle Q_2(f) &= \arctan\left[\frac{\eta_M(f)\sin[\psi_M(f)]}{\eta_M(f)\cos[\psi_M(f)]-1}\right] \\ &\quad -\arctan\left[\frac{\eta_M(f)\sin[\psi_M(f)]}{\eta_M(f)\cos[\psi_M(f)]+1}\right].\end{aligned} \tag{4.102}$$

For this phase function to be an odd function, $\angle Q_2(-f) = -\angle Q_2(f)$ must hold, i.e.

$$\begin{aligned}&\arctan\left[\frac{\eta_M(-f)\sin[\psi_M(-f)]}{\eta_M(-f)\cos[\psi_M(-f)]-1}\right] - \arctan\left[\frac{\eta_M(-f)\sin[\psi_M(-f)]}{\eta_M(-f)\cos[\psi_M(-f)]+1}\right] \\ &= -\arctan\left[\frac{\eta_M(f)\sin[\psi_M(f)]}{\eta_M(f)\cos[\psi_M(f)]-1}\right] + \arctan\left[\frac{\eta_M(f)\sin[\psi_M(f)]}{\eta_M(f)\cos[\psi_M(f)]+1}\right]\end{aligned} \tag{4.103}$$

Since $\arctan(\cdot)$ is an odd function itself, the above condition is only satisfied when $\eta_M(f)$ is an even function of frequency and $\psi_M(f)$ is an odd function of frequency.

The power response of $Q_2(f)$ is given by

$$|Q_2(f)|^2 = \frac{[\eta_M(f)]^2 + 1 - 2\eta_M(f)\cos[\psi_M(f)]}{[\eta_M(f)]^2 + 1 + 2\eta_M(f)\cos[\psi_M(f)]}. \tag{4.104}$$

For $|Q_2(f)|^2$ to be an even function of frequency, the following should be satisfied: $|Q_2(-f)|^2 = |Q_2(f)|^2$ or equivalently

$$\frac{[\eta_M(-f)]^2 + 1 - 2\eta_M(-f)\cos[\psi_M(-f)]}{[\eta_M(-f)]^2 + 1 + 2\eta_M(-f)\cos[\psi_M(-f)]} = \frac{[\eta_M(f)]^2 + 1 - 2\eta_M(f)\cos[\psi_M(f)]}{[\eta_M(f)]^2 + 1 + 2\eta_M(f)\cos[\psi_M(f)]}. \tag{4.105}$$

This requirement will only be satisfied if $\eta_M(f)$ is even function of frequency and $\psi_M(f)$ is either an even or and odd function of frequency.

Combining the requirements of (4.103) and (4.105), it follows that, in order for $Q_2(f)$ to exhibit Hermitian symmetry, the gain imbalance function $\eta_M(f)$ should be an even function of frequency and the phase imbalance function $\psi_M(f)$ should be an odd function of frequency, i.e. $\eta_M(f)e^{j\psi_M(f)}$ should exhibit Hermitian symmetry.

From the expression for $\psi_M(f)$, it can be seen that it is dependent on the phase responses of the LPFs, $\angle E_I(f)$ and $\angle E_Q(f)$, the baseband-equivalent phase responses of the BPFs, $\angle\tilde{G}_I(f)$ and $\angle\tilde{G}_Q(f)$ and the phase imbalance of the mixer, $\phi_I$ and $\phi_Q$. In practice, only $\angle E_I(f)$ and $\angle E_Q(f)$ will be odd functions of frequency, since they stem from real-valued filters. $\angle\tilde{G}_I(f)$ and $\angle\tilde{G}_Q(f)$ represent the one-sided passband phase responses of the BPF and will generally not be an odd function of frequency. Even when the contribution of these responses are ignored, the presence of phase imbalance in the mixer (i.e. $\phi_I - \phi_Q \neq 0$), will result in $\psi_M(f)$ not being an odd function.

$\eta_M(f)$ is a function of the magnitude responses of the LPFs, the baseband-equivalent magnitude response of the BPFs and the mixer imbalances. The responses of the LPFs will necessarily be even functions of frequency, since they directly represent the magnitude response of real filters. Since the gain imbalance of the mixer is considered to be constant with

frequency (see Section 2.5, p. 23), it too will be an even function of frequency. The baseband-equivalent magnitude responses of the BPFs, $|\tilde{G}_I(f)|$ and $|\tilde{G}_Q(f)|$, are not restricted to be even functions and will in practice generally not result in such.

From this discussion it is clear that $Q_2(f)$, in general, will not exhibit Hermitian symmetry in practice, due to the contribution of the imbalances between the BPFs and the phases of the LO signals in the mixer. It should be stressed that, even when the BPFs are not included in the imbalance analysis (as is often done in literature), $Q_2(f)$ will still not exhibit Hermitian symmetry, due to the mixer phase imbalance $\phi_I - \phi_Q$, which will not exhibit odd symmetry. The compensation filter will therefore be required to have a complex-valued transfer function.

For the case of the demodulator, the compensation response $P_2(f)$ was given in (4.4) as

$$P_2(f) = \frac{W_2(f)}{W_1^*(-f)}\,. \tag{4.106}$$

From (2.103) and (2.104) on p. 46, $W_1^*(-f)$ and $W_2(f)$ are given by

$$W_1^*(-f) = \frac{1}{2}\left[\beta_I e^{j\varphi_I} H_I(f)\tilde{L}_I^*(-f) + \beta_Q e^{j\varphi_Q} H_Q(f)\tilde{L}_Q^*(-f)\right] \tag{4.107}$$

$$W_2(f) = \frac{1}{2}\left[\beta_I e^{j\varphi_I} H_I(f)\tilde{L}_I^*(-f) - \beta_Q e^{j\varphi_Q} H_Q(f)\tilde{L}_Q^*(-f)\right]\,, \tag{4.108}$$

where the identities $H_I^*(-f) = H_I(f)$ and $H_Q^*(-f) = H_Q(f)$ were exploited.

Considering again the definitions of (2.115) to (2.118):

$$\kappa_I(f) = \beta_I |H_I(f)||\tilde{L}_I(f)| \tag{4.109}$$

$$\kappa_Q(f) = \beta_Q |H_Q(f)||\tilde{L}_Q(f)| \tag{4.110}$$

$$\chi_I(f) = \varphi_I - \angle H_I(f) - \angle \tilde{L}_I(f) \tag{4.111}$$

$$\chi_Q(f) = \varphi_Q - \angle H_Q(f) - \angle \tilde{L}_Q(f)\,. \tag{4.112}$$

$P_2(f)$ can be written in terms of the gain and phase imbalances:

$$\begin{aligned} \kappa_D(f) &= \kappa_I(f)/\kappa_Q(f) \\ \chi_D(f) &= \chi_I(f) - \chi_Q(f) \end{aligned} \tag{4.113}$$

as (after algebraic simplification)

$$P_2(f) = \frac{\kappa_D(-f)e^{j\chi_D(-f)} - 1}{\kappa_D(-f)e^{j\chi_D(-f)} + 1}\,. \tag{4.114}$$

Identical reasoning as was followed for the case of the modulator, is also applicable to the above expression, from which it can be concluded that $P_2(f)$ will not exhibit Hermitian symmetry in practice, due to the contribution of the imbalances between the BPFs and the phases of the LO signals in the mixer. The compensation filter derived from $P_2(f)$ will therefore also require a complex-valued transfer function.

The practical implementation of a digital filter with a complex transfer function, requires four filtering operations. The first step is to divide the complex transfer function into two

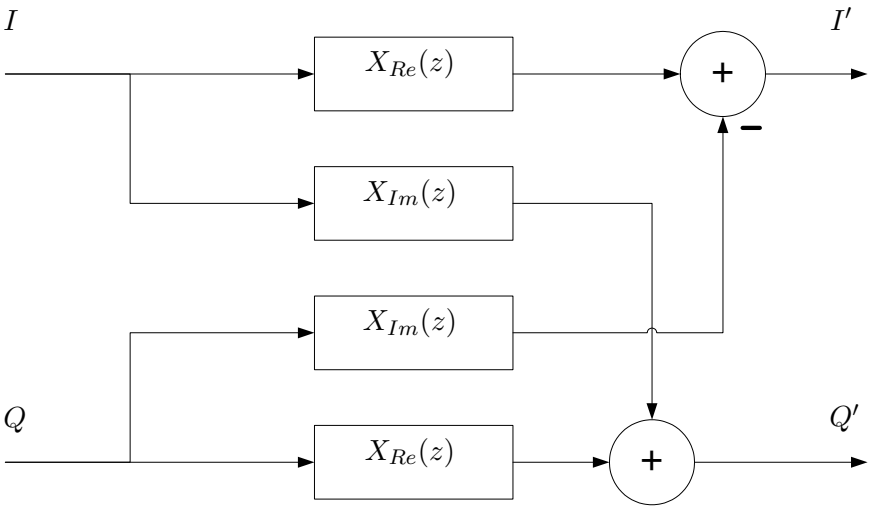


**Figure 4.6:** *Implementation of a complex-valued filter. Adapted from [35].*

filters, representing the real and imaginary parts of the transfer function. Taking a complex transfer function $X(z)$ as an example, the real and imaginary filter transfer functions are computed as [35]:

$$X_{Re}(z) = \frac{X(z) + X^*(z)}{2} \tag{4.115}$$

and

$$X_{Im}(z) = \frac{X(z) - X^*(z)}{2j}\,, \tag{4.116}$$

respectively. The implementation of the complex filter is then shown in Fig. 4.6, where $I$ and $Q$ represent the real and imaginary components of a complex signal.

If $X(z)$ now denotes either the modulator or demodulator imbalance compensation filter, the realisation of the compensation approaches derived in (4.2) and (4.6) in Section 4.2, is shown in Fig. 4.7. Recall that the compensation procedure involved subtracting the filtered complex conjugate of the original signal, from the original signal. The $I$ and $Q$ signal paths represent the real and imaginary parts of the complex signal in the digital domain of either the modulator or demodulator. Note that the time delay of $t_x$ samples in the direct feedthrough path of the $I$ and $Q$ signals (the original signal components), are required in order to account for the group delay of the compensation filters. The value of $t_x$ is computed from the designed filter as

$$t_x = \text{round}[K/2 - 1] \tag{4.117}$$

where $K$ denotes the number of taps in the filter.

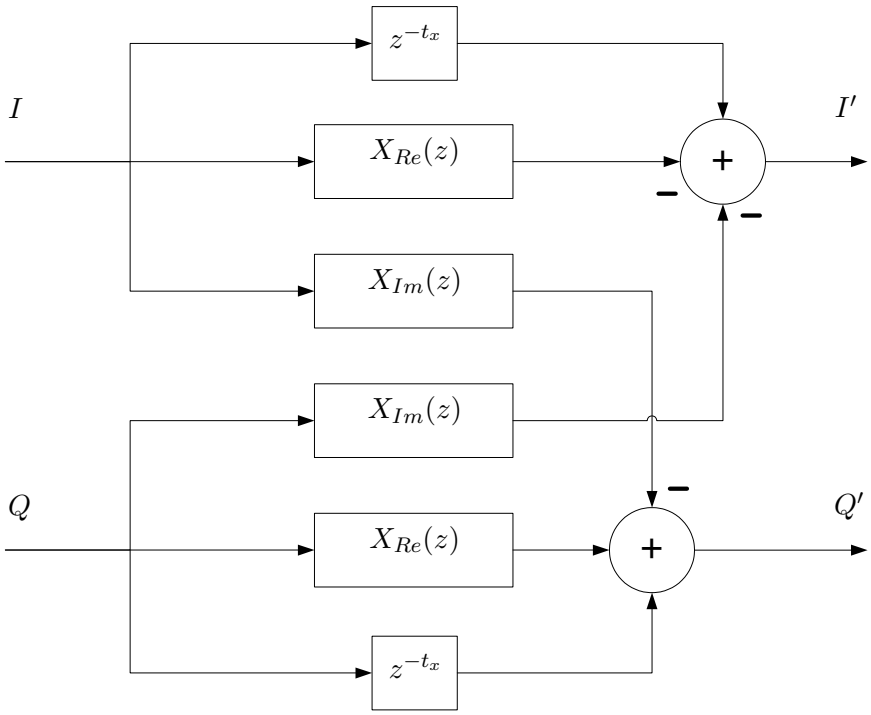


**Figure 4.7:** *Realisation of imbalance compensation using a complex compensation filter.*

### Special case: Imbalance contribution from BPFs are negligible

In the special case where the contribution of the BPF responses are truly negligible, imbalance compensation can be performed using a filter with a real valued transfer function in either the $I$ or $Q$ signals paths to equalise the responses of the two LPFs, and a separate phase-compensator to correct the frequency-independent phase imbalance of the quadrature mixer. The frequency-independent gain imbalance of the mixers are lumped with the gain imbalances of the LPFs, since it will not affect the even-symmetry of the resulting compensation filter's magnitude response.

In this approach, the frequency-independent phase imbalance contributions of the mixers need to be isolated from the estimated phase imbalance functions of the modulator and demodulator. The mixers' phase imbalance of the modulator and demodulator will be equal to the value of the phase imbalance functions $\psi_M(f)$ and $\varphi_D(f)$ at 0 Hz. This is because the phase imbalance contribution of the LPFs are constrained to be zero at 0 Hz, due to their odd symmetry. The frequency responses of real-valued compensation filters, which would serve to equalise the responses of the LPFs (along with the gain imbalance of the mixers) when implemented in the $Q$ signal paths, is given by

$$Q'(f) = \eta_M(f)e^{j[\psi_M(f)-\psi_D(0)]} \tag{4.118}$$

and

$$P'(f) = \kappa_D(f)e^{j[\chi_D(f)-\chi_D(0)]} \tag{4.119}$$

for the modulator and demodulator, respectively.

The compensator for the mixer phase imbalance takes the form of a cross-flow network, which effectively implements a vector multiplication between the $I$ and $Q$ signal paths and the inverse of the distortion matrices derived for the modulator and demodulator in (2.78) and (2.136), respectively. Note that the $I$ channel is once again used as reference.

Since the equalisation of the LPFs and the mixer phase imbalance compensation are now implemented as two separate procedures, the order in which they are implemented becomes important. Compensation should be performed in the reverse order than in which it was introduced (or will be introduced) in the analogue domain. For the modulator, the mixer imbalance compensation should therefore be performed first, followed by LPF equalisation. For demodulator compensation, the order should be reversed. Figs. 4.8 and 4.9 illustrate the full compensation structure for modulator and demodulator imbalance compensation, as implemented in their respective digital domains. Note that the time delays $-t_M$ and $-t_D$ account for the group delay of the compensation filter in the $I$ signal paths.

It should be noted that for the modulator, the phase imbalance function $\psi_M(f)$ is extracted explicitly by the imbalance extraction techniques presented in Section 4.3.3 for Scenario II and III. However, in the modulator extraction techniques developed for Scenario I, as well as the demodulator extraction techniques, $Q_2(f)$ or $P_2(f)$ are extracted directly, without the need to separate the contribution of the gain and phase imbalance contributions. If the compensation approach described above is therefore to be applied, i.e. splitting the realisation of compensation between a real-valued filter and a separate frequency-independent phase compensation, the frequency-dependent phase imbalance contributions $\psi_M(f)$ or $\varphi_D(f)$ will need to be isolated from $Q_2(f)$ or $P_2(f)$, respectively.

One approach would be to apply the same extraction techniques that were used for modulator imbalance extraction for Scenarios II and III. However, a method will be presented below which closely approximates the respective contributions of the gain and phase imbalances in $Q_2(f)$ or $P_2(f)$. This approach avoids the need for additional measurements.

For an alternative approach, consider the real and imaginary components of $P_2(f)$ (note that the same reasoning is valid for $Q_2(f)$). From the expression for $P_2(f)$ in (4.114), these quantities can be derived as

$$\mathcal{Re}\{P_2(f)\} = \frac{[\kappa_D(-f)\cos(\chi_D(-f))]^2+[\kappa_D(-f)\sin(\chi_D(-f))]^2-1}{[\kappa_D(-f)\cos(\chi_D(-f))]^2+2\kappa_D(-f)\cos(\chi_D(-f))+[\kappa_D(-f)\sin(\chi_D(-f))]^2+1} \tag{4.120}$$

and

$$\mathcal{Im}\{P_2(f)\} = \frac{2\kappa_D(-f)\sin[\chi_D(-f)]}{\{\kappa_D(-f)\cos[\chi_D(-f)]\}^2+2\kappa_D(-f)\cos[\chi_D(-f)]+\{\kappa_D(-f)\sin[\chi_D(-f)]\}^2+1} \tag{4.121}$$

respectively.

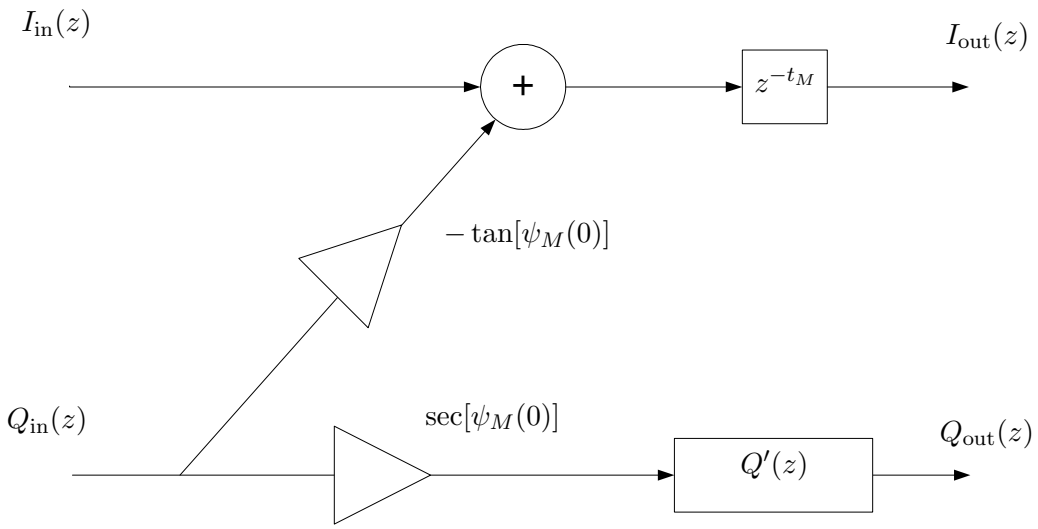


**Figure 4.8:** *Realisation of modulator imbalance compensation using a real compensation filter.*

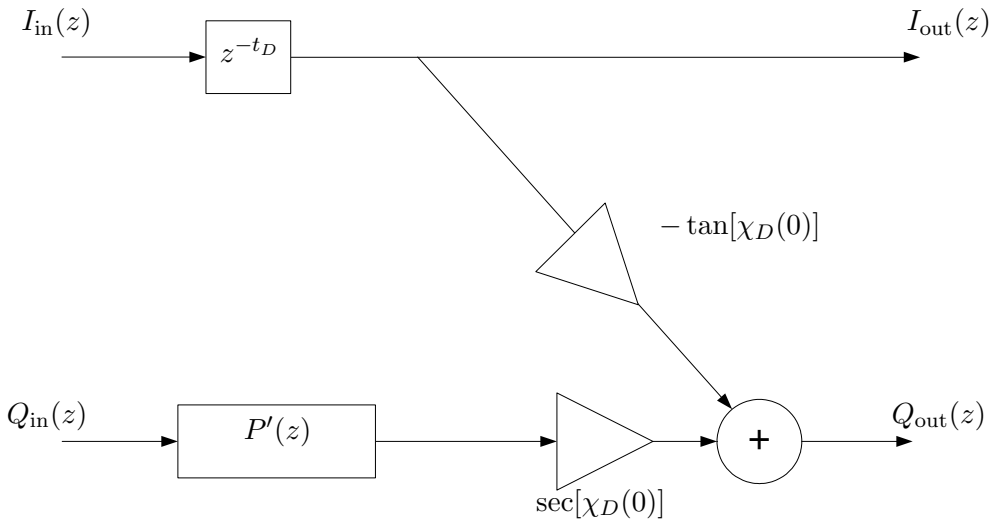


**Figure 4.9:** *Realisation of demodulator imbalance compensation using a real compensation filter.*

For small phase imbalances (as is mostly the case in practice), i.e. $\chi_D(-f) \to 0$, the real part of $P_2(f)$ can be written as

$$\lim_{\chi_D(-f)\to 0} \mathcal{R}e\{P_2(f)\} = \frac{\kappa_D - 1}{\kappa_D + 1}\,. \tag{4.122}$$

Similarly, for small gain imbalances, i.e. $\kappa_D(-f) \to 1$, the imaginary component of $P_2(f)$ becomes

$$\begin{aligned} \lim_{\kappa_D(-f)\to 1} \mathcal{I}m\{P_2(f)\} &= \frac{\sin[\chi_D(-f)]}{\cos[\chi_D(-f)] + 1} \\ &= \tan[(\chi_D(-f)/2]\,. \end{aligned} \tag{4.123}$$

For small gain and phase imbalances, the individual contributions of the gain, $\kappa_D(f)$, and phase, $\chi_D(f)$, imbalance functions in the extracted $P2(f)$, can therefore be approximated as

$$\widehat{\kappa_D}(f) = \frac{1 + \mathcal{R}e\{P_2(-f)\}}{1 - \mathcal{R}e\{P_2(-f)\}} \tag{4.124}$$

and

$$\widehat{\chi_D}(f) = 2\arctan(\mathcal{I}m\{P_2(-f)\})\,. \tag{4.125}$$

For practical imbalance values, the above expressions provide a very accurate approximation of the true underlying gain and phase imbalance functions, as will be verified in simulation in the subsection below.

### Determining whether the BPFs' effect is significant

In the previous subsection, it was argued that when the contributions of the BPF responses can be considered to be negligible, then frequency-dependent compensation can be performed using a filter with a real-valued transfer function and a separate phase compensator. Furthermore, it follows that analysis of the gain and phase imbalance functions constituting $Q_2(f)$ or $P_2(f)$, will deliver insight into whether or not the BPFs' responses are sufficiently matched. Note that the gain and phase imbalance functions, $\eta_M(f)$, $\psi_M(f)$, $\kappa_D(f)$ and $\chi_D(f)$, should not be confused with the magnitude and phase components of the complex functions $Q_2(f)$ or $P_2(f)$.

In order to verify whether the asymmetrical baseband-equivalent responses of the BPF will necessitate the design of a complex imbalance compensation filter, simply analyse the gain and phase imbalance functions, $\eta_M(f)$ and $\psi_M(f)$, or $\kappa_D(f)$ and $\chi_D(f)$. If the gain imbalance function, $\eta_M(f)$ or $\kappa_D(f)$, does not exhibit a symmetrical response around DC, or the phase imbalance function, $\psi_M(f)$ or $\chi_D(f)$, does not exhibit odd symmetry around DC after its value at DC has been subtracted, then a complex-valued compensation filter is required. If this is not the case, then compensation can be implemented using the compensation approach mentioned in the previous subsection, employing a real-valued filter with a separate scalar phase compensation.

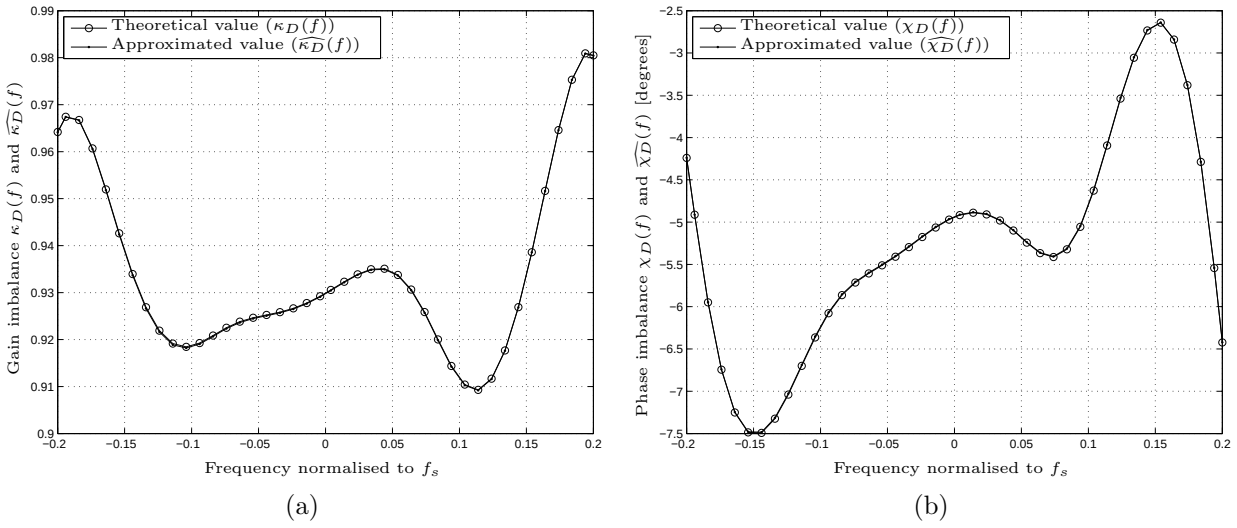


**Figure 4.10:** *The frequency-dependent gain (a) and phase (b) imbalance functions of the simulated demodulator with imbalance contributions from the LPFs, mixer and BPF. The theoretical quantities, computed with perfect knowledge of the simulated imbalances, are shown with the approximations of (4.124) and (4.125).*

In order to illustrate and validate this approach, the demodulator simulation architecture presented in Section 2.5.2 was used. The filter responses and mixer imbalances were chosen as described in Section 2.5.2. The imbalances included contributions from mismatched LPFs, the quadrature mixer and BPFs. Since perfect knowledge of the filter responses and mixer imbalances existed, the theoretical value of $P_2(f)$, as well as $\kappa_D(f)$ and $\chi_D(f)$ could be computed using the equations presented earlier in this section.

Given the theoretical value of $P_2(f)$, the estimations of $\kappa_D(f)$ and $\chi_D(f)$ could then be computed using (4.124) and (4.125). Fig. 4.10 shows the theoretical values of the gain and phase imbalance, as well as the estimated functions, for the given simulation setup. Firstly it is observed that the estimated values approximate the theoretical values extremely closely, even for this severe imbalance scenario. Secondly, note that with the presence of BPF imbalances, the gain imbalance function does not exhibit even symmetry and the phase imbalance function does not exhibit odd symmetry when the value at DC is subtracted.

As a further investigation, the BPF responses where then changed to be exactly equal. The same estimation process was then repeated for this scenario. Fig. 4.11 shows that, as predicted, the gain imbalance function now becomes an even function and the phase imbalance function becomes odd, if the offset phase at DC is subtracted. The offset phase at DC is also exactly equal to $-3°$, which is precisely what the phase imbalance of the mixer was set to.

These simulations serve as validation of the underlying theory and illustrate how it is feasible to employ a real-valued compensation filter together with a separate phase correction, when the BPFs are perfectly matched. This section has also now presented a convenient

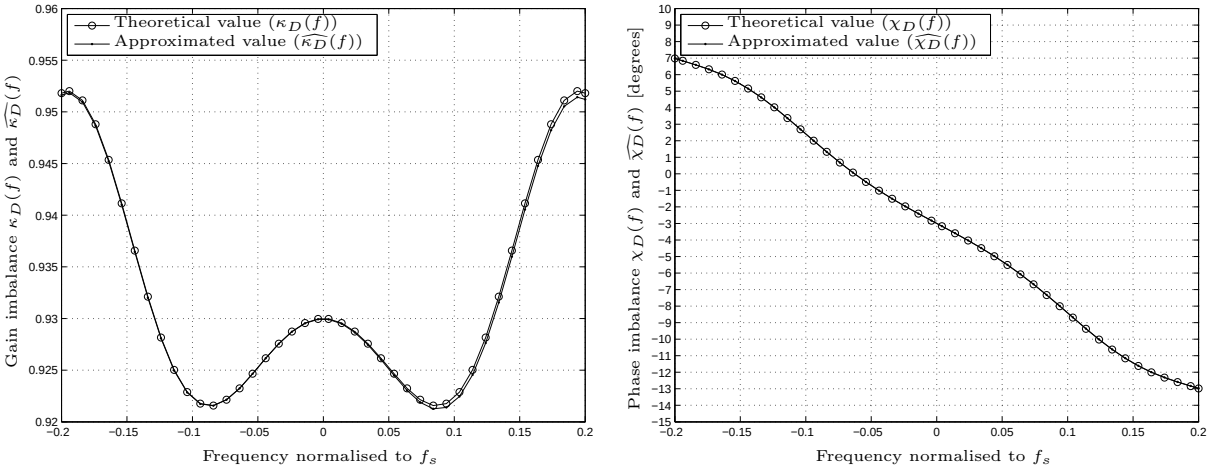


**Figure 4.11:** *The frequency-dependent gain (a) and phase (b) imbalance functions of the simulated demodulator with imbalance contributions from the LPFs and mixer. The BPF responses were perfectly matched. The theoretical quantities, computed with perfect knowledge of the simulated imbalances, are shown with the approximations of (4.124) and (4.125).*

way to validate the theory that it is insufficient to model a practical quadrature mixing front end simply using LPF responses, as is done for example in [31, 58, 59, 5, 4, 55]. In the practical hardware tests, the presence of BPF imbalances will be investigated by examining the symmetry of the extracted gain and phase imbalance functions. For the modulator, these functions will explicitly be extracted as a necessary step to derive the imbalance compensation function $Q_2(f)$. For the case of the demodulator, they will be estimated from the extracted $P_2(f)$ using (4.124) and (4.125), since it was shown here that this approximation delivers very accurate results even for severe imbalances.

### 4.4.2 Designing the digital compensation filter

The complex transfer function of the realised digital compensation filter can either be realised to have a finite impulse response (FIR filter) or an infinite impulse response (IIR). In general, an IIR filter requires a reduced implementation complexity since it often requires fewer coefficients to achieve the required frequency response, compared to an equivalent FIR implementation. On the other hand, care must be taken to ensure that the designed filter is stable. FIR filters are inherently stable (all their poles are located at the origin of the complex plane). Furthermore, a multitude of design techniques exist for the realisation of FIR filters.

In this dissertation, it was decided to implement FIR compensation filters. By examining the practical filter lengths that were required in the hardware implementation (to be presented in Section 5.3), it is seen that only relatively short filters were required (in the order of 31 taps). This makes the advantages of using IIR filters less applicable.

In this dissertation, a design method developed by Tuthill and Cantoni will be used to design digital FIR compensation filters, given the desired responses $Q_2(f)$ and $P_2(f)$. This method was originally proposed in [58] and later optimised in [59]. We will use their optimised design method, which results in FIR compensation filters, and uses least-squares (LS) optimisation with a cost function defined in the frequency domain. Although their technique was originally derived to design real-valued FIR filters, it was found that, with a few minor modifications, their technique is capable of also designing the complex-valued filters required for imbalance compensation. For a detailed discussion on Tuthill and Cantoni's design method, the reader is referred to Appendix A. A few comments on their design approach are, however, presented below.

In order to improve the numerical properties of the filter design solution matrix, the authors propose specifying the desired frequency response at $N$ frequency points that are uniformly distributed on the interval

$$\omega_n \in \Big[ -\xi\frac{\omega_s}{2}, \xi\frac{\omega_s}{2}\Big], \quad n = 1, 2, \ldots, N \ , \tag{4.126}$$

where $0 < \xi < 1$ and $\omega_s = 2\pi f_s$ is the sampling frequency. In such a way, the available degrees of freedom of the compensation filter are used more effectively on a chosen frequency band of interest, instead of the full Nyquist band. A small number of frequency points ensures numerical robustness; however, that in turn means that the cost function is specified for fewer points, making the solution less optimal to the actual problem at hand. To alleviate this trade-off, the authors of [59] propose designing a FIR compensation filter of length $K$, but only having $M \leq K$ non-zero (or active) taps. This approach has the advantage of significantly improving the numerical condition of the resulting solution matrix, therefore allowing a sufficient number frequency points ($N$) to be used [59]. During the implementation of Tuthill and Cantoni's design method in this dissertation, a normalised frequency band of interest from $-0.2$ to $0.2$ was chosen, with every second filter tap set to zero[1].

## 4.5 Conclusions

This chapter has shown how the effect of the frequency-dependent imbalances of the quadrature mixing front-end can be fully reversed through digital compensation. Novel techniques for extracting the imbalance parameters from spectral measurements were presented. These techniques exploit the mathematical relationships between the imbalance parameters of the relative image ratio (RIR), as were derived in Chapter 2. It was found that by using these models, the need for iterative searches for the optimal compensation parameters can be avoided.

Techniques for extracting both modulator and demodulator imbalances were presented. For demodulator imbalance extraction, test tones need be inserted into the radio front end.

---

[1]Setting every second filter tap equal to zero implies that only the frequency response between the normalised frequencies $-0.25$ to $0.25$ can be uniquely specified.

No synchronisation is, however, required between the test tone generator and the demodulator. A convenient solution is presented when a modulator exists in the same transceiver, since the modulator could supply the test tones by feeding its output directly into the demodulator. This approach only requires a feedback path and two switches to be added to a typical transceiver.

For modulator imbalance extraction, a measurement device is required to obtain an indication of the imbalances present in its front end. The extraction techniques of this chapter presented solutions to extract the modulator imbalances in the scenarios where phase- and frequency-coherent measurements can be made, as well as where this is not possible. Once again, a convenient solution is found when a demodulator exists on the same transceiver, which can be used as a measurement solution. In this chapter it was also shown that, even when an imbalanced modulator and demodulator are paired together for imbalance extraction, their imbalances can be separated and independently extracted by only observing the down-converted signal at the output of the demodulator, if a small frequency difference between their LO signals can be introduced.

The fact that single-frequency tones and standard frequency analysis using FFTs are employed in the extraction techniques, makes them widely applicable, since their implementation requires fairly standard signal processing procedures.

This chapter also presented solutions for converting the extracted imbalance parameters to a frequency-dependent compensation filter. An analysis was presented which described the characteristics of the required compensation filter, depending on the nature of the underlying imbalances. It was shown that, when the gain imbalance function is even and the phase imbalance (after the DC phase is removed), is odd, then a real-valued compensation filter can be employed, along with a separate phase compensation. However, when these criteria are not fulfilled, a complex filter is required. This insight stems directly from the inclusion of a bandpass response in the model of the imbalanced front end.

In summary, this chapter provided novel frequency-dependent imbalance extraction and compensation techniques for both the imbalanced modulator and demodulator, developed from the baseband-equivalent imbalance model derived in Chapter 2. These techniques rely on the use of very simple test tones, and are well suited to be implemented as a start-up procedure (that could be repeated at irregular intervals), since quadrature imbalances tend to vary slowly over time [20].

The next chapter will validate the developed imbalance extraction techniques, as well as the underlying models that were presented in the course of this dissertation, through simulations and a hardware implementation of a quadrature modulator and demodulator.

Chapter 6 will focus on the narrow band scenario, where frequency-dependent compensation is not required. Novel imbalance techniques will be developed which do not rely on the use of test signals for imbalance extraction, but rather follow a blind approach that uses the real received data to estimate the imbalances of the front-end.

# Chapter 5

# Performance evaluation

## 5.1 Introduction

Chapter 4 presented the theoretical derivation of novel imbalance extraction techniques for quadrature modulators and demodulators. In this chapter the image rejection performance of these extraction and associated compensation techniques will be evaluated through simulations and a practical hardware implementation of a quadrature modulator and demodulator.

The simulations presented in Section 5.2 will validate the theory of the developed imbalance extraction techniques, and verify their performance in the presence of AWGN and quantisation. The process of translating the extracted imbalance parameters to digital compensation filters will also be simulated and their compensation performance investigated.

Section 5.3 will then extend the validation of these techniques to a practical hardware quadrature modulator and demodulator implementation. The imbalance characteristics of a hardware quadrature modulator and demodulator system will be investigated. During these investigations, the need to model bandpass imbalances will be substantiated. Using the hardware implementation, it will then be illustrated how true frequency dependent imbalance compensation can be realised in practice, using the techniques developed in Chapter 4.

## 5.2 Simulations

This section will start with an overview of the simulation architecture. Subsequently, the simulations that were performed will be presented. These simulations will cover the demodulator and modulator imbalance extraction and compensation techniques separately.

### 5.2.1 Simulation overview

A MATLAB script-based simulation was developed to validate and verify the performance of the developed imbalance extraction and compensation techniques. The simulation platform incorporates the modulator and demodulator simulation blocks that were discussed and employed in Chapter 2 in Sections 2.5.1 and 2.5.2, respectively, to validate the baseband-

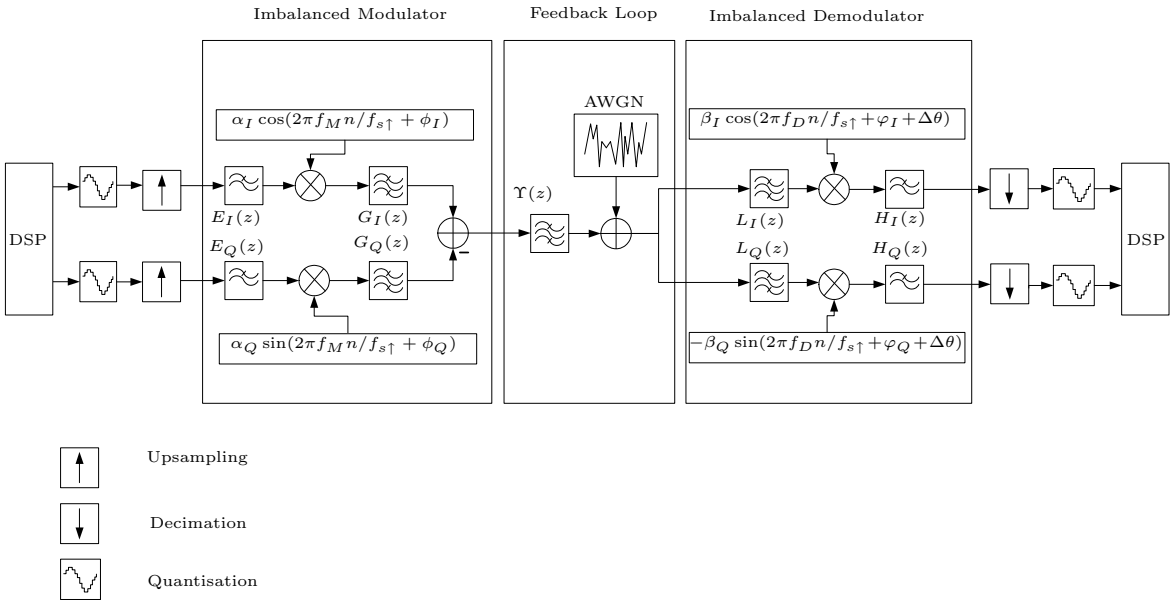


**Figure 5.1:** *Simulation architecture.*

equivalent model and expressions for the relative image ratio (RIR). The reader is referred to those sections for additional information.

Fig. 5.1 presents a block diagram of the simulation topology that will be used in this section. The figure depicts the typical setup that would allow simultaneous modulator and demodulator compensation to be performed. The output of the modulator is passed directly into the demodulator through a feedback path. The demodulator will therefore be used as the measurement device in order to extract the imbalances of the modulator. The modulator in turn will generate the test signals, required to the facilitate the extraction of its own imbalances, as well as those of the demodulator.

The implementation of the quadrature modulator and demodulator aims to replicate the topology of their passband hardware realisation, i.e. not the baseband-equivalent model. Although the baseband-equivalent models for the modulator and demodulator were validated in Chapter 2, implementing the passband topologies aids in truly validating the extraction techniques that were derived from the baseband-equivalent models.

As mentioned in Chapter 2, it was decided to simulate the 'continuous-time' portion of the architecture, using sufficiently oversampled discrete-time signals. The sampling rate used for the 'continuous time' blocks is denoted by $f_{s\uparrow}$, while the sampling rate for the baseband digital signals is denoted by $f_s$. Note that the sampling rate for the modulator and demodulator were chosen to be equal. The sampling rates were chosen such that $f_{s\uparrow}/f_s = 10$. The upsampling and decimation blocks therefore represent the DAC and ADC components, respectively, of a practical system. These sampling rate adjustments were implemented using MATLAB's `resample` function. The `resample` function adjusts the sampling rate of a signal using a polyphase implementation. Anti-aliasing or interpolation filtering is performed, while

**Table 5.1:** *Modulator filter specifications.*

| **Parameter** | $E_I(z)$ | $E_Q(z)$ | $G_I(z)$ | $G_Q(z)$ |
|---|---|---|---|---|
| Filter type | Chebyshev Lowpass | Chebyshev Lowpass | Chebyshev Bandpass | Chebyshev Bandpass |
| Order | 6 | 6 | 12 | 12 |
| Coefficients | real | real | real | real |
| Passband ripple [dB] | 1 | 1 | 1 | 1 |
| Cut off frequency $/f_{s\uparrow}$ | $\pm$0.0510 | $\pm$0.0475 | $\pm$(0.2705 and 0.3303) | $\pm$(0.2695 and 0.3310) |

**Table 5.2:** *Demodulator filter specifications.*

| **Parameter** | $H_I(z)$ | $H_Q(z)$ | $L_I(z)$ | $L_Q(z)$ |
|---|---|---|---|---|
| Filter type | Chebyshev Lowpass | Chebyshev Lowpass | Chebyshev Bandpass | Chebyshev Bandpass |
| Order | 6 | 6 | 12 | 12 |
| Coefficients | real | real | real | real |
| Passband ripple [dB] | 1 | 1 | 1 | 1 |
| Cut off frequency$/f_{s\uparrow}$ | $\pm$0.0515 | $\pm$0.0475 | $\pm$(0.2703 and 0.3300) | $\pm$(0.2687 and 0.3310) |

also compensating for the filter's delay. It was verified that these blocks do not contribute at all to the imbalances observed in the simulation.

In order to model the finite bit precision of practical sampler systems, quantisation blocks were included. These blocks assume that the input signal occupies the full dynamic range. For an input signal $x_{\text{in}}[n]$, the quantised output is computed using the following steps:

$$A_{\max} = \max\{|x_{\text{in}}[n]|\} \tag{5.1}$$

$$\varpi = 1 - 10^{-15} \tag{5.2}$$

$$L = 2^{B-1} \tag{5.3}$$

$$x_{\text{quantised}}[n] = \frac{A_{\max}\text{floor}\{\varpi L x_{\text{in}}[n]/A_{\max}\} + 0.5}{L} \tag{5.4}$$

where $B$ represent the bit precision and $n$ is the discrete time sample iterator.

All the filters in the simulation are implemented as Chebyshev digital filters with real valued coefficients. Note that $z$ denotes a variable in the z-transform frequency domain. The filter parameters were kept identical to those used in Chapter 2. For convenience, a summary of their specifications are presented here again, in Table 5.1 and Table 5.2. For the exact filter coefficients, the reader is referred to Table 2.2 on p. 35 and Table 2.6 on p. 51. Frequency-dependent imbalances were established by introducing small variations between the cut off frequencies of the corresponding filters in the $I$ and $Q$ channel.

The amplitude and phase of the oscillator signals in the modulator and demodulator were controlled in order to introduce frequency-independent quadrature imbalances. Table 5.3 presents a summary of the imbalance parameters in the oscillator signals of the modulator and demodulator. A frequency and phase difference ($\Delta f$ and $\Delta\theta$) were introduced between

**Table 5.3:** *Oscillator signal parameters.*

| Parameter | Description | Value |
|---|---|---|
| $f_{s\uparrow}/f_s$ | Oversampling ratio | 10 |
| $\Delta f/f_s$ | Normalised frequency difference between the LOs of the modulator and demodulator | 0.01 |
| $f_M/f_{s\uparrow}$ | Normalised modulator LO frequency | 0.3 |
| $f_D/f_{s\uparrow}$ | Normalised demodulator LO frequency | $(f_M - \Delta f)/f_{s\uparrow}$ |
| $\alpha_I/\alpha_Q$ | Modulator mixer gain imbalance | 1.05 |
| $\phi_I - \phi_Q$ | Modulator mixer phase imbalance | 3 ° |
| $\beta_I/\beta_Q$ | Demodulator mixer gain imbalance | 0.93 |
| $\varphi_I - \varphi_Q$ | Demodulator mixer phase imbalance | -3 ° |

the LO signals of the modulator and demodulator. The phase difference $\Delta\theta$ can be changed from measurement to measurement, in order to simulate the scenario where the sample timing between the modulator and demodulator is not synchronised.

The response of the feedback path is modelled by the inclusion of an additional bandpass filter, $\Upsilon(z)$. This real-valued filter is implemented as a third-order Chebyshev filter, with cut off frequencies normalised to $f_{s\uparrow}$ of $\pm 0.2590$ and $\pm 0.3390$. Additive white Gaussian noise (AWGN) can also be added to the signal in the feedback path and will be used to test the performance of the extraction techniques in the presence of noise.

### 5.2.2 Demodulator compensation

This section will focus on the imbalance extraction and compensation techniques of the demodulator, which were derived in Section 4.3.2. The validity of the technique will first be established, after which the extraction performance will be evaluated in the presence of noise and quantisation will be evaluated. The effectiveness of the compensation filter, designed using the extracted parameters, will then be investigated.

#### Validation of extraction technique

*Simulation objective*

This simulation aims to validate the demodulator extraction techniques presented in Section 4.3.2, as well as the compensation approach described in Section 4.2.1. The test-tone-based imbalance extraction technique developed for the demodulator, should be able to extract the imbalances of the demodulator (including contributions from the LPFs, the mixer as well a BPF response) at each test-tone frequency. When used for compensation, it is expected that each extracted coefficient will lead to a significant improvement in the RIR of the demodulator, at the corresponding frequency where the estimation was performed. However, it should be seen that when an extracted coefficient is used for compensation at a different

frequency, reduced compensation performance can be expected – thereby illustrating the need for a truly frequency dependent compensation approach in the form of a compensation filter.

*Simulation approach*

The compensation parameters of the demodulator, as a function of frequency (i.e. $P_2(f)$ as defined in Section 4.3.2), were extracted using a number of test tones generated by the modulator. The imbalances of the demodulator were extracted in the digital domain of the demodulator, using spectral analysis and the techniques developed in Section 4.3.2. In order to validate the *extraction* technique and verify its accuracy, the principle of demodulator compensation developed in Section 4.2.1 was applied. This involved applying the compensation parameter $P_2(-f_r)$, for a test tone at frequency $+f_r$ in the digital domain of the demodulator. This compensation approach is clearly impractical for signals with a wider frequency extent than a pure tone, but offers a convenient way of testing the validity and accuracy of the extraction process and the general compensation approach. In order to make the compensation technique practical, a compensation filter should be designed with a frequency response equal to $P_2(f)$, using the techniques of Section 4.4. The design of the compensation filter is treated in a subsequent simulation (see 'Verification of the compensation filter performance' on p. 125).

The extraction of demodulator compensation parameters was tested using a perfectly balanced modulator, as well as a modulator with quadrature imbalances of its own (without compensating for these imbalances in any way). This illustrates how the imbalances of the demodulator can indeed be separated from that of the modulator. As mentioned in Section 4.3.3, however, in order to be able to separate the imbalances of the modulator and demodulator, their LO frequencies should be offset slightly. For this reason, a frequency difference of $\Delta f/f_s = 0.01$ was introduced in the simulation, with the LO frequency of the demodulator chosen as $f_D = f_M - \Delta f$. Furthermore, the start phase of the demodulator oscillator signals $\Delta\theta$ was randomly assigned for each new measurement (each subsequent test tone), in order to simulate an uncertainty between the time that the modulator starts transmission of the test tone, and the time the demodulator commences its sampling process.

The general expression for the complex-valued test tone generated in the digital domain of the modulator is given by

$$s(n) = A_m \exp(j2\pi n f_m/f_s) \tag{5.5}$$

where the frequency $f_m$ was incremented in the simulation with each subsequent test tone, in order to cover the frequency band of interest. Taking into account the frequency difference of $\Delta f$, it means that a modulator tone at a normalised frequency of $f_m/f_s$, will result in a desired component in the digital domain of the demodulator at $f_r = f_m + \Delta f$, with an image component due to demodulator imbalances at $-f_r$.

The frequency band of interest was chosen to extend from $-0.2$ to $0.2$ in the digital domain of the demodulator, normalised to $f_s$. This was done to satisfy the requirement discussed in

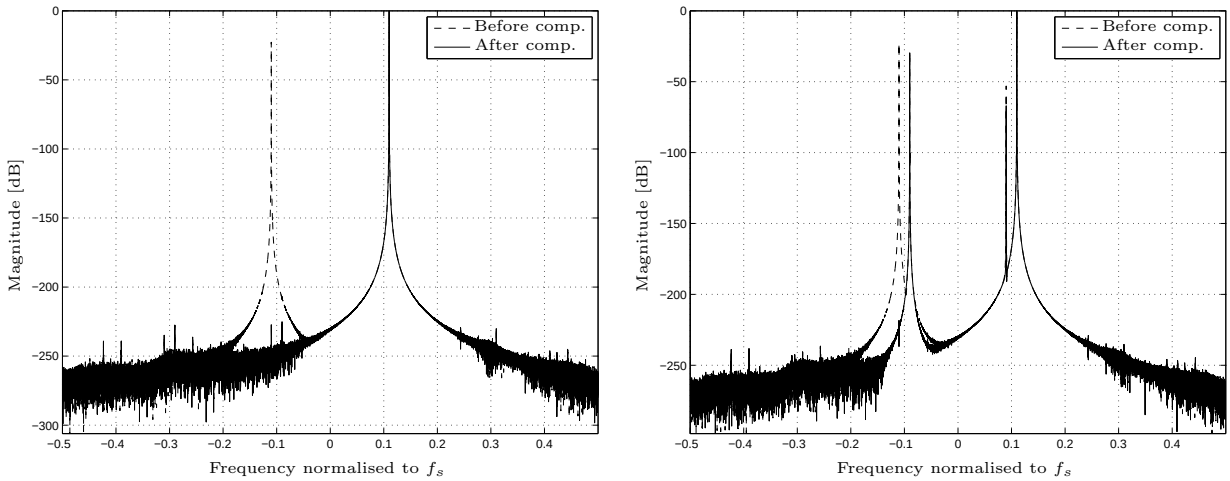


**Figure 5.2:** *Magnitude spectra in the digital domain of the demodulator, illustrating the effectiveness of the demodulator imbalance extraction technique. (a) illustrates compensation of demodulator imbalances when using a perfectly balanced modulator, while (b) illustrates the case where an imbalanced modulator was used. A frequency offset between the LOs of the modulator and demodulator allows the separation of the effects of modulator and demodulator imbalances in the frequency domain.*

Section 4.4.2, which explained that the compensation filter employs zero-valued coefficients in order to achieve more numerically robust results. With every second coefficient set to zero, as will be implemented in subsequent investigations in this section, the filter can only uniquely control its response in the normalised frequency range from $-0.25$ to 0.25. Note that this is a restriction due to the chosen implementation of the compensation filter and not a restriction of the extraction technique. Nevertheless, the region $-0.2$ to 0.2 represents a realistic usable frequency range, which would illustrate the frequency-dependent nature of the imbalances well.

Since the aim of this simulation is to validate the extraction technique and compensation approach, no AWGN was added in the feedback path and no quantisation was applied beyond the default 64-bit double, floating point precision that MATLAB implements. A long FFT (32768 sample points) was also used during spectral analysis in order to showcase the performance of the extraction technique sufficiently. In subsequent simulations, the extraction performance will be evaluated in the presence of noise, quantisation and shorter FFT lengths.

*Results and discussion*

Fig. 5.2(a) presents the spectra in the digital domain of the demodulator, before and after imbalance compensation, for the case where a perfectly balanced modulator was used. A desired component is seen to exist at $f_r/f_s = (f_m + \Delta f)/f_s = 0.11$, with the undesired image component at $-f_r/f_S = -0.11$. After compensation this image spur is completely

suppressed. Small spurious components with magnitudes in the order of −230 dBc are also observed. These components can be attributed to the sample rate conversion operations, and confirms that this process does not add any significant distortion to the simulation results.

Fig. 5.2(b) presents the case where an imbalanced modulator is employed to generate the test tone. In this case the passband input signal to the demodulator will no longer be a single-sideband signal with components at $\pm(f_M+fm)$, but will also contain image components due to modulator imbalances at $\pm(f_M - f_m)$. The down converted baseband signal will therefore contain four spectral components: the desired signal at $(f_m + \Delta f)/f_s = 0.11$, the image due to modulator imbalances at $(-f_m + \Delta f)/f_s = -0.09$, the image of the desired signal, due to demodulator imbalances at $-(f_m + \Delta f)/f_s = -0.11$ and finally the image of the modulator image spur, due to demodulator imbalances at $-(-f_m + \Delta f)/f_s = 0.09$. After applying the compensation derived for the desired component at 0.11, i.e. $P_2(-0.11)$, the image component at frequency −0.11 is seen to disappear completely. As expected, the image spur due to modulator imbalances is not affected. Importantly, the image component of the modulator imbalance spur, due to demodulator imbalances (the component at 0.09), is slightly attenuated after compensation with $P_2(-0.11)$, but still remains strong. This indicates that the compensation coefficient $P_2(-0.11)$, is not sufficiently the same as the compensation coefficient required to compensate for the image at frequency 0.09, i.e. $P_2(0.09)$. This illustrates the frequency-dependent nature of imbalances present in the demodulator. Fig. 5.3 presents the results of the extraction and compensation process, performed at 40 frequency points between the normalised (to $f_S$) frequencies −0.2 and 0.2. The RIR is shown as a function of the desired frequency component in the digital domain of the demodulator. The figure illustrates the measured RIR before compensation, as well as after compensation, using the appropriate compensation value in the extracted $P_2(f)$ for each corresponding test tone. Results are presented for both the case where a perfect modulator was used, as well as where the demodulator imbalances had to be extracted in the presence of modulator imbalances. In addition, a plot is also included which illustrates the effect of using only a single value in $P_2(f)$ (in this case $P_2(0.0940)$) to attempt compensation for all the input test tones.

The substantial improvement in terms of RIR, before and after applying the extracted values of $P_2(f)$ as compensation, indicates that the extraction process is valid and the model from which it was derived is accurate. By examining the RIR performance after a single compensation coefficient, extracted for an image component at $f_r/f_s = 0.094$, is applied to all test tones, it can be seen that the demodulator imbalances exhibit a strong frequency dependence. Very good image suppression is measured at the exact frequency where the imbalances were estimated at. However, the underlying demodulator imbalance response rapidly changes from this point, leaving the compensation coefficient inadequate to deliver sufficient image rejection. This effect was already noticed in the example spectra in Fig. 5.2(b), and emphasises the need for a true frequency-dependent compensation solution, in the form of a filter with frequency response equal to $P_2(f)$.

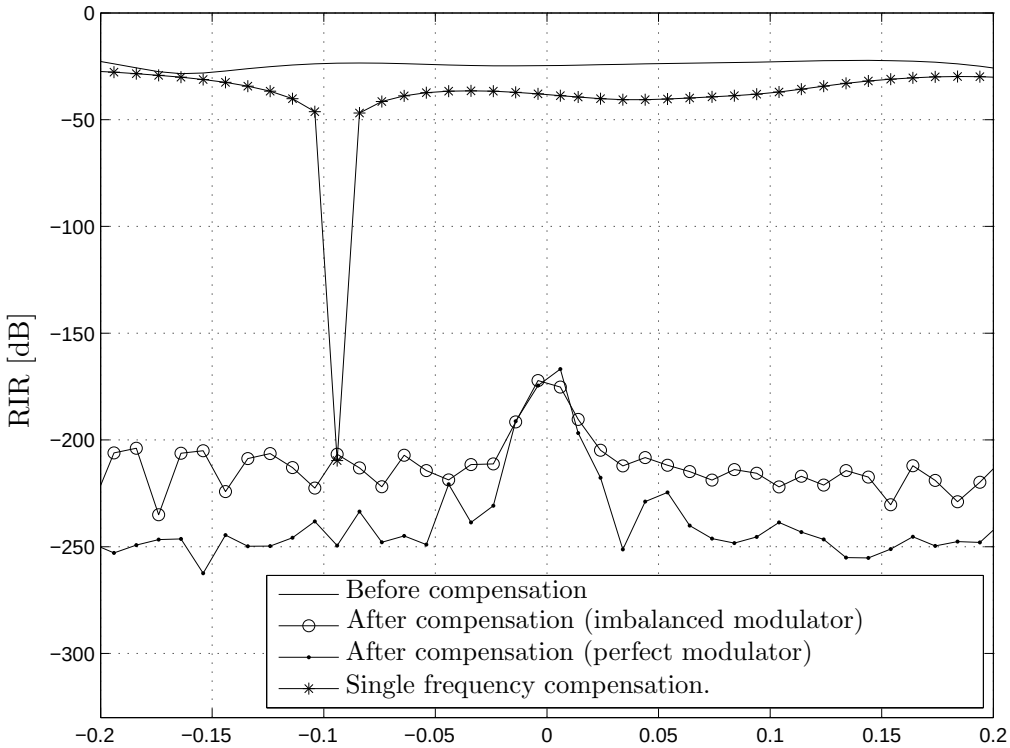


**Figure 5.3:** *Demodulator RIR, as a function of the frequency of the desired component of the test tone in the digital domain of the demodulator, before and after compensation. Results are presented for the case where a perfect modulator generated the test tones, as well as the case where an imbalanced one was employed.*

A slight difference is noticed between the RIR performance using a perfect modulator and an imbalanced one. The explanation for this can be found in the spectral plots of Fig. 5.2. From Fig. 5.2(b) it is seen that the small difference in the measured RIR, stems from the fact the RIR is measured in the frequency domain using an FFT and that in the case where modulator imbalances are also present, the roll off in the sidelobe structure of the image spur due to modulator imbalances is affecting the measurement. This highlights the fact that sufficient frequency separation should be ensured between the modulator and demodulator components, since their sidelobe structure will also affect the accuracy of the extracted imbalance parameters. This can be achieved by carefully choosing the LO frequency difference, number of FFT bins and amplitude windowing function. The same phenomenon is observed where the down converted digital signal lies close to DC, which implies that its image component is close by in frequency and its sidelobe structure is affecting the measurement. Although this effect is observed, the compensation performance can still be described as being more than sufficient for the chosen LO frequency offset.

**Extraction performance in the presence of additive white Gaussian noise**

*Simulation objective*

This simulation aims to investigate the demodulator imbalance extraction performance in the presence of AWGN. Although it is foreseen that the achievable RIR performance, after compensation, will be affected by AWGN, it is hypothesised that the RIR will not be limited to the actual signal to noise ratio (SNR) of the input signal to the demodulator, but can be improved through digital signal processing gain. The premise of this statement lies in the fact that imbalance extraction is performed using single frequency test tones and an FFT operation in the digital domain of the demodulator.

In an FFT computation on a signal containing white noise, the noise power in each FFT bin is determined by the power spectral density of the noise, multiplied by the bandwidth spanned by each bin. By increasing the number of FFT bins used during processing, a finer frequency resolution is obtained, resulting in less noise power in each FFT bin, with the total noise power remaining constant. When signals that have their energy concentrated at discrete frequencies (i.e. periodic time signals or sum of periodic time signals) are analysed in the presence of noise, SNR in the particular frequency bin where the signal's energy is concentrated, will be larger than the total SNR of the signal plus noise. In this experiment, we refer to this effect as the 'processing gain' associated with the FFT operation, and measurement signal-to-noise ratio at the bin where the signal energy is concentrated, as the 'SNR after processing.' The SNR after processing ($\mathrm{SNR}_{\mathrm{out}}$), can be written in terms of the SNR without processing ($\mathrm{SNR}_{\mathrm{in}}$), the samples in the amplitude windowing function $W_n[n]$ and the FFT length $N$, as

$$\mathrm{SNR}_{\mathrm{out}} = \mathrm{SNR}_{\mathrm{in}} + 10\log_{10}\left(\sum_{n=1}^{N} W_n[n]\right) \text{ dB}, \tag{5.6}$$

assuming the FFT length equals the number of actual signal samples used in the calculation (i.e. no zero-padding).

The test tones proposed for imbalance extraction satisfy the condition that their energy is confined to discrete frequency values (even after the effect of $I/Q$ imbalances). Since $I/Q$ imbalance extraction is performed using the FFT bins where this energy mainly resides, the accuracy of the extracted imbalance parameters should be limited by the SNR after processing, rather than the SNR of the input signal. Therefore, the observed RIR after processing, should correspond to the SNR after processing. Stated differently, it is hypothesised that one should be able to compensate for $I/Q$ imbalances up to the level that one can accurately observe the effect of the imbalances.

As a side note, it should be mentioned that in practice the SNR using a direct feedback path between the modulator and demodulator would be very high. This experiment, however, still provides insight into the performance bound on the derived extraction technique, due to noise.

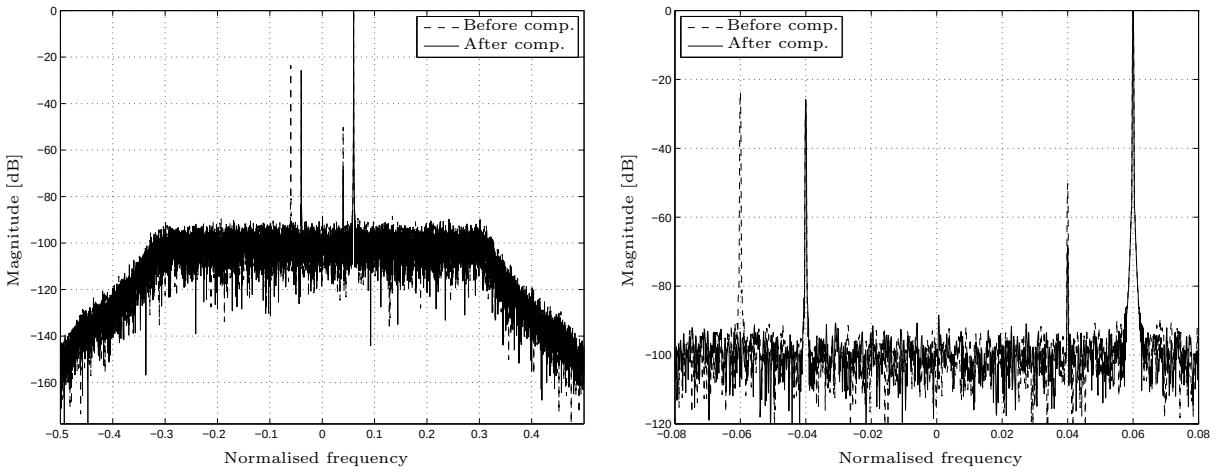


**Figure 5.4:** *An example magnitude spectrum of a test tone generated with an imbalanced modulator and received with an imbalanced demodulator, in the presence of AWGN. The SNR after processing in this case was set to 100 dB. The plot in (b) is a zoomed in version of the spectra in (a).*

*Simulation approach*

In this simulation, AWGN was added to the test signal in the feedback path. The noise variance was controlled to test the extraction performance at SNR values (after processing) of 120, 100, 80, 60 and 40 dB. The FFT length was fixed to 8192 samples. The demodulator imbalances were extracted at 40 frequencies located throughout the frequency band of interest (normalised frequencies $-0.2$ to 0.2), in the presence of modulator imbalances, since it was seen in the previous simulation on p. 114, that this does not effect the extraction performance. Compensation was applied in the same fashion as the previous simulation, where the corresponding extracted value of $P_2(f)$ is chosen as compensation coefficient, depending on the frequency of the test tone that is measured. No additional quantisation was introduced above the default 64-bit double, floating point precision of MATLAB.

*Results and discussion*

Fig. 5.4 presents the magnitude spectra of one of the test tones in the digital domain of the demodulator, in the presence of AWGN. In this case, the SNR after processing was set to 100 dB. In Fig. 5.4(a) the effect of the BPF is clearly visible, shaping the noise spectrum. It is observed that the demodulator compensation procedure manages to suppress the demodulator image spur down to the noise floor. Fig. 5.5 presents that RIR performance as a function of the frequency of the desired component in the digital domain of the demodulator. For each SNR value, the average of 100 runs across all 40 frequencies is presented. It is seen that the RIR corresponds well to the SNR after processing. The results confirm the hypothesis that imbalances of the demodulator can be extracted and compensated for down

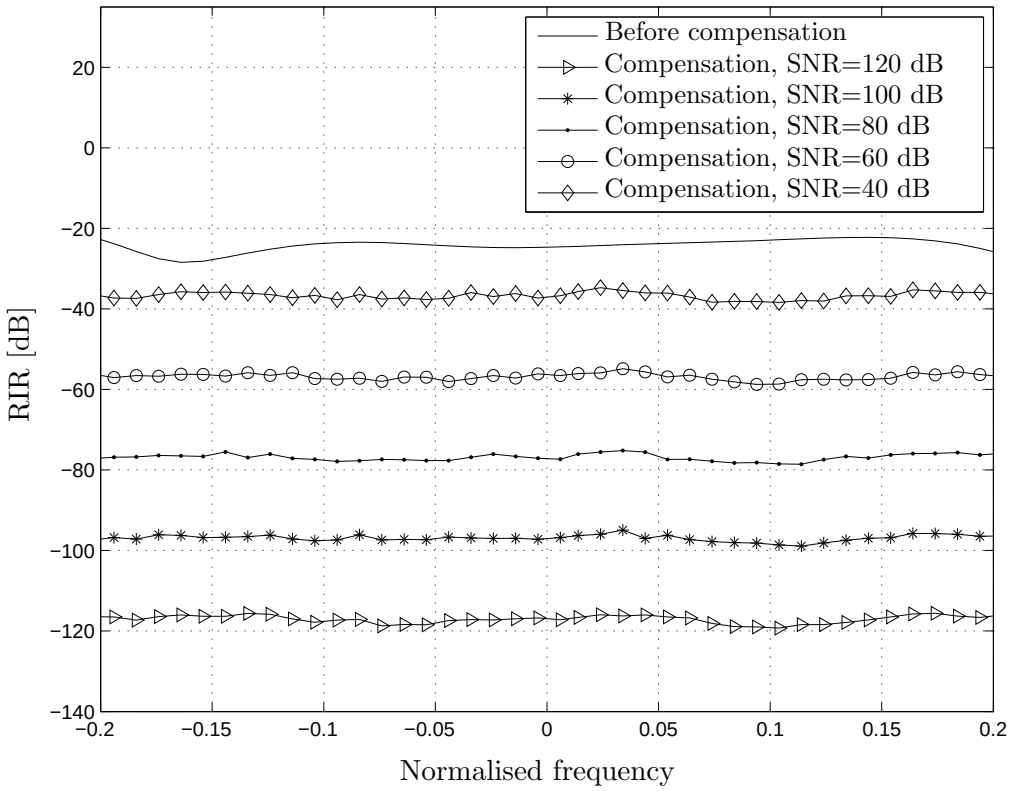


**Figure 5.5:** *Demodulator RIR performance after compensation, in the presence of AWGN. The SNR is specified after processing.*

to the measurement SNR after processing. This is a significant result, indicating that image signal suppression can be increased by increasing the FFT length.

### Verification of extraction performance in the presence of quantisation

*Simulation objective*

It is well known that the quantisation noise spectra of sinusoidal signals are not necessarily white [15, 69, 38]. For integer and some rational relationships between the sampling rate and the frequency of the sinusoidal signal, the quantisation error signal will be periodic and therefore result in line spectral components in the frequency domain, harmonically related to the input signal [38]. The interested reader can find a short discourse on the characteristics of quantisation noise in Appendix B. When the quantisation noise is concentrated in harmonic line spectral components, the processing gain (as discussed in the previous simulation) of the FFT can no longer effectively be used to suppress the noise power contribution per bin, as is the case for a stochastic signal with distributed frequency content.

This simulation aims to prove the hypotheses that quantisation noise, as with AWGN, limits the accuracy with which quadrature imbalances can be observed in the frequency domain, and will therefore also place a limit on the achievable RIR performance after com-

pensation. It is therefore expected that the spurious free dynamic range (SFDR) of the FFT measurement, should also form the compensation performance bound. It then follows that it should be possible to improve the extraction accuracy by choosing test tone frequencies which result in white, or near white, quantisation noise spectra, i.e. tone frequencies which result in higher SFDR during the measurement process. When the test tone frequencies are carefully chosen to satisfy this requirement, the compensation RIR performance should improve roughly 6 dB for each additional quantisation bit of the sampler system – in line with the expected improvement in SFDR as presented in (B.5) in Appendix B.

*Simulation approach*

For this simulation, the quantisation blocks indicated in the simulation topology of Fig. 5.1 were used to quantise the signal after the digital domain of the modulator and before the digital domain of the demodulator. This simulates the finite bit resolution sampler systems employed in practical systems. As mentioned in the overview of the simulation topology, the assumption is made that the input signals to these quantisation blocks occupy their full dynamic range and therefore use all the available bits. Processing inside the digital domains of the modulator and demodulator was still performed at MATLAB's IEEE-754 standard, 64-bit double, floating point precision. No AWGN was added and modulator imbalances were disabled.

The effect of the SFDR due to quantisation noise was investigated by simulating two test tone cases. In the first case, the test tone frequency was chosen so that the resulting quantisation noise spectrum exhibit line spectral components ($f_r/f_s = -0.05555555$). In the second case, the frequency was changed slightly ($f_r/f_s = -0.053249857349875$), such that an almost white quantisation noise spectrum resulted, with a higher SFDR. In both cases, the sampler precision was set to 10 bits and imbalance extraction and compensation were then performed at the test tone frequency.

A second simulation was performed to illustrate the relationship between the compensation performance and number of bits used during quantisation. For this simulation, the number of sampler bits were varied from 4 to 25, while imbalance extraction and compensation were performed at a single frequency point using a test tone. The frequency of each tone was chosen such that a white quantisation noise spectrum resulted, i.e. maximising the SFDR of the measurement. The simulation was repeated 100 times, each time varying the frequency of the test tone slightly in order to compute an average performance.

*Results and discussion*

Fig. 5.6 and 5.7 illustrate the magnitude spectra of the two test tone cases, before and after imbalance compensation. In Fig. 5.6, the test tone frequency was chosen such that the energy in quantisation noise spectrum is concentrated in harmonic, line spectral components. The SFDR in this case is about 67 dB. After imbalance compensation, it is seen that the RIR is improved from $-24$ dBc to $-64$ dBc – corresponding well to the SFDR of the FFT

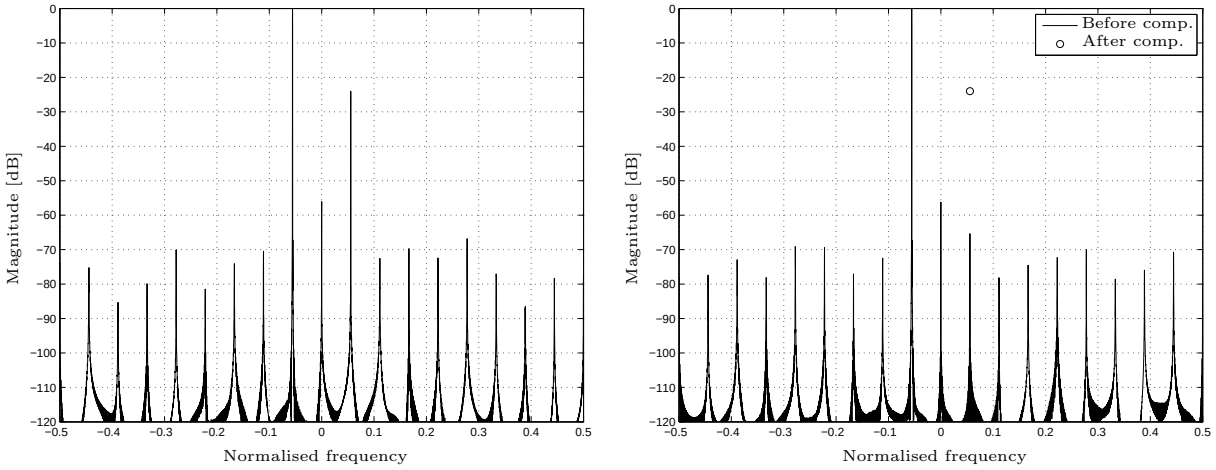


(a) (b)

**Figure 5.6:** *Magnitude spectra of a test tone after 10 bit quantisation, with desired component at $f_r/f_s = -0.05555555$, before (a) and after (b) demodulator imbalance compensation.*

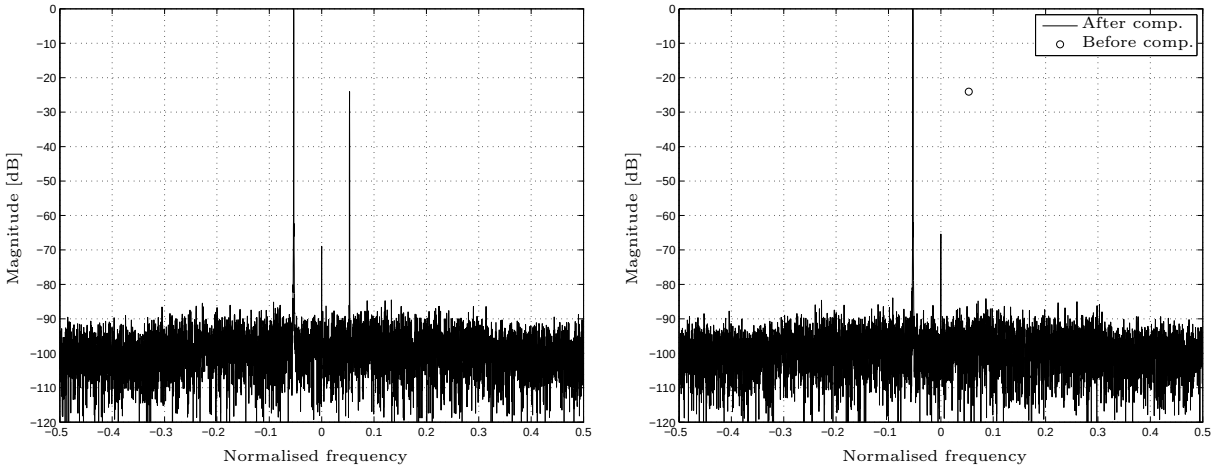


(a) (b)

**Figure 5.7:** *Magnitude spectra of a test tone after 10 bit quantisation, with desired component at $f_r/f_s = -0.053249857349875$, before (a) and after (b) demodulator imbalance compensation.*

measurement. In Fig. 5.7 the test tone frequency was chosen such that a white quantisation noise spectrum resulted. In this case the SFDR is in the order of 84 dB and it is seen that imbalance compensation now manages to achieve a RIR of −87 dBc. Once again this corresponds well with the SFDR of the measurement and illustrates how the achievable RIR can be significantly improved when the test tone frequency is chosen to achieve a white quantisation noise spectrum.

Fig. 5.8 presents the achievable RIR after compensation, as a function of the number of quantisation bits. The result is the average performance of 100 runs, where the test tone frequency was varied slightly in each run. Care was taken to ensure a white quantisation

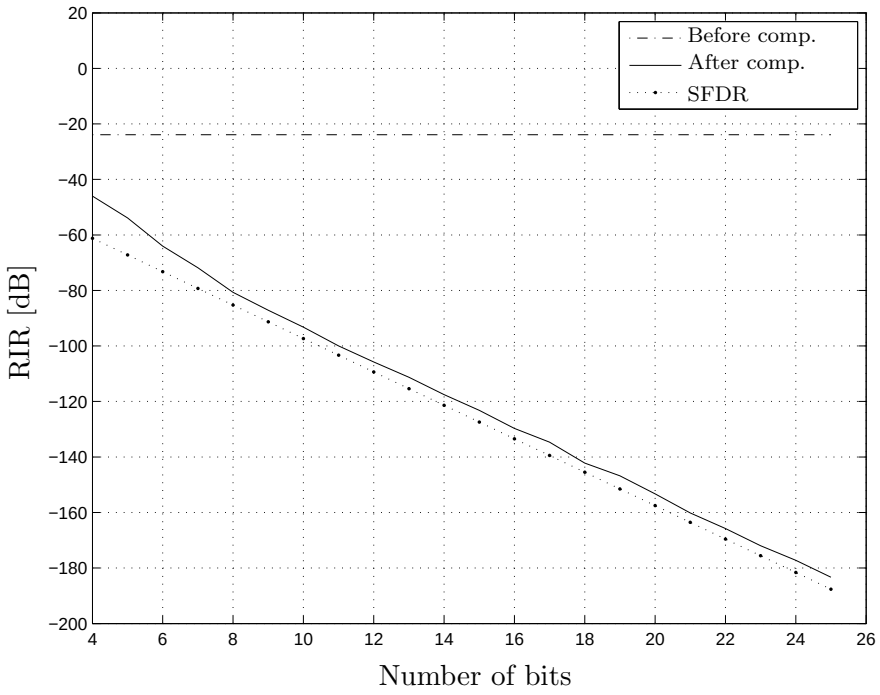


**Figure 5.8:** *The achievable RIR after compensation, as a function of the number of quantisation bits. The theoretical measurement SFDR (negated) for a white quantisation noise spectrum is also shown.*

noise spectrum resulted in each case. The theoretical measurement SFDR (negated) for a white quantisation noise spectrum is also shown. Using the result presented in Appendix B (B.5) and taking the FFT processing gain into account, the expression for this theoretical SFDR is given by

$$S_{\text{SFDR}}(B) \;=\; 1.76 + 6.02B + 10\log_{10}\left(\sum_{n=1}^{N} W_n[n]\right), \tag{5.7}$$

where $B$ represents the bit resolution and $W_n[n]$ the windowing function of length $N$.

The result in Fig. 5.8 indicates that the achievable RIR after compensation improves at the same rate as the measurement SFDR, thereby proving the hypothesis that the SFDR of the measurement will form the limit in terms of the achievable RIR performance. Furthermore, the RIR after compensation nearly reaches the theoretical SFDR bound for a white quantisation noise spectrum, after FFT processing. This then illustrates that through careful choice of the test tone frequencies (i.e. ensuring that the quantisation noise spectrum is white), the processing gain of the FFT can be used to improve the achievable RIR at the price of processing more samples (i.e. longer FFT length).

**Verification of the compensation filter performance**

*Simulation objective*

In the previous simulations it was shown how the parameters for imbalance compensation can be extracted using test tones at various frequencies throughout the frequency band of interest. Their accuracy was verified by using the extracted compensation value, which corresponds to the input test tone's frequency, as a frequency-independent compensation coefficient.

This simulation aims to illustrates how the extracted compensation values at the test tone frequencies, can be used to design a FIR compensation filter, which offers a true frequency dependent imbalance compensation solution. The performance loss, as a function of compensation filter length, is then investigated.

*Simulation approach*

In this simulation, the parameters of the compensation function $P_2(f)$ were once again extracted at various frequencies, through the use of test tones, as was the approach in the previous simulations. However, unlike the previous simulations, these parameters were then used to design a single complex compensation filter, with frequency response equal to the $P_2(f)$ as estimated at discrete points using the test tones. The compensation filter was designed using the procedure outlined in Section 4.4, using $|(P_2(f))|$ and $\arg[P_2(f)]$, respectively, as the desired gain and phase response of the filter.

The compensation filter was designed so that every second coefficient in its impulse response equalled zero (i.e. $L = 1$). The reason for this approach was justified in Section 4.4 and was used to improve the numerical robustness of the design procedure. The implication, though, is that the filter response can only be uniquely specified from frequencies $-0.25$ to 0.25, normalised to $f_s$ (the full Nyquist zone extends from $-0.5$ to 0.5). The frequency band of interest, over which the frequency response of the filter should be matched to $P_2(f)$, was therefore chosen to extend from $-0.2$ to 0.2 (normalised to $f_s$).

In the previous simulations, the accuracy to which the imbalance parameters can be extracted, was investigated in the presence of AWGN and quantisation. In this simulation, the aim is to verify the performance degradation, if any, when these parameters are now translated to a compensation filter, which provides true frequency-dependent compensation. For this reason, the simulations employed here did at first not incorporate AWGN or quantisation, since the effect of these non-idealities on the estimation of the imbalance parameters have already been investigated. Rather, this simulation firstly evaluated how the designed filter's compensation performance compared to the performance obtained by using the extracted imbalanced parameters directly for compensation (i.e. by carefully selecting the extracted compensation parameter based on the frequency of the input test tone). The effectiveness of the designed filter was tested by using a collection of test tones, filtering each in the demodulator's digital domain with the designed filter, and measuring the resultant RIR using spectral analysis.

A second simulation was then be used to test the performance of the compensation filter in the presence of AWGN. In both these simulations, the test tones were generated using an imbalanced modulator.

*Results and discussion*

Fig. 5.9 illustrates the effectiveness of the filter design procedure, as described in Section 4.4, by presenting the desired gain and phase response of the filter, as well as the gain and phase response of the realised filter, for different filter lengths. The desired gain and phase response of the filter is derived from $|(P_2(f)|$ and $\arg[P_2(f)]$, respectively, which has been estimated at 40 discrete frequency points in the frequency band of interest ($-0.2$ to 0.2), using the test tones generated by the modulator. The response of the designed filters follow the desired response in the frequency region $-0.2$ to 0.2, with the longer filter length of 61 taps following the desired response more closely then the short 15 tap filter. The filter responses repeat outside the frequency regions $\pm 0.25$.

Fig. 5.10 presents the results of using the designed compensation filter to compensate for demodulator imbalances. The compensation performance of different length filters are compared to the RIR performance achieved by selecting the correct extracted compensation coefficient in $P_2(f)$, based on the frequency of the test tone. Very low RIR levels of around $-140$ dBc can be achieved over the whole frequency band of interest, using a relatively short filter of only 61 taps (keeping in mind that it will only require the computational complexity of a 31 tap filter, since every second tap is set to zero). Even the filter length of 31 taps provides a RIR performance of $-80$ dBc. When considering the 15 tap filter, it is seen that the performance loss, relative to the reference extraction and compensation performance, becomes pronounced, yielding arguably insufficient performance for high performance communication systems.

Fig. 5.11 illustrates the results where the simulation was repeated, but for a SNR after processing (i.e. the SNR in the FFT measurement) of 80dB. From this figure it is seen that the performance of the compensation filter is independently limited by the accuracy with which the imbalance parameters can be extracted, as well as the number of taps in the filter.

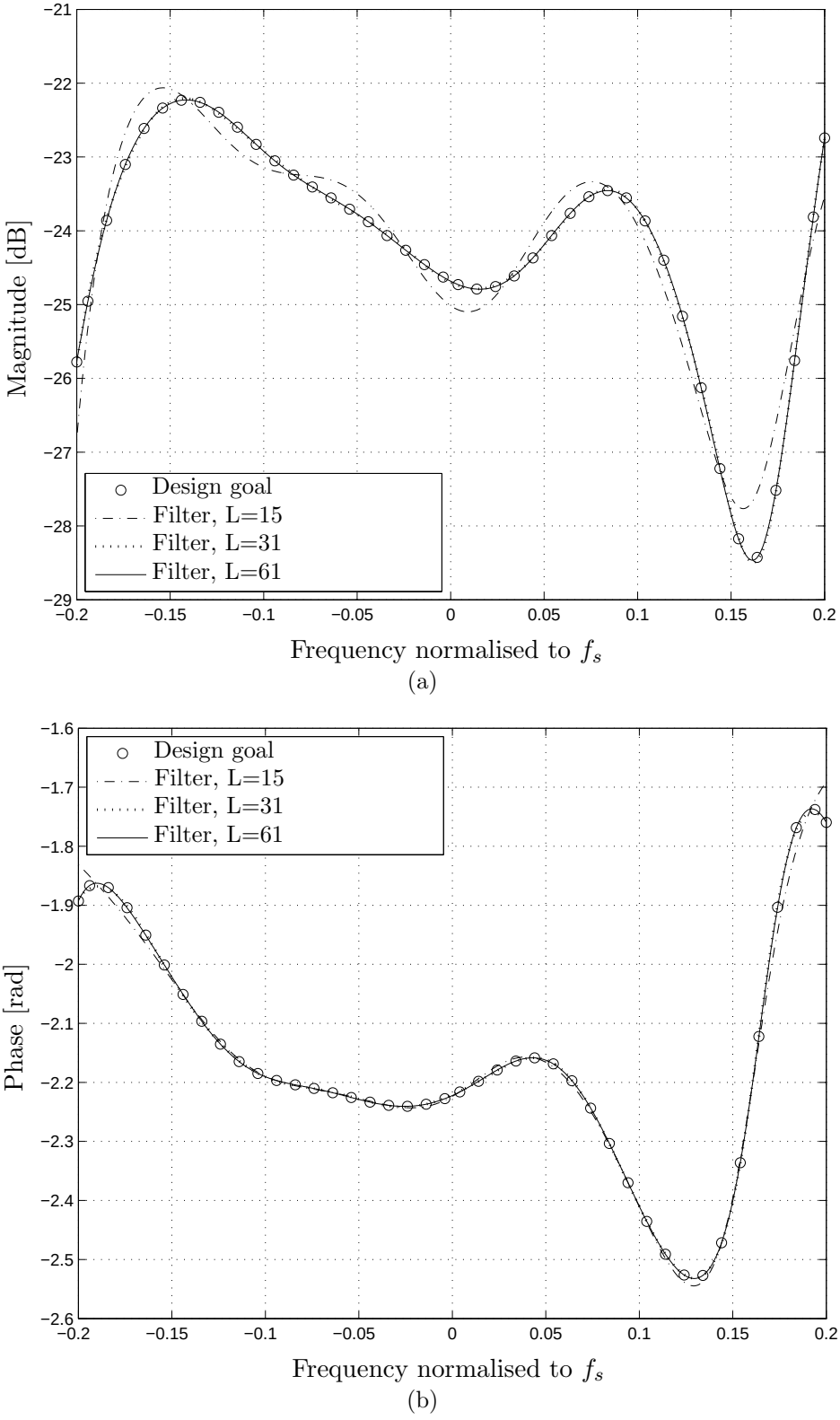


**Figure 5.9:** *Gain (a) and phase (b) response of the realised demodulator imbalance compensation filter, as a function of filter length. For the phase plot, the group delay of the filter was removed in order to show agreement with the desired phase response.*

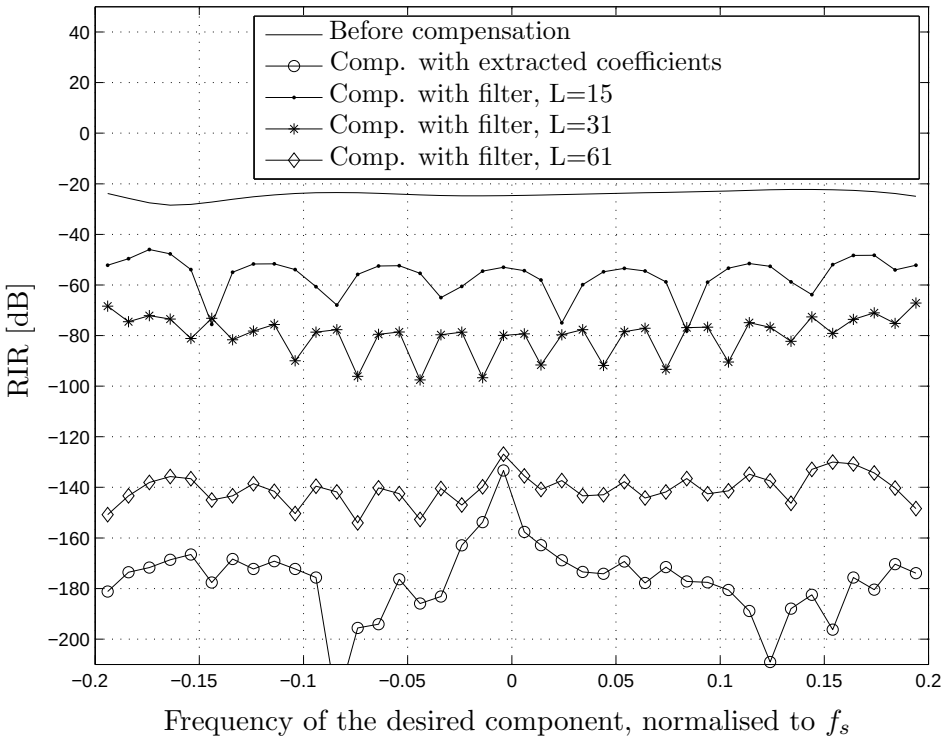


**Figure 5.10:** *RIR performance after compensation with the realised demodulator compensation filter. The performance for different filter lengths are presented. For reference, the performance when the extracted imbalance parameters are used directly for compensation, are also shown. In this case, no AWGN was added in the feedback path.*

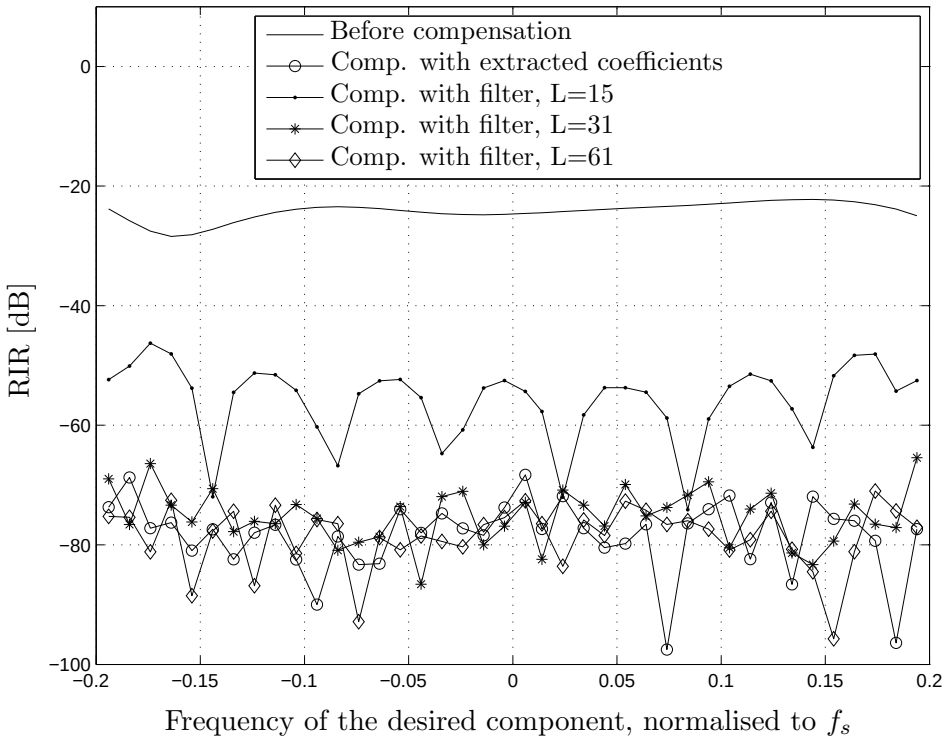


**Figure 5.11:** *RIR performance after compensation with the realised demodulator compensation filter. The performance for different filter lengths are presented. For reference, the performance when the extracted imbalance parameters are used directly for compensation, are also shown. In this case, the SNR after processing was set to 80 dB.*

### 5.2.3 Modulator compensation

This section will repeat the simulation approach that was used to validate and verify the performance of the demodulator compensation techniques, for the techniques derived for modulator compensation. The modulator extraction techniques were presented in Section 4.3.3. Since many of the simulations are very similar to those performed for the demodulator in the previous subsection, they will only briefly be described here, with reference to a more detailed discussion in the section on demodulator compensation.

The simulations regarding modulator compensation will be structured as follows. Firstly the modulator imbalance extraction technique for Scenario I (modulator and demodulator synchronised in frequency and in sample timing) will be validated. This scenario addresses the case where full LO and sample timing can be established between the modulator and demodulator. Due to the similarity between this technique and the demodulator imbalance extraction technique, the performance evaluations in noise and quantisation performed in the demodulator simulation section, would also be applicable here and is therefore not presented again. The focus is then rather shifted to the modulator imbalance extraction technique applicable to Scenarios II and III.

Scenarios II and III refers to the case where the carrier and timing synchronisation cannot be assumed or established between the modulator and demodulator. In this case the imbalances of the modulator are extracted in the digital domain of the demodulator, using the magnitude information obtained during spectral analysis on the baseband signal. These scenarios are likely to occur in practical systems and will be used in the hardware implementation, presented in Section 5.3. The performance of this extraction technique will then be investigated in the presence of noise and quantisation.

Finally, the performance of a compensation filter, realised from the extracted imbalance parameters, will be investigated.

#### Validation of extraction technique - Scenario I

*Simulation objective*

Scenario I refers to the case where LO frequency and sample timing synchronisation can be established between the modulator and demodulator.

This simulation aims to validate the modulator extraction techniques presented in Section 4.3.3 for Scenario I, as well as the modulator compensation approach described in Section 4.2.2. As with the validation of the demodulator imbalance extraction technique, the test-tone-based imbalance extraction technique developed for this scenario should be able to extract the imbalances of the modulator at each test tone frequency. When these extracted coefficients are then subsequently used for compensation, using the approach outlined in Section 4.2.2, each coefficient should be able to significantly improve the RIR of the modulator at the frequency where it was estimated. It is expected, however, that when these coefficients are used for compensation at different frequencies, the compensation will be less

efficient, due to the underlying frequency dependent nature of the modulator imbalances in the simulation.

*Simulation approach*

In this simulation, the compensation parameters of the modulator, as a function of frequency (i.e. $Q_2(f)$ as defined in Section 4.2.2), will be extracted using a number of test tones generated by the modulator. The imbalances of the modulator will extracted in the digital domain of the demodulator, using spectral analysis and the techniques developed in Section 4.3.3 for Scenario I. In order to validate the extraction technique and verify its performance, the principle of modulator compensation developed in Section 4.2.2 was be applied.

As was discussed in Section 4.3.3, this approach of Scenario I is not suitable to be used when the demodulator contributes additional imbalances of its own (unless they are first compensated for). For this reason, a perfect demodulator was used as a measurement device in the simulation and the frequency difference $\Delta f$ was set to zero. A constant non-zero phase change $\Delta\theta$ was chosen as the starting phase of the demodulator LO signal. No AWGN was added in the feedback path and no additional quantisation was applied. A long FFT (32768 points) was also used during spectral analysis in order to showcase the performance of the extraction technique.

*Results and discussion*

Fig. 5.12 presents the results of the extraction and compensation process, performed at 40 frequency points between frequencies $-0.2$ and 0.2, normalised with respect to $f_s$. The RIR is shown as a function of the desired frequency component in the digital domain of the demodulator. The figure illustrates the measured RIR before compensation, as well as after compensation using the appropriate compensation value in the extracted $Q_2(f)$, for each corresponding test tone. As can be concluded from the vast improvement in the measured RIR after compensation, the extraction process is valid for the case where synchronisation exists between the modulator and the measurement device. The slightly higher RIR after compensation close to DC is once again due to the sidelobes of the image signal interfering with the measurement process, since its separation from the desired component is smaller near DC.

Fig. 5.13 illustrates the magnitude spectra of one of the test tones in the digital domain of the demodulator, before and after compensation with the extracted imbalance parameters for that frequency. In Fig. 5.13(a) LO frequency and sample timing synchronisation between the modulator and demodulator were ensured, as was the case when obtaining the results of Fig. 5.12. In Fig. 5.13(b), the phase of the starting phase of the demodulator was chosen randomly for each test tone, simulating an uncertainty in the time that the demodulator starts sampling the test tone, relative to the time the modulator commenced transmission (non-synchronised sample timing). From the this spectral plot, it is seen that the extraction technique fails to extract the correct imbalance parameters in the presence of a non-synchronised sample timing, as was predicted in the theory derived in Section 4.3.3.

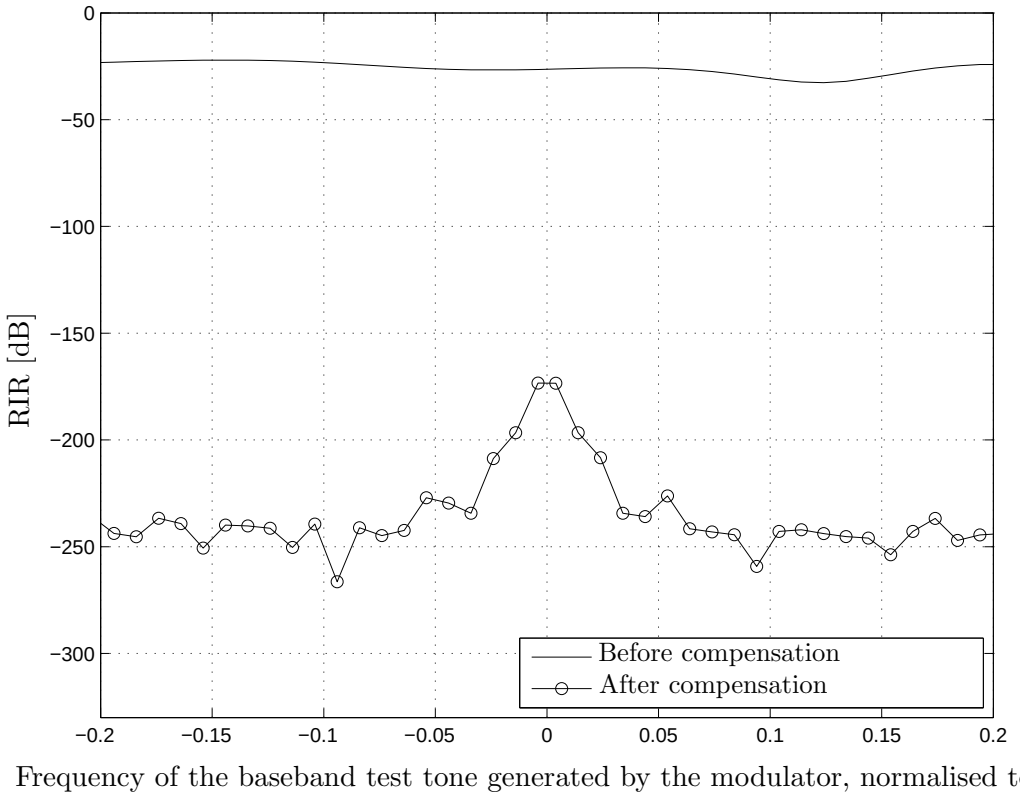


**Figure 5.12:** *Modulator RIR, as a function of the baseband frequency of the test tone at the modulator, before and after compensation, for Scenario I.*

### Validation of extraction technique - Scenario II and III

*Simulation objective*

Scenario II in Section 4.3.3 refers to the case where there the sample timing between the modulator and demodulator cannot be synchronised, while in Scenario III the frequencies of their LOs also differ. In both these cases, it was seen that this results in an unknown phase rotation on the down converted signal at the demodulator. Subsequently, a compensation technique which only uses the magnitude spectra of the measured test tone, was derived.

This simulation aims to validate the modulator extraction technique presented in Section 4.3.3 that is applicable to Scenarios II and III. The same test-tone-approach that was followed in the previous simulation for Scenario I, will be followed. The resulting extraction and compensation behaviour is expected to agree with that observed in the simulation of Scenario I, i.e. that the extracted imbalance parameters will lead to significant RIR improvements for the signal frequencies at which they were estimated, but fail to provide effective compensation for input signals at different frequencies.

*Simulation approach*

In order to validate this extraction technique, the previous simulation (aimed at validating the modulator extraction technique for Scenario I) was repeated, but this time with an offset

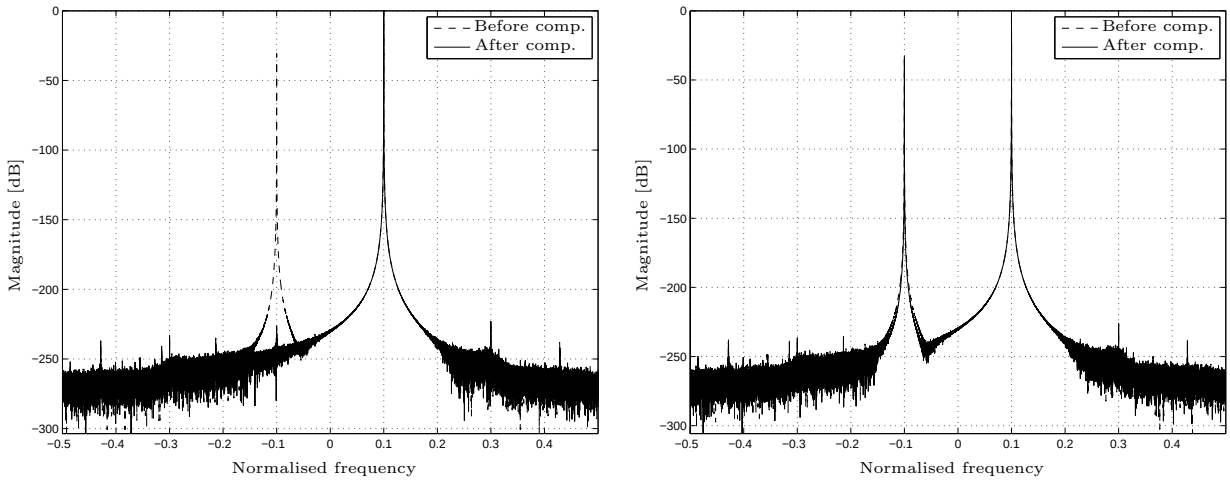


**Figure 5.13:** *Magnitude spectra illustrating effectiveness of the modulator extraction techniques presented for Scenario I. In (a) LO frequency and sample timing synchronisation between the modulator and demodulator were ensured. In (b) it is shown how the technique fails to extract the correct imbalance parameters when sample timing synchronisation cannot be ensured.*

between the LO of the modulator and demodulator. Furthermore, a random starting phase was assigned to the LO of the demodulator for each transmission by the modulator.

Once again the effect of noise and quantisation was ignored. An FFT length of 32768 was used.

*Results and discussion*

Recall from the discussion on the imbalance extraction technique for Scenario II and III on p. 82, that the magnitude spectrum of the test tones are used to extract the gain and phase imbalances as functions of frequency, $\eta_M(f)$ and $\psi_M$ respectively, which are then used to compute the desired compensation function $Q_2(f)$. Fig. 5.14 presents the results of the extraction of these functions. The theoretical values of these functions were also computed, using (2.48) to (2.51) on p. 31, along with knowledge of the filter frequency responses and mixer imbalances. The results indicate that the gain and phase functions can be very accurately estimated using the modulator imbalance extraction technique developed for Scenarios II and III.

Fig. 5.15 presents the results of the extraction and compensation process, performed at 40 frequency points between the normalised frequencies $-0.2$ and 0.2. The RIR is shown as a function of the test tone frequency generated in the baseband of the modulator. The figure illustrates the measured RIR before compensation, as well as after compensation using the appropriate compensation value in the extracted $Q_2(f)$, for each corresponding test tone. Results are presented for both the case where a perfect demodulator was used, as well as where the modulator imbalances had to be extracted in the presence of demodulator

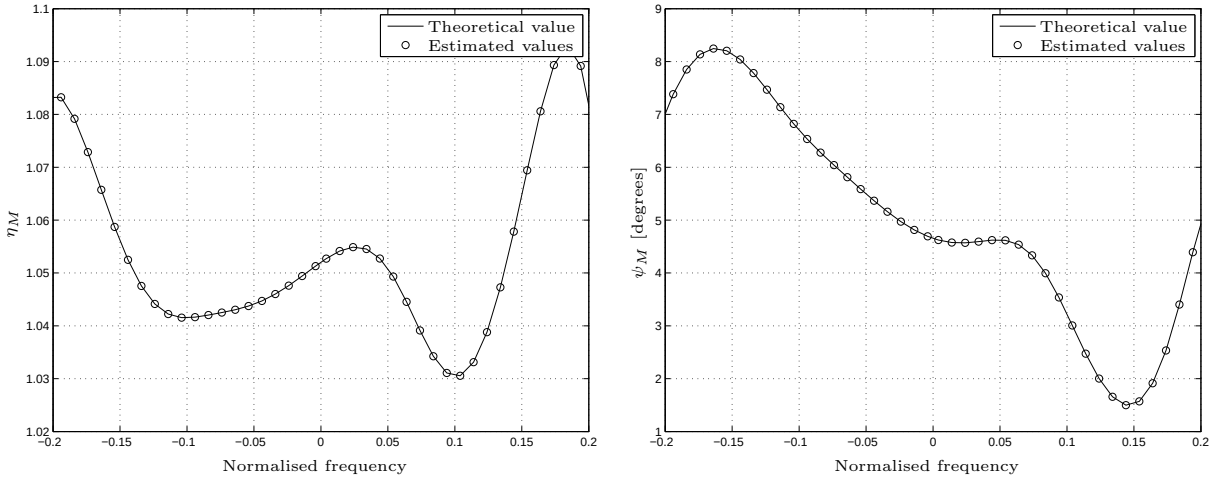


(a) (b)

**Figure 5.14:** *The gain and phase imbalance extraction performance of the modulator compensation techniques for Scenario II and III. The theoretical gain and phase imbalance of the modulator in the simulation, are also shown.*

imbalances. In addition, a plot is also included which illustrates the effect of using only a single value in $Q_2(f)$ (in this case $Q_2(0.104)$) to attempt compensation for all the input test tones.

Evaluating the vast improvement in terms of RIR, before and after applying the extracted values of $Q_2(f)$ as compensation, it can be concluded that the extraction process and underlying model is valid. The RIR performance after a single compensation coefficient (extracted for an image component at $f_r/f_s = 0.104$), is applied to all test tones, shows that the modulator imbalances exhibit a strong frequency dependence. Very good image suppression is measured at the input frequency for which coefficients were derived, however the underlying demodulator imbalance response rapidly changes from this point, leaving the compensation coefficient inadequate to deliver sufficient image rejection. This highlights the need for frequency-dependent imbalance compensation.

Once again, the slight difference between the RIR performance using a perfect demodulator and an imbalanced one, is attributed to the sidelobe structure of the demodulator imbalance spurs, which interferes with the measurement. The performance degradation in this case is negligible but highlights the fact that sufficient frequency spacing should be allowed for when choosing the offset frequency $\Delta f$. Fig. 5.16(b) shows some magnitude spectra measured in the digital domain of the demodulator, illustrating the effectiveness of the modulator imbalance extraction (and subsequent compensation) technique, even when employed with an imbalanced quadrature demodulator. Note that the image spur remaining in Fig. 5.16 (b) is due to the imbalance of the demodulator. The frequency difference $\Delta f$ is clearly seen in the separation between the image spurs due to modulator and demodulator imbalances.

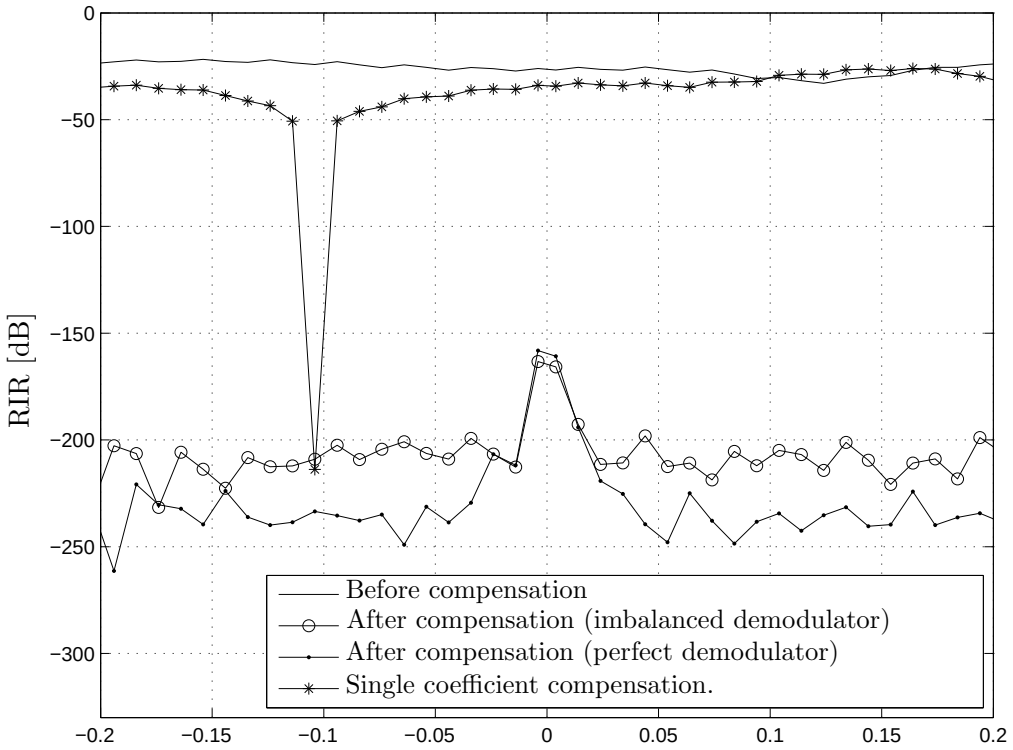


**Figure 5.15:** *Modulator RIR, as a function of the frequency of the test tone frequency in the digital domain of the modulator, before and after compensation. Results are presented for the case where a perfect demodulator is used as a measurement device, as well as the case where an imbalanced one was employed.*

### Verification of extraction performance for Scenario II and III in the presence of additive white Gaussian noise

*Simulation objective*

In this simulation the performance of the modulator imbalance extraction and compensation technique developed for Scenarios II and III, will be investigated. Analogous to the AWGN simulation performed for the demodulator in the previous section, it is expected that the achievable RIR performance will be limited to the SNR after processing (as observed with an FFT operation in the digital domain of the demodulator), since test tones are once again employed during the extraction process.

*Simulation approach*

The same approach as with the previous modulator simulation was followed here, except that AWGN was added to the test signal in the feedback path. The extraction performance was evaluated using 40 test tones over the frequency band of interest (normalised frequencies from $-0.2$ to 0.2), as a function of the SNR after processing in the digital domain of the demodulator.

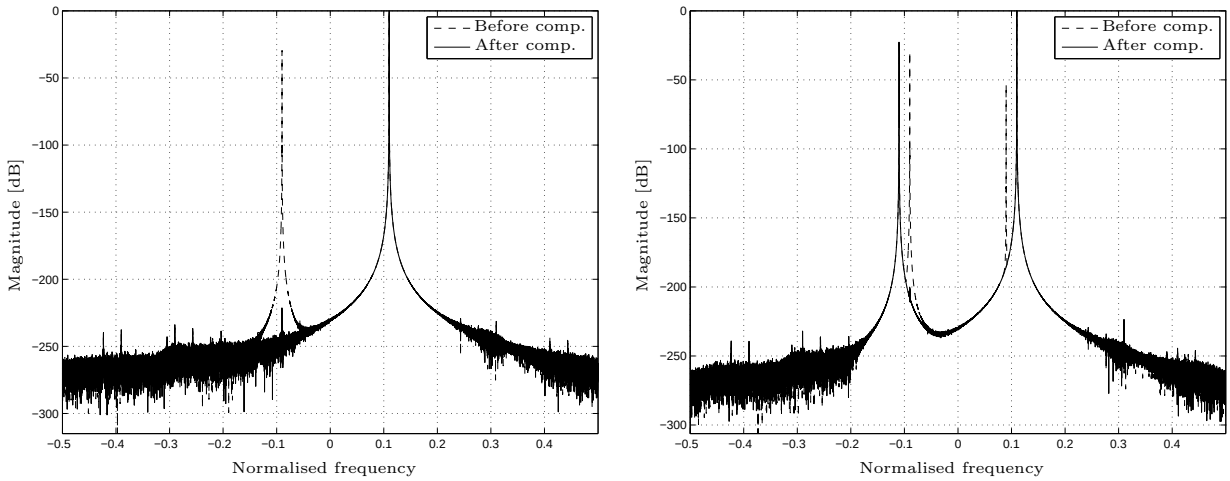


**Figure 5.16:** *Magnitude spectra in the digital domain of the demodulator, illustrating the effectiveness of the modulator imbalance extraction technique. (a) illustrates compensation of modulator imbalances when measured using a perfectly balanced demodulator, while (b) illustrates the case where an imbalanced demodulator was used.*

The noise variance in the AWGN block was controlled to test the extraction performance at SNR-after-processing values of 120, 100, 80, 60 and 40 dB. The FFT length was fixed to 8192 samples. No additional quantisation was introduced above the default 64-bit double floating point precision of MATLAB.

As with the previous simulation, the modulator imbalances were extracted using an imbalanced demodulator and a frequency offset between the LOs of the modulator and the demodulator. A random starting phase was assigned to the LO of the demodulator before each transmission of the modulator, in order to simulate unsynchronised sample timing.

*Results and discussion*

Fig. 5.17 presents the magnitude spectra of one of the test tones in the digital domain of the demodulator, in the presence of AWGN. In this case, the SNR after processing was set to 100 dB. In Fig. 5.17(a) the effect of the BPF is clearly seen, shaping the noise spectra. Since it is clearly seen that, after filtering by the BPF, the noise spectra are no longer white, the computed noise variance of the AWGN block will result in slightly higher noise level in the passband (region $-0.3$ to 0.3 in the digital domain), than specified. Nevertheless, it is seen that the modulator compensation procedure manages to suppress the modulator image spur down to the measurement noise floor. Fig. 5.18 presents that RIR performance as a function of the frequency of the baseband test tone. For each SNR value, the average of 100 runs across all 40 frequencies is presented. The results confirm that, as was the case for demodulator imbalance extraction, the imbalances of the modulator can be extracted and compensated for down to the measurement SNR after processing. The significance is once again that the RIR performance can be improved by simply increasing the FFT length.

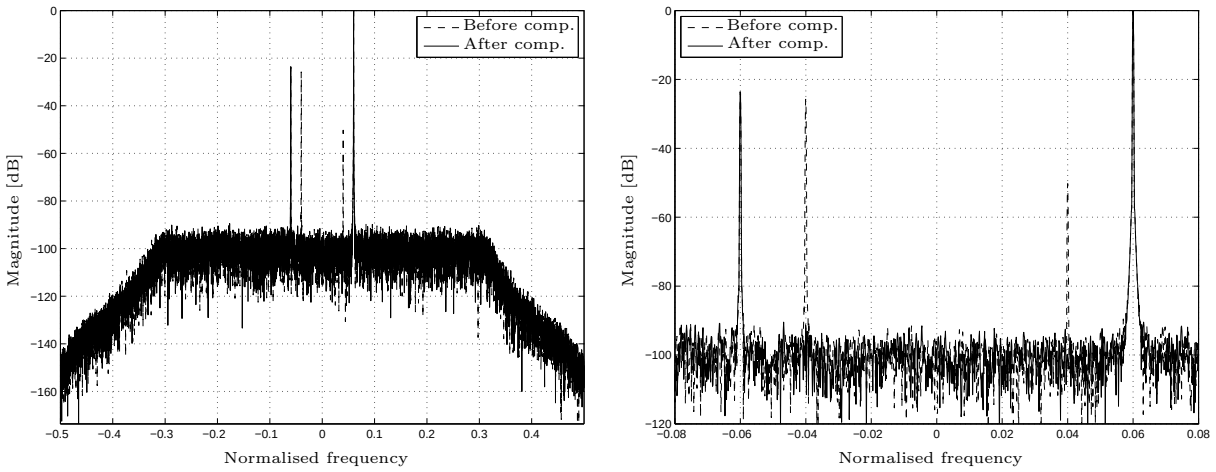


(a) (b)

**Figure 5.17:** *An example magnitude spectra of a test tone generated with an imbalanced modulator and received with an imbalanced demodulator, in the presence of AWGN. The SNR after processing in this case was set to 100 dB. The plot in (b) is a zoomed in version of the spectra in (a).*

### Imbalance extraction performance in the presence of quantisation noise

*Simulation objective*

This simulation investigates the performance of the modulator imbalance extraction technique applicable to Scenario II and III, in the presence of signal quantisation. As with the simulation performed similarly for the demodulator in the previous section, it is expected that the achievable RIR performance after compensation, will be limited by the measurement SFDR, due to quantisation. Once again, this should illustrate how the imbalance extraction performance can be improved upon, by choosing test tone frequencies which result in white quantisation noise spectra. In these cases the processing gain of the FFT operation can be harnessed to improve the measurement SFDR and therefore also the accuracy with which the imbalance parameters can be extracted.

*Simulation approach*

In this simulation, the extraction and compensation performance were tested as a function of the number of quantisation bits of the sampler system. The quantisation blocks indicated in the simulation topology of Fig. 5.1 was used to quantise the signal after the digital domain of the modulator and before the digital domain of the demodulator. The number of bits were varied from 4 to 25 bits. At each bit precision, test tone frequencies were used which resulted in white quantisation noise spectra. The extraction and compensation performance were tested by extracting the imbalances at using a test tone and applying the extracted parameters as compensation on the same frequency. In order to obtain an indication of the average performance, 100 test tones per quantisation setting were used, each at a slightly different frequency. Demodulator imbalances were disabled.

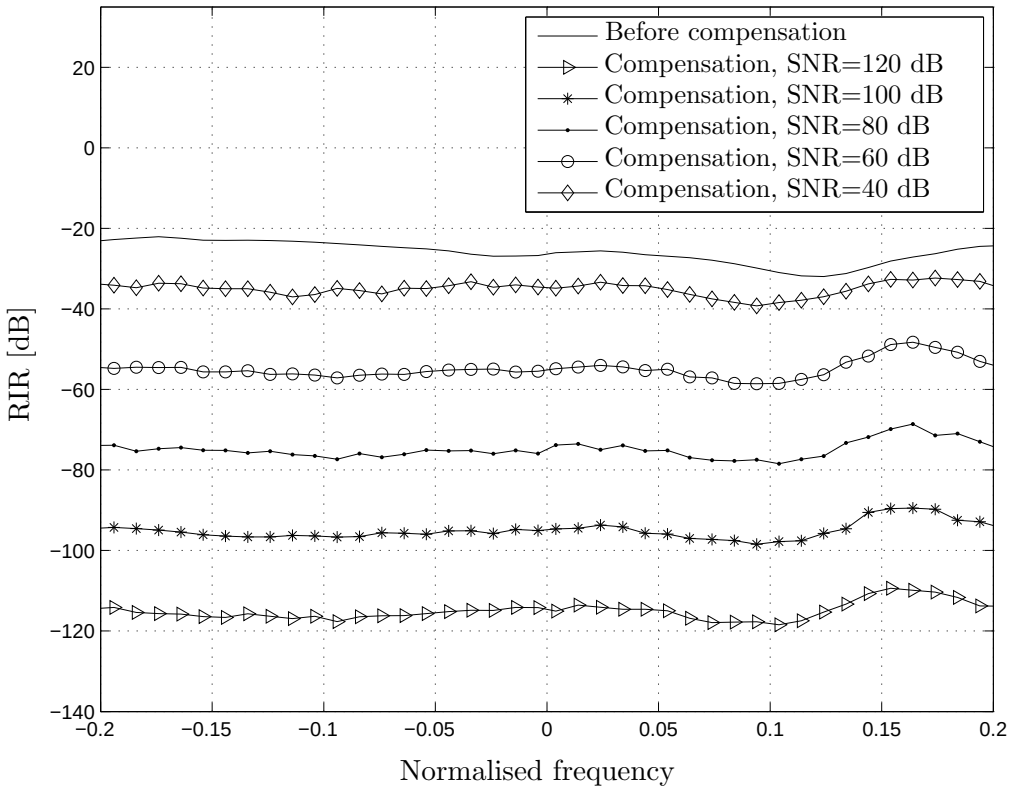


**Figure 5.18:** *Modulator RIR performance after compensation, in the presence of AWGN,for Scenarios II and III. The SNR is specified after processing.*

*Results and discussion*

Fig. 5.19 presents the achievable RIR after compensation, as a function of the number of quantisation bits. The theoretical measurement SFDR (negated) for a white quantisation noise spectrum is also shown, which was computed using (5.7).

When compared to the demodulator result in Fig. 5.8 on p. 124, it is seen that the RIR results of the modulator is about 3 dB worse than that of the demodulator. This could be explained by the fact that the modulator extraction process requires the consecutive transmission of two tones (one at the desired frequency and one at the image frequency, see Section 4.3.3 on p. 89), compared to the single tone required for demodulator imbalance extraction. During the processing of each of these tones, the magnitude estimation errors due to quantisation noise should be uncorrelated between the two measurements. However, since the estimation of the modulator imbalance parameters are a function of both tone-measurements, a 3 dB loss compensation performance can be expected, on average, compared to the demodulator case. The modulator RIR performance of Fig. 5.19 does, however, illustrate that the achievable RIR performance improves at the same rate as the theoretical SFDR due to quantisation noise with a white frequency spectrum (at roughly 6 dB per bit) – illustrating how the RIR performance is determined by the SFDR. As with the demodulator, it can also be concluded from this result that through careful choice of the test

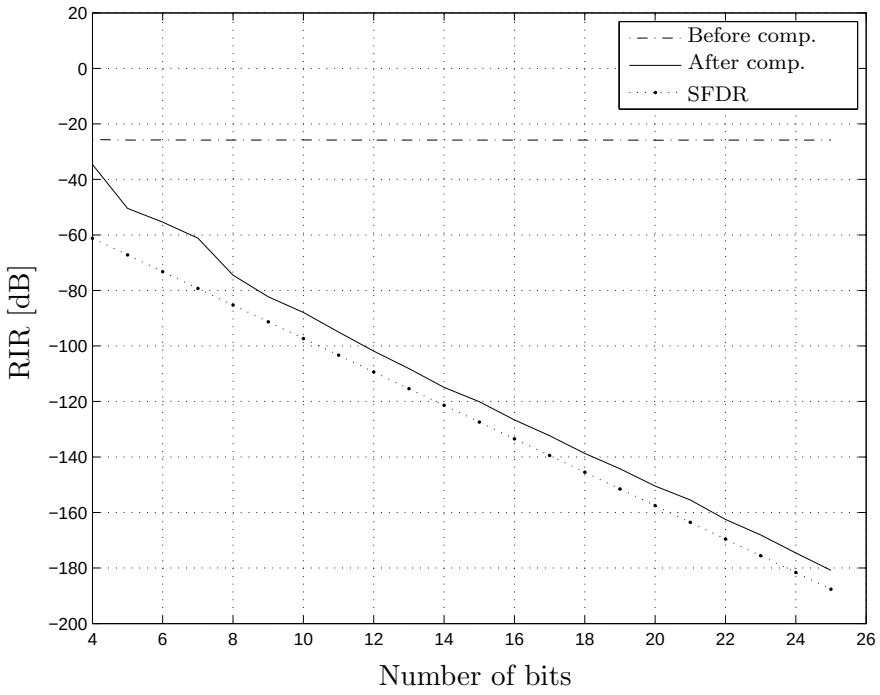


**Figure 5.19:** *The achievable modulator RIR after compensation, as a function of the number of quantisation bits. The theoretical measurement SFDR (negated) for a white quantisation noise spectrum is also shown.*

tone frequencies (i.e. ensuring that the quantisation noise spectrum is white), the processing gain of the FFT can be used to improve the achievable RIR. This conclusion is based on the fact that the calculation of the theoretical SFDR included the effect of the FFT processing gain.

### Verification of the compensation filter performance

*Simulation objective*

This simulation aims illustrates how the extracted modulator compensation values at the test tone frequencies, can be used to design a FIR compensation filter, which offers a true frequency dependent imbalance compensation solution. As with the demodulator, the performance loss, as a function of compensation filter length, is then investigated. From a similar simulation performed for the demodulator (see p. 125) it can be expected that even relatively short filters (with 30 to 60 filter taps), should be able to represent the desired frequency response accurately enough to deliver RIR performance of as low as −80 dBc.

*Simulation approach*

In this simulation, the parameters of the compensation function $Q_2(f)$ was once again extracted at various frequencies, using the test tone-based technique derived for modulator

imbalance extraction, Scenario II and III. However, unlike the previous simulations, these parameters were then be used to design a single complex compensation filter, with frequency response equal to $Q_2(f)$, estimated at discrete points using the test tones. An imbalanced demodulator was employed as measurement device, with a LO frequency slightly offset from that of the modulator.

The compensation filter was designed using the procedure outlined in Section 4.4, using $|Q_2(f)|$ and $\angle Q_2(f)$, respectively, as the desired gain and phase response of the filter. The effectiveness of the filter was investigated by using it to pre-filter various baseband test tones in the modulator's digital domain, passing them through the imbalanced modulator and demodulator, and measuring the modulator RIR after in the digital domain of the demodulator using an FFT.

As with the demodulator, the compensation filter was designed in such a way that every second coefficient in its impulse response equals zero. The frequency band of interest was also chosen to extend from $-0.2$ to 0.2 (normalised in relation to $f_s$). The simulation was performed for an infinite SNR as well as a more realistic SNR of 80 dB (after processing).

*Results and discussion*

Fig. 5.20 illustrates the effectiveness of the filter design procedure, as described in Section 4.4, by presenting the desired gain and phase response of the filter, as well as the gain and phase response of the realised filter, for different filter lengths. The desired gain and phase response of the filter is derived from $|Q_2(f)|$ and $\angle Q_2(f)$, respectively, which was estimated at 40 discrete frequency points in the frequency band of interest ($-0.2$ to 0.2), using the test tones generated by the imbalanced modulator. It is seen how the response of the designed filters follow the desired response in the frequency region $-0.2$ to 0.2, with the longer filter length of 61 taps following the desired response more closely than the short 15-tap filter.

Fig. 5.21 presents the results of using the designed compensation filter to compensate for modulator imbalances. The compensation performance of different length filters are compared to the RIR performance achieved by selecting the correct extracted compensation coefficient in $Q_2(f)$, based on the frequency of the test tone. It is seen that the compensation performance corresponds well with that obtained during the simulation of the demodulator compensation filters (see p. 125).

Fig. 5.22 illustrates the results where the simulation was repeated, but for a SNR after processing of 80 dB. From this figure it is seen that the performance of the compensation filter is independently limited by the accuracy with which the imbalance parameters can be extracted, as well as the number of taps in the filter. This is identical to what was observed for the demodulator compensation filters.

It can be concluded that, in practice, the compensation performance obtained using compensation filters, will most likely be limited by the accuracy with which the desired response can be estimated, rather than the process of translating the desired response to an actual filter.

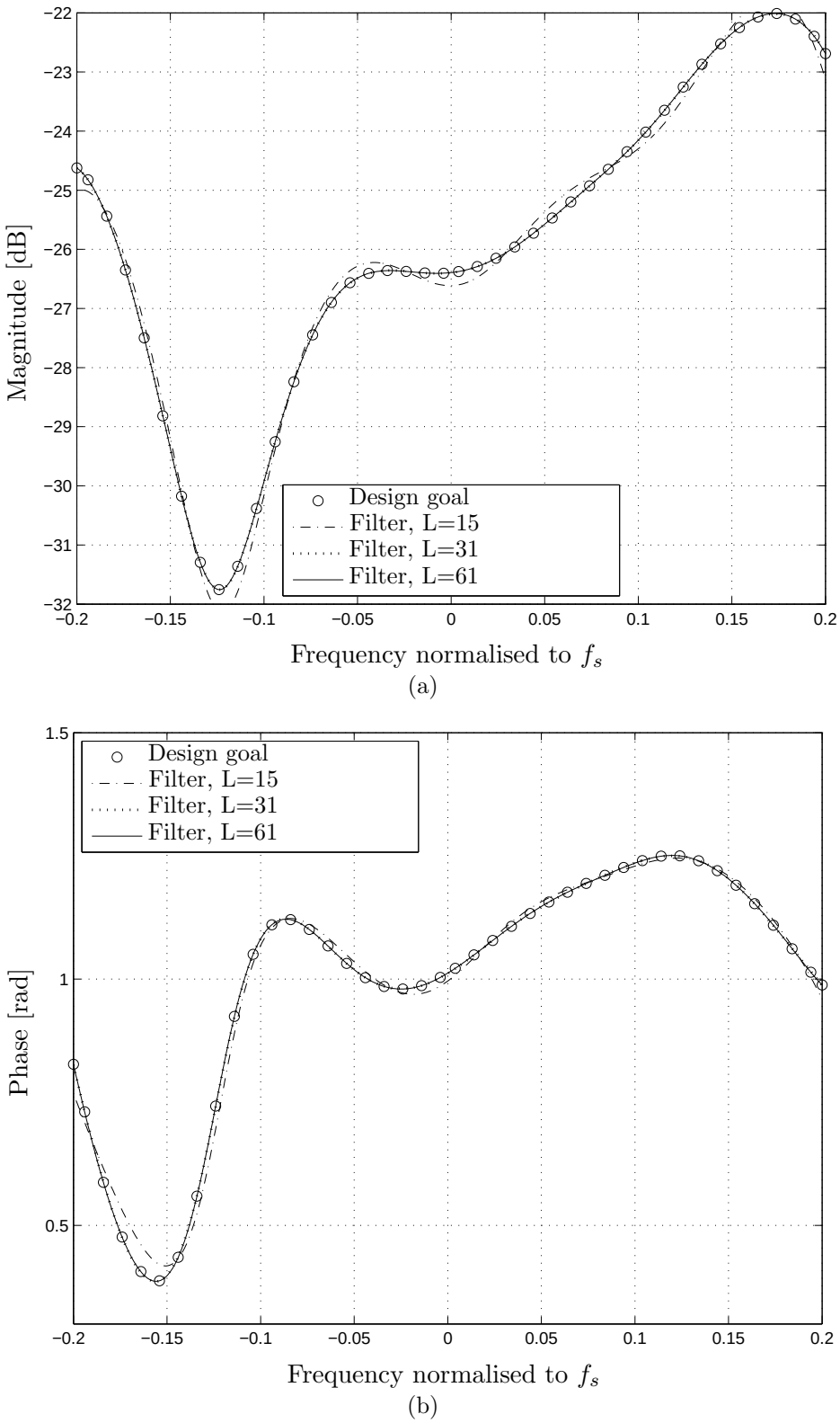


**Figure 5.20:** *Gain (a) and phase (b) response of the realised modulator imbalance compensation filter, as a function of filter length. For the phase plot, the group delay of the filter was remove in order to show agreement with the desired phase response.*

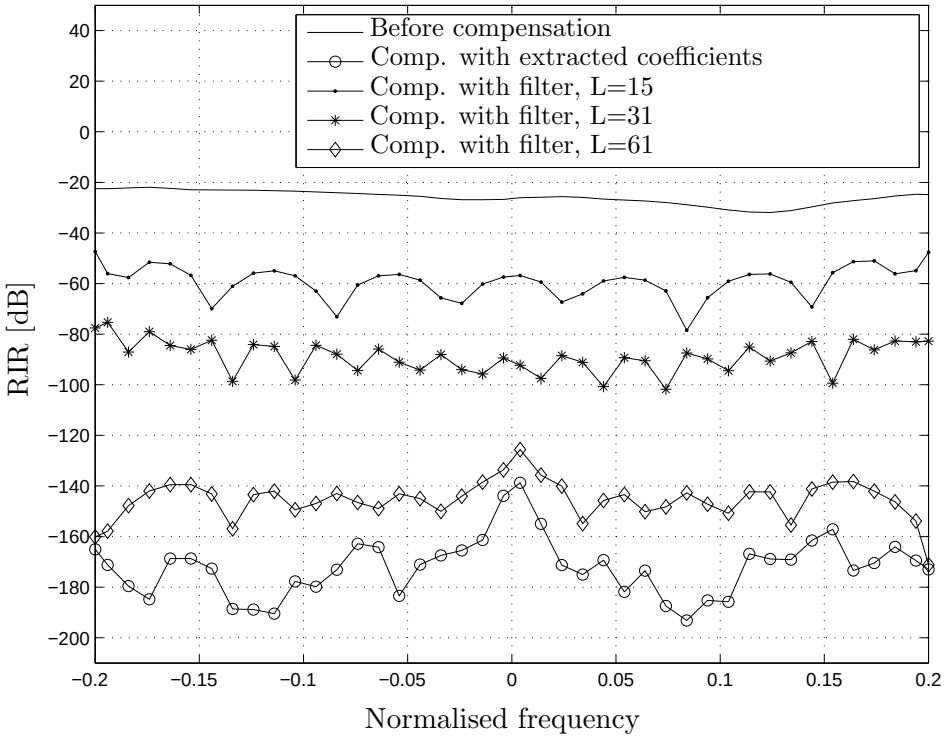


**Figure 5.21:** *RIR performance after compensation with the realised modulator compensation filter. The performance for different filter lengths are presented. For reference, the performance when the extracted imbalance parameters are used directly for compensation, are also shown. In this case, no AWGN was added in the feedback path.*

### 5.2.4 Summary and conclusions

The simulations in this section served to validate the novel imbalance extraction techniques presented in Chapter 4, as well as to verify their performance in the presence of additive noise and quantisation. It also implicitly validated the underlying baseband-equivalent models of Chapter 2, that were used to derive the extraction techniques.

For both the modulator and demodulator extraction techniques, it was seen that the SFDR of the measurement determines the limit to which the imbalances can be extracted. When the extraction is performed in the presence of AWGN it was seen that since the test signals are tones, the processing gain of the FFT can be used to increase the SFDR of the measurement, and therefore also the accuracy of the imbalance estimation, by increasing the number of samples processed in the FFT.

It was seen that quantisation can result in spectral components that range from harmonic tones, to a white noise spectrum, depending on the amplitude of the tone, as well as the relationship between the frequency of the tone and the sampling rate. It is therefore important to choose the frequencies of the compensation test tones such that a white quantisation noise spectrum results. Not only will this result in a lower SFDR for a given FFT length

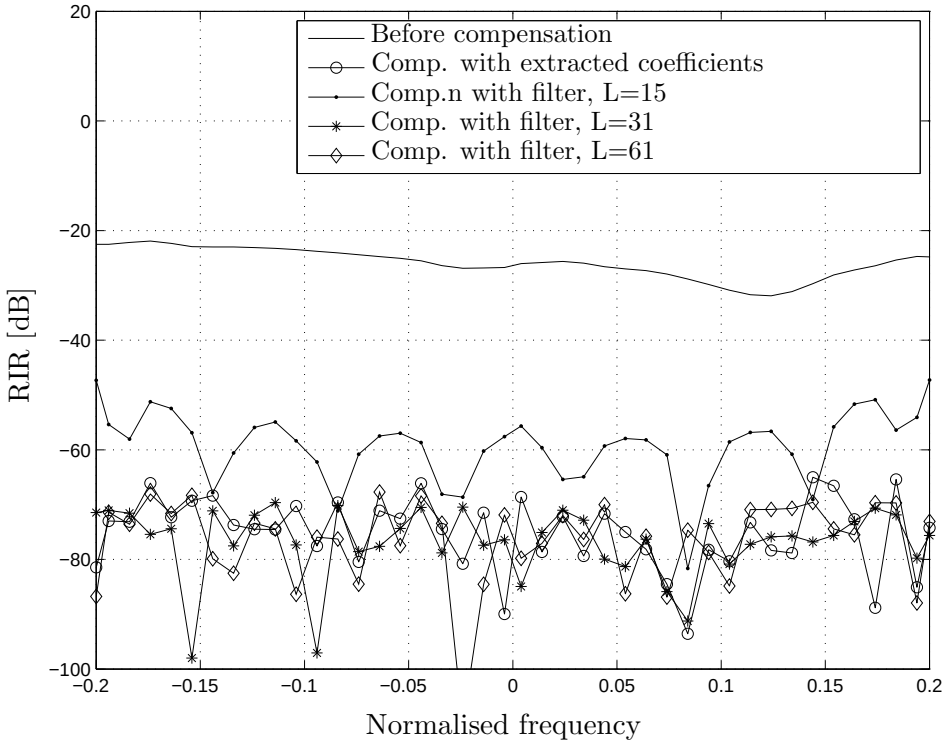


**Figure 5.22:** *RIR performance after compensation with the realised modulator compensation filter. The performance for different filter lengths are presented. For reference, the performance when the extracted imbalance parameters are used directly for compensation, are also shown. In this case, the SNR after processing was set to 80 dB.*

(since the quantisation noise energy is spread across more frequency components), but the processing gain of the FFT can be used to increase the SFDR by increasing the FFT length.

The simulations finally also illustrated the performance of the compensation filters. It was shown that significant imbalance compensation can be achieved with a 61-tap filter, with every second filter tap chosen to be zero.

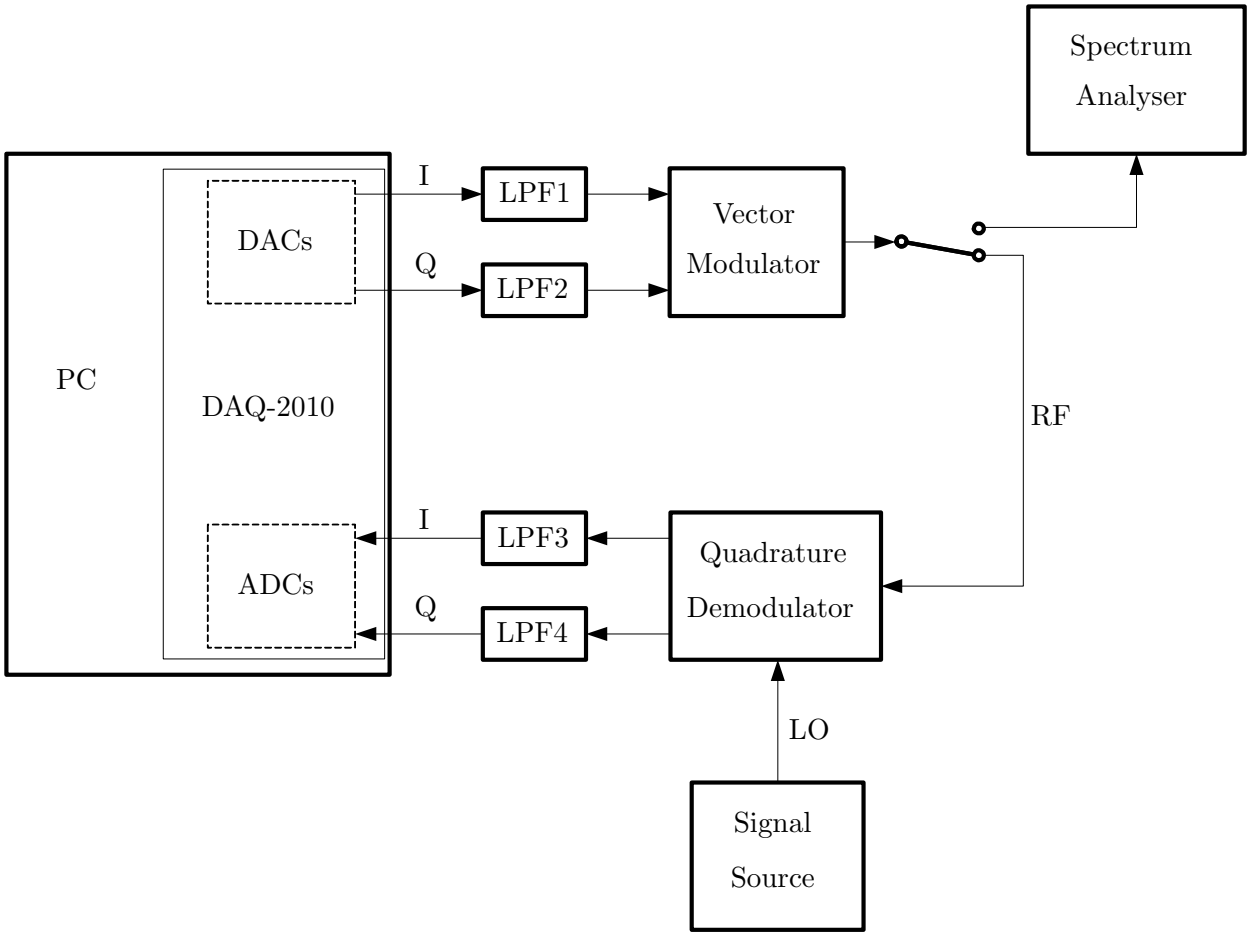


**Figure 5.23:** *Hardware setup used for the hardware implementation tests.*

## 5.3 Performance evaluation: Hardware implementation

In the previous section, the imbalance compensation techniques that were derived in this chapter were validated and their performance verified under different operating scenarios. This section will extend the validation process further by using a hardware implementation of a quadrature modulator and demodulator to test the effectiveness of the compensation techniques in practice. These tests will also serve as a validation of the underlying distortion models that were derived in Chapter 2.

### 5.3.1 Hardware measurement setup

Figure 5.23 shows the setup that was used to practically implement and test the imbalance and offset extraction and compensation techniques that were developed in this study. A desktop PC was used to perform all the needed digital signal processing and also to interface

**Table 5.4:** *Operating settings of the DAQ-2010.*

| **Parameter** | **ADCs** | **DACs** |
|---|---|---|
| Bits precision | 12 | 14 |
| Input/output range [V] | 0 to +5 | –10 to +10 |
| Sampling rate [samples/s] | $1 \times 10^6$ | $1 \times 10^6$ |

with the DAQ-2010 data acquisition card. An Rohde and Schwarz (R&S) SMIQ04 signal generator and vector modulator was used to implement a quadrature upmixer. A R&S spectrum analyser was used to inspect the spectrum of the RF up-mixed signal. The quadrature down-mixer was implemented with an RF2713 monolithically integrated circuit (IC) from RF Micro Devices. An R&S SML03 signal generator supplied the LO signal to the RF2713 IC.

The setup therefore represents the scenario where an imbalanced quadrature modulator is paired with an imbalanced quadrature demodulator in a transceiver. The imbalanced demodulator will be used as a measurement device, while the imbalanced modulator will generate the test tone that will be used to extract the imbalances of both the modulator and demodulator.

The next few subsections will discuss each component of the hardware implementation in more detail.

### Software implementation

All the digital signal processing was implemented using 64-bit double precision floating point numbers, on an Intel Core 2 Duo 3.00 GHz PC with 2 GB RAM, running a Linux operating system. Most of the extraction and compensation algorithms were developed in C++, using the software-defined radio (SDR) library [18, 53], developed at Stellenbosch University. The filter design algorithm was, however, implemented in MATLAB. The SDR library was also used for interfacing with the data acquisition cards. During the course of this study, a number of new library blocks were contributed to the SDR library.

### Signal conversion

Signal conversion between the digital and analogue domain was done through the use of a NuDAQ® DAQ-2010 data acquisition card from ADLINK Technology Inc. This card has a 32-bit PCI-Bus interface and slots directly into a PC. The operating settings of the DAQ-2010 that were used for this study are summarised in Table 5.4.

### Quadrature up mixing

The quadrature up-mixing was implemented with an R&S SMIQ04B signal generator and vector modulator. The SMIQ04B has the capability to perform quadrature vector modu-

**Table 5.5:** *Quadrature impairment settings of the SMIQ04B for this study.*

| Impairment parameter | Value |
|---|---|
| (LO) Leakage | 1.86% |
| (Gain) Imbalance | 4.9% |
| Quadrature offset (phase error) | 5.2° |

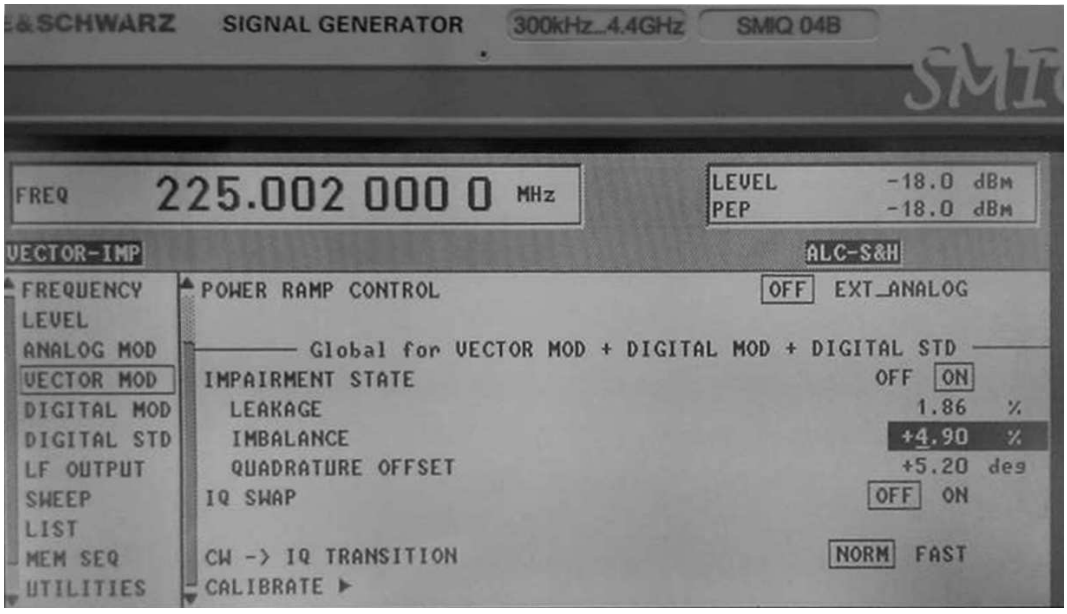


**Figure 5.24:** *IQ impairment settings of the R&S SMIQ04B vector modulator, as used during the practical experiments.*

lation up to a carrier frequency of 4.4 GHz. The SMIQ04B does not require an external LO signal to perform vector modulation, since it also provides signal generator capabilities. The carrier frequency for the vector modulator was chosen to be 225.002 MHz. As will be seen later, this is 2 kHz above that of the quadrature down-mixer that was used. This was done to ensure that imbalances of the demodulator do not influence the extraction of the imbalances of the modulator (as was discussed in Section 4.3.3).

The vector modulation of the SMIQ04B can be done with adjustable gain imbalance, phase error and oscillator leak-through levels. This allows for a very versatile testing platform for the compensation algorithms in a hardware setup. The quadrature impairments of the SMIQ04B that were used in this study, are shown in Table 5.5. A photo of the SMIQ's user interface is shown in Fig. 5.24.

### Quadrature down-mixing

An RF2713 IC was used to perform quadrature down-mixing. The RF2713 is a monolithically integrated quadrature up- or down-mixer IC, by RF Micro Devices. The application circuit

**Table 5.6:** *Typical imbalance and offset errors of the RF2713 IC [44].*

| Impairment parameter | Typical value | Worst case value |
|---|---|---|
| I/Q amplitude balance (Gain imbalance) | 1.012 | 1.059 |
| Quadrature phase error | 1° | – |
| DC output | 2.4 V | 2.8 V |
| DC offset | $\leq$ 10 mV | 100 mV |

to implement the RF2713 IC as a quadrature down-mixer can be found in its datasheet [44]. The RF21713's operating frequency range is from 100 kHz to 250 MHz. The RF2713 IC needs an external oscillator signal at twice the desired carrier frequency. This signal was supplied by a R&S SML03 signal generator. The carrier frequency was chosen to be 225 MHz, and therefore a 450 MHz signal was supplied by the SML03. Therefore an effective 2 kHz frequency offset existed between the LOs of the modulator and the demodulator.

The RF2713 IC is a good example of a typical low-cost, low-power quadrature mixer IC that could be used for digital and analogue receivers and transmitters [44]. As such, it was seen as a good candidate to test the performance of the developed software compensation techniques of this study. The typical imbalance and offset values of the RF2713, according to its datasheet, are shown in Table 5.6.

### Lowpass filters

The LPFs used in the front-end of the modulator were active second-order Butterworth filters. The filters were constructed using the Sallen-Key configuration. The filters were designed to be identical, with 3 dB cut-off frequencies of 200 kHz. However, due to discrete component tolerances, these cut-off frequencies varied from filter to filter. The cut-off frequencies were chosen to conform to the frequency band of interest over which the imbalance compensation was to be performed. The normalised frequency band of interest was chosen from $-0.2$ to 0.2, which corresponds to $-200$ kHz to 200 kHz for the 1 MHz sampling rate that was employed.

For the demodulator, SMA connectorised LPFs from Mini Circuits[1] were employed. The cut-off frequency of these filters was nominally 10.7 MHz. This cut-off frequency was deemed sufficient, since these filters are used to reject the double-frequency components that will be generated around $2 \times 225$ MHz $= 450$ MHz due to the mixing process in the demodulator.

### Calibration tone generation

In the practical tests, the imbalanced modulator setup is used to generate all test tones required for extracting the imbalances of both the modulator and the demodulator.

[1]See www.minicircuits.com

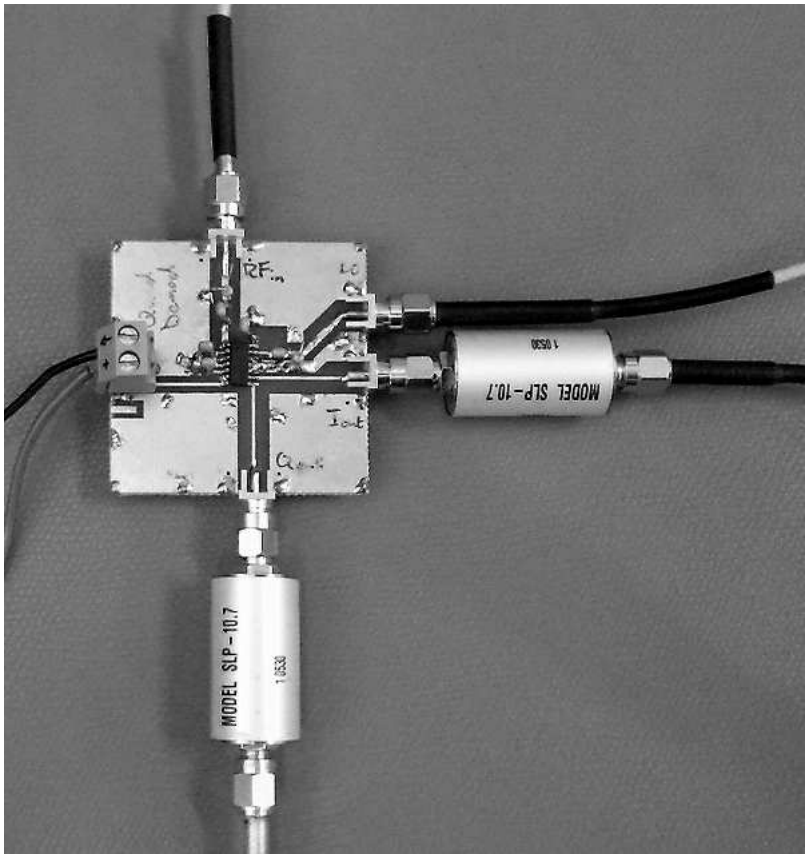


**Figure 5.25:** *The RF2713 IC implemented in a demodulator configuration with external 10.7 MHz LPFs.*

#### Passband spectral analysis

An R&S spectrum analyser was included in the setup in order to confirm the correct working of the modulator, as well as to measure the passband SFDR after modulation.

### 5.3.2 Modulator imbalance compensation

#### Aim of experiment

The aim of this experiment is to validate the modulator imbalance extraction and compensation techniques, developed in Chapter 4, on a hardware implementation of a quadrature modulator. As described below in the 'Experiment approach', the modulator extraction technique applicable to Scenario II and III is applicable, since no synchronisation in terms of LO frequency or sample timing was established between the modulator and demodulator.

From the simulation preformed earlier in this chapter (see Section 5.2.3), it is expected that the imbalance extraction and subsequent compensation performance would be limited to the SFDR due to AWGN and quantisation. This result will be verified for a practical setup in this experiment.

Furthermore, this experiment investigates the effectiveness of realising and implementing FIR compensation filters from the extracted imbalance function. Their compensation performance will be compared to the compensation results obtained using the individually extracted imbalance parameters for compensation. From the simulation results, it is expected that it should be possible to design compensation filters which manage to achieve the same RIR performance as the individually applied compensation parameters in the filter specification. The difference is, of course, that the filters represent a true frequency-dependent compensation solution. The RIR performance is therefore expected to be limited by the extraction accuracy and not the translation of the extracted parameters to an actual filter, even for relatively low order filters.

Finally, this experiment aims to investigate the characteristics of the underlying imbalance response of a practical modulator, in terms of its symmetry around DC. It is expected that some bandpass imbalance response should be present, therefore necessitating the use of complex-valued FIR filters.

**Experimental approach**

Modulator imbalance extraction was facilitated through test tones generated in the digital domain of the modulator, passed through the DACs and transmitted by the imbalanced modulator, which was realised with the SMIQ04 vector modulator. The RF output signal was routed into the imbalanced demodulator, down-converted, sampled by the ADCs and streamed to the memory of the PC. The imbalance extraction techniques were then performed through software on the PC.

Since an imbalanced modulator was used for test tone generation, as well as the measurement device, a frequency offset between the LOs of the modulator and demodulator was required. Furthermore there existed an unknown delay between the time that the modulator commenced the transmission of the test tone and the time that the demodulator started to sample the down-converted signal. This implied that, for modulator imbalance compensation, the technique derived for Scenario II and III should be used to extract the imbalances. During the imbalance extraction process, an 8192 point FFT was used with Blackman amplitude windowing.

Forty test tones were generated over a 400 kHz frequency band of interest. This relates to a frequency range from $-0.2$ to 0.2, when normalised with respect to the sampling rate of 1 MHz. At each test tone frequency, the extraction procedure was repeated four times – each subsequent run first applied the extracted imbalance parameters of the previous run as compensation, extracted new imbalance estimates, and then updated the previous gain and phase estimation with newly extracted parameters. The extracted gain and phase imbalances were updated according to the following update rules: $\eta_{M,k+1} = \eta_{M,k} \times \eta_{M,new}$ and $\psi_{M,k+1} = \psi_{M,k} + \psi_{M,new}$, where the subscript $k$ denotes the iteration number. This was done in an effort to obtain some additional averaging, however it was found that this procedure did not result in improved RIR performance after more than two repetitions per

frequency point.

Once the compensation function $Q_2(f)$ had been estimated at the discrete test tone frequencies, the compensation filter was derived using the techniques discussed in Section 4.4. The effectiveness of the compensation filter was evaluated by repeating the sequence of test tones, but this time pre-filtering each with the realised compensation filter, and measuring the resultant RIR in the digital domain of the demodulator.

**Results and discussion**

Fig. 5.26 shows the magnitude response of a test tone in the digital domain of the demodulator. The tone was generated at a normalised frequency of $-0.094$ ($-94$ kHz) in the digital domain of the modulator. In Fig. 5.26 (a) the whole Nyquist bandwidth is shown, before compensation. The desired component (now at a normalised frequency $-0.092$ in the demodulator's digital domain, due to the LO offset of 2 kHz), as well as image components due to modulator and demodulator imbalances are present. The RIR of the modulator for this input tone is seen to be $-22$ dB, while the demodulator RIR is $-39$ dB. The quantisation noise produces spurious components with magnitudes of up to $-51$ dBc and various components at around $-60$ dBc. In addition, some non-linear distortion is observed in the form of harmonics and intermodulation products, the strongest of which is seen to be about $-28$ dBc. A modulator carrier leak through component is observed at 0.002 (due to the LO offset of 2 kHz). Note that the DC component of the demodulator was removed before spectral analysis, by subtracting the mean of the received signal.

Although the realised hardware system suffers from much undesired spurious content, the scope of this dissertation is limited to the mitigation of the effect of quadrature imbalances. In reality, some mitigational tactics would be required to improve the total SFDR of the transceiver.

Fig. 5.26 (b) illustrates a zoomed-in version the magnitude spectrum, before and after applying the extracted value for $Q_2(f)$ as modulator compensation. The undesired modulator image component is reduced in magnitude from $-30$ dBc to $-60$ dBc. This is also the level at which the quantisation spurs occurs. The demodulator image spur remains unchanged.

The modulator gain and phase imbalance extraction procedure was repeated at 40 different frequencies throughout the frequency band of interest. Fig. 5.27 presents the extracted gain and phase imbalance functions, respectively, as defined in (2.55) and (2.56). It is clearly seen that the values extracted at normalised frequencies $-0.114$ and $-0.104$ do not fit the smooth trend exhibited by the rest of the extracted points. It will be shown in the RIR performance plots, that the extracted imbalanced at these two frequencies also do not provide effective compensation. It is not clear why the extraction process failed to effectively extract the imbalance parameters at these points. It is likely that some of the spurious content present in the spectrum of the down converted signal aligned with the desired and image components at those frequencies, therefore distorting the measurement. The points were discarded as outliers and a linear interpolation was done to obtain new values at these

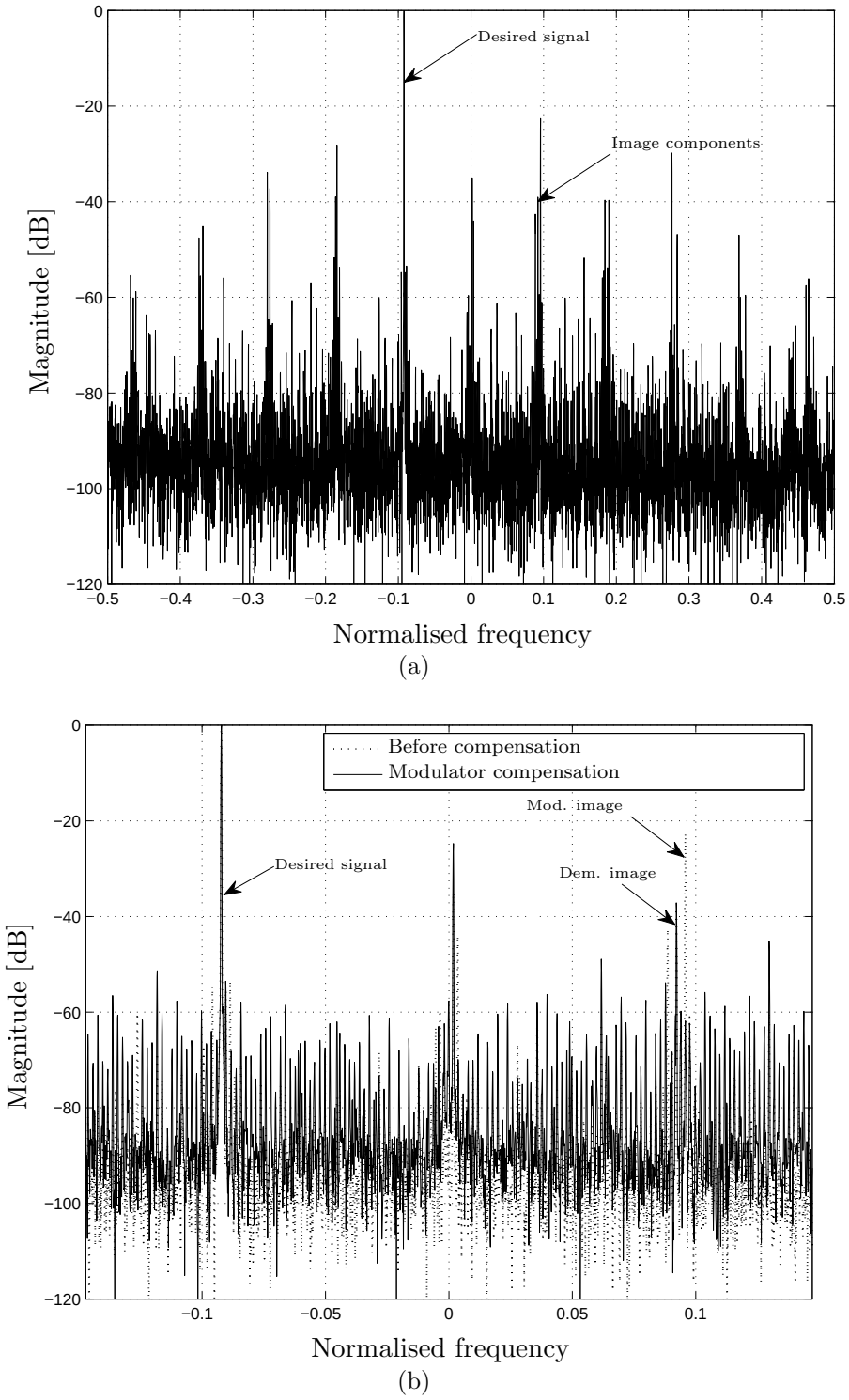


**Figure 5.26:** *Magnitude response of a test tone in the digital domain of the demodulator. (a) shows the whole Nyquist zone, while (b) shows a zoomed in version of the area around DC, showing the effectiveness of modulator compensation. The spur due to demodulator imbalances remains unchanged.*

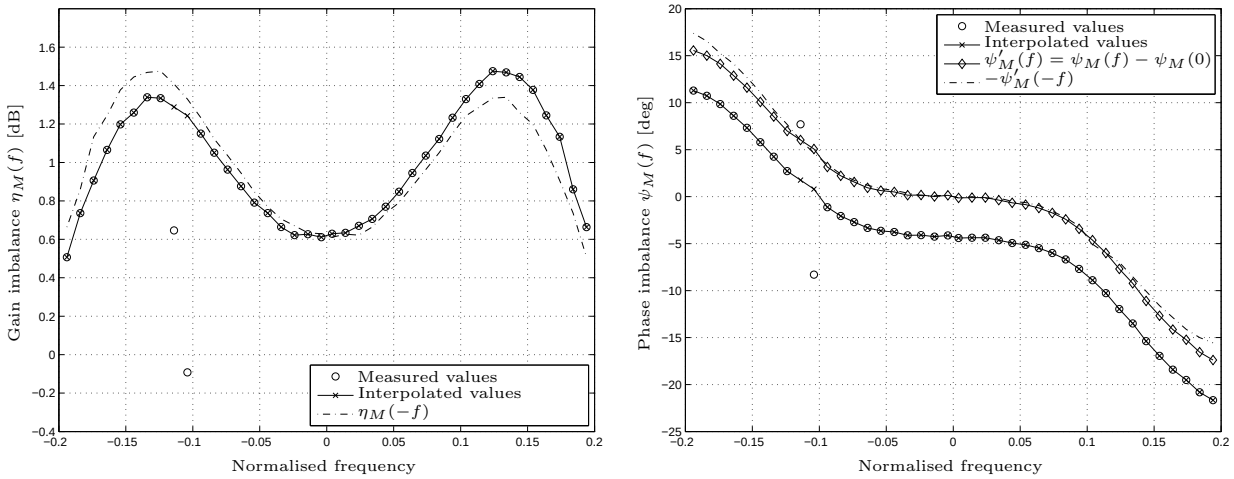


(a) Gain imbalance (b) Phase imbalance

**Figure 5.27:** *Extracted gain (a) and phase (b) imbalance of the modulator, as a function of the normalised frequency. For each graph, additional functions are provided to aid in visually determining whether the gain function imbalance function is even and whether the phase imbalance function is odd after removal of the phase offset at DC.*

frequencies. The interpolation was performed separately for the gain and phase imbalance functions. These interpolated values are also shown in the figure.

Fig. 5.27 can also be used to evaluate the symmetry of the gain and phase imbalance functions. Plots to aid in this evaluation was also added to the figure. The gain imbalance function exhibits an almost even symmetry around 0 Hz, but does show aberrations that indicate the presence of an asymmetrical bandpass response. The symmetry of the phase imbalance function is also shown after removal of the phase offset at DC. The phase imbalance has approximately odd symmetry. However, it deviates from this symmetry at higher frequencies. The phase imbalance at DC agrees well with the 5.2 degrees mixer phase imbalance set on the SMIQ04 vector modulator.

The deviation from even and odd symmetry exhibited by the gain and phase imbalance function, confirms the argument that the frequency-dependent imbalances of quadrature mixers cannot simply be modelled as an imbalanced LPF response, and strengthens the case for the inclusion of the BPF mismatches in the imbalance model. Note that this asymmetrical behaviour will be much more pronounced in the demodulator measurements in the next section. It is likely that since the SMIQ04 (used as the hardware implementation of a quadrature modulator), is inherently a wideband system capable of modulating signals on a carrier up to 4.4 GHz, its bandpass response in its signal paths should be relatively well behaved over the small frequency extent over which it was used in this experiment. This is not the case for the demodulator implementation presented next, which uses a low cost hardware quadrature mixer IC.

To achieve optimal compensation performance, complex-valued compensation filters were

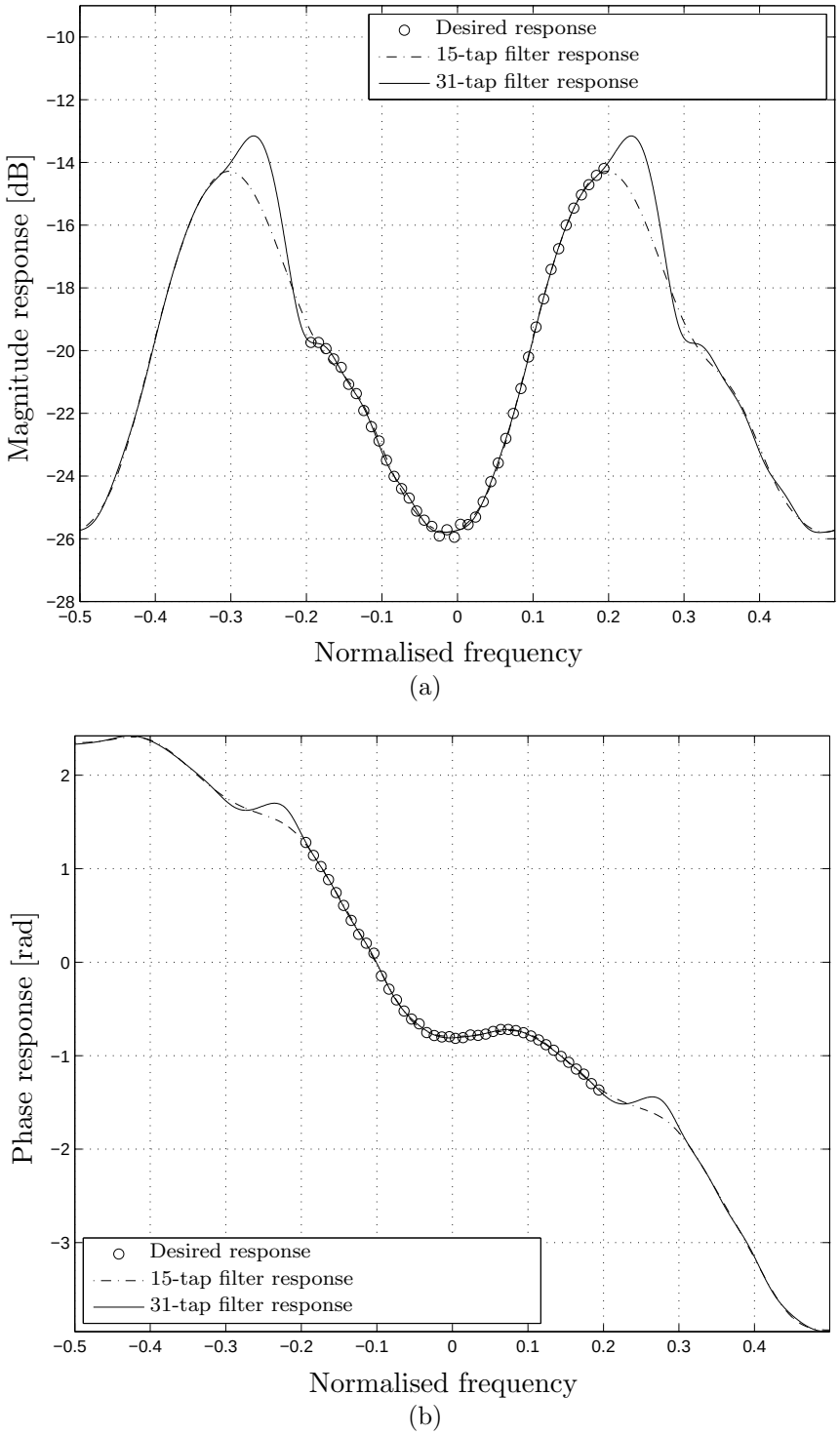


**Figure 5.28:** *Magnitude (a) and phase (b) response of two realised modulator compensation filters of different lengths. The desired response, as estimated through the imbalance extraction process is also shown.*

designed, which closely approximates the desired response at positive and negative frequencies.

The extracted gain and phase imbalances, as a function of frequency, was subsequently

used to compute the complex frequency response of the compensation filter, $Q_2(f)$, according to (4.65):

$$Q_2(f) = \frac{\eta_M(f)e^{j\psi_M(f)} - 1}{\eta_M(f)e^{j\psi_M(f)} + 1}\,. \tag{5.8}$$

From this desired filter response, two compensation filters of different lengths were designed: one with 15 taps and one with 31 taps, according to the procedure outlined in Section 4.4. The magnitude and phase response of the realised filters are shown in Fig. 5.28, along with the desired response, as estimated through the imbalance extraction process. Fig. 5.28 shows that the magnitude response does not exhibit even symmetry around DC and the phase response is not an odd function of frequency, even when the offset phase at DC is subtracted. This again indicates, as explained in Section 4.4, the presence of bandpass frequency-dependent imbalances, which are not included in imbalance models found in literature. A compensation filter with a complex transfer function is therefore necessary to compensate for the frequency-dependent imbalances.

Finally, the realised compensation filters were implemented, separately, in the digital domain of the modulator, in order to pre-filter the digital signal before it passes through the imbalanced modulator. The resulting RIR after compensation was tested by retransmitting the series of test tones, this time pre-filtered the signal with the chosen compensation filter. The RIR was then measured in the digital domain of the demodulator. Fig. 5.29 presents the RIR of the modulator, before and after applying various forms of compensation. For each case, the RIR was measured in the digital domain of the demodulator, using test tones spaced throughout the frequency band of interest.

In the figure, the case is presented where only a single coefficient, in this case $Q_2(0.104)$, is applied as a scalar compensation coefficient to all test tones transmitted by the modulator – an approach often proposed in literature when frequency independent imbalances are assumed. It is seen that although this value provides good image suppression for the input frequency for which it was derived for ($f = -0.104$), the RIR performance quickly deteriorates for frequencies further from the this point. This illustrates a strong frequency dependence in the $I/Q$ imbalances of the modulator, yielding a frequency independent compensation approach inadequate for this implementation.

Secondly, the extracted imbalance parameters (the estimate of $Q_2(f)$ at discrete points) are tested to evaluate their effectiveness. This is done by applying the appropriate entry in $Q_2(f)$ as a scalar compensation value, based upon the frequency of the test tone that is to be transmitted. Note that for this test the original extracted values for frequencies $-0.114$ and -0.104 were used and not the interpolated corrections. In Fig. 5.26(b), the quantisation noise spurs seem to occupy levels as high as $-51$ dBc, with quite a few spurs on the region of $-60$ dBc. From the simulation results on the extraction performance in the presence of quantisation noise, it can therefore be expected that the modulator imbalance extraction performance should result in a RIR that is also in this region. The resultant RIR in Fig. 5.29 shows, with the exception of the frequency points 0.114 and 0.104, the extracted imbalance

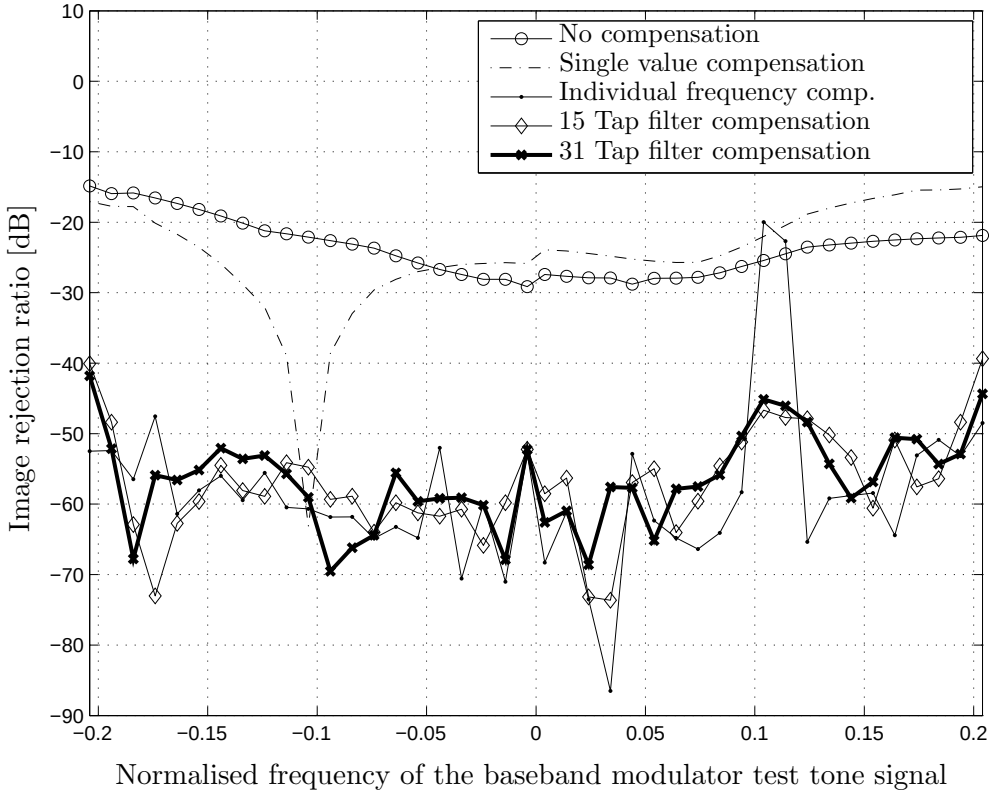


**Figure 5.29:** *RIR of the modulator as a function of frequency, before and after imbalance compensation.*

parameters offer very significant improvement in the RIR of the modulator. The resultant RIR also agrees with the behaviour confirmed through simulation, in that it is approximately limited to the SFDR due to quantisation. As predicted from the extracted gain and phase imbalance graphs, the compensation coefficients at $Q_2(-0.114)$ and $Q_2(-0.104)$ do not offer valid compensation.

Finally, the graphs in Fig. 5.29 present the resultant RIR when the realised compensation filters are employed in the modulator to facilitate imbalance compensation. Both the 31-tap and the 15-tap filter perform equally well, on par with the individually applied coefficients in $Q_2(f)$. This is because in this case, the RIR performance is limited by the accuracy to which the imbalance parameters can be extracted and not by the filter realisation or filter length. In the region where the interpolated values for $Q_2(-0.114)$ and $Q_2(-0.104)$ were used, the filter manages to improve the RIR significantly, although a slight performance degradation is present. The performance in this area could have been improved through the use of more sophisticated interpolation procedures, such a spline fitting, instead of a simple linear fit between the neighbouring values.

### 5.3.3 Demodulator imbalance compensation

#### Aim of experiment

The aim of this experiment is to validate the demodulator imbalance extraction and compensation technique, developed in Chapter 4, on a hardware implementation of a quadrature demodulator.

Similarly to the previous experiment regarding modulator compensation, this simulation also aims to investigate the limit on the achievable RIR performance, as a function of the SFDR due to AWGN and quantisation.

Digital FIR compensation filters will be designed and their compensation performance compared to the case where the individual compensation parameters at each test tone frequency is used for compensation. As with the modulator, the RIR performance using compensation filters, is expected to be limited by the extraction accuracy and not the translation of the extracted parameters to an actual filter, even for relatively low order filters.

This simulation then finally also aims to investigate the characteristics of the underlying imbalance response of a practical demodulator, in terms of its symmetry around DC. It is expected that a more pronounced bandpass imbalance response, compared to the case of the hardware modulator, should be present. This is expected since the RF2713 IC used in the demodulator implementation is not a wideband device, as was the case with the *R&S* SMIQ04 vector modulator used to implement the quadrature modulator. Complex-valued FIR filters should therefore be required.

#### Experimental approach

The modulator was used to generate the test tones required to extract the imbalance of the demodulator, as well as to test the effectiveness of the compensation. During these tests, the compensation filters of the modulator were left in place, when it was used for test tone generation. The demodulator imbalances were extracted in the digital domain of the demodulator, using spectral analysis and the techniques developed in Section 4.3.2. During the extraction process, an 8192 FFT was used with Blackman windowing.

Forty test tones were employed throughout a 400 kHz frequency band of interest. This relates to a normalised (to the digital sampling rate) frequency range from $-0.2$ to 0.2.

Once the compensation function $P_2(f)$ had been estimated at the discrete frequency points corresponding to the employed test tones, the compensation filter was derived using the techniques discussed in Section 4.4. The effectiveness of the compensation filter was evaluated by repeating the sequence of test tones and filtering the down converted signals with the realised compensation filter.

#### Results and discussion

Fig. 5.30 shows the magnitude spectra of a test tone in the digital domain of the demodulator, before and after testing the demodulator extraction accuracy by applying the extracted value

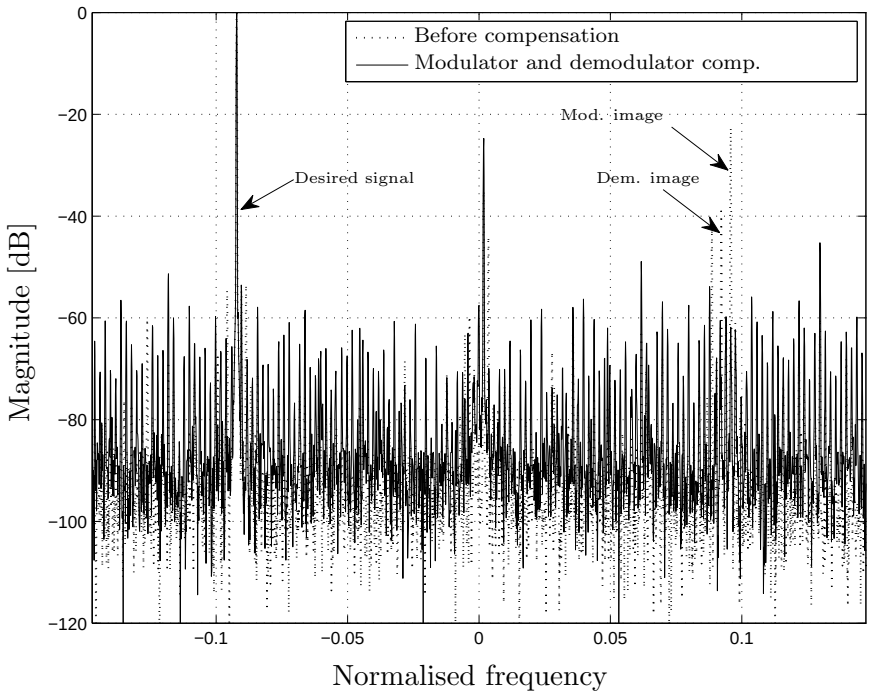


**Figure 5.30:** *Magnitude response of a test tone in the digital domain of the demodulator during demodulator compensation, illustrating the effectiveness of demodulator and modulator compensation. The spur due to modulator compensation was already compensated for in the previous experiment.*

for $P_2(f)$ as compensation. The undesired demodulator image component is reduced in magnitude from $-39$ dBc to $-71$ dBc. This is lower than many of the spurious components due to quantisation noise. Note that the spur due to modulator imbalances was compensated for in the previous experiment.

The demodulator imbalance compensation function $P_2(f)$ was extracted at discrete frequencies throughout the frequency band of interest, using the novel extraction techniques developed in Chapter 4. In order to investigate the symmetry of the gain and phase imbalance functions $\kappa_D(f)$ and $\chi_D(f)$, they were estimated from the extracted $P_2(f)$, using the method described in Section 4.4.1 in (4.124) and (4.125). The resultant gain and phase imbalance functions are presented in Fig. 5.31. From Fig. 5.31(a), it is seen that the gain imbalance function is not a symmetrical function of frequency. The phase imbalance function in Fig. 5.31(b), shows that, when the offset phase at DC is removed, the function does not exhibit odd symmetry – the frequency-flipped and negated version is provided as visual aid. The estimation process to obtain the gain and phase functions from $P_2(f)$ has been validated in Section 4.4.1 where it was shown that even for severe imbalances, the approximations for $\kappa_D(f)$ and $\chi_D(f)$ are very accurate. To prove this point further, the approximated functions $\widehat{\kappa_D}(f)$ and $\widehat{\chi_D}(f)$ were used to reconstruct an estimation for $P_2(f)$. The originally extracted $P_2(f)$ and its reconstruction using the approximations for the gain and phase im-

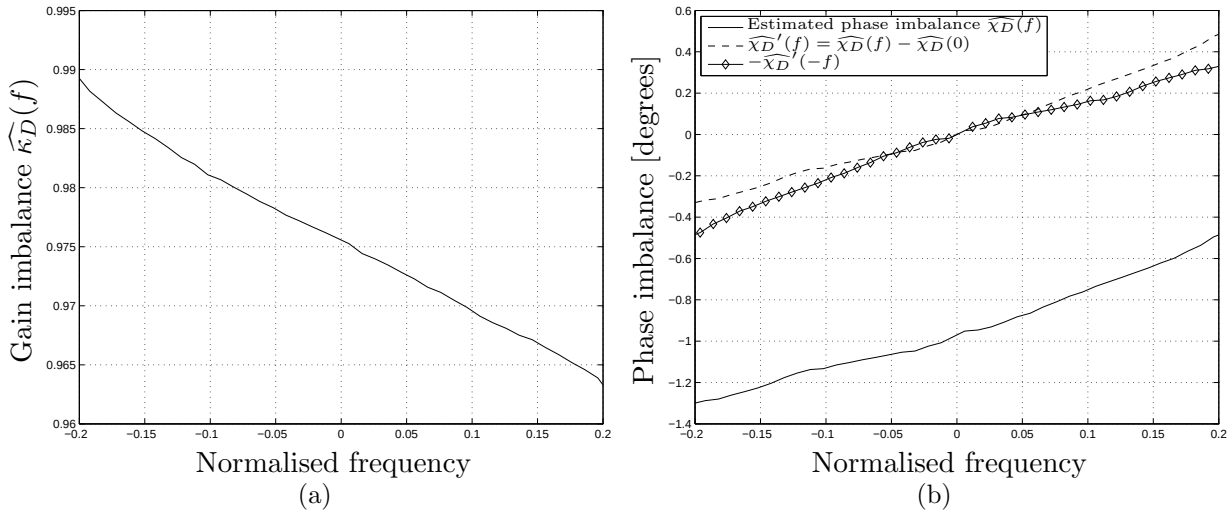


**Figure 5.31:** *Approximate contribution of the gain (a) and phase (b) imbalance functions to the extracted demodulator imbalance function $P_2(f)$. In (b) the phase imbalance function is also shown with the offset at DC removed. The frequency flipped and negated value of this function is also presented in order to visually evaluate whether the function is odd. It is seen that this is not the case.*

balance functions, are shown in Fig. 5.32, split into the magnitude and phase of $P_2(f)$. The approximated gain and phase imbalance functions reproduce $P_2(f)$ very closely.

From the asymmetry in the graphs, it can be concluded that a bandpass imbalance is present in the demodulator, which cannot be modelled by only considering imbalanced LPFs. The frequency-dependent imbalances of the demodulator can therefore not be compensated for by using a real-valued filter; it requires a complex-valued filter. This result validates the inclusion of a BPF imbalance in the modelling of quadrature imbalances, since it manages to model the full behaviour of the frequency-dependent imbalances observed in a practical hardware quadrature demodulator.

The extracted response for $P_2(f)$, was used to design two compensation filters of different lengths: one with 13 taps and one with 31 taps, according to the procedure outlined in Section 4.4. The magnitude and phase response of the realised filters are shown in Fig. 5.34, along with the desired responses, as estimated through the imbalance extraction process. It is noticed that the 14 tap filter offers a visibly poorer approximation of the desired response, compared to the approximation of the 31-tap filter. As was found with the practical implementation of the modulator, the desired compensation filter magnitude response is not not an even function and the phase response is not an odd function of frequency. This again confirms that a BPF imbalance response is present and should be modelled in the imbalance modelling process. The use of a compensation filter with a complex-valued transfer function is also necessary in order to effectively compensate for the frequency-dependent imbalances.

Fig. 5.33 presents the RIR of the demodulator, before and after applying different imbalance compensation approaches. For compensation approach each case, the RIR was mea-

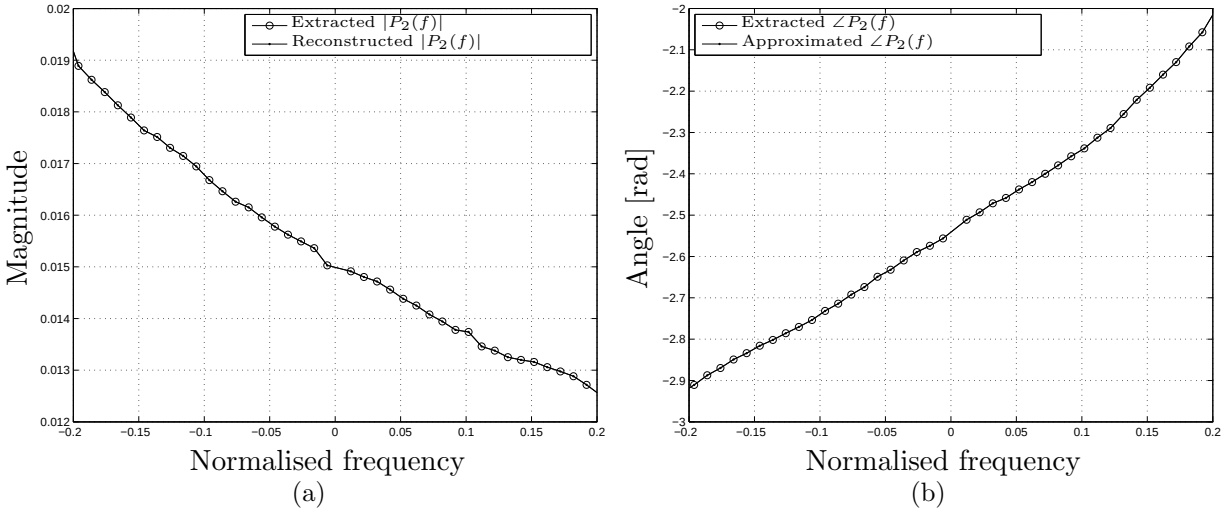


**Figure 5.32:** *The magnitude (a) and phase (b) of the extracted demodulator imbalance function $P_2(f)$, along with the reconstructed version using the estimated gain $\widehat{\kappa_D}(f)$ and phase $\widehat{\chi_D}(f)$ functions.*

sured in the digital domain of the demodulator, using test tones throughout the frequency band of interest. In the figure, the case is presented where only a single coefficient, in this case $P_2(0.112)$, applied as a scalar compensation coefficient to all test tones transmitted by the modulator. It is seen that although this value provides good image suppression at the input frequency it was derived for ($f = -0.112$), the RIR quickly increases for frequencies further from the this point. As was observed at the modulator, this illustrates a strong frequency dependence in the $I/Q$ imbalances of the demodulator as well.

Secondly, the extracted imbalance parameters (the estimation of $P_2(f)$ at discrete points) are tested to evaluate their effectiveness. This is done by applying the appropriate entry in $P_2(f)$ as a scalar compensation value, based upon the frequency of the test tone that is to be transmitted. In Fig. 5.30(a), the quantisation noise spurs seem to occupy levels as high as -51 dBc, with quite a few spurs on the region of $-60$ dBc. From the simulation results on the extraction performance in the presence of quantisation noise, it can therefore be expected that the demodulator imbalance extraction performance should perform slightly better than this level. When analysing the resultant RIR in Fig. 5.33, it is seen that the extracted imbalance parameters realise a very significant improvement in the RIR performance of the demodulator. The resultant RIR level does also agree with behaviour confirmed through simulation, in that the image component is rejected to the approximate SFDR level due to quantisation.

Finally, the graphs in Fig. 5.33 also present the resultant RIR when the realised demodulator compensation filters are employed to facilitate imbalance compensation. It is seen that the 31-tap filter performs as well, as the compensation results achieved by using the individually selected coefficients. This indicates that in this case there is no perfor-

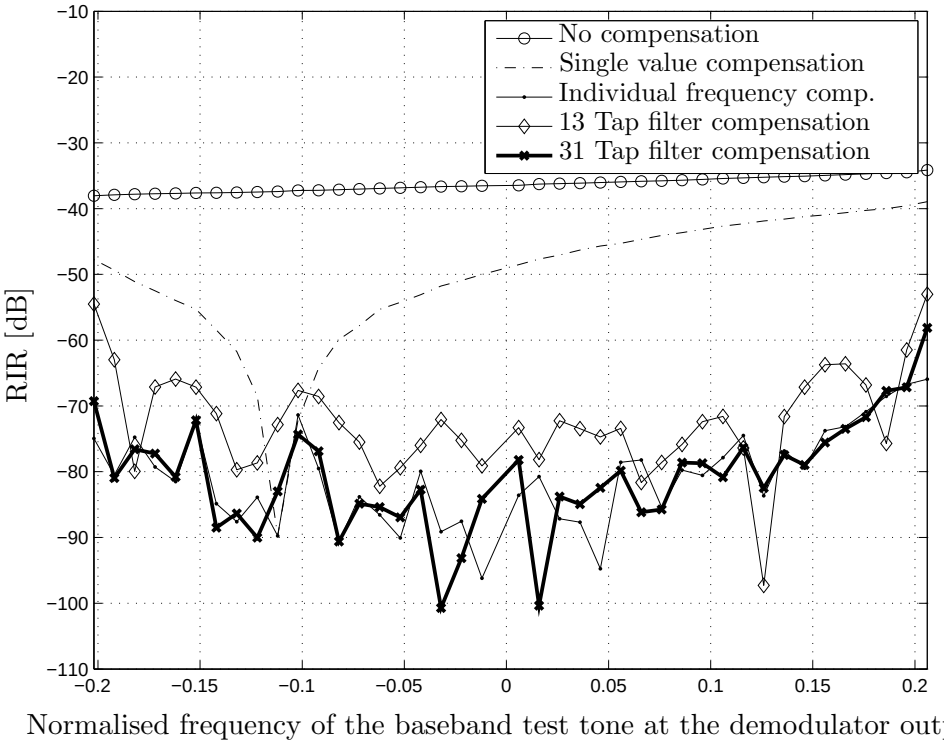


**Figure 5.33:** *RIR of the modulator as a function of frequency, before and after imbalance compensation.*

mance loss when realising the frequency-dependent compensation solution. As expected, the 13-tap filter delivers poorer RIR performance. However, it still achieves a very significant RIR improvement compared to condition before compensation. In this case, the imbalance performance is clearly limited by the filter length.

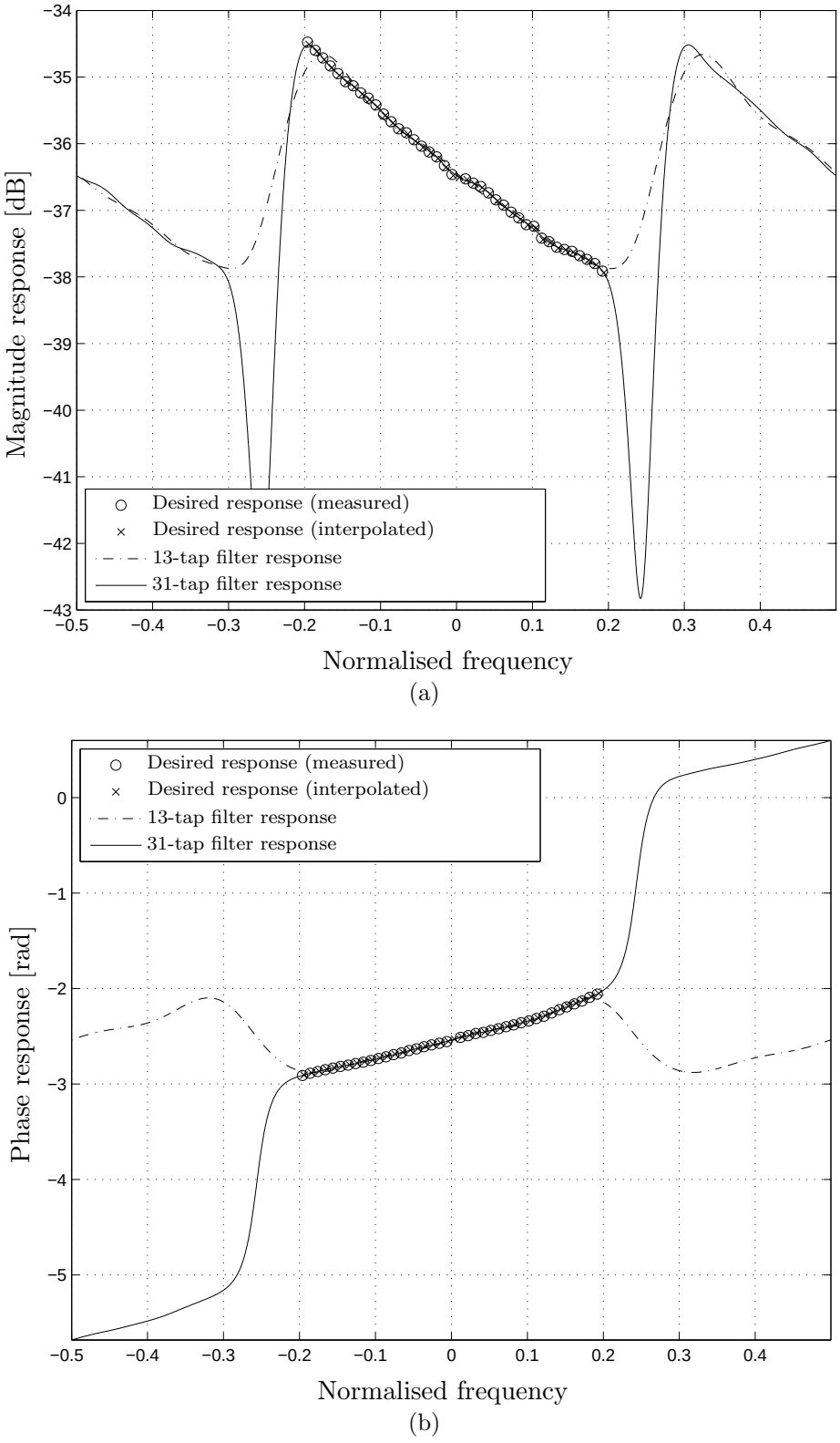


**Figure 5.34:** *Magnitude (a) and phase (b) response of two realised modulator compensation filters of different lengths. The desired response, as estimated through the imbalance extraction process is also shown.*

### 5.3.4 Summary and conclusions

In this section, the theory derived so far in this dissertation was validated through a hardware implementation of an imbalanced quadrature modulator and demodulator pair. The hardware topology represented the practical case where the imbalanced modulator generated test tones which are then fed directly into the demodulator through a feedback path, for analysis in the digital domain of the demodulator. This could form part of a practical start-up calibration procedure, after which the transceiver can switch to normal operation.

For modulator imbalance extraction, the techniques derived for Scenarios II and II in Section 4.3.3 were used, since there existed a frequency difference between the LOs of the modulator and the demodulator, as well as an unknown delay between their sampling start times. For both the modulator and demodulator, the extracted imbalance parameters were then used to design complex-valued compensation filters.

The RIR results showed a strong frequency dependence in the $I/Q$ imbalances of both the modulator and demodulator. This was confirmed by attempting to achieve compensation over the whole frequency band of interest, using only a single extracted imbalance value.

The accuracy of the extracted compensation parameters were verified, by using them directly for compensation (i.e. by choosing the right complex compensation coefficient, based on the frequency of the test tone), and retransmitting the sequence of test tones. For the modulator, it was found that this compensation procedure managed to achieve 30 dB to 40 dB RIR improvement. By analysing the SFDR due to quantisation noise, the RIR performance after calibration was found to agree well with the simulation results, which indicated that the expected RIR after compensation would be in the order of the SFDR due to quantisation. Demodulator compensation managed to achieve superior results, achieving 40 dB to 50 dB RIR improvement. This was expected from the simulation results of the demodulator and modulator extraction performance in the presence of quantisation, which indicated that the modulator was more sensitive to the effect of quantisation. It was clear in the hardware implementation that the effect of quantisation was the limiting factor to the achievable imbalance extraction accuracy.

The use of discretely estimated imbalance values of $Q_2(f)$ or $P_2(f)$ for compensation when retransmitting the test tones, offers a convenient way to verify the accuracy of the extracted imbalance parameters, before using them to design the compensation filter. Using this approach, two distorted imbalance correction coefficients in the modulator extraction process, could be identified and replaced by interpolated values. The interpolation was simple, since the gain and phase imbalances was a smooth, slowly varying function of frequency.

From the extracted frequency response specification of the compensation filters, it was seen that the desired magnitude responses do not exhibit even symmetry around DC and the phase responses are not odd functions of frequency (when the DC phase offset is removed). As explained in Section 4.4, this indicates the presence of bandpass frequency-dependent imbalance contributions, which are not included in imbalance models found in literature. Compensation filters with complex transfer functions are therefore required to compensate

for an frequency-dependent imbalances of this nature, in both the modulator and demodulator.

The RIR performance of the modulator and demodulator compensation filters showed that relatively low order filters were required to match the RIR performance obtained by using the individual coefficients for compensation. For the modulator, the 15-tap filter performed equally as well as the 31-tap filter, which in turn performs as well as the individually extracted coefficients. In this case the filter length was therefore not the limiting factor in the RIR performance, but rather the accuracy of the extracted imbalance parameters. For the demodulator, a 31-tap filter provided identical performance to the extracted coefficients, while the 13-tap filter, however, exhibited a loss in RIR performance.

## 5.4 Conclusions

In this chapter, the imbalance extraction and compensation techniques developed in Chapter 4 were validated and their performance verified, through simulations and a practical hardware implementation.

Simulations confirmed that the developed imbalance extraction and compensation techniques can completely remove the effect of quadrature imbalances. It was seen that the extraction accuracy of the techniques in AWGN and quantisation will be limited to the SFDR of the measurement (after FFT processing). This provides the advantage that the processing gain of the FFT can be employed (by computing longer FFTs containing more signal points) to increase the SFDR of the measurement and therefore also the accuracy of the extracted imbalance parameters, since tones are used as test signals for imbalance extraction. Care should be taken to ensure that the quantisation noise spectrum is white, in order for the processing gain of the FFT to be effective. The practical hardware implementation showed that, for the specific setup, quantisation noise presented the limit in terms of the extraction accuracy.

The practical hardware measurements confirmed the presence of a bandpass response resulting in assymetric gain imbalance and phase error responses, as a function of frequency. This provides merit to the approach to include bandpass imbalances in imbalance models developed in Chapter 2 and highlights the need for complex-valued compensation filters. Current techniques in literature would be insufficient to compensate for this frequency-dependent nature of the imbalances observed in the hardware implementation.

In this dissertation, a least-squares method developed by Tuthill and Cantoni [59] was proposed to design the compensation filters, after their desired frequency responses were determined through the imbalance extraction process. It was verified in the hardware implementation that, in practice, relatively short filters are sufficient to provide frequency-dependent compensation. For the hardware implementation, 31-tap complex FIR filters provided RIR performance on par with applying the extracted compensation parameters directly for each corresponding signal frequency.

The results obtained during the hardware implementation presented in this chapter, serve as a validation of the imbalance extraction techniques, as well as the underlying models that were presented in the course of this dissertation.

# Chapter 6

# Blind $I/Q$ imbalance estimation

## 6.1 Introduction

In Chapter 4, novel techniques for frequency-dependent $I/Q$ imbalance compensation were presented. These techniques were well suited to be performed on the quadrature mixing transceiver as an automatic start-up procedure. Since $I/Q$ imbalances drift slowly over time [20], it may be necessary to repeat the compensation process periodically, which will require a brief break in normal operation.

There may, however, be some advantage to using live data to extract the imbalances of the quadrature mixing front-end, since $I/Q$ imbalance compensation can then be performed without a break in normal operation. If this could further be achieved without the need for any extra hardware, it would certainly prove a very attractive solution. In some scenarios this might even be the only possibility to extract quadrature imbalances, for example in applications where access to the physical front-end is not possible, such as a transceiver in an orbiting satellite.

In this chapter such a technique is presented. This technique can be classified as a blind compensation technique, since it does not use test signals or test sequences to extract the $I/Q$ imbalance and offset errors of quadrature mixing front-end. It is able to separate and extract the $I/Q$ imbalances of the quadrature modulator and demodulator, using only the received signal.

The compensation technique developed in this chapter is a direct consequence of the imbalance models that were developed thus far in the Chapter 2. This chapter extends the models and ideas developed in this dissertation, into the important field of digital modulation. The results presented in this chapter offer an indication of the value of quadrature compensation in well understood metrics, such as the increase in bit error-rate (BER) of the communication system.

As discussed in Chapter 3, the most popular blind approaches include the use of blind source separation (BSS) [65, 48, 47, 11], interference canceler (IC) based methods [65, 61, 12] and those relying on knowledge of the second-order statistics [72, 48, 47, 66, 2]. BSS separates signals based on their assumed statistical independence. A popular BSS algorithm

is the EASI algorithm [65, 48, 47], which uses non-linear functions to extract the signal's higher-order statistics. BSS methods can track $I/Q$ imbalances over time, but can be very computationally expensive, and are sensitive to additive noise and symbol timing errors [72, 65].

Blind methods involving second-order statistics are often considered attractive due to their relatively low implementation complexity, compared to methods such as blind source separation (BSS) [72]. Second-order statistic-based methods also do not assume a specific modulation scheme, as is the case with equaliser-based compensation methods, but make some assumption on the statistics of the desired signal, which makes these techniques generally much more widely applicable. In their work in [72], Windisch and Fettweis propose a technique suitable for low-IF receivers: $I/Q$ imbalances are extracted from averages of $N$ samples, but requires that both the desired and image signal be mixed down from their digital IF frequency to 0 Hz during the extraction process. In [48], Rykaczewski and Jondral propose a block-averaging method termed 'stat', which extracts the $I/Q$ imbalances by assuming that the $I$ and $Q$ channels are independent and have equal mean power. Valkame et. al. propose a whitening transform in [66], based on eigenvalue decomposition, that can be implemented either in block form or adaptively. This transform decorrelates the $I$ and $Q$ signals, but introduces an additional unknown rotation-reflection effect on the whitened signal, which needs to be resolved. In [2] Antilla et. al. present a method similar to that of Windisch and Fettweis, which is applicable to both low-IF and zero-IF receivers. This method uses block averages to extract the complex image rejection ratio (RIR). When used for compensation, this leaves an unknown amplitude scaling and phase rotation on the compensated signal. All of the abovementioned techniques using second order statistics, assume frequency-independent imbalances and focus on demodulator compensation. A perfectly balanced modulator is thus assumed to have generated the passband signal (if quadrature mixing was used).

The main contribution of this chapter is a computationally efficient blind $I/Q$ compensation approach that targets quadrature imbalances across the full transmitter-receiver system, and extracts the actual $I/Q$ impairments, up to the choice of a reference channel, directly. In other words, an imbalanced modulator and demodulator is assumed, where the technique aims to separate and extract the imbalances of the both the modulator and demodulator. Unlike the methods of Windisch and Fettweis in [72, 74], this method is applicable to both zero-IF and low-IF transceivers. This technique also does not only aim to decorrelate the $I$ and $Q$ signals as is done by Valkama et. al. and Antilla et. al. in [2] and [66], but extracts the exact $I/Q$ imbalance parameters relative to the choice of the reference ($I$ or $Q$) channel.

The proposed method relies on knowledge of the second-order statistics of the received signal and uses a Cholesky decomposition of the received signal's covariance matrix to extract the $I/Q$ imbalances. This technique is derived by using a matrix notation during system modelling, which enables linear algebra techniques to be employed to address the problem of imbalance extraction.

The proposed technique can be implemented in a block-based fashion or by using the adaptive variant that will also be presented. The adaptive variant enabled imbalance tracking over time and reduces the memory requirements of the techniques.

Analysis is presented on the effect of noise, a frequency-selective channel, and a frequency offset between transmitter and receiver local oscillators. It is then demonstrated that $I/Q$ compensation can be effectively combined with multipath equalisation.

The rest of the chapter is structured as follow. Section 6.2 discusses how the quadrature mixing front end is well suited to facilitate the direct modulation of digital signals. It then shows the effect that the quadrature imbalances have on the signal constellation of a digital modulation scheme. A convenient matrix notation is introduced, which will be used in the rest of the chapter to develop the imbalance extraction techniques using linear algebra techniques. Section 6.3 provides the principles behind digital compensation for frequency-independent imbalances, assuming that the imbalances could be extracted, using the matrix notation approach. In Section 6.4 the actual novel blind imbalance extraction techniques for the modulator and demodulator are presented. Section 6.5 extends the discussion on the extraction techniques, by addressing some of the practical aspects which might affect the performance of the techniques in practice. Performance simulations are then presented in Section 6.6 to validate the theory and verify the techniques' performance under nonideal operating conditions. Finally, Section 6.7 concludes the chapter.

## 6.2 Quadrature mixing and digital modulation schemes

In systems employing digital modulation schemes, an alphabet of $M$ signal waveforms are used to transmit binary data over a communication channel [40, p. 340]. The number of digital bits that each signal waveform represents is given by $\log_2 M$ bits.

In this study two specific sets of signal waveforms are of specific interest, due to the convenient way in which they can be realised with the quadrature mixing topology. Both sets contain $M$ two-dimensional bandpass signal waveforms. The first set uses carrier-phase modulation whereas the second uses carrier-phase as well as carrier-amplitude modulation to represent the digital data.

### 6.2.1 Carrier-phase modulation

A set of $M$ carrier-phase modulated signal waveforms, $u(t)$ can be written as [40, p. 355]

$$u(t) = g_T(t)\cos\left(2\pi t f_c + \frac{2\pi k}{M}\right), \quad k \in 0, 1, \ldots, M-1, \quad 0 \leq t \leq T_s \ , \tag{6.1}$$

where $f_c$ is the carrier frequency, $T_s$ is the symbol period in seconds and $g_T(t)$ is the baseband pulse shaping. In this discussion, we will neglect the effect of inter-symbol interference (ISI) or the need for matched filtering. As such, we will assume that $g_T(t)$ is a rectangular pulse of length $T$, with unity amplitude and its effect will therefore be ignored for the rest of this chapter.

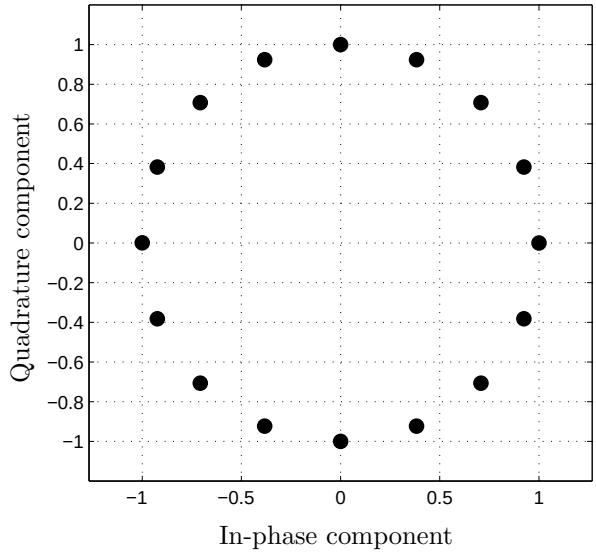


**Figure 6.1:** *Signal constellation of 16-PSK.*

The expression for $u(t)$ can be expanded as [40]

$$u(t) = A_{kI}\cos(2\pi t f_c) - A_{kQ}\sin(2\pi t f_c) \ , \tag{6.2}$$

where $A_{kI}$ and $A_{kQ}$ are given by

$$A_{kI} = \cos(2\pi k/M), \quad k \in 0, 1, \ldots, M-1 \tag{6.3}$$

$$A_{kQ} = \sin(2\pi k/M), \quad k \in 0, 1, \ldots, M-1 \ . \tag{6.4}$$

This form of digital modulation is known as $M$-ary phase shift keying (M-PSK). By comparing equation (6.2) with the architecture of the quadrature modulator that was presented in Chapter 2 in Figure 2.7, we see that the M-PSK modulator can be implemented very conveniently using a quadrature modulator. During digital baseband modulation the $I$ and $Q$ channels' amplitudes are simply assigned the appropriate values from the possible values of $A_{kI}$ and $A_{kQ}$ respectively. The pulse shaping filter $g_T(t)$ can also be implemented in the digital domain, thus adding to the flexibility of the modulator.

In the rest of this chapter, we will use the convention that the digital baseband symbol of length $T_s$ seconds will be represented by a two-component vector, $\boldsymbol{a}(n)$. This notation is similar to the vector notion that was used in the rest of the study, except that $\boldsymbol{a}(n)$ now represents the two components of the $n^{th}$ digital symbol, i.e.

$$\boldsymbol{a}(n) = [A_{kI} \ \ A_{kQ}]^T, \quad k \in 0, 1, \ldots, M-1 \ . \tag{6.5}$$

The components of $\boldsymbol{a}(n)$ can therefore generally be interpreted as the real and imaginary components of the complex baseband signal.

This notation will allow us to indicate how the symbol space is transformed in the presence of quadrature imbalances. An example of the signal constellation of 16-PSK is shown in Figure 6.1.

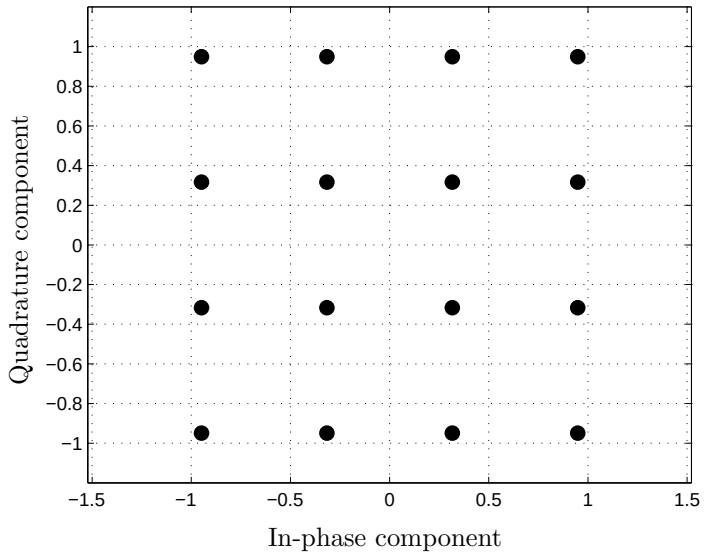


**Figure 6.2:** *Signal constellation of rectangular 16-QAM.*

### 6.2.2 Carrier-phase-amplitude modulation

Similar to the discussion on carrier-phase modulation, a set of $M$ carrier-phase-amplitude modulated signal waveforms can be written as [40, p. 358]

$$\begin{aligned} u(t) = A_l g_T(t) \cos\left(2\pi t f_c + \theta_p\right), \quad l &\in 1, 2, \ldots, M_1, \quad 0 \leq t \leq T_s \ , \\ p &\in 1, 2, \ldots, M_2 \\ k &\in 0, 1, \ldots, M \ , \end{aligned} \tag{6.6}$$

where $M = M_1 M_2$. The expression for $u(t)$ can be expanded as

$$u(t) = g_T(t) A_{kI} \cos\left(2\pi t f_c\right) - g_T(t) A_{kQ} \sin\left(2\pi t f_c\right) \ , \tag{6.7}$$

where $A_{kI}$ and $A_{kQ}$ is given by

$$A_{kI} = A_l \cos(\theta_p), \quad k \in 0, 1, \ldots, M-1 \tag{6.8}$$

$$A_{kQ} = A_l \sin(\theta_p), \quad k \in 0, 1, \ldots, M-1 \ . \tag{6.9}$$

In the rest of the discussion, the pulse shaping filter $g_T(t)$ will once again be neglected. Note that any arbitrary mapping between $k$ and $l$ and $p$ might be assigned. This form of digital modulation is known as $M$-ary quadrature amplitude modulation (M-QAM). From (6.7) it is seen that the quadrature modulator can again be employed to realise M-QAM, with $\boldsymbol{a}(n)$ again given as

$$\boldsymbol{a}(n) = \left[A_{kI} \ \ A_{kQ}\right]^T, \quad k \in 0, 1, \ldots, M-1 \ . \tag{6.10}$$

An example of the signal constellation of rectangular 16-QAM is shown in Figure 6.2.

### 6.2.3 Effect of $I/Q$ imbalances on digital modulation schemes

This section will investigate the effect of frequency-independent quadrature imbalances on the signal constellation of digital signals, using a cascaded imbalanced modulator and demodulator for communication.

When an imbalanced zero-IF quadrature mixing transmitter is used to generate the digital modulation schemes above, the signal space will be distorted. Using the results of (2.76), the baseband-equivalent output of the quadrature modulator, interpreted in the symbol space, is given as

$$\tilde{\boldsymbol{u}}(n) = \boldsymbol{M}\boldsymbol{a}(n)\,, \tag{6.11}$$

where the modulator imbalance matrix $\boldsymbol{M}$ was defined in (2.77) as

$$\boldsymbol{M} = \begin{bmatrix} \eta_I \cos(\psi_I) & -\eta_Q \sin(\psi_Q) \\ \eta_I \sin(\psi_I) & \eta_Q \cos(\psi_Q) \end{bmatrix}, \tag{6.12}$$

where $n$ denotes the symbol iterator at $t = nT_s$. The frequency-independent gain and phase imbalance of the modulator is given by $\eta_M = \eta_I/\eta_Q$ and $\psi_M = \psi_I - \psi_Q$ respectively.

A zero-IF quadrature mixing receiver can be used to demodulate both M-PSK and M-QAM signals directly. When an imbalanced zero-IF demodulator is used to demodulate the signal, its output in the symbol space is given as

$$\begin{aligned} \boldsymbol{z'}(n) &= \boldsymbol{D}\left[\boldsymbol{R}(n)\tilde{\boldsymbol{u}}(n) + \tilde{\boldsymbol{v}}(n)\right] \\ &= \boldsymbol{D}\boldsymbol{R}(n)\boldsymbol{M}\boldsymbol{a}(n) + \boldsymbol{D}\tilde{\boldsymbol{v}}(n)\,, \end{aligned} \tag{6.13}$$

where

$$\boldsymbol{R}(n) = \begin{bmatrix} \cos(2\pi\Delta f n T_s + \Delta\theta) & \sin(2\pi\Delta f n T_s + \Delta\theta) \\ -\sin(2\pi\Delta f n T_s + \Delta\theta) & \cos(2\pi\Delta f n T_s + \Delta\theta) \end{bmatrix}$$

models the presence of a frequency difference $\Delta f$ and phase offset $\Delta\theta$ between the LOs of the quadrature modulator and demodulator. The demodulator distortion matrix was derived in (2.135) as

$$\boldsymbol{D} = \begin{bmatrix} \kappa_I \cos(\chi_I) & \kappa_I \sin(\chi_I) \\ -\kappa_Q \sin(\chi_Q) & \kappa_Q \cos(\chi_Q) \end{bmatrix}, \tag{6.14}$$

with the frequency-independent gain and phase imbalance of the demodulator given by $\kappa_D = \kappa_I/\kappa_Q$ and $\varphi_D = \varphi_I - \varphi_Q$, respectively.

The two components of the noise vector $\widetilde{\boldsymbol{v}}(n)$ are assumed to be samples from two zero mean independent and identically distributed (i.i.d.) random processes. The covariance matrix $\boldsymbol{C}$ of $\widetilde{\boldsymbol{v}}(n)$ is therefore given by $\mathrm{diag}[\sigma^2/2, \sigma^2/2]$[1], where $\sigma^2$ is the variance of the

[1] diag[·] refers to a diagonal matrix with its diagonal elements specified in brackets.

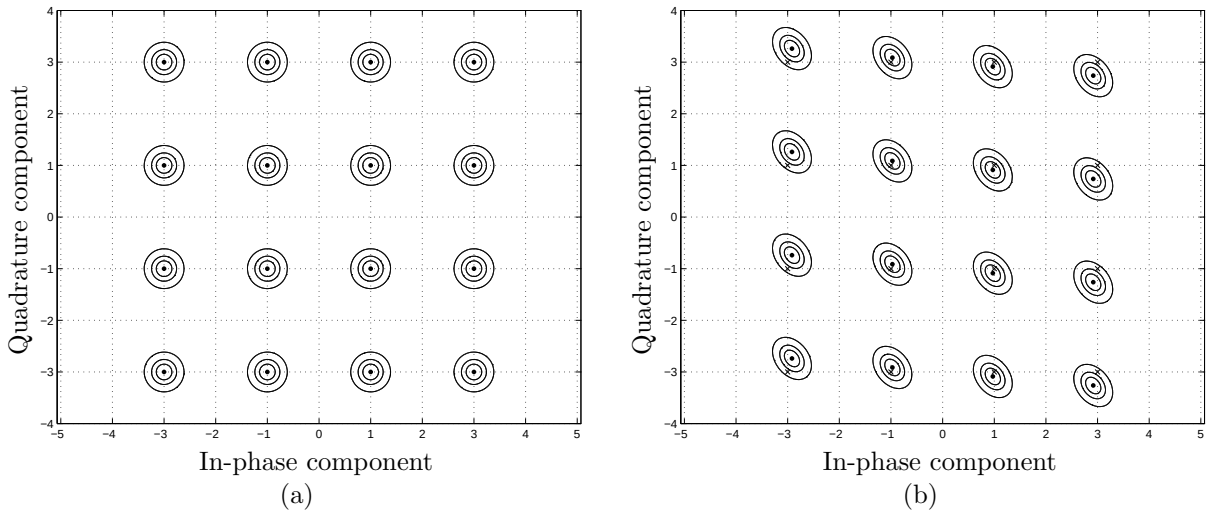


**Figure 6.3:** *The signal space constellation of 16-QAM, before (a) and after (b) I/Q imbalancing. The PDF of the noise component is indicated with contour lines. The original signal positions in (b) are marked with crosses.*

passband noise $v(t)$. When the noise has passed through the imbalanced demodulator, the covariance matrix $\boldsymbol{C'}$ of the noise component $\boldsymbol{D}\widetilde{\boldsymbol{v}}(n)$ in (6.13), becomes [9, 75]

$$\boldsymbol{C'} = \boldsymbol{D}\boldsymbol{C}\boldsymbol{D}^T \ . \tag{6.15}$$

If the real and imaginary components of the noise vector $\widetilde{\boldsymbol{v}}(n)$ are uncorrelated zero-mean, Gaussian random variables, then the joint conditional probability density function (PDF) of $\boldsymbol{z'}(n)$ dependent on the transmitted symbol $\boldsymbol{a}(n)$, can be written as [40, p. 158]

$$f\left[\boldsymbol{z'}(n)|\boldsymbol{a}(n)\right] = \frac{1}{2\pi\sqrt{\det(\boldsymbol{C'})}} \times$$
$$\exp\left[-\frac{1}{2}\left[\boldsymbol{z'}(n) - \boldsymbol{D}\boldsymbol{R}(n)\boldsymbol{M}\boldsymbol{a}(n)\right]\boldsymbol{C'}^{-1}\left[\boldsymbol{z'}(n) - \boldsymbol{D}\boldsymbol{R}(n)\boldsymbol{M}\boldsymbol{a}(n)\right]^T\right] . \tag{6.16}$$

It is seen that quadrature imbalances in the modulator and demodulator distort the signal space and establish correlation between the $I$ and $Q$ channels' signals [22]. This distortion of the signal space causes an increase in the bit error rate (BER) [9, 10, 22, 32, 76]. The distortion of the signal constellation is shown graphically in Figure 6.3, where the constellation of 16-QAM is shown before and after imbalances, for the case where carrier synchronisation has been established, i.e. $\boldsymbol{R}(n) = \boldsymbol{I}^2$. The PDF of the noise is also indicated with contour lines. It can be seen that the two components of the noise vector are no longer independent, after they have passed through the imbalanced demodulator. The signal space distortion is more severe for symbols further away from the origin. Therefore, for higher-order modulation schemes, the decrease in the BER would most likely be dominated by the contribution of symbol errors at the edges of the constellation [75, p. 77].

[2] $\boldsymbol{I}$ represents the $2 \times 2$ identity matrix, [1 0; 0 1]

## 6.3 Principle of digital compensation

When the imbalances of the quadrature modulator and demodulator can be modelled as invertible transforms, then compensation can be achieved by applying the inverse transform. It was also shown in this dissertation that the imbalance inverse transform can be applied in the digital domain of the quadrature modulator or demodulator. This section will elaborate on these ideas, and show how it is possible to compensate for frequency-independent imbalance and offset errors in the digital domain. Once it is shown how knowledge of the analogue front-end's imbalance parameters can be used to reverse their detrimental effects through compensation in the digital domain, the subsequent sections will discuss their blind extraction.

### 6.3.1 I/Q imbalance compensation

In this section it will be shown that the linear distortion matrices $\boldsymbol{M}$ and $\boldsymbol{D}$, derived in (2.77) and (2.135), are invertible for all practical imbalance scenarios.

For the distortion matrices to be invertible, their determinants should be non-zero [30, p. 110]. The determinants of $\boldsymbol{M}$ and $\boldsymbol{D}$ are given by

$$\det(\boldsymbol{M}) = \eta_I \eta_Q \cos(\psi_I - \psi_Q) \tag{6.17}$$

$$\det(\boldsymbol{D}) = \kappa_I \kappa_Q \cos(\chi_I - \chi_Q) \ . \tag{6.18}$$

The above equations can be written in terms of the gain imbalance and phase error of each. Choosing the $Q$ channel as reference and normalising its amplitude to unity, the determinants of $\boldsymbol{M}$ and $\boldsymbol{D}$ become

$$\det(\boldsymbol{M}) = \eta_M \cos(\psi_M) \tag{6.19}$$

$$\det(\boldsymbol{D}) = \kappa_M \cos(\chi_M) \ . \tag{6.20}$$

The determinants of $\boldsymbol{M}$ and $\boldsymbol{D}$ will be non-zero as long as $\eta_M \neq 0$, $\kappa_D \neq 0$, $\psi_M \neq \pm\pi/2$ and $\chi_D \neq \pm\pi/2$. These constraints will always be met in practical quadrature mixers and therefore it will always be possible to invert the transformation matrices $\boldsymbol{M}$ and $\boldsymbol{D}$.

When the gain imbalances and phase errors can be estimated perfectly, then applying the inverse of $\boldsymbol{M}$ and $\boldsymbol{D}$ would result in reversing the effect of the front-end's imbalances. In a practical system $\boldsymbol{M}$ and $\boldsymbol{D}$ may not be estimated perfectly. The effect of using such imperfect estimation during compensation will now be investigated. This discussion will be conducted separately for the modulator and demodulator.

#### Modulator compensation

Modulator compensation is achieved by predistorting the digital message signal with the compensation matrix. Let $\widehat{x}$ denote the estimate of a parameter $x$, so that the estimated compensation matrix can be denoted by $\widehat{\boldsymbol{M}}^{-1}$. The resulting predistorted baseband message

signal therefore becomes $\widehat{\boldsymbol{M}}^{-1}\boldsymbol{a}(n)$. The complex baseband-equivalent of the transmitted signal after $I/Q$ imbalance compensation can then be written as

$$\tilde{\boldsymbol{u}}(n) = \boldsymbol{M}\widehat{\boldsymbol{M}}^{-1}\boldsymbol{a}(n)\,. \tag{6.21}$$

When the estimation of the imbalances is perfect, then $\widehat{\boldsymbol{M}} = \boldsymbol{M}$ and $\boldsymbol{M}\widehat{\boldsymbol{M}}^{-1} = \boldsymbol{I}$, thus completely cancelling the effect of the imbalanced frontend.

Using the $Q$ channel as reference (i.e. $\psi_Q = 0$, $\psi_I = \psi_M$, $\eta_Q = 1$ and $\eta_D = \eta_I$) $M$ becomes (from (2.79))

$$\boldsymbol{M} \;=\; \begin{bmatrix} \eta_M\cos(\psi_M) & 0 \\ \eta_M\sin(\psi_M) & 1 \end{bmatrix}. \tag{6.22}$$

The estimate of the inverse of $\boldsymbol{M}$ can therefore be written as

$$\widehat{\boldsymbol{M}}^{-1} \;=\; \begin{bmatrix} 1/\widehat{\eta}_M\sec(\widehat{\psi}_M) & 0 \\ -\tan(\widehat{\psi}_M) & 1 \end{bmatrix}. \tag{6.23}$$

The resultant distortion matrix after $I/Q$ imbalance compensation is

$$\begin{aligned} \boldsymbol{M}_{\text{res}} &= \boldsymbol{M}\widehat{\boldsymbol{M}}^{-1} \\ &= \begin{bmatrix} \eta_M\cos(\psi_M) & 0 \\ \eta_M\sin(\psi_M) & 1 \end{bmatrix} \begin{bmatrix} 1/\widehat{\eta}_M\sec(\widehat{\psi}_M) & 0 \\ -\tan(\widehat{\psi}_M) & 1 \end{bmatrix} \\ &= \begin{bmatrix} \frac{\eta_M\cos(\psi_M)}{\widehat{\eta}_M\cos(\widehat{\psi}_M)} & 0 \\ \frac{\eta_M\sin(\psi_M)-\widehat{\eta}_M\sin(\widehat{\psi}_M)}{\widehat{\eta}_M\cos(\widehat{\psi}_M)} & 1 \end{bmatrix}. \end{aligned} \tag{6.24}$$

It can be verified by algebraic simplification, that the relative image ratio (RIR) of the modulator, which was introduced in Chapter 2, Section 2.5.1, can be written as a function of the distortion matrix $\boldsymbol{M}$ using the following expression:

$$\frac{P_{\text{image}}}{P_{\text{desired}}}(\boldsymbol{M}) = \frac{\Big([\boldsymbol{M}]_{11} - [\boldsymbol{M}]_{22}\Big)^2 + \Big([\boldsymbol{M}]_{21} + [\boldsymbol{M}]_{12}\Big)^2}{\Big([\boldsymbol{M}]_{11} + [\boldsymbol{M}]_{22}\Big)^2 + \Big([\boldsymbol{M}]_{21} - [\boldsymbol{M}]_{12}\Big)^2} \tag{6.25}$$

where the notation $[\boldsymbol{M}]_{12}$ denotes the second element in the first row of the matrix $\boldsymbol{M}$. Using this relationship and the expression for $\boldsymbol{M}$ in (6.22), the relative power of the undesired image component of the modulator before compensation is

$$\frac{P_{\text{image}}}{P_{\text{desired}}}(\boldsymbol{M}) = \frac{\eta_M^2 + 1 - 2\eta_M\cos(\psi_M)}{\eta_M^2 + 1 + 2\eta_M\cos(\psi_M)}\,, \tag{6.26}$$

which is identical to (2.68) on p. 39. To determine the relative image power after imbalance compensation, $\boldsymbol{M}_{\text{res}}$ is used instead of $\boldsymbol{M}$ in (6.25), resulting in

$$\frac{P_{\text{image}}}{P_{\text{desired}}}(\boldsymbol{M}_{\text{res}}) = \frac{\left(\frac{\eta_M}{\widehat{\eta}_M}\right)^2 + 1 - 2\left(\frac{\eta_M}{\widehat{\eta}_M}\right)\cos(\psi_M - \widehat{\psi}_M)}{\left(\frac{\eta_M}{\widehat{\eta}_M}\right)^2 + 1 + 2\left(\frac{\eta_M}{\widehat{\eta}_M}\right)\cos(\psi_M - \widehat{\psi}_M)}. \tag{6.27}$$

If we compare (6.26) and (6.27), it is seen that after imbalance compensation has been performed, the power of the relative image component of the modulator becomes equivalent to that of a modulator with a gain imbalance of $\eta_M/\widehat{\eta}_M$ and a phase error of $\psi_M - \widehat{\psi}_M$. It can be seen that when the estimated imbalance parameters become equal to the true imbalance values, then no gain imbalance or phase error exists after compensation and the power of the relative image component becomes 0.

**Demodulator compensation**

Demodulator compensation is similar to that of the modulator, except that compensation now occurs in the digital domain, after the signal has passed through the imbalanced front-end. The compensation matrix, $\widehat{\boldsymbol{D}}^{-1}$, is therefore applied as a post-correction matrix. The received signal after imbalance compensation can be written as

$$\boldsymbol{z'}(n) \;=\; \widehat{\boldsymbol{D}}^{-1}\boldsymbol{D}\tilde{\boldsymbol{u}}(n)\,. \tag{6.28}$$

With the $Q$ channel as a reference, the imbalance distortion matrix $\boldsymbol{D}$ is given by (see (2.137) on p. 57)

$$\boldsymbol{D} \;=\; \kappa_Q \begin{bmatrix} \kappa_D\cos(\chi_D) & \kappa_D\sin(\chi_D) \\ 0 & 1 \end{bmatrix}. \tag{6.29}$$

The estimate of the compensation (inverse) matrix is given by

$$\widehat{\boldsymbol{D}}^{-1} = \begin{bmatrix} 1/\widehat{\kappa}_D\sec(\widehat{\chi}_D) & -\tan(\widehat{\chi}_D) \\ 0 & 1 \end{bmatrix}. \tag{6.30}$$

The resultant distortion matrix after compensation is performed is

$$\begin{aligned} \boldsymbol{D}_{\text{res}} &= \widehat{\boldsymbol{D}}^{-1}\boldsymbol{D} \\ &= \begin{bmatrix} 1/\widehat{\kappa}_D\sec(\widehat{\chi}_D) & -\tan(\widehat{\chi}_D) \\ 0 & 1 \end{bmatrix} \begin{bmatrix} \kappa_D\cos(\chi_D) & \kappa_D\sin(\chi_D) \\ 0 & 1 \end{bmatrix} \\ &= \begin{bmatrix} \frac{\kappa_D\cos(\chi_D)}{\widehat{\kappa}_D\cos(\widehat{\chi}_D)} & \frac{\kappa_D\sin(\chi_D)-\widehat{\kappa}_D\sin(\widehat{\chi}_D)}{\widehat{\kappa}_D\cos(\widehat{\chi}_D)} \\ 0 & 1 \end{bmatrix}. \end{aligned} \tag{6.31}$$

The relative power of the undesired image component due to the imbalances of the demodulator can also be computed from its distortion matrix using the relationship of (6.25). The relative power of the image component at the output of the demodulator, before compensation is therefore given by

$$\frac{P_{\text{image}}}{P_{\text{desired}}}(\boldsymbol{D}) = \frac{\kappa_D^2 + 1 - 2\kappa_D\cos(\chi_D)}{\kappa_D^2 + 1 + 2\kappa_D\cos(\chi_D)}. \tag{6.32}$$

After compensation, the power of the relative sideband becomes

$$\frac{P_{\text{image}}}{P_{\text{desired}}}(\boldsymbol{D}_{\text{res}}) = \frac{\left(\frac{\kappa_D}{\widehat{\kappa}_D}\right)^2 + 1 - 2\left(\frac{\kappa_D}{\widehat{\kappa}_D}\right)\cos(\chi_D - \widehat{\chi}_D)}{\left(\frac{\kappa_D}{\widehat{\kappa}_D}\right)^2 + 1 + 2\left(\frac{\kappa_D}{\widehat{\kappa}_D}\right)\cos(\chi_D - \widehat{\chi}_D)}. \tag{6.33}$$

If we compare (6.32) and (6.33) we see that, as with the modulator, after compensation the demodulator's image rejection is equal to a demodulator with gain imbalance of $\kappa_D/\widehat{\kappa}_D$ and phase error of $\chi_D - \widehat{\chi}_D$, as expected.

Now that the principles behind using estimations of the quadrature imbalances for digital compensation have been presented, the next section will focus extracting these estimates.

## 6.4 $I/Q$ imbalance extraction

This section will present a novel blind imbalance extraction technique, which relies on knowledge of the second-order statistics of the received data. The general approach will be applicable to modulator and demodulator imbalance extraction.

In Chapter 4 it was demonstrated that, in principle, a frequency difference between the LO signals of the quadrature modulator and demodulator, enables their respective imbalance contributions to be extracted separately through analysis on the received signal. In this section, it will be shown how this principle can now once again be employed to separate and extract both the modulator and demodulator imbalance distortion matrices ($\boldsymbol{M}$ and $\boldsymbol{D}$), when they occur as a pair, over a communication channel.

It should be noted that the idea of using a frequency offset to separate the imbalances of the modulator and demodulator has also been mentioned by Rykaczewski and Jondral [48]. In their work, the idea is simply mentioned, without any mathematical motivation and no analysis of cascaded imbalances, proving that this approach provides the theoretical imbalance isolation. In this dissertation, the idea of using a frequency offset to separate the imbalance contributions of the modulator and demodulator has been developed independently using the modelling approach presented in Chapter 2. The principle of using a frequency offset is now simply shown to be applicable to the digital modulation case as well, and will be shown analytically to provide a means to separate the imbalance contributions.

Although the cascaded quadrature modulator and demodulator case will be used for the development of the technique, the underlying principles are still just as valid when only the modulator or demodulator employs quadrature mixing. In such a case, the complexity of the problem is simply reduced. These special cases will also be considered.

### 6.4.1 Demodulator compensation

#### Cascaded imbalanced modulator and demodulator case – Technique 1

For convenience, the expression for the received symbol in a cascaded imbalance scenario, (6.13), is presented here again:

$$\boldsymbol{z'}(n) = \boldsymbol{D}\boldsymbol{R}(n)\boldsymbol{M}\boldsymbol{a}(n) + \boldsymbol{D}\tilde{\boldsymbol{v}}(n). \tag{6.34}$$

Firstly, consider the effect of a frequency difference between the LOs of the modulator and demodulator. A frequency offset will cause the rotation matrix $\boldsymbol{R}(n)$ in (6.34) to be time

variant (i.e. a function of $n$) and results in a constant rotation of the signal constellation at the receiver. When the signal constellation is observed over an integer multiple of a $2\pi$ rotation, the rotation will diagonalise the covariance matrix of $\boldsymbol{R}(n)\boldsymbol{M}\boldsymbol{a}(n)$ in (6.34). Also, since the components of the noise vector $\widetilde{\boldsymbol{v}}(n)$ are considered to be independent, the covariance matrix of $\boldsymbol{R}(n)\boldsymbol{M}\boldsymbol{a}(n)+\widetilde{\boldsymbol{v}}(n)$ in (6.13) will be a diagonal matrix, when observed over a multiple of $2\pi$ rotation of $\boldsymbol{R}(n)$. Let $\boldsymbol{F}$ denote the covariance matrix of $\boldsymbol{R}(n)\boldsymbol{M}\boldsymbol{a}(n)+\widetilde{\boldsymbol{v}}(n)$, and be given by

$$\boldsymbol{F} = \begin{bmatrix} \rho^2 & 0 \\ 0 & \rho^2 \end{bmatrix} . \tag{6.35}$$

The resultant covariance matrix of $\boldsymbol{z'}(n)$ can then be written in terms of $\boldsymbol{F}$ as

$$\boldsymbol{F'} = \boldsymbol{D}\boldsymbol{F}\boldsymbol{D}^T . \tag{6.36}$$

Any symmetric, positive-definite matrix $\boldsymbol{A} \in \mathbb{R}^{n\times n}$ can be uniquely factorised as $\boldsymbol{A} = \boldsymbol{G}\boldsymbol{G}^T$, where $\boldsymbol{G} \in \mathbb{R}^{n\times n}$ is a unique lower-triangular matrix (e.g. see [23, p. 141]). This is known as the Cholesky factorisation of $\boldsymbol{A}$. Since the covariance matrix $\boldsymbol{F}$ will be a diagonal matrix with positive entries, it is also a symmetric, positive definite matrix [23, p. 140]. In this case, the positive definiteness of $\boldsymbol{F'}$ depends only on the distortion matrix $\boldsymbol{D}$. If $\boldsymbol{D}$ has full rank, then $\boldsymbol{F'}$ will necessarily be positive definite [23, p. 140]. $\boldsymbol{D}$ will always have full rank unless $\chi_D = \pm\pi/2$ or $\kappa_D = 0$. When $\boldsymbol{F'}$ can be assumed to be symmetric and positive definite, we can define the Cholesky factorisation of $\boldsymbol{F'}$ as

$$\boldsymbol{F'} = \boldsymbol{H}\boldsymbol{H}^T , \tag{6.37}$$

where $\boldsymbol{H} \in \mathbb{R}^{2\times 2}$ is a unique lower-triangular matrix. Using (6.36) and the assumption that $\boldsymbol{F}$ is a diagonal matrix, we can write $\boldsymbol{F'}$ as

$$\boldsymbol{F'} = \boldsymbol{D}\boldsymbol{F}^{1/2}(\boldsymbol{F}^{1/2}\boldsymbol{D})^T . \tag{6.38}$$

The distortion matrix $\boldsymbol{D}$ can be modeled as a lower-triangular matrix, by using the $I$ channel as a reference in(2.135). When the $I$ channel's phase is used as the reference phase, then $\chi_I = 0$ and $\chi_Q = -\chi_D$. Likewise, when using the $I$ channel as reference, $\kappa_I$ can be normalised to unity and thus $\kappa_D = 1/\kappa_Q$. The distortion matrix $\boldsymbol{D}$ then becomes

$$\boldsymbol{D} = \begin{bmatrix} 1 & 0 \\ 1/\kappa_D \sin(\chi_D) & 1/\kappa_D \cos(\chi_D) \end{bmatrix} . \tag{6.39}$$

Using this result and the fact that Cholesky factorisation provides unique solutions, eqs. (6.37) and (6.38) imply that

$$\boldsymbol{H} = \boldsymbol{D}\boldsymbol{F}^{1/2} = \rho\boldsymbol{D} , \tag{6.40}$$

if we use the $I$ channel as reference. Since $\rho^2$ (on the diagonal of $\boldsymbol{F}$) is generally not known in a practical system, the imbalances $\chi_D$ and $\kappa_D$ must be extracted from $\boldsymbol{H}$:

$$\chi_D = \tan^{-1}\left(\frac{[\boldsymbol{H}]_{21}}{[\boldsymbol{H}]_{22}}\right) \tag{6.41}$$

$$\kappa_D = \frac{\sqrt{[\boldsymbol{H}]_{21}^2 + [\boldsymbol{H}]_{22}^2}}{[\boldsymbol{H}]_{11}}, \tag{6.42}$$

where $[\boldsymbol{H}]_{ij}$ is the $j^{\text{th}}$ element in the $i^{\text{th}}$ row of $\boldsymbol{H}$. Compensation for the quadrature imbalances of the demodulator is now performed by using the parameters obtained in eqs. (6.41) and (6.42) to compute the inverse of $\boldsymbol{D}$. The inverse of $\boldsymbol{H}$ could also be used as the compensation matrix, thus avoiding the computational complexity of computing eqs. (6.41) and (6.42). The effect will be a scaling of the signal space of $1/\rho$, which may be perfectly acceptable in practice and can be lumped with the unknown channel gain.

### Special case: Perfect Modulator

Consider the case where only an imbalanced demodulator is used, i.e. there are no imbalance contributions from the modulator (this is the assumption for almost all the blind techniques referenced in Chapter 3). The expression for the received signal in this case becomes

$$\boldsymbol{z'}(n) = \boldsymbol{D}\left[\boldsymbol{R}(n)\boldsymbol{a}(n) + \tilde{\boldsymbol{v}}(n)\right] . \tag{6.43}$$

It is assumed as before that the covariance matrix of the noise component $\tilde{\boldsymbol{v}}(n)$ will be a diagonal matrix, due to its two components being uncorrelated. The covariance matrix of $\boldsymbol{R}(n)\boldsymbol{a}(n)$, however, is given by

$$\boldsymbol{Y_R} = \boldsymbol{R}(n)\boldsymbol{Y}\boldsymbol{R}(n)^T , \tag{6.44}$$

where $\boldsymbol{Y}$ denotes the covariance matrix of the signal $\boldsymbol{a}(n)$.

If the $I$ and $Q$ components of $\boldsymbol{a}(n)$ are uncorrelated and have equal mean power (this is true for all rectangular QAM, $M$-PSK ($M > 2$) and OFDM multi-carrier signals [66]), then the covariance matrix of the source signal $\boldsymbol{a}(n)$ is given by

$$\boldsymbol{Y} = \begin{bmatrix} \lambda^2 & 0 \\ 0 & \lambda^2 \end{bmatrix} , \tag{6.45}$$

where $\lambda^2$ denotes the variance of $\boldsymbol{a}(n)$. In this case, the covariance matrix $\boldsymbol{Y_R}$ becomes

$$\boldsymbol{Y_R} \;=\; \boldsymbol{R}(n)\boldsymbol{Y}\boldsymbol{R}(n)^T = \lambda^2\boldsymbol{R}(n)\boldsymbol{R}(n)^T = \lambda^2\boldsymbol{I} \tag{6.46}$$

since any rotation matrix $\boldsymbol{R}(n)$ has the property $\boldsymbol{R}(n)\boldsymbol{R}(n)^T = \boldsymbol{I}$. Since $\boldsymbol{Y_R}$ is in this case also a diagonal matrix, it follows that the covariance matrix of $\boldsymbol{R}(n)\boldsymbol{a}(n) + \tilde{\boldsymbol{v}}(n)$ will also be diagonal because the noise and signal contributions are independent and uncorrelated. This then results in the previous subsection's techniques being directly applicable.

Note that if the $I$ and $Q$ components of $\boldsymbol{a}(n)$ did not exhibit equal mean power (but were still uncorrelated), then one of two scenarios can result:

1. If $\boldsymbol{R}(n)$ represents a frequency offset (i.e. it is a functions of $n$), then $\boldsymbol{Y_R}$ will be diagonalised when observed over a $2\pi$ rotation and the same scenario results as discussed in the previous subsection on the cascaded modulator and demodulator case.

2. If $\boldsymbol{R}$ represents a phase offset (i.e. it is not a function of $n$), then $\boldsymbol{Y_R}$ will generally not exhibit a diagonal structure (except if the phase offset is an exact multiple of $\pi/2$). In this case the phase offset will need to be removed using standard carrier phase recovery techniques, before the techniques presented below for modulator imbalance extraction can be directly applied to extract the demodulator imbalances.

It is therefore seen that, when a frequency offset exists between the carrier frequency of the desired signal and the LO of the demodulator, then the demodulator imbalances can be extracted from the received signal irrespective of the statistics of the underlying signal, since the observed covariance matrix is diagonalised by the rotation of the frequency offset.

If, however, this rotation is not present, but instead just a phase shift exists, then the imbalances of the demodulator can be extracted without the need for phase synchronisation, if the real and imaginary components of the transmitted signal were uncorrelated and have equal mean power. If the two components do not have equal mean power, then the phase offset should be removed through synchronisation before extracting the imbalances using the technique presented under modulator imbalance extraction in the next subsection. Fig. 6.4 in Section 6.4.4 presents a flow diagram view of this reasoning process.

### 6.4.2 Modulator compensation

#### Cascaded imbalanced modulator and demodulator case – Technique 2

In the cascaded imbalanced modulator and demodulator scenario, it is assumed that the demodulator imbalances have been extracted and compensated for, using the techniques presented in the previous subsection on demodulator imbalance extraction in the cascaded case.

Once the imbalances of the demodulator are extracted and compensated for, the remaining imbalances in the received signal can be attributed to the modulator.

Consider the received signal after demodulator compensation:

$$\boldsymbol{D}^{-1}\boldsymbol{z'}(n) = \boldsymbol{R}(n)\boldsymbol{M}\boldsymbol{a}(n) + \widetilde{\boldsymbol{v}}(n)\,. \tag{6.47}$$

Notice, however, that the covariance matrix of $\boldsymbol{RM}\boldsymbol{a}(n)$ is given by $\boldsymbol{R}(n)\boldsymbol{M}\boldsymbol{Y}[\boldsymbol{R}(n)\boldsymbol{M}]^T$. Unlike the case of the imbalanced demodulator, the presence of the rotation matrix $\boldsymbol{R}$ will prohibit the methods of the previous section to be implemented here, since $\boldsymbol{R}(n)\boldsymbol{M}$ is not a lower triangular matrix.

At this stage it is therefore concluded that conventional methods should be used to accomplish carrier phase synchronisation, inverting the effect of the rotation matrix $\boldsymbol{R}(n)$.

Assuming perfect compensation of the demodulator imbalance matrix $\boldsymbol{D}$ and rotation matrix $\boldsymbol{R}(n)$, the demodulated signal becomes

$$\boldsymbol{R}(n)^{-1}\boldsymbol{D}^{-1}\boldsymbol{z'}(n) = \boldsymbol{M}\boldsymbol{a}(n) + \boldsymbol{R}(n)^{-1}\widetilde{\boldsymbol{v}}(n)\,. \tag{6.48}$$

For modulator compensation we will assume a digital modulation scheme with a signal space constellation which is symmetrical about both the real and imaginary axes. We furthermore assume that any offset from the origin is removed are assumed (equal power in the two axis is not assumed). It will also be assumed that each of the $M$ symbols in the symbol alphabet is equally probable to be transmitted. The covariance matrix, $\boldsymbol{Y}$, of the constellation points $\boldsymbol{a}(n)$ in the $M$-symbol alphabet (the signal space constellation) will then be a $2 \times 2$ diagonal matrix given by

$$\boldsymbol{Y} = \begin{bmatrix} \lambda_I^2 & 0 \\ 0 & \lambda_Q^2 \end{bmatrix}, \tag{6.49}$$

where $\lambda_I^2$ and $\lambda_Q^2$ denote the variances of the in-phase and quadrature components of the signal constellation, respectively. Note that in general, the exact values of $\lambda_I^2$ and $\lambda_Q^2$ in the received signal will not be known, since the signal would have encountered many unknown scaling factors in the transmission and reception process. The ratio $\lambda_I/\lambda_Q$ is, however, inherent to the signal constellation of the chosen modulation scheme, and will be known *a priori*. If $\lambda_M$ now denotes this ratio, i.e. $\lambda_M = \lambda_I/\lambda_Q$, then $\boldsymbol{Y}$ can be rewritten in terms of the known $\lambda_M$ and the unknown $\lambda_Q$ as

$$\boldsymbol{Y} = \lambda_Q^2 \begin{bmatrix} \lambda_M^2 & 0 \\ 0 & 1 \end{bmatrix}. \tag{6.50}$$

The covariance matrix of the noiseless signal space constellation after modulator imbalances is given by

$$\boldsymbol{Y'} = \boldsymbol{M}\boldsymbol{Y}\boldsymbol{M}^T\,. \tag{6.51}$$

Since $\boldsymbol{Y'}$ has exactly the same form as $\boldsymbol{F'}$ in (6.38), a similar imbalance extraction procedure to the one that was used for the demodulator can be used for extracting the modulator imbalances. In this case, the distortion matrix $\boldsymbol{M}$ can be modelled as a lower-triangular matrix by using the $Q$ channel as a reference. The subsequent expression for $\boldsymbol{M}$ when the $Q$ channel is used as reference was derived in (2.79) and is presented here again:

$$\boldsymbol{M} \;=\; \begin{bmatrix} \eta_M \cos(\psi_M) & 0 \\ \eta_M \sin(\psi_M) & 1 \end{bmatrix}. \tag{6.52}$$

Note that, since the $Q$ channel was used as reference, $\eta_Q$ has been normalised to unity.

Cholesky factorisation can be performed on $\boldsymbol{Y'}$, yielding

$$\boldsymbol{Y'} = \boldsymbol{E}\boldsymbol{E}^T \tag{6.53}$$

where $\boldsymbol{E}$ represents the lower triangular matrix

$$\boldsymbol{E} = \boldsymbol{M}\boldsymbol{Y}^{1/2} = \lambda_Q \boldsymbol{M} \begin{bmatrix} \lambda_M & 0 \\ 0 & 1 \end{bmatrix}. \tag{6.54}$$

Since the scaling $\lambda_M$ is known it can be removed, yielding

$$\begin{aligned} \boldsymbol{E}' &= \boldsymbol{E} \begin{bmatrix} 1/\lambda_M & 0 \\ 0 & 1 \end{bmatrix} \\ &= \lambda_Q \boldsymbol{M}\,. \end{aligned} \tag{6.55}$$

This is exactly the same result that was arrived at during the demodulator extraction development. The inverse of $\boldsymbol{E'}$ can therefore be used directly for compensation, resulting in an unknown scaling of $1/\lambda_Q$. Since compensation is implemented in the digital domain of the quadrature modulator, this can arguably be corrected fairly easily, by simply restoring the transmit signal to the appropriate magnitude. Alternatively, the gain and phase imbalances can also directly be extracted from $\boldsymbol{E}'$ as

$$\varphi_M = \tan^{-1}\left(\frac{[\boldsymbol{E'}]_{21}}{[\boldsymbol{E'}]_{11}}\right) \tag{6.56}$$

$$\eta_M = \frac{\sqrt{[\boldsymbol{E'}]_{11}^2 + [\boldsymbol{E'}]_{21}^2}}{[\boldsymbol{E'}]_{22}}. \tag{6.57}$$

Compensation for the quadrature imbalances of the modulator is now performed by using the $I/Q$ imbalance parameters to compute the inverse of $\boldsymbol{M}$ and relaying this information as control data back to the modulator to be applied in the digital domain there.

Note that the technique discussed in this section is also applicable to the demodulator special case where a perfect modulator was used, but where the two components in $\boldsymbol{a}(n)$ does not have equal mean power. The only difference is that the final expressions for the gain and phase imbalance extraction in eqs. (6.57) and (6.56) should be substituted with those applicable to the demodulator, as presented in eqs. (6.42) and (6.41).

#### Special case: Perfect demodulator

In the case where a perfect demodulator is used at reception, the imbalance matrix $\boldsymbol{D} = \boldsymbol{I}$. If a frequency or phase offset is, however, present (i.e. $\boldsymbol{R}(n) \neq \boldsymbol{I}$), then it will still need to be removed using standard carrier synchronisation techniques. The technique described above for modulator imbalance extraction for the cascaded case, is thus directly applicable in the case where only modulator imbalances were encountered.

### 6.4.3 An adaptive algorithm

In practice, the distorted covariance matrix $\boldsymbol{F'}$ and $\boldsymbol{Y'}$ can be estimated using sample averages over $N$ received symbols (the block-based approach). Alternatively, the Cholesky

decomposition of the covariance matrix of the received signal can be computed adaptively, without explicitly computing the covariance matrix. One such algorithm is given by [19]

$$\boldsymbol{y(k)} = \boldsymbol{W(k)x(k)} \tag{6.58}$$

$$\boldsymbol{W(k+1)} = (1+\mu)\boldsymbol{W(k)} - \mu \cdot \text{tril}\left[\boldsymbol{y(k)y^T(k)}\right]\boldsymbol{W(k)}\,. \tag{6.59}$$

In the above algorithm, $k$ denotes the iteration, $\boldsymbol{x}$ the input sample, $\mu$ the positive step size and tril() takes the lower triangular matrix of its argument. $\boldsymbol{W}$ is the $2 \times 2$ adapted matrix; in this case, $\boldsymbol{W}$ denotes the inverse of the Cholesky factorisation of the covariance matrix of $\boldsymbol{x}$. $\boldsymbol{W}$ therefore already represents the compensation matrix when the real and imaginary components of $\boldsymbol{a}(n)$ have equal mean power, and no further inversion is required in this case. This approach is attractive, since it has a low computational complexity and enables adaptive tracking of $I/Q$ imbalances over time. It is also more memory-efficient than a block-based approach.

### 6.4.4 Technique summary

In the chapter so far, techniques for blind imbalance modulator and demodulator extraction and compensation have been presented. It was seen that different approaches should be followed, depending on the scenario (cascaded modulator and demodulator imbalances, modulator imbalances only, demodulator imbalances only), as well as the synchronisation (full synchronisation, frequency offset, phase offset) and the statistics of the baseband signal $\boldsymbol{a}(n)$ (correlated, uncorrelated equal mean power, uncorrelated unequal mean power).

Fig. 6.4 provides a flow diagram that describes which extraction technique is applicable in each scenario.

### 6.4.5 Generalisation to low-IF transceivers

Although the analysis in this chapter focused on a zero-IF architecture, the techniques derived are also applicable to quadrature transceivers operating in a low-IF fashion, if the same assumptions on the baseband signal holds true.

It was seen that the only underlying requirements on the baseband signal $\boldsymbol{a}(n)$ are that its two quadrature components should be uncorrelated (i.e. it should have a diagonal covariance matrix), and in some cases that these components exhibit equal mean power. If the desired baseband signal in the low-IF topology complies to these requirements, then the techniques in this chapter are directly applicable.

As an example, consider a multi-frequency channel system, where a number of independent data signals are each modulated onto its own digital subcarrier. The baseband signal for a $J$-channel system is then given by

$$\boldsymbol{a}(n) = \boldsymbol{R_1}(n)\boldsymbol{a_1}(n) + \boldsymbol{R_2}(n)\boldsymbol{a_1}(n) + \ldots + \boldsymbol{R_J}(n)\boldsymbol{a_J}(n) \tag{6.60}$$

where each rotation matrix $\boldsymbol{R_x}(n)$ represents the digital subcarrier frequency offset. Note that since each individual channel signal is rotated by a time-varying rotation matrix, the

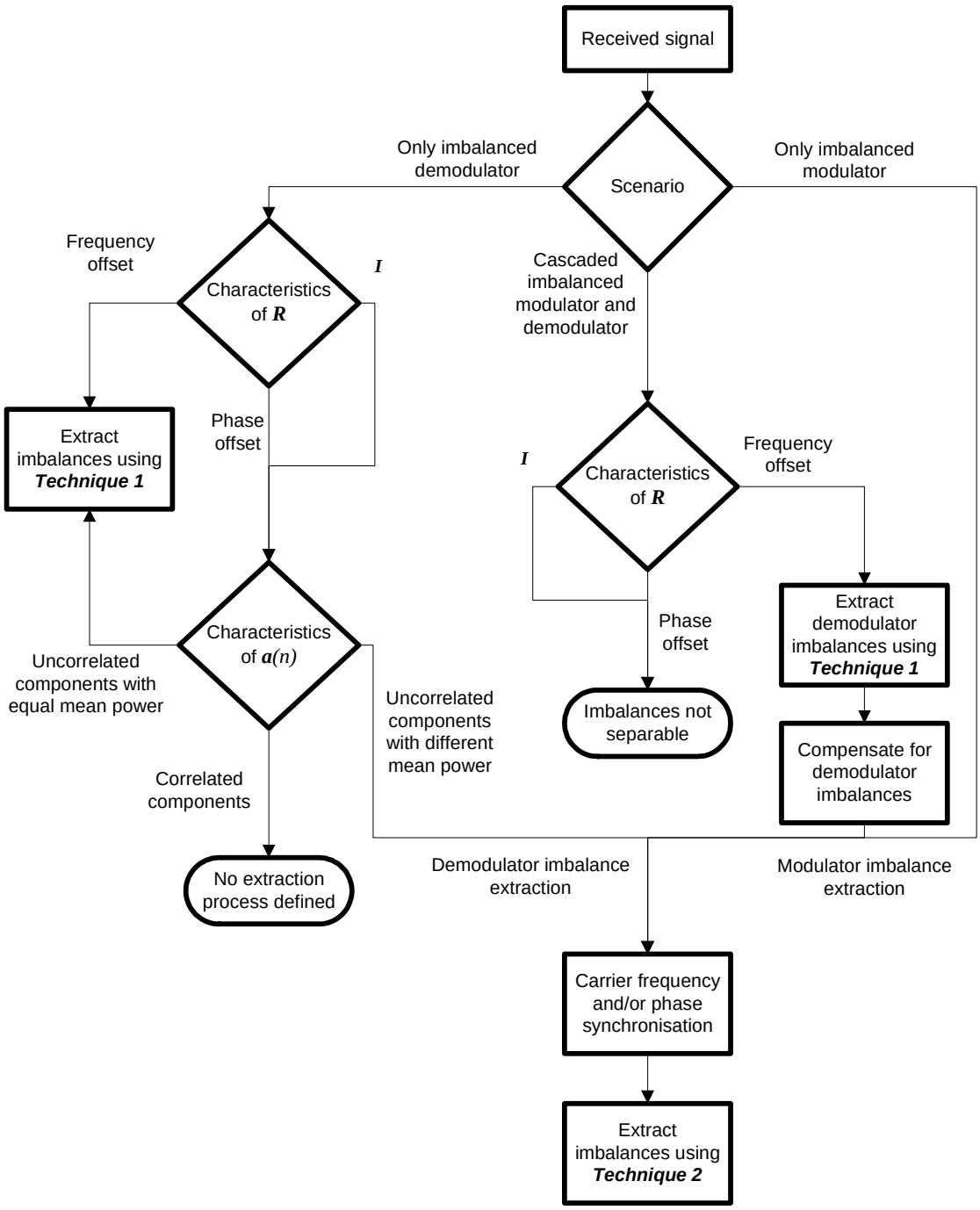


**Figure 6.4:** *Flow diagram illustrating the applicable extraction techniques and processing steps for different imbalance scenarios. Technique 1 refers to the extraction technique developed for the demodulator, in Section 6.4.1. Technique 2 refers to the extraction technique developed for the modulator in Section 6.4.2.*

covariance of each rotating channel signal will be approximately diagonal when observed over time. Since the signals of each frequency channel can be assumed to be independent sources, it then follows that the covariance matrix of $\boldsymbol{a}(n)$ will also be diagonal when observed over time, which means that all the techniques presented in this chapter are directly applicable

to this example.

## 6.5 Practical performance issues

In this section, issues which will affect the performance of the developed blind imbalance extraction techniques will be discussed. This includes the technique's sensitivity towards the LO frequency offset in terms of observing an $2\pi$ rotation, the effect of channel noise on modulator imbalance extraction, as well as the effect of a frequency-selective communications channel.

### 6.5.1 Sensitivity to LO frequency offset

In practice, the exact value of the local oscillator frequency offset (used to isolate the demodulator imbalances from that of the modulator) may not be known. Also, when this frequency offset is normalised with respect to the symbol sampling rate, it will almost certainly result in an irrational number, due to the lack of frequency coherence between the transmitter and receiver local oscillators. The combined rotation and symbol sampling will then produce an aperiodic sampling sequence. It is therefore unlikely that the rotating symbol space will be observed over an exact multiple of a $2\pi$ rotation in practice. However, as the number of symbols used in the imbalance estimation is increased to include many cycles of the approximate $2\pi$ constellation rotation, the residual estimation error diminishes. This is verified in Simulation 1 (Section 6.6).

### 6.5.2 Effect of noise

From (6.48) it can be seen that the i.i.d. channel noise term $\boldsymbol{R}(n)^{-1}\tilde{\boldsymbol{v}}(n)$ will cause diagonal loading on the covariance matrix of the signal space $\boldsymbol{M}\boldsymbol{a}(n)$, introducing an estimation error in the modulator compensation parameters. The reliability of the modulator imbalance extraction is consequently a function of the signal to noise ratio (SNR), as is confirmed in Simulation 2 (Section 6.6.2). Analogous to the modulator case, any noise entering the system after the demodulator will also have the same detrimental effect on the demodulator compensation performance. However, the signal plus noise power entering the demodulator is usually much larger than the noise introduced after the demodulator, thus rendering the latter's effect on performance negligible.

### 6.5.3 Effect of a frequency-selective channel

During transmission through a frequency-selective channel, the transmitted signal is convolved with the impulse response of the channel. Using the cascaded imbalance expression in (6.13), the effect of a frequency-selective channel may be included in the cascaded system

as

$$\boldsymbol{z'}(n) = \boldsymbol{D}\Big\{\boldsymbol{R}(n)\sum_{l=1}^{L}\Big[\boldsymbol{H}(l)\boldsymbol{M}\boldsymbol{a}(n-L+l)\Big] + \widetilde{\boldsymbol{v}}(n)\Big\} \tag{6.61}$$

where the matrix $\boldsymbol{H}(l)$ contains the elements of a complex channel impulse response $h(l) = h_I(l) + jh_Q(l)$ of length $L$. $\boldsymbol{H}(l)$ is constructed from $h(l)$ as

$$\boldsymbol{H}(l) = \begin{bmatrix} h_I(l) & -h_Q(l) \\ h_Q(l) & h_I(l) \end{bmatrix}. \tag{6.62}$$

Since the LO frequency offset will still serve to diagonalise the covariance matrix of $\sum_{l=1}^{L}\Big[\boldsymbol{H}(l)\boldsymbol{M}\boldsymbol{a}(n-L+l)\Big]$, the frequency-selective channel will not affect the demodulator imbalance extraction performance.

When the demodulator special case of Section 6.4.1 is considered (when a perfect modulator is employed), the received signal becomes

$$\boldsymbol{z''}(n) = \boldsymbol{D}\Big\{\boldsymbol{R}(n)\sum_{l=1}^{L}\Big[\boldsymbol{H}(l)\boldsymbol{a}(n-L+l)\Big] + \widetilde{\boldsymbol{v}}(n)\Big\}. \tag{6.63}$$

To simplify the discussion developed below, let

$$\boldsymbol{s}(n,l) = \boldsymbol{H}(l)\boldsymbol{a}(n-L+l) \tag{6.64}$$

and

$$\boldsymbol{a_H}(n) = \sum_{l=1}^{L}\boldsymbol{s}(n,l) \tag{6.65}$$

so that

$$\boldsymbol{z''}(n) = \boldsymbol{D}\Big\{\boldsymbol{R}(n)\boldsymbol{a_H}(n) + \widetilde{\boldsymbol{v}}(n)\Big\}. \tag{6.66}$$

When a signal with initially uncorrelated $I$ and $Q$ components with equal variance passes through a complex frequency-selective channel, the output's components will also be uncorrelated [66]. This statement is easily proven: Consider that

$$\boldsymbol{H}(l)\boldsymbol{H}(l)^T = [h_I(l)^2 + h_Q(l)^2]\boldsymbol{I}. \tag{6.67}$$

For the case where the real and imaginary components of $\boldsymbol{a}(n)$ are uncorrelated and have equal variance, the covariance matrix of $\boldsymbol{a}(n)$ was defined in (6.45) as $\boldsymbol{Y} = \mathrm{diag}[\lambda^2,\ \lambda^2]$. The covariance matrix of $\boldsymbol{s}(n,l)$ is therefore given by the diagonal matrix $\boldsymbol{H}(l)\boldsymbol{Y}\boldsymbol{H}(l)^T = \lambda^2[h_I(l)^2+h_Q(l)^2]\boldsymbol{I}$. Since the $L$ terms in the sum in $\boldsymbol{a_H}(n)$ are uncorrelated and independent, it follows that the covariance matrix of $\boldsymbol{a_H}(n)$ will also be a diagonal matrix with identical entries.

Consequently, (6.66) represents exactly the same form as was analysed in (6.46), where it was shown how in this case, the rotational matrix will not affect the diagonal property of the signal covariance matrix and thus also not affect imbalance extraction at all.

It can therefore be concluded that the frequency-selective channel will also have no effect on demodulator imbalance extraction, when the original signal's real and imaginary components are uncorrelated with equal variance. This is confirmed in Simulations 3 and 5 (Section 6.6).

For modulator imbalance extraction the above analysis does not hold, and therefore as with the carrier frequency and phase offset, if the effect of the channel is thus not removed before imbalance extraction, it will distort the extracted compensation parameters.

Although there is a strong connection between $I/Q$ imbalances and channel equalisation performance, the authors of [49] argue that demodulator imbalances will affect the channel equalisation process more than modulator imbalances. Since a LO frequency offset allows us to extract and compensate for demodulator imbalances independent of the channel, it can be expected that the remaining effect of modulator impairments on channel equalisation will be small. This statement is investigated further in Simulation 2 (Section 6.6).

## 6.6 Simulation results

In order to verify the performance of the proposed compensation techniques under different operating scenarios, MATLAB simulations were performed. The simulations were performed using the baseband-equivalent models developed in this chapter.

### 6.6.1 Simulation 1: Sensitivity to the LO frequency offset

#### Aim of simulation

Investigate the sensitivity of the modulator and demodulator imbalance separation process, towards the exact LO frequency offset, or whether or not an observation over an exact $2\pi$ rotation is generally required.

#### Simulation approach

In this simulation imbalance extraction was performed using the block-based approach. A 64-QAM system with $\eta_M = \kappa_D = 1.05$ and $\psi_M = \chi_D = 5^\circ$ was simulated at a SNR per bit (SNR/bit or $E_b/N_0$) of 15 dB. Irrational numbers were chosen for the LO frequency offsets in the simulations, to mimic the non-coherent frequency references of independent transmitters and receivers. The relative image ratio (RIR) of the demodulator, as derived in (6.33) was used as the performance benchmark. As a reference, the case of no modulator imbalances with no LO frequency offset is also tested for reference.

#### Results and discussion

Fig. 6.5 illustrates the insensitivity of the modulator-demodulator imbalance isolation process to the local oscillator frequency offset. Since no noticeable performance degradation

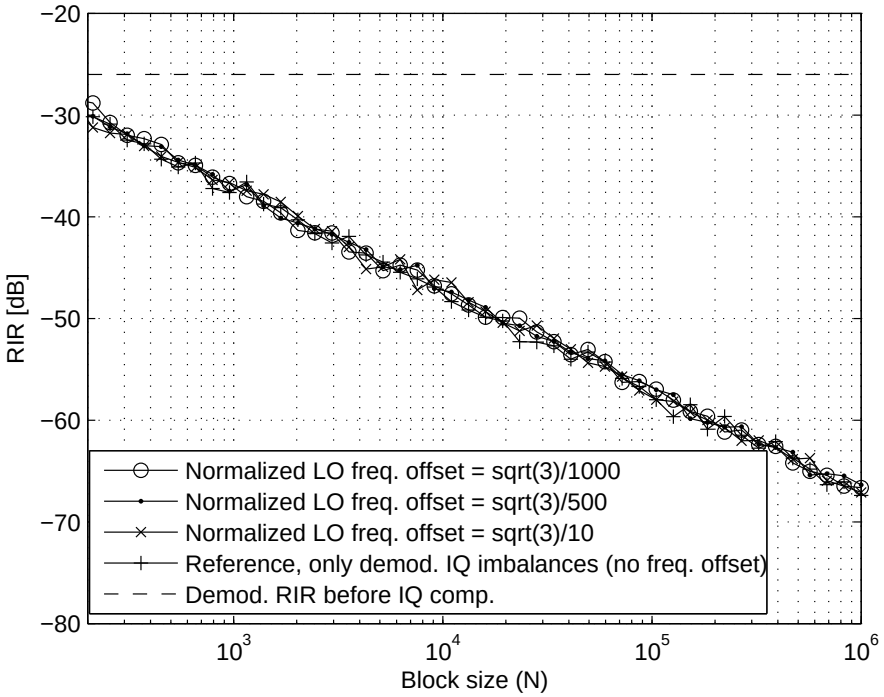


**Figure 6.5:** *The RIR of an imbalanced 64-QAM demodulator after compensation, indicating the insensitivity of the modulator-demodulator imbalance isolation process towards the LO frequency offset. Imbalance parameters were* $\eta_M = \kappa_D = 1.05$ *(0.42 dB) and* $\psi_M = \chi_D = 5°$ *(RIR of* $-26$ *dB).*

could be observed when compared to the reference, it is concluded that the accuracy to which the demodulator imbalances can be isolated and estimated when an imbalanced modulator is insensitive to the LO frequency offset and its $2\pi$ rotation of the signal space, when a sufficient number of symbols is used in the estimation. In this case even 100 symbols delivered no noticeable performance degradation.

### 6.6.2 Simulation 2: Effect of the communications channel

#### Aim of simulation

Verify the respective sensitivity of the blind imbalance extraction techniques of the modulator and demodulator, towards the effect of a noisy, frequency-selective communication channel.

#### Simulation approach

In this simulation, a 16-QAM system was simulated. The approach was to employ a noisy, frequency-selective communication channel and then separately simulate the extraction of modulator and demodulator imbalances. Simultaneous separation of imbalances was verified in the previous simulation; therefore, in order to isolate the effect of the channel on the

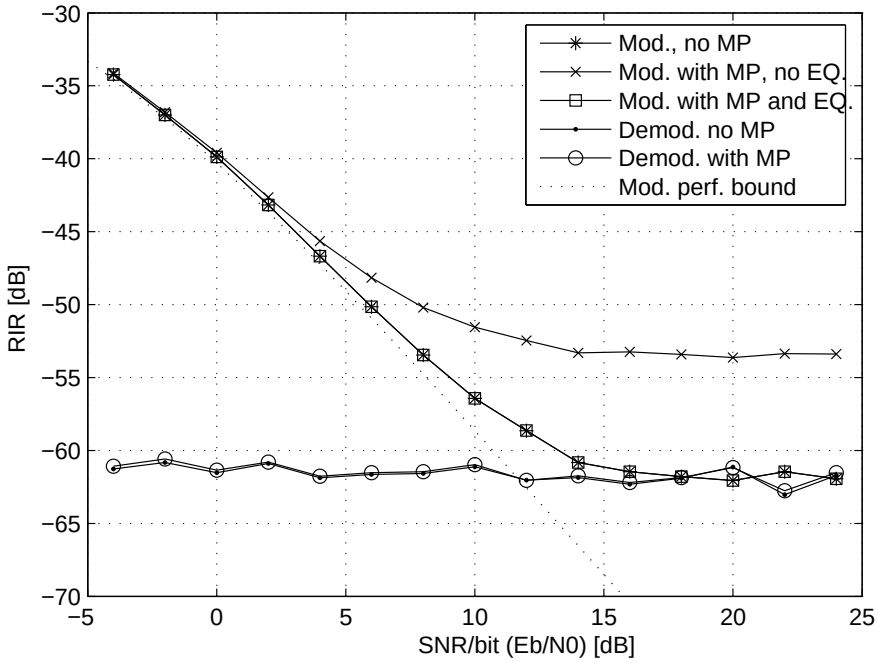


**Figure 6.6:** *Effectiveness of modulator imbalance compensation (in terms of RIR at the modulator after compensation) on a 16-QAM system over a noisy multipath (MP) channel, with and without channel equalisation (EQ). Imbalance parameters were* $\eta_M = 1.05$ *(0.42 dB) and* $\psi_M = 5°$ *(RIR of* $-26$ *dB). The multipath channel* $h(l) = [0.8660 + j0.5000 \;\; 0.0643 + j0.0766 \;\; 0.0098 - j0.0017]$. *The dotted line indicates the performance bound when extracting imbalance parameters from a diagonally loaded covariance matrix (see text). Demodulator performance in the presence of the same channel is also shown.*

performance of the extraction techniques, the extraction process was first performed using an imbalanced modulator with a perfect demodulator and then vice versa.

To investigate the extraction performance of the modulator, the modulator's imbalances ($\eta_M = 1.05$, $\psi_M = 5°$) were extracted at a perfect demodulator, after the signal had passed through a noisy (AWGN), multipath channel ($h(l) = [0.866 + j0.5 \;\; 0.0643 + j0.0766 \;\; 0.0098 - j0.0017]$ with symbol spacing), with and without channel equalisation. Channel equalisation was performed using a zero-forcing equaliser (ZFE) (see e.g. [39, p. 661] for implementation details). The SNR per bit was varied from $-4$ to 24 dB.

Subsequently, the extraction performance of an imbalanced demodulator ($\kappa_D = 1.05$, $\chi_D = 5°$) was investigated using the same channel, with data generated by a perfect modulator.

For both cases, the modulator and demodulator imbalances were extracted using the block-based approach, with $N = 5 \times 10^5$.

**Results and discussion**

Fig. 6.6 shows the effect of the channel noise and multipath propagation on the compensated RIR performance of a modulator and demodulator. The RIR performance was determined using the expressions in eqs. (6.27) and (6.33).

Also shown is the performance bound obtained when the theoretical covariance matrix of the signal constellation, distorted by modulator $I/Q$ imbalances and diagonally loaded with values equal to the noise variance, is subjected to the Cholesky factorisation process. This procedure thus provides the theoretical performance bound for modulator extraction performance in the presence of noise, disregarding the effect of multipath fading.

From Fig. 6.6 it can be seen that, as expected, the diagonal loading caused by channel noise affects the modulator performance, but not that of the demodulator. At high SNR, the multipath effects dominate the modulator performance, but has no effect on the demodulator. When channel equalisation is performed before the modulator imbalances are estimated, the loss in compensation performance can be regained. After channel equalisation, the modulator performance at high SNR, like that of the demodulator, is dominated by the number of symbols used in the imbalance estimation process.

Comparison with Fig. 6.5 at $N = 5 \times 10^5$ where the same imbalances were introduced on a 64-QAM system, also demonstrates the compensation technique's insensitivity toward the specific modulation scheme, assuming a symmetrical constellation.

### 6.6.3 Simulation 3: BER Performance

**Aim of simulation**

Verify the complete compensation performance of a cascaded imbalanced modulator and demodulator, in a noisy frequency-selective channel, as a function of the achievable bit error rate (BER).

**Simulation approach**

The performance of the proposed technique was evaluated in a cascaded imbalanced modulator and demodulator scenario, where the coupling effect of the modulator and demodulator imbalances was removed with the use of a normalised LO frequency offset of $\sqrt{3}/500$ rad/symbol. No effort was made to ensure an observation period of an exact $2\pi$ rotation.

Two cases were investigated, both investigating 64-QAM systems. The first case represents a more ideal scenario, employing only a noisy channel and assuming perfect synchronisation and symbol timing at the receiver.

The second case represents a more realistic scenario, employing a noisy channel with multipath fading. Nyquist filters with a roll-off factor of 0.5 were used, and a symbol timing error of 5% was introduced. Zero-forcing channel equalisation was performed after demodulator $I/Q$ compensation.

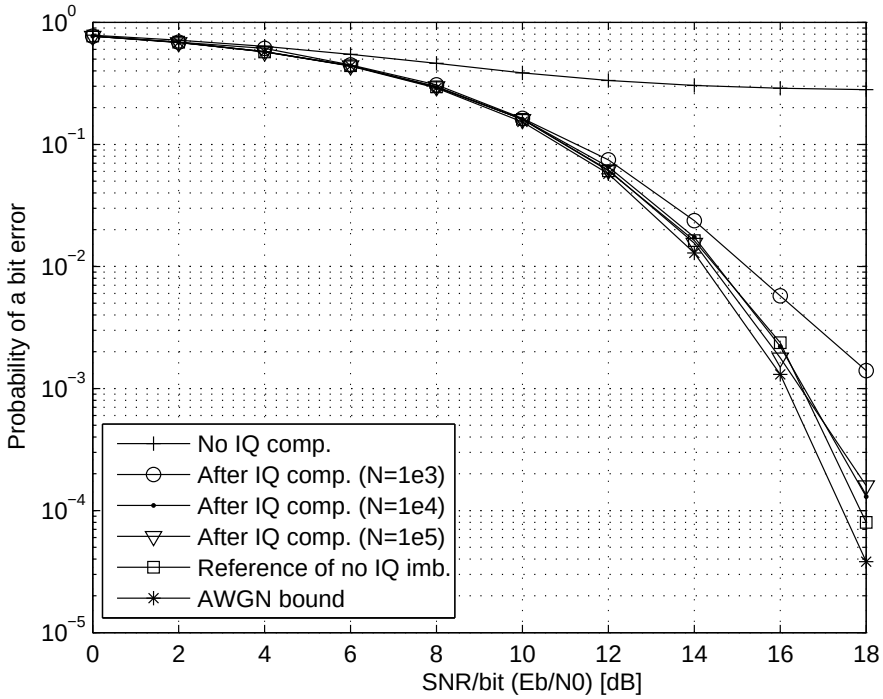


**Figure 6.7:** *BER performance of 64-QAM in an AWGN channel,* $\eta_M = \kappa_D = 1.05$ *(0.42 dB) and* $\psi_M = \chi_D = 5°$*. The normalised LO frequency offset was* $\sqrt{3}/500$ *rad/symbol.*

Imbalance estimation using the block-based approach was performed at the various noise levels and then used for compensation at that noise level. The block lengths used for the imbalance estimation was also varied. The imbalances of the modulator were extracted at the receiver and compensated for at the transmitter. For each SNR/bit setting, the BER was measured at the receiver, before and after employing the extracted compensation.

### Results and discussion

Fig. 6.7 shows the bit error rate (BER) performance of the 64-QAM system in an additive white Gaussian noise (AWGN) channel, with perfect synchronisation and symbol timing. Imbalance values of $\eta_M = \kappa_D = 1.05$ and $\psi_M = \chi_D = 5°$ were introduced. The number of symbols used to estimate the imbalances, $N$, is also shown. The technique improves the BER to the reference level (no $I/Q$ imbalances) for the cases $N = 10^4$ and $N = 10^5$ and manages to improve the BER performance significantly even for $N = 10^3$.

Fig. 6.8 shows the results for the more realistic scenario, again employing 64-QAM. Nyquist filters with a roll-off factor of 0.5 were used, and a symbol timing error of 5% were introduced. Zero-forcing channel equalisation was performed after demodulator $I/Q$ compensation. In this figure a noisy multipath channel with impulse response $h(l) = [0.9962 + j0.0872 \quad 0.0643 + j0.0766 \quad 0.0492 - j0.0087]$ (symbol period spacing) was simulated. As a reference, a system without any $I/Q$ imbalance, but with the same Nyquist

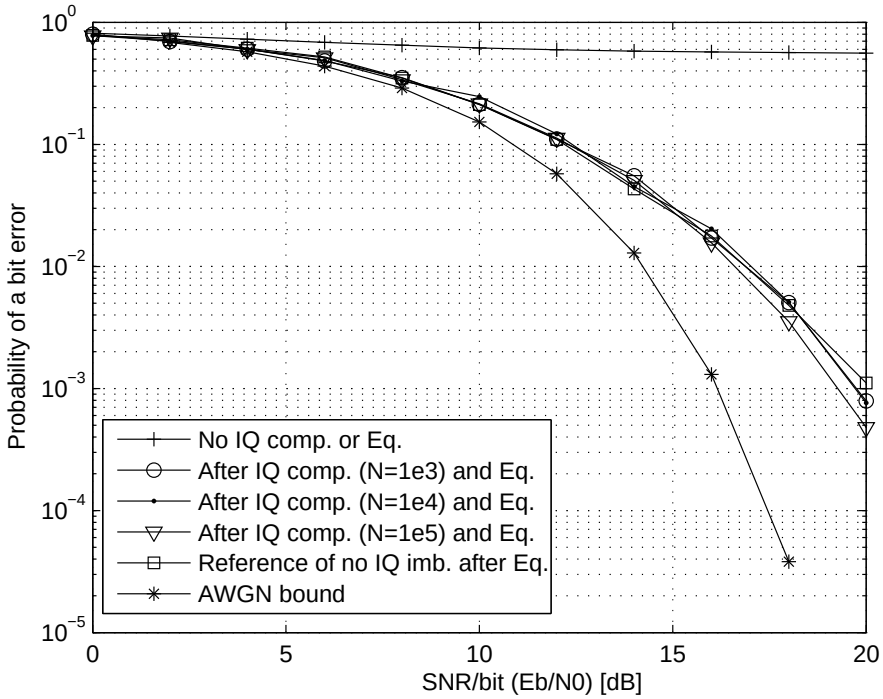


**Figure 6.8:** *BER performance of 64-QAM in a multipath channel* ($h(l) = [0.9962 + j0.0872 \;\; 0.0643 + j0.0766 \;\; 0.0492 - j0.0087]$)*, with symbol timing error of* 5%*, and imbalances of* $\eta_M = \kappa_D = 1.05$ *(0.42 dB) and* $\psi_M = \chi_D = 5°$*. The normalised LO frequency offset was* $\sqrt{3}/500$ *rad/symbol. BER performance is shown before* $I/Q$ *compensation (IQ comp.) or channel equalisation (Eq.), as well as after* $I/Q$ *compensation with different values of* $N$*. As a reference, the system performance without any* $I/Q$ *imbalances is also shown.*

filters, and symbol timing error was also employed and subjected to channel equalisation. From the figure it is seen that the proposed technique again recovers the performance loss due to $I/Q$ imbalances to the level of the reference system with no $I/Q$ imbalances. The remaining performance loss (compared to the AWGN bound shown) is attributed to the channel equalisation loss and symbol timing error.

Comparing the reference system with no $I/Q$ imbalances, to the graph before $I/Q$ compensation, it is seen that the quadrature imbalances have a severe impact of the BER performance. After $I/Q$ compensation the BER is improved significantly, completely regaining the performance loss due the $I/Q$ imbalances.

### 6.6.4 Simulation 4: Comparison to other methods

#### Aim of simulation

Compare the extraction performance of the blind compensation technique developed in this chapter, to other methods in literature that also use second order statistics in their approach.

#### Simulation approach

The performance of the proposed technique was compared to two other techniques from literature, that uses second-order statistics in a block-based estimation: the technique of Anttila et al. [2] and the 'stat' method of [48]. The low-IF method of [71] was not considered due to its similarity to that of Anttila et al. and the fact that it is restricted to low-IF receivers, requiring extra mixing and filtering operations in its implementation.

The three methods all have comparable computational complexities. In the experiment, an imbalanced demodulator ($\kappa_D = 1.05$ and $\chi_D = 5°$) was used with 64-QAM modulation. The symbol rate was defined to be 3.84 MHz, at an RF center frequency of 2 GHz. A multipath fading channel was used, with a power delay profile following the Vehicular A model [28] and a mobility of 100 km/h. No frequency synchronisation was performed at the receiver, and the normalised LO frequency offset was $\sqrt{3}/1000$ rad/symbol. Compensation parameters were estimated for various SNR/bit values. These parameters were then used to determine the RIR capability of the receiver after compensation at that SNR/bit. The RIR before compensation was $-26$ dB.

#### Results and discussion

Figure 6.9 shows the average of 1000 runs. All three techniques essentially perform equally well, and their performance is not severely affected by the non-idealities introduced in the simulation. It is also shown that the performance of the technique presented in this dissertation is indeed independent of frequency synchronisation.

### 6.6.5 Simulation 5: Adaptive algorithm performance

#### Aim of simulation

Verify the performance of the adaptive variant of the developed blind compensation technique in a noisy multipath environment.

#### Simulation approach

The adaptive (iterative) version of the proposed technique (Section 6.4.3) was tested on an imbalanced ($\kappa_D = 1.05$ and $\chi_D = 5°$) demodulator using 64-QAM modulation. The channel and mobility parameters were chosen to be the same as for Simulation 4. A frequency offset of $\sqrt{3}/1000$ rad/symbol was used with a SNR/bit of 15 dB.

#### Results and discussion

Fig. 6.10 shows the convergence performance of the iterative algorithm, expressed in terms of the RIR performance of the demodulator after compensation, averaged over 100 runs. As a comparison, the simulation was repeated without the multipath fading channel.

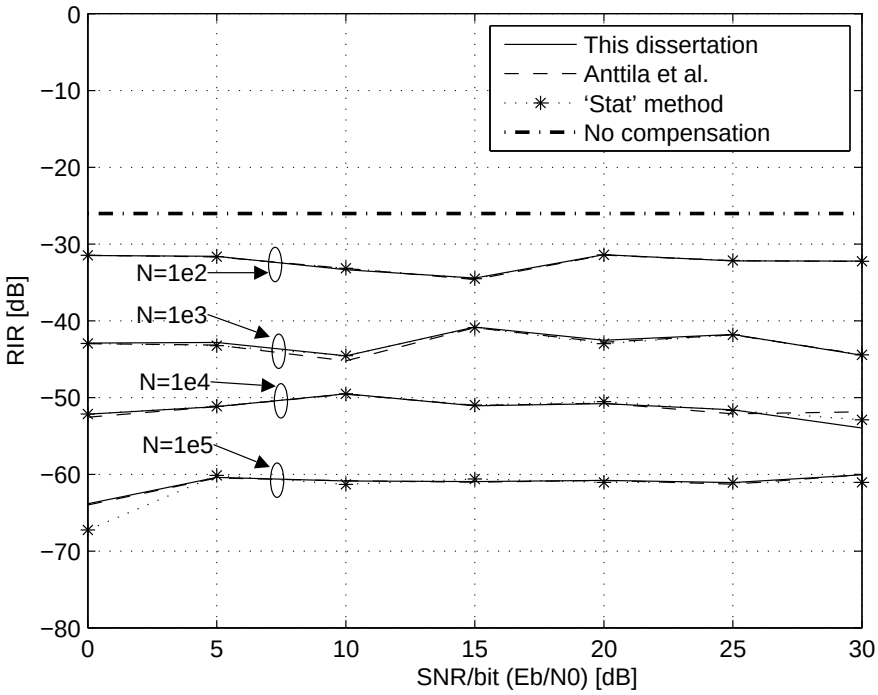


**Figure 6.9:** *Comparison of the image suppression capabilities of the proposed technique to that of Anttila et al. [2] and the 'stat' method of [48]. The received signal was 64-QAM, with a normalised LO frequency offset of* $\sqrt{3}/1000$ *rad/symbol, in a fading multipath channel defined by the Vehicular A model [28], with* 100 *km/h mobility. Receiver imbalances are* $\kappa_D = 1.05$ *(0.42 dB) and* $\chi_D = 5°$ *(RIR of* $-26$ *dB). N denotes the block size used during estimation.*

It is seen that the compensation performance remains unaffected by the fading multipath channel. Comparing the result to that of the previous simulation in Fig. 6.9, it is seen that a small performance loss is incurred (about 5 dB in terms of RIR performance) using the adaptive version, relative to the block-based approach, when comparing the number of samples used in the estimate. The adaptive variant does, however, not have the memory requirements of the block based approach.

## 6.7 Conclusions

This chapter introduced a novel blind frequency-independent compensation approach for correcting $I/Q$ imbalances inherent to practical quadrature mixing transceivers, based on knowledge of the second-order statistics of the received signal. Unlike other techniques found in literature, the proposed technique does not only aim to decorrelate the $I$ and $Q$ signals, but can extract the exact gain and phase imbalances directly, relative to the chosen reference signal path ($I$ or $Q$ path), through a Cholesky decomposition of the received signal's

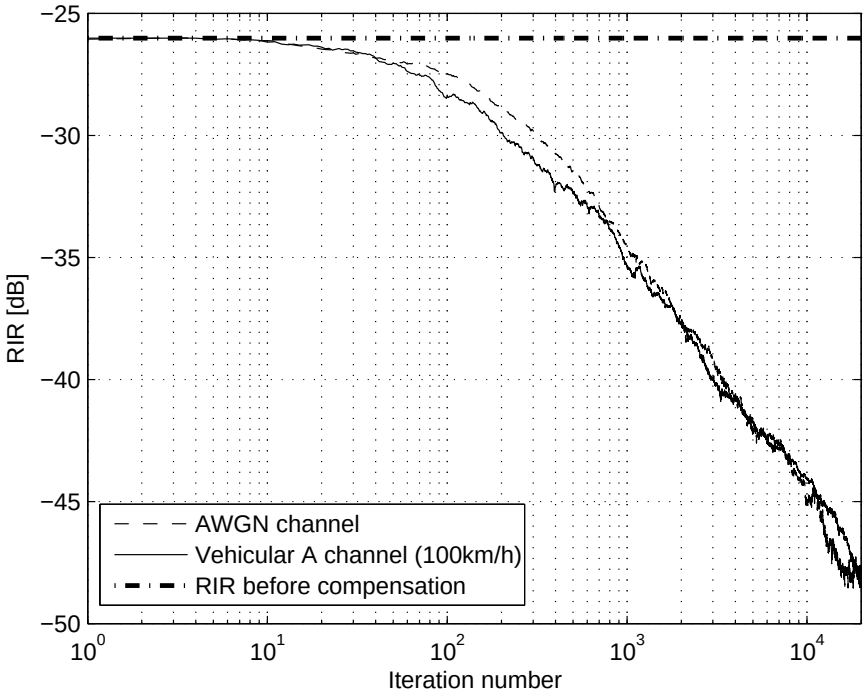


**Figure 6.10:** *The performance of the adaptive version of the proposed technique. The received signal was 64-QAM, with a LO frequency offset of* $\sqrt{3}/1000$ *rad/symbol. A fading multipath channel, defined by the Vehicular A model [28] with 100 km/h mobility, was used. The SNR/bit was 15 dB with receiver* $I/Q$ *imbalances of* $\kappa_D = 1.05$ *(0.42 dB) and* $\chi_D = 5°$ *(RIR of* $-26$ *dB). The step size was* $\mu = 0.0001$*.*

covariance matrix. The developed extraction technique can be implemented in a block-based approach or using a low-complexity, adaptive version. It was seen that a small performance loss in incurred by using the adaptive approach, however the memory requirements of the technique is drastically reduced.

Another unique contribution of the this chapter is that it investigated the cascaded imbalanced modulator and demodulator scenario. It was showed analytically how the imbalances of the modulator and demodulator can be separated and extracted in a blind fashion, using only the statistical properties of the received signal. The decoupling of the modulator and demodulator imbalances are done on the premise of a frequency offset between the their respective LO signals – a principle that was established in Chapter 2 already and was shown to be applicable here again. Simulation results indicated that, given enough samples in the estimation process, the separation of the modulator and demodulator imbalances is insensitive towards the choice of frequency offset, or whether an exact $2\pi$ rotation is observed.

Demodulator imbalance extraction was shown analytically and through simulation, to be independent of carrier frequency or phase offset or even the effect of a frequency-selective channel, assuming that the real and quadrature components of the baseband signal were

originally uncorrelated with equal variance. For modulator imbalances to be extracted at the demodulator it was, however, seen that carrier synchronisation and channel equalisation need to be performed before its imbalances can be extracted. In simulation this approach was shown to be feasible.

Demodulator imbalance extraction was found to be essentially only limited by the number of samples used in the estimation process, irrespective of the SNR. For modulator imbalance extraction, it was shown how additive noise causes diagonal loading of the estimated compensation matrix, thus reducing the accuracy of the estimation.

Simulation results furthermore indicate that the proposed techniques manage to restore the implementation loss in BER due to quadrature imbalances, even in a challenging scenario using high order modulation schemes, in a multipath environment with symbol timing errors.

Even though the techniques were developed from a zero-IF perspective, the compensation techniques are generally applicable to low-IF topologies as well, as long as the assumptions on the statistics of the desired signal hold true.

# Chapter 7

# Conclusions

## 7.1 Summary of work done

In this study, the limitations on the performance of quadrature mixing, namely its sensitivity towards gain and phase imbalances between the two signal paths, have been thoroughly analysed. Baseband-equivalent models have been developed from first principles, which model the frequency-dependent imbalances of both the quadrature modulator and demodulator. It should be noted that most authors in literature only model the frequency-independent quadrature imbalances. Of those that do present some form of frequency-dependent model, it is mostly restricted to the demodulator, where the assumption is made that frequency-dependent imbalances can be represented through mismatched LPFs. The developed models in this dissertation extend the current frequency-dependent modelling found in literature by also modelling bandpass imbalances, which manages to explain the asymmetrical gain and phase imbalance observed in practical hardware implementations of quadrature mixing front ends, for both the quadrature modulator and demodulator. The models presented in literature for frequency-dependent and independent imbalances were shown to be special cases of the models derived in this study.

The developed baseband-equivalent models were subsequently used to derive novel frequency-dependent imbalance extraction and compensation techniques. Based on the extensive modelling, this study was able to show that with appropriate test signals, the frequency-dependent imbalances of the quadrature modulator and demodulator can be extracted directly through spectral analysis, without the need for iterative search techniques or adaptive approaches. The imbalances are extracted from the received signal in the digital domain of the receiver. Compensation is then implemented in the digital domain of the modulator and demodulator.

The case of a cascaded imbalanced modulator and demodulator was also investigated – this case has received very little attention in literature. It was shown that the frequency-dependent imbalance contributions of the modulator and demodulator can be separated and extracted from only observing the received signal, given appropriate test signals and the ability to introduce a small frequency offset between the LO signals of the modulator and

demodulator. This then led to the the introduction of a technique for automatic transceiver calibration, exploiting the fact that a quadrature modulator and demodulator will typically exist on the same device. In this solution, the modulator generates the required test signals and feeds it directly into the demodulator, using the demodulator as the measurement device. The imbalances of both the modulator and demodulator are then extracted from the received test signals in the digital domain of the demodulator. This approach lends itself well to being implemented as a rapid start-up calibration procedure, and simply requires a feedback path to be added to the existing transceiver topology (i.e. no additional mixers, ADCs or other equipment).

A procedure was then presented to convert the extracted imbalance parameters of the modulator and demodulator into a compensation filter, providing frequency-dependent imbalance compensation over the whole frequency band of interest.

The validity and performance of the derived compensation techniques were investigated through simulations and a practical hardware implementation. The simulations validated the compensation techniques and the underlying models, while also investigating their performance in the presence of practical non-idealities, such as noise and quantisation. The hardware implementation served to validate the modelling approach proposed in this dissertation, by showing that practical quadrature front ends exhibit asymmetrical gain and phase imbalance functions over frequency, rendering current models in literature inadequate to accurately model this behaviour or lead to efficient compensation strategies to compensate for this effect. The hardware implementation was then used to show that the extraction and compensation techniques of this dissertation manage to achieve a vast improvement in the obtained image rejection performance of the quadrature front ends.

An investigation into the possibility of performing quadrature imbalance compensation using only live data and no test signals, led to the development of a novel, blind, quadrature imbalance compensation technique. This technique is applicable to narrow band cases where frequency-independent imbalances can be assumed. The developed technique uses the second-order statistics of the received signal to extract the imbalances of the front end. In the development of this technique, the cascaded imbalanced modulator and demodulator pair was considered, illustrating once again that the imbalances of both can be separated and extracted from the received signal, this time using a blind approach, if a frequency difference exists between the LO signals.

## 7.2 Conclusions

The conclusions of this section will be divided into those related to the imbalance modelling, frequency-dependent imbalance compensation and blind frequency-independent compensation. References will be made throughout this section to the hypotheses defined in Chapter 1.

### 7.2.1 Modelling

From the modelling of the frequency-dependent imbalances of the quadrature modulator and demodulator presented in Chapter 2, new insight into the characteristics of the imbalances was obtained.

By using the developed baseband-equivalent imbalance models, it was seen that the relative image ratio (RIR) of both the modulator and demodulator are dependent on the cascaded frequency response of their $I$ and $Q$ channels and the LO signals of their mixers. This is significant, since it follows that the imbalances of any contributing section in the front end, can be cancelled by that of another section. For instance, LPF mismatches may mitigate the imbalances of the mixer at certain frequencies. In fact, it is this exact principle that is used when baseband compensation filters are employed to compensate for the cascaded imbalances of the front end, including passband effects.

Although many similarities exist between the nature of the imbalances of the modulator and demodulator, some differences were also discovered that have not been noted in literature before. The most interesting difference between the $I/Q$ imbalances of the modulator and demodulator, involves the position in the frequency domain where the $I$ and $Q$ channels need to be matched to ensure image rejection, as well as the role of the bandpass imbalances (which have not been modelled in literature before). For the modulator it was seen that, in order to reject the image frequency related to some desired signal, the frequency response of the $I$ and $Q$ channels (including the mixer LO signals), should be matched in gain and phase, at the frequency where the image signals needs to be suppressed. In the case of the demodulator, it was found that the *image* signal component is suppressed if the channels are matched at the frequency of the *desired* component. This insight is lost when bandpass imbalances are not modelled, since it is the asymmetry in frequency of their baseband-equivalent contribution that leads to this insight. Furthermore, it was seen that the ratio between the gain of the bandpass response at the frequencies of the image and desired component, can further scale the RIR of the modulator. For the demodulator, this effect is not seen.

The modelling process revealed that, when the frequency-dependent imbalances of the quadrature mixing front end are modelled as imbalanced LPFs, the gain imbalance function of the front end would be symmetrical over frequency. Similarly, the phase imbalance function would be an odd function of frequency, if the phase offset at DC is subtracted – it was shown how this phase offset should be equal to the phase imbalance of the mixer if indeed only lowpass filter imbalances existed. When the gain and phase imbalance functions of a practical quadrature modulator and demodulator were measured in Chapter 4, it was seen that both these functions exhibit asymmetrical shapes as a function of frequency. This proves Hypothesis 1.1:

**Hypothesis 1.1:**

The common modelling approach in literature, where frequency-dependent imbalance are modelled as mismatched LPFs, fail to explain the asymmetrical gain and phase

imbalance characteristics observed in practical hardware quadrature mixer implementations.

This also implies that simply attempting to equalise the responses of the two LPFs will not yield the optimal solution to accomplish frequency-dependent imbalance compensation. By including the contributions of bandpass imbalances, the models derived in this dissertation were shown to cater for asymmetrical gain and phase imbalance functions. This was confirmed in simulation where the image rejection performance of the quadrature mixing front ends, constituting imbalance contributions from the LPFs, imbalanced LO signals, as well as BPF imbalances, were correctly predicted from the baseband-equivalent models (see Sections 2.5.1 and 2.5.2). In simulation it was also shown how the gain and phase imbalance functions change from even and odd functions to asymmetrical functions with the addition of a bandpass imbalance response (see Section 4.4.1), as was observed in the practical hardware measurements in Section 5.3. This confirms Hypothesis 1.2:

**Hypothesis 1.2:**

The modelling approach proposed in this dissertation is capable of modelling the asymmetrical frequency-dependent imbalance characteristics observed in practical hardware quadrature mixer implementations.

### 7.2.2 Frequency-dependent imbalance extraction and compensation

Novel techniques that use simple test tones to extract modulator and demodulator frequency-dependent imbalances, were presented in Chapter 4. These techniques were shown to be able to extract the imbalances of both the modulator and demodulator directly from the frequency spectrum of the received signal, using simple test tones. The accuracy of these extraction techniques were confirmed in simulation and through a hardware implementation in Chapter 5, where the RIR of both the modulator and demodulator could be improved significantly when the extracted parameters were implemented as compensation. This proves Hypothesis 2.1:

**Hypothesis 2.1:**

The baseband-equivalent models of this dissertation, together with simple test signals, will enable the direct extraction of quadrature imbalances, through spectral analysis.

It was seen through performance simulations in Chapter 5, that the performance of the extraction techniques will in practice be limited to the SFDR of the measurement (i.e. after FFT processing). In an AWGN environment, the extraction accuracy can therefore be improved by simply increasing the length of the FFT used for spectral analysis, since this will reduce the noise power contribution per bin, without reducing the signal power in its corresponding bin. Care should be taken to ensure that the quantisation noise spectrum is as white as possible, for the processing gain of the FFT to be effective in lowering the

quantisation noise contribution per bin. The practical hardware implementation showed that, for the specific setup, quantisation noise presented the limit in terms of the extraction accuracy.

Solutions for converting the extracted imbalance parameters over the frequency band of interest, into a frequency-dependent compensation filter was presented in Section 4.4. It was shown through analysis and confirmed through simulation that, when the BPF imbalances exist in the front end, then the resulting gain and phase imbalance functions will be asymmetrical functions of frequency. It was shown analytically and through simulation how this in turn will lead to a desired compensation filter response that does not exhibit Hermitian symmetry. In this case, only a filter with a complex-valued transfer function will be able to exhibit the required frequency response. It was furthermore shown analytically that, when the gain imbalance function is even and the phase imbalance (after the DC phase is removed) is odd, (as will be the case when the frequency-dependent imbalances can sufficiently be represented by an imbalanced LPF) then a real-valued compensation filter can be employed, along with separate phase compensation.

Since it was shown in Section 5.3 that the extracted gain and phase imbalance functions of the practical quadrature modulator and demodulator are asymmetrical functions of frequency, it can be concluded that only a complex-valued compensation filter will be able to effectively compensate for imbalances of this nature. This confirms Hypothesis 2.2:

**Hypothesis 2.2:**

> In order to effectively compensate for the frequency-dependent imbalances characteristics exhibited by practical modulators and demodulators, a complex-valued compensation filter is essential.

Subsequently, such complex-valued FIR compensation filters were designed and tested in the hardware implementation. It was found that the RIR of both the practical modulator and demodulator could be improved by at least 30-40 dB. This confirms Hypothesis 2.3:

**Hypothesis 2.3:**

> The imbalance extraction and compensation techniques of this dissertation will be effective in significantly improving the image rejection capabilities of a practical hardware implementation of a quadrature modulator and demodulator.

It was verified in the hardware implementation that, in practice, relatively short filters are sufficient to provide frequency-dependent compensation, since the gain and phase imbalance functions of practical quadrature systems should be fairly smooth functions over frequency.

It was also confirmed that, for the practical hardware implementation presented in this dissertation, the imbalances of the front end changes substantially over frequency, yielding a conventional frequency-independent compensation approach inadequate. This was measured by using the imbalances extracted at a single frequency, to apply compensation for all frequencies in the frequency band of interest.

In the development of the imbalance extraction techniques of Chapter 4, it was shown how the imbalances of a cascaded modulator and demodulator can be separated and individually extracted from the same received signal. This was shown to be possible using the correct test signals – in this case test tones and by ensuring that a small frequency offset can be introduced between the LO signals of the modulator and demodulator. The underlying principle in this case is the fact that, due to the frequency offset, the image components of the test tone due to modulator and demodulator imbalances will reside at different frequencies. Since the extraction techniques extract the imbalances directly from the frequency spectrum of the received signal, it simply becomes a matter of analysing the right spur in the frequency domain, in order to extract either the modulator imbalances, or those of the demodulator. The validity of this approach was tested in simulation as well as in the hardware implementation, where the setup involved exactly this scenario: an imbalanced modulator, generating test tones that are directly fed into a demodulator for imbalance extraction in its digital domain. When used for compensation, the extracted imbalances proved to individually compensate the modulator and demodulator's imbalances, therefore proving that they were successfully separated. This proves Hypothesis 3:

**Hypothesis 3:**

> The frequency-dependent imbalance contributions of a cascaded quadrature modulator and demodulator can be separated and extracted from the same signal, given an appropriate choice of test signal and a small frequency difference between the local oscillator (LO) signals of the two quadrature mixers.

### 7.2.3 Blind frequency-independent imbalance extraction and compensation

Chapter 6 presented the development of a novel blind imbalance extraction and compensation technique, which uses the second-order statistics of the received signal to extract the imbalances of the front end. The underlying principle is that quadrature imbalances will introduce correlation between a signal's real and imaginary components that were previously uncorrelated prior to transmission. Through analysis of the covariance matrix of a signal that has passed through an imbalanced quadrature front end, the effect of quadrature imbalances can be identified. It is therefore assumed that the original signal's real and imaginary components are uncorrelated (and generally have equal mean power). In this case a Cholesky decomposition can be used to extract the imbalances of the front end from the covariance matrix of the received signal.

In the analysis of Chapter 6, the cascaded imbalanced modulator and demodulator case was addressed, where it was shown that, once again, a frequency offset between their respective LOs enables the separation of their imbalance effects. In this case the frequency offset was shown to diagonalise the covariance matrix of the signal, including all the effects before the demodulator, and therefore the correlation observed in the received signal's covariance

matrix can be attributed to demodulator imbalances. After demodulator compensation and carrier synchronisation, the observed correlation in the covariance matrix of the resultant signal can now be attributed to the modulator imbalances, and therefore the same technique can again be employed to extract the imbalances of the modulator. The analytical derivation was verified through various simulations presented in the Chapter 6. This proves Hypothesis 4:

**Hypothesis 4:**

The frequency-independent imbalances of a cascaded quadrature modulator and demodulator can be separated and extracted using the second-order statistics of the received signal, during normal operation, without knowledge of the exact data that was transmitted.

Another conclusion from the development of the blind technique is that demodulator imbalance extraction is independent of carrier frequency or phase offset or the effect of a frequency-selective channel. For modulator imbalances to be extracted at the demodulator it was, however, seen that carrier synchronisation and channel equalisation need to be performed before its imbalances can be extracted. Furthermore, it was seen that AWGN in the transmission channel does not deteriorate the performance of demodulator imbalance extraction, but does limit the performance of the modulator, since it causes diagonal loading of the analysed covariance matrix.

## 7.3 Summary of contributions

The novel contributions of this dissertation are discussed below and are grouped as pertaining to imbalance modelling, as well as the two novel imbalance compensation approaches that were developed in this dissertation.

### 7.3.1 Modelling

- An in-depth mathematical analysis, from first principles, of the detrimental effects of imbalances on the image rejection performance of the quadrature mixing front-end, was performed. This analysis include both frequency-independent and dependent imbalances of the quadrature modulator and demodulator. Very little literature currently exists on the modelling of modulator frequency-dependent imbalances.

- The current modelling approaches in literature was shown to be inadequate to fully model the imbalance characteristics observed in practical quadrature mixing front ends. The compensation techniques based on these models will therefore not be able to provide effectively frequency-dependent compensation.

- The models presented in this dissertation extended the current theory by also modelling the bandpass imbalances present in practical quadrature front ends. This has

significant effect on the compensation approach which should be followed in order to effectively compensate for imbalances of this nature. The validity of this approach was established through measurements of the imbalance characteristics of a hardware quadrature mixing implementation.

- The models derived in this dissertation can be seen as general models, for which all other models referenced from literature were shown to be special cases.

- The models presented in this dissertation provide unique insight into the interaction and characteristics of the different imbalance contributions in the front end that has not been presented in literature before. This insight informed the compensation approach. Three approaches were presented, including a frequency-independent solution, a frequency-dependent solution involving a real-valued compensation filter with separate phase correction, as well as a complex-valued compensation filter. The scenario where each approach is applicable was shown directly from the modelling.

### 7.3.2 Novel frequency-dependent imbalance compensation techniques

- Novel frequency-dependent imbalance compensation techniques were presented for the quadrature modulator and demodulator. These techniques showed that using the developed baseband-equivalent models and appropriate test signals, the quadrature imbalances of the modulator and demodulator can be extracted directly, without the need for iterative search techniques.

- Analysis was presented for the cascaded imbalance case where an imbalanced quadrature modulator and demodulator are employed. A strategy was presented to separate and extract the imbalance contributions of the modulator and demodulator from the down converted received signal.

- A solution for automatic transceiver imbalance compensation was presented, which exploits the scenario where a quadrature modulator and demodulator exists on the same transceiver. The technique is intended as a rapid start-up calibration procedure, which could be repeated at irregular intervals if required. This approach only requires a feedback path to be added to the existing transceiver architecture.

- The effectiveness of the developed compensation techniques was verified in simulation and a practical hardware implementation of a quadrature modulator and demodulator.

### 7.3.3 A novel frequency-independent blind imbalance compensation technique

- A novel blind imbalance compensation approach was developed with two different implementational forms: a block-based approach, as well as an adaptive variant which tracks the imbalances in the front end over time.
- It was shown analytically and through simulation how modulator and demodulator imbalances can be separated and extracted by only analysing the received signal, without knowledge of the transmitted signal.
- It was shown analytically how the technique is inherently independent of frequency of phase synchronisation and a frequency selective channel.
- The performance of the technique was verified through simulation, in the presence of additive white Gaussian noise (AWGN), as well as in a frequency-selective channel.

## 7.4 Concluding remarks

Arguments dismissing the quadrature demodulator and modulator as viable mixing front-ends on grounds of their sensitivity towards mismatches between their two signal paths, can no longer be seen as valid when digital compensation is possible. In this study it was shown that the advantages of the quadrature mixing front end can indeed be harnessed by reversing the imbalance and offset errors in the digital domain. Precision-designed hardware is therefore not required to implement a quadrature mixing front-end. Rather, the emphasis can now be shifted towards using low-cost components in conjunction with software compensation algorithms.

# Bibliography


[1] ABIDI, A. A., "Direct-Conversion Radio Transceivers for Digital Communications." *IEEE Journal of Solid-State Circuits*, December 1995, Vol. 30, No. 12, pp. 1399–1410.

[2] ANTTILA, L. *et al.*, "Blind moment estimation techniques for I/Q imbalance compensation in quadrature receivers." in *Proc. IEEE Int. Symp. Pers., Indoor, Mobile Radio Commun. (PIMRC'06)*, (Helsinki, Finland), pp. 2611–2614, September 2006.

[3] ANTTILA, L., VALKAMA, M., and RENFORS, M., "Blind moment estimation techniques for I/Q imbalance compensation in quadrature receivers." in *Proc. IEEE Int. Symp. Pers., Indoor, Mobile Radio Commun. (PIMRC'06)*, (Helsinki, Finland), pp. 2611–2614, 2006.

[4] ANTTILA, L., VALKAMA, M., and RENFORS, M., "Blind Compensation of Frequency-Selective I/Q Imbalances in Quadrature Radio Receivers: Circularity -Based Approach." in *IEEE Int. Conf. on Acoustics, Speech and Sig. Proc. (ICASSP 2007)*, vol. 3, (Helsinki, Finland), pp. III–245 – III–248, 2007.

[5] ANTTILA, L., VALKAMA, M., and RENFORS, M., "Circularity-Based I/Q Imbalance Compensation in Wideband Direct-Conversion Receivers." July 2008, Vol. 57, No. 4, pp. 2099 – 2113.

[6] BENNETT, W. R., "Spectra of quantized signals." *Bell Systems Technical Journal*, 1948, Vol. 27, pp. 446–472.

[7] CARDOSO, J.-F. and LAHELD, B. H., "Equivariant adaptive source separation." *IEEE Transactions on Signal Processing*, December 1996, Vol. 44, No. 12, pp. 3017–3030.

[8] CAVERS, J. K., "New methods for adaptation of quadrature modulators and demodulators in amplifier linearization circuits." *IEEE Transactions on Vehicular Technology*, August 1997, Vol. 46, No. 3, pp. 707–716.

[9] CAVERS, J. K. and LIAO, M. W., "Adaptive compensation for imbalance and offset losses in direct conversion transceivers." *IEEE Transactions on Vehicular Technology*, November 1993, Vol. 42, No. 4, pp. 581–588.

[10] CETIN, E., KALE, I., and MORLING, R. C. S., "On the structure, convergence and performance of an adaptive I/Q mismatch corrector." *IEEE 56th Vehicular Technology Conference (VTC 2002-Fall)*, 24-28 September 2002, Vol. 4, pp. 2288–2292.

[11] CETIN, E., KALE, I., and MORLING, R. C. S., "Performance of an adaptive homodyne receiver in the presence of multipath, Rayleigh-fading and time-varying quadrature errors." *Proceedings of the 2003 International Symposium on Circuits and Systems (ISCAS 2003)*, 25-28 May 2003, Vol. 4, pp. 69–72.

[12] CETIN, E., KALE, I., and MORLING, R., "Adaptive compensation of analog front-end I/Q mismatches in digital receivers." *The 2001 IEEE International Symposium on Circuits and Systems (ISCAS 2001)*, 6-9 May 2001, Vol. 4, pp. 370–373.

[13] CHAKRA, S. A. and HUYART, B., "Auto calibration with training sequences for wireless local loop at 26 GHz." *IEEE Microwave and Wireless Components Letters*, August 2004, Vol. 14, No. 8, pp. 392–394.

[14] CHURCHILL, F. E., OGAR, G. W., and THOMPSON, B. J., "The Correction of I and Q Errors in a Coherent Processor." *IEEE Transactions on Aerospace and Electronic Systems*, January 1981, Vol. AES-17, pp. 131–137.

[15] CLAASEN, T. A. C. M. and JONGEPIER, A., "Model for the power spectral density of quantization noise." *IEEE Transactions on Acoustics, Speech, Signal Processing*, 1981, Vol. ASSP-29, pp. 914–917.

[16] COMPERNOLLE, D. and VAN GERVEN, S., "Signal separation in a symmetric adaptive noise canceler by output decorrelation." *IEEE International Conference on Acoustics, Speech, and Signal Processing, 1992. ICASSP-92*, 23-26 March 1992, Vol. 4, pp. 221–224.

[17] CROLS, J. and STEYAERT, M. S. J., "Low-IF Topologies for High-Performance Analog Front Ends of Fully Integrated Receivers." *IEEE Transactions on Circuits and SystemsII: Analog and Digital Signal Processing*, March 1998, Vol. 45, No. 3, pp. 269–282.

[18] CRONJÉ, J. J., *Software Architecture Design of a Software Defined Radio System*. Masters thesis, Stellenbosch University, 2004.

[19] DOUGLAS, S. C., "Simple adaptive algorithms for Choleski, LDT$^T$, QR and eigenvalue decomposition of autocorrelation matrices for sensor array data." *Conf. record of the thirty-fifth Asilomar conf. on sys. and computers 2001*, 2001, Vol. 2, pp. 1134–1138.

[20] FAULKNER, M. and LEYONHJELM, S. A., "The Effect of Reconstruction Filters on Direct Upconversion in a Multichannel Environment." *IEEE Transactions on Vehicular Technology*, February 1995, Vol. 44, No. 1, pp. 95–102.

[21] FAULKNER, M., MATTSSON, T., and YATES, W., "Automatic adjustment of quadrature modulators." *IEEE Electronics Letters*, 31 January 1991, Vol. 27, No. 3, pp. 214–216.

[22] GEORGIADIS, A., "Gain, Phase Imbalance, and Phase Noise Effects on Error Vector Magnitude." *IEEE Transactions on Vehicular Technology*, March 2004, Vol. 53, No. 2, pp. 443–449.

[23] GOLUB, G. H. and VAN LOAN, C. F., *Matrix Computations*. Second edition. Baltimore and London: The Johns Hopkins University Press, 1989.

[24] HAYKIN, S., *Adaptive filter theory*. Fourth edition. Upper Saddle River, New Jersey: Prentice-Hall, 2002.

[25] HILBORN, D. S., STAPLETON, S. P., and CAVERS, J. K., "An adaptive direct conversion transmitter." *IEEE Transactions on Vehicular Technology*, May 1994, Vol. 43, No. 2, pp. 223–233.

[26] HUANG, X., "On transmitter gain/phase imbalance compensation at receiver." *IEEE Communications Letters*, November 2000, Vol. 4, No. 11, pp. 363–365.

[27] HYVÄRINEN, A., KARHUNEN, J., and OJA, E., *Independent component analysis*. New York: John Wiley & sons, Inc., 2001.

[28] ITU, "Guidelines for the evaluation of radio transmission technologies for IMT-2000." *Recommendation ITU-R M.1225*, 1997.

[29] KISS, P. and PRODANOV, V., "One-tap wideband I/Q compensation for zero-IF filters." *IEEE Transactions on Circuits and Systems I: Regular Papers*, June 2004, Vol. 51, No. 6, pp. 1062–1074.

[30] LAY, D. C., *Linear Algebra and its Applications*. Reading, Massachusetts: Addison-Wesley, 2000.

[31] LIM, A. G. K. C., SREERAM, V., and WANG, G.-Q., "Digital compensation in IQ modulators using adaptive FIR filters." *IEEE Transactions on Vehicular Technology*, November 2004, Vol. 53, No. 6, pp. 1809–1817.

[32] LIU, C.-L., "Impacts of I/Q Imbalance on QPSK-OFDM-QAM Detection." *IEEE Transactions on Consumer Electronics*, August 1998, Vol. 44, No. 3, pp. 984–989.

[33] MARCHESANI, R., "Digital precompensation of imperfections in quadrature modulators." *IEEE Transactions on Communications*, April 2000, Vol. 48, No. 4, pp. 552–556.

[34] MARSH, D., "Software-defined radio tunes in." *EDN*, March 3 2005, pp. 52–63.

[35] MARTIN, K. W., "Complex Signal Processing is Not Complex." *IEEE Transactions on Circuits and Systems*, 2004, Vol. 51, No. 9, No. 9, pp. 1823 – 1836.

[36] MIRABBASI, S. and MARTIN, K., "Classical and Modern Receiver Architectures." *IEEE Communications Magazine*, November 2000, pp. 132–139.

[37] MITRA, S. K., *Digital Signal Processing – a Computer-Based Approach*. Second edition. New York: McGraw-Hill, 2002.

[38] PEREZ-ALCAZAR, P. R. and SANTOS, A., "Relationship between sampling rate and quantization noise." *4th International Conference on Digital Signal Processing, DSP 2002*, 2002, Vol. 2, pp. 807 – 810.

[39] PROAKIS, J. G., *Digital Communications*. Fourth edition. Boston: McGraw-Hill, 2001.

[40] PROAKIS, J. G. and SALEHI, M., *Communication Systems Engineering*. Second edition. New Jersey: Prentice-Hall, 2002.

[41] RAZAVI, B., "Design Considerations for Direct-Conversion Receivers." *IEEE Transactions on Circuits and SystemsII: Analog and Digital Signal Processing*, June 1997, Vol. 44, No. 6, pp. 428–435.

[42] RAZAVI, B., *RF Microelectronics*. Upper Saddle River, NJ: Prentice-Hall, 1998.

[43] REDL, S. M., WEBER, M. K., and OLIPHANT, M. W., *An Introduction to GSM*. Norwood, MA: Artech House, Inc., 1995.

[44] RF MICRO DEVICES, Greensboro. *RF2713 Quadrature Modulator/Demodulator*, 2003.

[45] RYKACZEWSKI, P. *et al.*, "Multimode detector and I/Q imbalance compensator in a software defined radio." *2004 IEEE Radio and Wireless Conference*, 19-22 September 2004, pp. 521–524.

[46] RYKACZEWSKI, P. *et al.*, "Signal path optimization in Software-defined Radio Systems." *IEEE Transactions on Microwave Theory and Techniques*, March 2005, Vol. 53, No. 3, Part 2, pp. 1056–1064.

[47] RYKACZEWSKI, P. *et al.*, "Non-data-aided I/Q imbalance compensation using measured receiver front-end signals." in *Proc. IEEE Int. Symp. Pers., Indoor, Mobile Radio Commun. (PIMRC06)*, (Helsinki, Finland), 2006.

[48] RYKACZEWSKI, P. and JONDRAL, F., "Blind I/Q Imbalance Compensation in Multipath Environments." in *Proc. Int. Symp. Circuits and Systems, 2007. (ISCAS'07)*, (New Orleans, LA), pp. 29–32, May 2007.

[49] RYKACZEWSKI, P., VALKAMA, M., and RENFORS, M., "On the Connection of I/Q Imbalance and Channel Equalization in Direct-Conversion Transceivers." *IEEE Trans. Veh. Technol.*, May 2008, Vol. 57, No. 3, pp. 1630–1636.

[50] SOHN, I.-H., JEONG, E.-R., and LEE, Y. H., "Data-aided approach to I/Q mismatch and DC offset compensation in communication receivers." *IEEE Communications Letters*, December 2002, Vol. 6, No. 12, pp. 547–549.

[51] SOUTH AFRICAN BUREAU OF STANDARDS. *Digital broadcasting systems for television sound and data services – Framing structure, channel coding and modulation for cable systems*, 1994. SABS ETS 300 429:1994.

[52] SOUTH AFRICAN BUREAU OF STANDARDS. *Low power radio broadcast transmission - Part 2: FM transmissions*, 1997. SABS 1790–2:1997.

[53] STELLENBOSCH UNIVERSITY, "SDR Research Group Home Page." `http://www.dsp.sun.ac.za/sdr`.

[54] STORMYRBAKKEN, C., *Automatic compensation for inaccuracies in quadrature mixers*. Masters thesis, Stellenbosch University, 2005.

[55] TARIGHAT, A., BAGHERI, R., and SAYED, A. H., "Compensation Schemes and Performance Analysis of IQ Imbalances in OFDM Receivers." *IEEE Trans. Signal Processing*, August 2005, Vol. 53, No. 8, pp. 3257–3268.

[56] TSURUMI, H. and SUZUKI, Y., "Broadband RF Stage Architecture for Software-defined Radio in Handheld Terminal Applications." *IEEE Communications Magazine*, February 1999, pp. 90–95.

[57] TUBBAX, J. *et al.*, "Compensation of IQ Imbalance and Phase Noise in OFDM Systems." *IEEE Trans. Wireless Commun.*, May 2005, Vol. 4, No. 3, pp. 872–877.

[58] TUTHILL, J. and CANTONI, A., "Optimum precompensation filters for IQ modulation systems." *IEEE Transactions on Communications*, October 1999, Vol. 47, No. 10, pp. 1466–1468.

[59] TUTHILL, J. and CANTONI, A., "Efficient compensation for frequency-dependent errors in analog reconstruction filters used in IQ modulators." *IEEE Transactions on Communications*, March 2005, Vol. 53, No. 3, pp. 489–496.

[60] VALKAMA, M., *Advanced I/Q signal processing for wideband receivers: Models and Algorithms*. Ph.D. dissertation, Tampere University of Technology, 2001.

[61] VALKAMA, M. and RENFORS, M., "A novel image rejection architecture for quadrature radio receivers." *IEEE Transactions on Circuits and Systems II: Express Briefs*, February 2004, Vol. 51, No. 2, pp. 61–68.

[62] VALKAMA, M., RENFORS, M., and KOIVUNEN, V., "Blind source separation based I/Q imbalance compensation." *The IEEE Adaptive Systems for Signal Processing, Communications, and Control Symposium (AS-SPCC 2000)*, 1-4 October 2000, pp. 310–314.

[63] VALKAMA, M., RENFORS, M., and KOIVUNEN, V., "BSS based I/Q imbalance compensation in communication receivers in the presence of symbol timing errors." *Second International Workshop on Independent Component Analysis and Blind Signal Separation*, June 2000, pp. 393–398.

[64] VALKAMA, M., RENFORS, M., and KOIVUNEN, V., "On the performance of interference canceller based I/Q imbalance compensation." *IEEE International Conference on Acoustics, Speech, and Signal Processing (ICASSP 2000)*, 5-9 June 2000, Vol. 5, pp. 2885–2888.

[65] VALKAMA, M., RENFORS, M., and KOIVUNEN, V., "Advanced methods for I/Q imbalance compensation in communication receivers." *IEEE Transactions on Signal Processing*, October 2001, Vol. 49, No. 10, pp. 2335–2344.

[66] VALKAMA, M., RENFORS, M., and KOIVUNEN, V., "Blind signal estimation in conjugate signal models with application to I/Q imbalance compensation." *IEEE Signal Processing Lett.*, November 2005, Vol. 12, pp. 733–736.

[67] VAN ROOYEN, G.-J., *Baseband Compensation Principles for Defects in Quadrature Signal Conversion and Processing*. Ph.D. dissertation, Stellenbosch University, 2004.

[68] WEITZEL, C. E., "RF Power Amplifiers for Cell-phones." *2003 GaAs Mantech Conference Digest*, 2003. Paper 2.2.

[69] WIDROW, B. and KOLLAR, I., *Quantization Noise*. Cambridge: Cambridge University Press, 2008.

[70] WIDROW, B. and STEARNS, S. D., *Adaptive signal processing*. Englewood Cliffs, New Jersey: Prentice-Hall, 1985.

[71] WINDISCH, M. and FETTWEIS, G., "Adaptive I/Q imbalance compensation in low-IF transmitter architectures." *2004 IEEE 60th Vehicular Technology Conference*, September 2004, Vol. 3, pp. 2096–2100.

[72] WINDISCH, M. and FETTWEIS, G., "Blind I/Q imbalance parameter estimation and compensation in low-IF receivers." *First International Symposium on Control, Communications and Signal Processing*, 2004, pp. 75–78.

[73] WINDISCH, M. and FETTWEIS, G., "Performance analysis for blind I/Q imbalance compensation in low-IF receivers." *First International Symposium on Control, Communications and Signal Processing*, 2004, pp. 323–326.

[74] WINDISCH, M. and FETTWEIS, G., "Standard-Independent I/Q Imbalance Compensation in OFDM Direct-Conversion Receivers." in *Proc. 9th Int. OFDM-Workshop (InOWo'04)*, (Dresden, Germany), September 2004.

[75] WOJTIUK, J. J., "Analysis of Frequency Conversion for M-QAM and M-PSK Modems." Master's thesis, The University of South Australia School of Electronic Engineering, Mawson Lakes, South Australia, 1995.

[76] WRIGHT, A. R. and NAYLOR, P. A., "I/Q mismatch compensation in zero-IF OFDM receivers with application to DAB." *2003 IEEE International Conference on Acoustics, Speech, and Signal Processing (ICASSP 2003)*, 6-10 April 2003, Vol. 2, pp. 329–332.

[77] XING, G., SHEN, M., and LIU, H., "Frequency offset and I/Q imbalance compensation for direct-conversion receivers." *IEEE Transactions on Wireless Communications*, March 2005, Vol. 4, No. 2, pp. 673–680.

[78] YU, L. and SNELGROVE, W. M., "A novel adaptive mismatch cancellation system for quadrature IF radio receivers." *IEEE Transactions on Circuits and Systems II: Analog and Digital Signal Processing*, June 1999, Vol. 46, No. 6, pp. 789–801.

# Appendix A

# FIR filter design using least squares optimisation – a method by Tuthill and Cantoni

In their work (see [59]), Tuthill and Cantoni poses the design goal to find the optimum tap weights of a length $K$ FIR compensation filter, such that the difference between some desired response and the a cascaded response of the designed filter and a current system response, is minimised. Let the FIR tap weights be contained in the vector $\boldsymbol{g} \in \mathbb{C}^{K\times 1}$. For a given desired response $D(e^{j\omega T})$ and a current system response $H_d(e^{j\omega T})$, [59] suggests that one can construct an appropriate cost function in the frequency domain as

$$\min_{g} J(g) = \sum_{n=1}^{N} \left| D(e^{j\omega_n T}) - \boldsymbol{g}^T \boldsymbol{s}(e^{j\omega_n T}) H_d(e^{j\omega_n T}) \right|^2 \ , \tag{A.1}$$

where $\omega = 2\pi f$ and $T$ indicates the discrete time sampling period. The $k^{\text{th}}$ row in the vector $\boldsymbol{s}(e^{j\omega T}) \in \mathbb{C}^{K\times 1}$ is given by

$$\left[\boldsymbol{s}(e^{j\omega T})\right]_k = e^{-j\omega(k-1)T}, \quad k = 1, 2, \ldots K. \tag{A.2}$$

This cost function makes sense since $\boldsymbol{g}^T \boldsymbol{s}(e^{j\omega_n T})$ is the discrete Fourier transform (DFT) of the FIR compensation filter at frequency $\omega_n$. $\boldsymbol{g}^T \boldsymbol{s}(e^{j\omega_n T}) H_d(e^{j\omega_n T})$ denotes the cascaded effect of the compensation FIR filter with the estimation of the current system's response, at frequency $\omega_n$.

For the purpose of using this technique for the design of an $I/Q$ imbalance compensation filter, the desired response was chosen to be equal to either $Q_2(f)$ or $P_2(f)$ (as derived in Section 4.2.2), for the respective cases of modulator or demodulator compensation, as extracted at $N$ frequency points using the test tones. The current system response $H_d(e^{j\omega_n T})$ is not applicable, and was set to unity.

The cost function defined in equation (A.1), can be written in matrix form as [59]

$$J(\boldsymbol{g}) = \gamma - \boldsymbol{g}^T \boldsymbol{p} + \frac{1}{2} \boldsymbol{g}^T \boldsymbol{R} \boldsymbol{g}, \tag{A.3}$$

where $\boldsymbol{R} \in \mathbb{R}^{K\times K}$, $\boldsymbol{p} \in \mathbb{R}^{K\times 1}$ and $\gamma$ are defined as [1]

$$\boldsymbol{R} = 2\sum_{n=1}^{N} \mathcal{R}e\Big\{ \boldsymbol{s}(e^{j\omega_n T})\boldsymbol{s}^H(e^{j\omega_n T}) \left|H_d(e^{j\omega_n T})\right|^2 \Big\} \tag{A.4}$$

$$\boldsymbol{p} = 2\sum_{n=1}^{N} \mathcal{R}e\Big\{ D(e^{j\omega_n T})\boldsymbol{s}^*(e^{j\omega_n T})H_d^*(e^{j\omega_n T}) \Big\} \tag{A.5}$$

$$\gamma = \sum_{n=1}^{N} \left|D(e^{j\omega_n T})\right|^2 . \tag{A.6}$$

In order to find the optimum tap weights which would minimise equation (A.3), the cost function must be differentiated towards $\boldsymbol{g}$ and equated to zero [70, p. 21]. Differentiating $J(\boldsymbol{g})$ in terms of the tap weights $\boldsymbol{g}$ yields

$$\frac{\partial J(\boldsymbol{g})}{\partial \boldsymbol{g}} = -\boldsymbol{p} + \boldsymbol{R}\boldsymbol{g} \ . \tag{A.7}$$

Equating this derivative to zero, yields the optimum tap weights $\boldsymbol{g}^{\text{opt}} \in \mathbb{R}^{K\times 1}$ as

$$\boldsymbol{g}^{\text{opt}} = \boldsymbol{R}^{-1}\boldsymbol{p} \ . \tag{A.8}$$

It is thus seen that in order to compute the optimum tap weights, a set of linear equations has to be solved. This process is complicated by the fact that, due to numerical issues, the solution matrix may become ill-conditioned [59] (i.e. $\boldsymbol{R}$ becomes close to singular). Usually, some regularisation process is performed to improve the numerical properties of the solution matrix [59]. For example, in [58] the authors noted that the eigenvalues of $\boldsymbol{R}$ drop off sharply at a certain point. After this drop-off the eigenvalues are close to zero and could be discarded, improving the numerical condition of $\boldsymbol{R}$. In [59], the authors provide two other techniques to improve the conditioning of the solution matrix. These methods were used in this study and will be discussed next.

The first technique involves the choice of the $N$ frequency points where the cost function $J(\boldsymbol{g})$ is evaluated. The authors of [59] suggest choosing $N$ frequency points that are uniformly distributed on the interval[2]

$$\omega_n \in \Big[ -\xi\frac{\omega_s}{2}, \xi\frac{\omega_s}{2}\Big], \quad n = 1, 2, \ldots, N \ , \tag{A.9}$$

where $0 < \xi < 1$ and $\omega_s = 2\pi f_s$ is the sampling frequency. By choosing $\xi < 1$, very small values of $H_d(e^{j\omega_n T})$ are avoided, which improves the numerical properties of the solution matrix [59]. Another advantage is that the available degrees of freedom of the compensation

---

[1] Equation A.4 contains a small modification to the original text of [59]. In the original text the real operator, $\mathcal{R}e$, is not included.

[2] In [59], Tuthill and Cantoni define $\omega_n \in \Big(0, \xi\frac{\omega_s}{2}\Big]$, aligning with their goal to design real-valued FIR filters. By including negative frequencies, their design method was found to be capable of designing complex valued FIR filters as well.

filter are used more effectively on the chosen frequency band of interest. The authors of [59] do, however, note that there exists a trade-off when choosing the number of frequency points, $N$. A small number of frequency points ensures numerical robustness; however, that in turn means that the cost function is specified for less points, making the solution less optimal to the actual problem at hand. To alleviate this trade-off, the authors of [59] present a second method to improve the numerical properties of the solution matrix.

The second technique involves keeping the length of the FIR compensation filter as $K$, but only having $M \leq K$ active taps. This involves having $L$ zero-valued taps between each active tap. This approach has the advantage of significantly improving the numerical condition of the resulting solution matrix, thus allowing a sufficient number frequency points ($N$) to be used [59]. Results presented in [59] show that the same performance was achieved using a FIR filter designed in this way using a value $L = 2$, as was achieved by a FIR filter with all its taps active, using the eigenvalue-based regularisation process of [58]. What is gained through the use of fewer active taps, is that the computational burden of the design process, as well as the actual filtering operation of the implemented filter are significantly reduced. The details of adapting the cost function to take into account the fact that not all taps are active, is presented in Appendix A.

To implement the method of reduced active filter taps, the following procedure, as outlined in [59], has to be used. Note that because not all taps of $\boldsymbol{g}$ are active (i.e. non-zero), the $i^{\text{th}}$ element of the filter tap weight vector $\boldsymbol{g}$ now becomes

$$[\boldsymbol{g}]_i = \begin{cases} g_i & i \in S^A, \\ 0 & i \in S^Z, \end{cases} \quad g_i \in \mathbb{R}, \tag{A.10}$$

with $S^A$ being the length $M$ ordered list of indices of non-zero entries in the vector $\boldsymbol{g}$ and is given as

$$S^A = \{1, L+2, 2L+3, \ldots, K\} \ . \tag{A.11}$$

$S^Z$ is the length $K - M$ ordered list of indices of zero-valued entries in the vector $\boldsymbol{g}$. A new vector $\boldsymbol{q} \in \mathbb{R}^{M \times 1}$ is now defined containing the $M$ non-zero taps of $\boldsymbol{g}$. The $i^{\text{th}}$ value of $\boldsymbol{q}$ is given by

$$[\boldsymbol{q}]_i = [\boldsymbol{g}]_{[S^A]_i}, \quad i = 1, 2, \ldots, M \ . \tag{A.12}$$

In [59], it is shown that the cost function $J(\boldsymbol{g})$ of (A.3) can be written as a function of this new tap weight vector as

$$J(\boldsymbol{q}) = \gamma - \boldsymbol{q}^T \boldsymbol{p}_U + \frac{1}{2} \boldsymbol{q}^T \boldsymbol{R}_U \boldsymbol{q} \ , \tag{A.13}$$

where $\boldsymbol{R}_U \in \mathbb{R}^{M \times M}$ and $\boldsymbol{p}_U \in \mathbb{R}^{M \times 1}$ are derived from $\boldsymbol{R}$ and $\boldsymbol{p}$, respectively, as

$$[\boldsymbol{R}_U]_{i,j} = [\boldsymbol{R}]_{[S^A]_i, [S^A]_j} \ , \quad i, j = 1, 2, \ldots, M \tag{A.14}$$

$$[\boldsymbol{p}_U]_k = [\boldsymbol{p}]_{[S^A]_k} \ , \quad k = 1, 2, \ldots, M \ . \tag{A.15}$$

The optimum weight tap vector which would minimise $J(\boldsymbol{q})$ is then similar to $J(\boldsymbol{g})$, given by [59]

$$\boldsymbol{q}^{\text{opt}} = \boldsymbol{R}_U^{-1}\boldsymbol{p}_U \ . \tag{A.16}$$

From $\boldsymbol{q}^{\text{opt}}$, the FIR filter taps are computed by simply inserting $L$ zero-valued taps between each successive value in $\boldsymbol{q}^{\text{opt}}$.

# Appendix B

# Quantisation noise spectra of periodic signals

A commonly used method to model quantisation noise, was presented by Bennett in 1948 [6]. In his work he proposes that the effect of quantisation noise can be modelled as a desired signal with an additive white noise source, since the quantisation error signal should be 'practically independent' from the desired signal. In his work, Bennett showed that the mean square error due to quantisation is given by $E_o^2/12$, where $E_o$ represents the quantisation interval size. For a sinusoidal input of full scale amplitude $V_{fs}$, quantised using a bit resolution $B$, $E_o$ is given by

$$E_o = \frac{V_{fs}}{2^{B-1}}\,. \tag{B.1}$$

The quantisation noise power is subsequently given by

$$P_{Qn} = \frac{V_{fs}^2}{(12)2^{2B-2}}\,. \tag{B.2}$$

The desired signal power is given by

$$P_s = V_{FS}^2/2 \tag{B.3}$$

and thus the signal to quantisation noise ratio (SQNR) is given by

$$\begin{aligned} SQNR(B) &= \frac{P_s}{P_{Qn}} \\ &= (12)(2^{2B-2})\,. \end{aligned} \tag{B.4}$$

On a decibel scale the above expression is written as the well known result:

$$SQNR_{dB}(B) = 10\log_{10}(12/6) + 20B\log_{10}(20) \tag{B.5}$$

$$= 1.76 + 6.02B\,. \tag{B.6}$$

The above result thus predicts the dynamic range of signal when the quantisation noise spectra can be considered to be white. Claasen and Jongepier [15], however, argues that the quantisation noise spectra will only be white if the signal that is being quantised exhibits

sufficient variation. This criteria is not always satisfied by sinusoidal signals, for which the quantisation noise spectra can exhibit line spectral components, harmonically related to the input signal's frequency.

A number of authors have presented conditions to ensure whiteness of the quantisation noise spectra. Widrow and Kollar summarises the premise of these conditions as [69, p.561]:

> "The basic issue is, when performing analog-to-digital conversion on an input signal, how fine must the quantization be in order that the quantization noise be white? In general, the higher the sampling rate, the finer the quantization must be to achieve whiteness of the quantization noise."

Widrow and Kollar subsequently presents one such condition for whiteness, for sinusoidal input signals, which is a slight modification of a condition originally given by Claasen and Jongepier in [15]. Widrow and Kollar suggests that in order to ensure a white quantisation spectrum for a sinusoidal input signal, the sampling rate $f_s$ should be chosen such that [69, p.554],

$$f_s < 0.5\pi f_0 A/E_0 \tag{B.7}$$

where $f_0$ represent the input frequency, $A$ the amplitude and $E_0$ the quantisation interval. It is the opinion of the author, though, that this result seem to be more applicable when large oversampling ratios are considered.

Perez-Alcazar and Santos [38] show, through simulation, that the quantisation noise spectra related to sinusoidal input signals, seem to behave in a chaotic manner, exhibiting a well defined structure for some frequencies and less structure (more stochastic) for others. They confirm that the quantisation noise spectra contains harmonic components, when there exists an integer relationship between the input signal frequency and the sampling rate, as well as for some rational relationships between the two. They also show that the signal amplitude and phase effect the structure of these harmonics.